NATURAL DYE EXTRACT FROM *Ixora siamensis* AS LIGHT HARVESTER FOR DYE-SENSITIZED SOLAR CELLS WITH NANOSTRUCTURED TiO_2

NUR AMIRAH BINTI MAT NOR

FACULTY OF SCIENCE
UNIVERSITY OF MALAYA
KUALA LUMPUR

2019

NATURAL DYE EXTRACT FROM *Ixora siamensis* AS LIGHT HARVESTER FOR DYE-SENSITIZED SOLAR CELLS WITH NANOSTRUCTURED TiO_2

NUR AMIRAH BINTI MAT NOR

THESIS SUBMITTED IN FULFILMENT OF THE REQUIREMENTS FOR THE DEGREE OF DOCTOR OF PHILOSOPHY

DEPARTMENT OF PHYSICS
FACULTY OF SCIENCE
UNIVERSITY OF MALAYA
KUALA LUMPUR

2019

UNIVERSITY OF MALAYA

ORIGINAL LITERARY WORK DECLARATION

Name of Candidate: **NUR AMIRAH BINTI MAT NOR**

Matric No: **SHC130103**

Name of Degree: **DOCTOR OF PHILOSOPHY (EXCEPT MATHEMATICS & SCIENCE PHILOSOPHY)**

Title of Thesis ("this Work"):

NATURAL DYE EXTRACT FROM *Ixora siamensis* AS LIGHT HARVESTER FOR DYE-SENSITIZED SOLAR CELLS WITH NANOSTRUCTURED TiO_2 Field of Study: **EXPERIMENTAL PHYSICS**

I do solemnly and sincerely declare that:

(1) I am the sole author/writer of this Work;
(2) This Work is original;
(3) Any use of any work in which copyright exists was done by way of fair dealing and for permitted purposes and any excerpt or extract from, or reference to or reproduction of any copyright work has been disclosed expressly and sufficiently and the title of the Work and its authorship have been acknowledged in this Work;
(4) I do not have any actual knowledge nor do I ought reasonably to know that the making of this work constitutes an infringement of any copyright work;
(5) I hereby assign all and every rights in the copyright to this Work to the University of Malaya ("UM"), who henceforth shall be owner of the copyright in this Work and that any reproduction or use in any form or by any means whatsoever is prohibited without the written consent of UM having been first had and obtained;
(6) I am fully aware that if in the course of making this Work I have infringed any copyright whether intentionally or otherwise, I may be subject to legal action or any other action as may be determined by UM.

Candidate's Signature Date:

Subscribed and solemnly declared before,

Witness's Signature Date:

Name:

Designation:

NATURAL DYE EXTRACT FROM *Ixora siamensis* AS LIGHT HARVESTER FOR DYE-SENSITIZED SOLAR CELLS WITH NANOSTRUCTURED TiO_2

ABSTRACT

Research towards new natural dye sources along with eco-friendly and cost-effective technologies have greatly aided in various applications. Dye-sensitized solar cells (DSSCs) become more interesting since a huge variety of natural dyes from various sources can be used as light harvesting elements which provide the charge carriers. In this study, the natural dye has been extracted from *Ixora siamensis* or locally known as "jejarum" which is revealed to have the presence of anthocyanin compounds containing cyanidin-3-rutinoside, delphinidin glucoside and peonidin-3-glucoside. Response surface methodologies (RSM) were used to investigate the effect of extraction parameters and evaluate the optimized extraction conditions. The anthocyanin extraction from fruit pericarp of *Ixora siamensis* was performed by using acidified methanol in temperature between 30 and 80 ℃. The fruit pericarp of *Ixora siamensis* have been soaked for 60 to 180 min in acidified methanol with different trifluoroacetic acid (TFA) content between 0.5 to 3%. The optimized extraction parameter were 0.5% TFA, 119 min soaking time and 80 ℃ temperature. The anthocyanin extraction has been used as photosensitizer in DSSCs because anthocyanin compound has carbonyl or hydroxyl groups that can attach effectively to the surface of the porous TiO_2 film. Dye-sensitized solar cells were fabricated by sandwiching the PAN-based gel polymer electrolytes between TiO_2/dye photoanode and platinum (Pt) as the counter electrode. The morphology of the TiO_2 also played important roles in achieving high power conversion efficiency. TiO_2 electrospun materials have been produced via electrospinning technique in order to investigate the potential of these nanostructures, which will be used as metal oxide semiconductor in DSSCs application. The structures and morphology of the electrospun material have been characterized by FESEM and XRD analysis. The

efficiency for DSSCs application using P25 TiO_2 nanoparticle electrodes (D3) was (1.076 ± 0.042)% when soaked in 3 wt.% dye solution. The composite electrode of TiO_2 nanoparticle-nanorod (NPs-NRs) with inclusion of 10 wt.% NRs (CP1) have been fabricated and resulted in an increase of efficiency to (1.317 ± 0.035)% when soaked in 3 wt.% dye solution. In order to increase the efficiency performance, two types of additives; chenodeoxycholic acid (CDCA) ferulic acid (FA) are used. On addition of 1 wt.% CDCA (C1), the efficiency slightly increased to (1.393 ± 0.039)% with short current density, J_{sc} of (4.835 ± 0.095) mA cm^{-2}, open circuit voltage, V_{oc} of (0.458 ± 0.006) V and fill factor, *FF* of (0.629 ± 0.010). On addition of 3 wt.% of FA (F3), the efficiency enhanced to (1.917 ± 0.045)% with short circuit current density, J_{sc} of (6.178 ± 0.128) mA cm^{-2}, open circuit voltage, V_{oc} of (0.473 ± 0.009) V and fill factor, *FF* of (0.656 ± 0.010). It has been shown in this work that addition of CDCA and FA to the anthocyanin solution improves the efficiency of the DSSCs.

Keywords: *Ixora siamensis*, Natural dye, Anthocyanin, TiO_2, Electrospinning, Dye-sensitized solar cells (DSSCs).

PEWARNA SEMULAJADI DARIPADA *Ixora siamensis* SEBAGAI PENUAI CAHAYA DENGAN TiO_2 YANG BERSTRUKTUR NANO UNTUK SEL SOLAR PEMEKA WARNA

ABSTRAK

Penyelidikan ke arah sumber pewarna semulajadi yang baru bersama dengan teknologi mesra alam dan kos efektif telah banyak membantu dalam pelbagai aplikasi. Sel solar pemeka warna (DSSCs) menjadi lebih menarik kerana pelbagai jenis pewarna semulajadi dari pelbagai sumber boleh digunakan sebagai unsur penuaian cahaya yang menyediakan pembawa caj. Dalam kajian ini, pewarna semulajadi telah diekstrak daripada *Ixora siamensis* atau dikenali sebagai "jejarum" yang menunjukkan kehadiran sebatian antosianin yang mengandungi sianidin-3-rutinosida, delfinidin glukosida dan peonidin-3-glukosida. Metodologi permukaan tindak balas (RSM) digunakan untuk menyiasat kesan parameter pengekstrakan dan menilai keadaan pengekstrakan yang dioptimumkan. Pengekstrakan antosianin dari kulit buah *Ixora siamensis* telah dilakukan dengan menggunakan metanol berasid dalam suhu antara 30 dan 80 ℃. Kulit buah *Ixora siamensis* telah direndam selama 60 hingga 180 minit dalam metanol berasid dengan pelbagai kandungan asid trifluoroacetic (TFA) dalam julat 0.5 hingga 3%. Parameter pengekstrakan optimum ialah 0.5% TFA, 119 minit waktu merendam dan suhu 80 ℃. Pengekstrakan antosianin telah digunakan sebagai pemeka cahaya dalam DSSCs kerana sebatian antosianin mempunyai kumpulan karbonil atau hidroksil yang dapat melekat secara efektif ke permukaan lapisan TiO_2 berpori. Sel solar yang sensitif dibuat dengan mengapit elektrolit polimer gel berasaskan PAN antara TiO_2/pewarna fotoanod dan platinum (Pt) sebagai elektrod kaunter. Morfologi TiO_2 juga memainkan peranan penting dalam mencapai kecekapan penukaran kuasa yang tinggi. Bahan elektrospun TiO_2 telah dihasilkan melalui teknik elektroputaran untuk mengkaji potensi nanostruktur ini untuk digunakan sebagai semikonduktor logam oksida dalam aplikasi DSSCs. Struktur dan morfologi bahan elektrospun telah dicirikan oleh analisis FESEM dan XRD. Kecekapan

untuk aplikasi DSSC menggunakan elektrod nanopartikel P25 TiO_2 (D3) adalah (1.076 ± 0.042)% apabila direndam dalam 3 wt.% larutan pewarna. Komposit elektrod TiO_2 nanopartikel-nanorod telah direka untuk meningkatkan prestasi kecekapan dalam aplikasi DSSCs. Elektrod komposit TiO_2 nanopartikel-nanorod (NPs-NRs) dengan penggunaan 10 wt.% NRs (CP1) menghasilkan peningkatan kecekapan (1.317 ± 0.035)% apabila direndam dalam 3 wt.% larutan pewarna. Dalam usaha untuk meningkatkan kecekapan, dua jenis asid ditambah iaitu asid chenodeoxycholic (CDCA) dan asid ferulik (FA). Pada penambahan berat 1 wt.% CDCA (C1), kecekapan telah meningkat sedikit kepada (1.393 ± 0.039)% dengan J_{sc} iaitu (4.835 ± 0.095) mA cm^{-2}, V_{oc} = (0.458 ± 0.006) V dan *FF* = (0.629 ± 0.010). Dengan penambahan 3 wt.% FA (F3), kecekapan dipertingkatkan kepada (1.917 ± 0.045)% dengan J_{sc} iaitu (6.178 ± 0.128) mA cm^{-2}, V_{oc} = (0.473 ± 0.009) V dan *FF* = (0.656 ± 0.010). Penyelidikan ini telah menunjukkan bahawa dengan penambahan CDCA dan FA terhadap larutan antosianin telah meningkatkan kecekapan DSSCs.

Kata kunci: *Ixora siamensis*, Pewarna semulajadi, Antosianin, TiO_2, Elektroputaran, Sel solar pemeka warna (DSSCs).

ACKNOWLEDGEMENTS

Above all, I would like to thank Allah S.W.T. for giving me patience and strength throughout the whole period of this study.

I wish to express my highest gratitude to my guide and supervisor, **Professor. Dr. Abdul Kariem bin Mohd Arof**, for the constant support, suggestions and motivation that I received from him during my PhD journey. I have been extremely lucky to have a supervisor who cared so much about my work and who responded to my questions and queries so promptly. Your guidance is deeply appreciated.

Special thanks to University of Malaya for the PPP PG167-2014B grant award and providing research facilities to help completing my study. Not forgotten, I wish to thank all technical staff in the Department of Physics, Faculty of Science for all the help and assistance.

A huge appreciation to **Ministry of Higher Education (MOHE)** for the MyBrain 15 Scholarship awarded to me for my PhD study in University of Malaya. Thank you very much for funding me during conducting my research.

My sincere thanks and infinite appreciation to my parents (Mat Nor bin Chik and Rosnani binti Abdul Ghani) and my siblings for their prayers, moral support and for always being there whenever I needed it.

Last but not list, to all members of Centre for Ionics University of Malaya (CIUM), thank you for the help, advice and all cherish moments we have experienced. I wish to thank once again to all the people who helped me in one way or another for the successful completion of my research work.

TABLE OF CONTENTS

LIST OF FIGURES

LIST OF TABLES

LIST OF SYMBOLS AND ABBREVIATIONS

J-V	:	current density-voltage
η	:	efficiency
P_{in}	:	incident power density
hv	:	incoming photon
I_2	:	iodine
I^-/I_3^-	:	iodide/triiodide
λ_{max}	:	maximum absorption wavelength
M_w	:	molecular weight
V_{oc}	:	open circuit voltage
J_{opt}	:	optimum current density
V_{opt}	:	optimum voltage
O_2	:	oxygen
R_s	:	series resistant
R_{sh}	:	shunt resistance
J_{sc}	:	short circuit current
wt.%	:	weight percentage
A	:	absorbance
ANOVA	:	analysis of variance
BBD	:	box-behnken designs
BMII	:	1-butyl-3-methylimidazolium iodide
CDCA	:	chenodeoxycholic acid
COOH	:	carboxylic acid
DSSC	:	dye-sensitized solar cell
EC	:	ethylene carbonate

EDX	:	energy dispersive analysis of x-rays
EIS	:	electrochemical impedance spectroscopy
FA	:	ferulic acid
FESEM	:	field emission scanning electron microscopy
FF	:	fill factor
FTO	:	fluorine-tin oxide
GPE	:	gel polymer electrolytes
IPCE	:	incident photon to current efficiency
LiI	:	lithium iodide
min	:	minute
MOS	:	metal oxide semiconductor
NP	:	nanoparticle
NR	:	nanorod
NPs-NRs	:	nanoparticles-nanorods
HNO_3	:	nitric acid
PV	:	photovoltaic
Pt	:	platinum
PAN	:	poly(acrylonitrile)
PEG	:	poly(ethylene glycol)
PVP	:	polyvinylpyrrolidone
PC	:	propylene carbonate
rpm	:	revolutions per minute
RSM	:	response surface methodology
Ru	:	ruthenium
s	:	second
TPAI	:	tetrapropyl ammonium iodide

TTIP	:	titanium (IV) isopropoxide
TiO_2	:	titanium dioxide
TCO	:	transparent conducting oxide
TFA	:	trifluoroacetic acid
UV	:	ultraviolet
UV-Vis	:	uv-visible
XRD	:	x-ray diffraction

CHAPTER 1: INTRODUCTION

1.1 Background

Energy is a necessity for survival of mankind and its demand increases with world population increase. The world is now facing an energy crisis (Susanti et al., 2014). Efforts are being devoted to overcome this problem. Most of the energy consumed by the world depends on fossil fuel. Fossil fuel is relatively cheap and easy to use. However, fossils fuels are non-renewable (Susanti et al., 2014; Jonathan et al., 2016) and are facing rapid resource depletion while the energy demand seems to grow on a daily basis. Hence, alternative sustainable energy resources that are inexpensive and eco-friendly need to be developed and utilized if this problem is to be overcome (Gong et al., 2012; Al-Bat'hi et al., 2013; Susanti et al., 2014; Jonathan et al., 2016). As is widely known, the exhaust from combustion of fossil fuels has resulted in environmental pollution and global warming. This can lead to the greenhouse effect (Gong et al., 2012). Thus, for comfort of mankind, a green and continuous energy supply is a necessity (Jonathan et al., 2016).

The ever increasing world's energy consumption has created a heavy demand for the development of renewable energy sources (Gassim et al., 2014; Susanti et al., 2014; Godibo et al., 2015; Jonathan et al., 2016). Renewable energy does not only ensure future energy supply but is also free from carbon dioxide emission (Gassim et al., 2014). Replacing fossil fuel with renewable energy resources can at the same time avoid negative effects on the climate. Environment and health are also major challenge facing scientists and researchers (Nazeeruddin et al., 2011; Godibo et al., 2015). The resolution is made more difficult when the cost is to be cheap.

In the author's opinion, among many non-contaminating sources of renewable energy such as hydro, geothermal and wind, solar energy has a greater potential as an energy

source in the future. A lot of energy reaches the earth daily and if tapped accordingly can provide limitless free energy. Solar energy can be considered to have the greatest prospect and potential (Nazeeruddin et al., 2011; Susanti et al., 2014). The sun's energy can be collected and used for heating purposes or directly converted to produce electricity using photovoltaic cells. However, the application is currently limited due to the high cost per watt of electricity (Al-Bat'hi et al., 2013). There are different types of solar cells available in the market. At present, commercial solar cells are based on inorganic silicon semiconductors (Al-Bat'hi et al., 2013; Godibo et al., 2015) and their photoelectric conversion efficiency is relatively high (Chang et al., 2010). The production cost is still expensive although it has been successfully reduced. A wide area is also required to assemble the solar panels. According to Grätzel (2003), dye-sensitized solar cells (DSSCs) have captivated great interest due to their beneficial aspects in terms of environmental friendliness and minimal production cost.

The future for dye-sensitized solar cells (DSSCs) as an alternative option to replace the silicon-based solar cells is quite promising (Song et al., 2005). DSSC is a semiconductor photovoltaic device and is classified as the third generation solar cells. These devices directly converts solar radiation into electric current and are long lasting. A typical photoelectrochemical cell or DSSC comprises a dye-capped nanocrystalline porous semiconductor photoanode or working electrode, a metal counter electrode and a redox mediator containing electrolyte. For normal or standard photovoltaics, the semiconductor absorbs light and transports the charge carrier. In DSSCs, these two functions are separated. Charge separation occurs at the interface of the sensitizer and the semiconductor and the charges or electrons that have reached the counter electrode are reunited with the holes (oxidized sensitizer molecules) through the redox mediators. As such the conduction mechanism is different (Grätzel, 2003; Ludin et al., 2014).

1.2 Problem Statement

The DSSC cell performance is primarily dependent on the quality of the dye sensitizer and the semiconductor component (e.g. TiO_2, ZnO etc.) used in the fabrication of the cell. The type of dyes used in DSSCs include organic and ruthenium (Ru)-based dyes. Organic dyes include coumarin, merocyanine, cyanine, indoline, hemicyanine, triphenylamine, dialkylaniline, phenothiazine and tetrahydroquinoline (Shelke et al., 2013) while Ru-based dyes are coded as N719, N3 and N749 (Shalini et al., 2016). These dyes are expensive and the author is of the opinion that if the DSSC is commercialized, the cost may still be uncomfortably high and the cost of a watt per unit area of electricity may also remain relatively high. Natural dyes or sensitizers offer a suitable alternative to the DSSCs. Natural dyes are utilized as sensitizers in DSSCs due to their eco-friendliness, easy to prepare, abundant, cheap cost and biodegradable (Adedokun et al., 2016). Morever, the dye from *Ixora siamensis* is still underutilized and the potential of this species need to be explored. Natural dyes can be obtained by solvent extraction of the pigments from flowers, fruits and leaves of lower and higher plants. These natural pigments include chlorophyll, carotenoid, betalain and anthocyanin to name a few. Many of the research on natural sensitizers focused on either chlorophyll or anthocyanin (Shahid et al., 2013; Hug et al., 2014; Ludin et al., 2014; Gokilamani et al., 2015). Natural dyes extraction from *Ixora* species contained anthocyanin (Patil & Datar, 2015). Anthocyanin play role in the visible spectrum of the dye extraction, hence also responsible for the photosensitizer effect in DSSC. Although natural dyes are cheap and readily available, their use is not without problems. Natural dyes are not as stable as the synthetic and Ru-based dyes. Efficiency of the natural dye-sensitized solar cells is low. A number of natural dyes have been reported for their performance in DSSCs and their energy conversion efficiencies is around 1% (Wongcharee et al., 2007; Zhou et al., 2011; Reda et al., 2014; Hug et al., 2014), hence this work focusing on increasing the efficiency

performance. Good sensitizing performance is dependent on the dye extracting medium such as the solvents (Singh et al., 2014). The extraction parameters also influence the yield of natural dye extraction. Different species have different optimal conditions for the extraction process. Hence, optimization of these parameters is necessary in order to obtain the highest anthocyanin content from the extract of *Ixora siamensis.*

Another important part in DSSC devices is the semiconducting metal oxide. The oxide semiconductor material not only holds the dye molecule, but also accepts and transports the photo-electrons. The ideal semiconductor should possess rapid electron transport and have a high surface area. TiO_2 nanoparticles have been employed as the mesoporous semiconductor material in DSSCs because of its large internal surface area. Hence high dye adsorption will take place and in turn provide more effective photocurrent generation (Selvaraj et al., 2018). To improve the efficiency of the DSSCs employing anthocyanin from *Ixora siamensis,* the TiO_2 mesoporous layer will be composed of TiO_2 nanoparticles and nanorods. TiO_2 nanorods are known to exhibit good light scattering and electron transport properties (Lee et al., 2014; Wang et al., 2015). The idea behind this is to combine the advantages of commercially available TiO_2 nanoparticles with TiO_2 nanorods that have the potential for enhancing the DSSC performance. Electrospinning was chosen as the tool to produce the TiO_2 nanorods compared to other complex fabrication methods due to its versatility, simplicity and relatively low-cost.

1.3 Objectives of the Thesis

In this thesis, DSSCs are fabricated from a combination of materials in order to promote good DSSC efficiency. There are many factors influencing the extraction and colour variation of natural dye. These include the extracting solvent, solvent composition, temperature during extraction, time for extraction and pH (Cacace &

Mazza, 2003). However, in this thesis we restrict ourselves to the composition of extracting solvent, temperature and time for extraction to determine the parameters that can result in the maximum extraction yield. To the author's knowledge, reports utilizing anthocyanin extraction from the fruit pericarp of *Ixora siamensis* is rather limited.

Other than natural dyes, the morphology of the semiconductor oxide is important for good DSSC performance. It is known that the performance of DSSCs with TiO_2 nanoparticles (NPs) is often restricted in part due to insufficient electron transport (Sugathan et al*.,* 2015). Using electrospinning method, 1-D TiO_2 materials can be produced. This can provide additional pathways for electron transport. DSSC photoanode with 1-D nanorods has exhibited good performance with improved efficiency (Lu et al*.,* 2015). The dye used in DSSCs acts as the photon collector or light harvester to convert solar energy into electricity. To increase the overall efficiency of natural dye-TiO_2-based DSSCs, additives such as CDCA and FA were added into the natural dye solutions. These additives contain -COOH functional group that can help to anchor the dye to the TiO_2 metal oxide surface. This can influence the electron injection rate and energy conversion efficiency in DSSCs.

Hence, the objectives in this study are summarized as follows:

1. To identify the type of anthocyanins in the solvent extract of fruit pericarp from *Ixora siamensis* by the method of chromatography.
2. To optimize the extraction parameters for the anthocyanin dyes using response surface methodology (RSM), which will be discussed in detail in the next chapter.
3. To investigate potential of the extracted natural sensitizer from fruit pericarp of *Ixora siamensis* in DSSCs that used commercial TiO_2 nanoparticles in the

mesoporous layer. The effects of different weight percentage of dyes used were examined for optimization.

4. To obtain one dimensional (1-D) TiO_2 nanorods (NRs) by combining sol-gel and electrospinning methods followed with sintering and mechanical grinding.
5. To evaluate the potential of TiO_2 nanorods in combination with commercial TiO_2 nanoparticles (NPs) in the mesoporous layer of the photoanode in DSSCs with the optimized dye percentage obtained from objective number 3.
6. To study the effect of CDCA and FA additives on the efficiency of DSSC with the optimized NP-NR ratio obtained from objective number 5.

1.4 Scope of the Thesis

This thesis consists of eight chapters. The first chapter outlines the problem statement, research objectives that makes part of this introductory chapter. Chapter 2 gives an inexhaustive overview on the types of DSSCs, working principle, components, as well as the selection and properties of the materials commonly used in DSSC fabrication. Chapter 3 describes the details of anthocyanin preparation for optimized extraction by response surface methodology (RSM), synthesis and preparation of TiO_2 semiconductor photoanode. This chapter also includes the details for characterizations such as chromatography, visible absorption spectroscopy, CIELAB colourimetric spectroscopy, x-ray diffraction (XRD), field emission scanning electron microscopy (FESEM) and energy dispersive analysis of x-rays (EDX). Electrical characterization of DSSCs include *J-V* characterizations, incident photon to current efficiency (IPCE) and electrochemical impedance spectroscopy (EIS) analysis.

Chapter 4 presents the results for the optimized extraction parameters of the natural dye from fruit pericarps of *Ixora siamensis* by response surface methodology (RSM).

This chapter also presents the chromatography experiment that enables the identification of the anthocyanin content in the extract. The optimized anthocyanin extracted from *Ixora siamensis* will be further used as sensitizer in DSSC fabrication. Chapter 5 displays the results from the preparation of TiO_2 nanostructures by implementing sol-gel synthesis and electrospinning method, followed with post-treatment process in order to achieve the desired compound. This chapter included the study on relationship between polymer concentration with the average fiber and bead diameters. The optimized polymer concentration were further used in order to investigate the effect of applied voltages on the average fiber and bead diameters, with the aim to produce beadless uniform nanofibers. The results covers the morphology of TiO_2 nanofibers through FESEM analysis. The beadless nanofibers formed were further subjected to different calcination temperatures and grinding processes to obtain TiO_2 nanorods. This chapter also covers the morphology, elemental and structural analysis of TiO_2 nanorod materials through FESEM, EDX and XRD. The anatase TiO_2 nanorods obtained were used with the commercial nanoparticles to produce composite nanoparticle-nanorod photoanode. The morphology of the composite at different nanorod percentages were also observed via FESEM analysis.

Chapter 6 displays the results on the performance of DSSCs fabricated using the commercial TiO_2 nanoparticles in search for the optimum weight percentages of anthocyanin from *Ixora siamensis* as natural sensitizer. The dye extraction parameters have been optimized in Chapter 4. The optimized weight percentage of anthocyanin that contributed to the highest efficiency was used for further DSSCs systems. This chapter also covers the fabrication of composite DSSCs which are made up of commercial TiO_2 nanoparticles (NPs) combined with nanorods (NRs). The composite cells sensitized with optimized anthocyanin concentration were evaluated for their performance to determine

the optimum nanorod percentage to be mixed with the TiO_2 NPs. Results on the use of additives (CDCA and FA) to improve the efficiency of the composite DSSCs at the optimum NP:NR ratio are also displayed in this chapter. Chapter 7 discusses all the results obtained and Chapter 8 concludes the thesis highlighting the major findings and recommendations for future investigation.

CHAPTER 2: LITERATURE REVIEW

2.1 Introduction

This chapter provides an inexhaustive overview of the progress on solar cells, DSSCs, the materials used and the reasons for using them. In particular, we provide some information on the choice of anthocyanin and TiO_2 nanostructures as the component materials for fabrication of DSSCs.

2.2 Solar Cells

Solar cells collect light and convert them into electricity via electrons and holes production and ending with recombination of electrons and holes. Photovoltaic comprises the words of 'photo' that means light and 'volt', which is a measure of electricity (Luceño-Sánchez et al., 2019). There are three generations of solar cells. The first generation have high efficiency (~25%). The cost of production is however expensive, although it has been successfully lowered and very pure silicon is needed (Luceño-Sánchez et al., 2019). Cadmium telluride (CdTe) or copper indium gallium selenide (CuInGaSe) thin film solar cells comprise the 2nd generation cells. Their efficiency is lower than first generation crystalline silicon cells, but are less expensive to produce. The thickness has been reduced to a few microns (Swami, 2012). Eventhough the price is lower, there are difficulty on market acceptance since it is confirmed that the product based are unsafe to our environment and health (Charles & Janusz, 2005). The third generation is a new concept which is said to be an even cheaper technology and considered as nanophotovoltaic solar cells technology. These include dye-sensitized solar cells (DSSCs), quantum dot and perovskite cells. Nevertheless, the greener solar cells technology using low material and manufacturing costs with acceptable efficiency should be considered. The third generation solar cell technology is expected to make an impact in renewable energy devices (Swami, 2012; Luceño-Sánchez et al., 2019).

2.2.1 Dye-sensitized Solar Cells (DSSCs)

DSSCs have gained much attention in the R & D of renewable energy devices. In silicon solar cells, silicon is the photoelectron source. It also provides the electric field for electron and hole separation and to create a current. In DSSCs, the semiconductor layer transports the electrons provided by the dye. Electrons and holes in the oxidized dye occur at the dye and semiconductor interface. The DSSC has different medium for light collection/carrier production (dye) and the electron transport (TiO_2 nanoparticles) (Luceño-Sánchez et al., 2019). In DSSC, the effective electron injection into semiconductor is dependent on the first monolayer that adsorbs the dye. The effective surface area can be improved by utilization of TiO_2 nanoporous. The TiO_2 nanocrystalline film has attractive feature in terms of effective charge transport of the photo-generated electrons that passing through all the particles. Nanoporous semiconductors act as electron acceptor and electronic conductor (Würfel et al., 2008). The great advantages of DSSC systems is their ease of fabrication and the use of low cost materials. Hence, the third generation technology is expected to make a great contribution in the advancement of photovoltaics. The possibility of production under mild conditions, enables production cost to be less expensive than the earlier cell designs (Luceño-Sánchez et al., 2019).

The concept of DSSCs is based on the principle of plant photosynthesis. O'Regan and Grätzel were the first to propose these cells in 1991. The cells were then called dye-sensitized solar cells (DSSCs). The first DSSC is based on a 10-µm-thick, optical transparent film of TiO_2 nanoparticles and monolayer dye as light harvester exhibited an efficiency exceeding 7% and the IPCE was about 80% (O'Regan and Grätzel, 1991). The efficiency reached 11.4% in 2011 (Taya et al., 2013; Suhaimi et al., 2015). Efficiency increased to 13% on utilizing with semiconducting oxides that are porous and porphyrin based dyes (Mathew et al., 2014). These triumphs have garnered more efforts to improve

the performance of DSSCs. DSSC research became more fascinating since many sources of dyes including environmental friendly natural dyes that can act as light harvester to provide electron-hole production. DSSCs usually comprise five components which are (Nazeeruddin et al., 2011; Gong et al., 2012; Shalini et al., 2015; Adedokun et al., 2016):

(i) transparent glass slide with a conductive oxide layer. Common ones are fluorine doped tin oxide (FTO) or indium doped tin oxide (ITO).

(ii) metal oxide semiconductor (MOS) layer (TiO_2 NPs), for electron to travel from inside the cell to the external circuit.

(iii) a dye sensitizer with anchoring units to adhere on the MOS. The dye absorbs energy from the incident photons to excite electrons into the MOS.

(iv) a redox mediator containing electrolyte to transport electrons from the counter electrode of the DSSC back to the holes in the oxidized dye molecule for regeneration.

(v) a cathode, consisting of a conducting glass slide with platinum deposited onto it for promoting electrons to the triiodide ions in the electrolyte.

DSSC is an electrochemical semiconductor photovoltaic apparatus, which functions to convert solar radiation into electricity (Gong et al., 2012; Shalini et al., 2015), Figure 2.1.

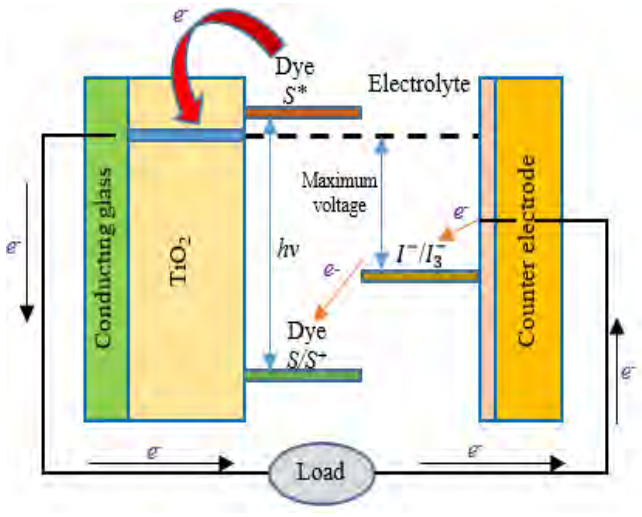

Figure 2.1: Schematic diagram of DSSCs.

The DSSC can be characterized electrically by *J-V* characteristic measurements from which parameters like photon conversion efficiency (η), open circuit potential (V_{oc}), short circuit current density (J_{sc}), fill factor (*FF*), interface charge resistance (series resistance, R_s and shunt resistance, R_{sh}), incident photon to current efficiency (IPCE) and electrochemical impedance spectroscopy (EIS). These characteristic are dependant on the morphology of the MOS, spectroscopic properties of dye and ionic conductivity of the electrolyte (Mehmood et al., 2014). The working principle of the DSSC, role of every component, the selection and requirement as well as properties of selected materials will be dealt in the coming sections.

2.2.2 Working Principle of DSSCs

The DSSC functions quite similarly to photosynthesis. In photosynthesis, chlorophyll is the light harvester whereas in DSSC, it is the dye. Light harvesting produces the photoelectrons. In photosynthesis, carbon dioxide (CO_2) is the electron acceptor and in DSSC, it is the MOS. The electrolyte in DSSC is substituted by water in the photosynthesis process. The DSSC has a multilayered structure to increase light absorption and electron collection efficiency (Adedokun et al., 2016). The photoanode consists of a fluorine doped tin oxide (FTO) transparent conducting glass that has been deposited with the TiO_2 semiconductor layers and soaked in the dye. Hence, DSSC is an electrochemical semiconductor photovoltaic device (Gong et al., 2012; Shalini et al., 2015).

The dye in this work is an anthocyanin extract from the fruit pericarps of *Ixora siamensis*. Polyacrylonitrile based gel polymer electrolyte containing I^-/I_3^- redox mediator and platinum (Pt) cathode have been used in DSSC fabrication. For good performance, a compact and mesoporous TiO_2 layers were deposited on the FTO glass

with the mesoporous layer over the compact layer. The working principle of a DSSC can be explained as follows (Shalini et al., 2015; Maabong et al., 2015):

When illuminated, the photons *(hv)* absorbed by the sensitizer molecules gained energy and are excited. The energy gained enabled the natural sensitizer molecules to enter the lowest unoccupied molecular orbital (LUMO) in the excited state *(D*)* from the highest occupied molecular orbital (HOMO) *(D)*.

$$hv + D \rightarrow D^* \quad (2.1)$$

In the LUMO, the sensitizer molecules are also oxidized resulting electrons to enter the TiO_2 conduction band. The charge transfer occurs via the TiO_2-dye interfacial interface due to a strong coupling between the anchoring groups of the dye molecules and the TiO_2 semiconductor surface (Thomas et al., 2014). The reaction occurs as follows:

$$D^* + TiO_2 \rightarrow D^+ + e_{cb}^-(TiO_2) \quad (2.2)$$

Electrons that have entered the TiO_2 conduction band will diffuse to the TCO layer (as a result of an electron concentration gradient) and travel through the external circuit to the platinum cathode where the electrons will reduce the triiodide ions into iodide ions. The I^- ions will diffuse to the photoanode through the electrolyte. At the photoanode, the I^- ions release two electrons that will fill the holes in the dye molecules and becomes I_3^- again. The triiodide ion moves to the cathode and the redox process repeats. The dye is hence regenerated. The redox process can be represented as follows:

$$2D^+ + 3I^- \rightarrow 2D + I_3^- \quad \text{(oxidation of } I^-\text{)} \quad (2.3)$$

$$I_3^- + 2e^- \rightarrow 3I^- \quad \text{(reduction of } I_3^-\text{)} \quad (2.4)$$

The energy difference between the redox mediator in the electrolyte and TiO_2 Fermi level gives rise to the voltage at open circuit. In order to achieve a high current generation and prevent losses in the cell efficiency, the oxidation of iodide (equation 2.3) and the reduction of triiodide (equation 2.4) ion must successfully compete with the electron recombination processes to prevent current reduction. These recombination reactions are as shown below (Calogero & Di Marco, 2008; Nazeeruddin et al., 2011; Ludin et al., 2014): Figure 2.2 illustrates the schematic diagram and working mechanism in DSSCs.

$$D^+ + e_{cb}^-(TiO_2) \rightarrow D + TiO_2 \quad (2.5)$$

$$I_3^- + 2e_{cb}^-(TiO_2) \rightarrow 3I^- + TiO_2 \quad (2.6)$$

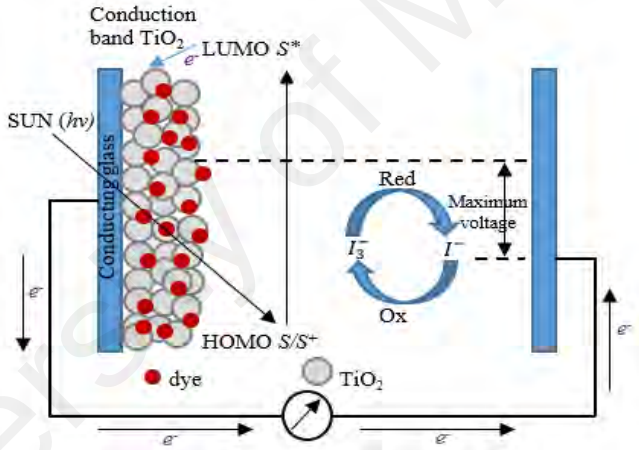

Figure 2.2: Schematic representation and working principle in DSSC.

2.2.3 Components of DSSCs

As mentioned before, the conversion of light into electricity by DSSC is based on the sensitization of a dye that causes electrons to finally enter a semiconductor with wide band gap. In this study, TiO_2 with energy gap 3.2 eV was used. When the electrons have entered the TiO_2 semiconductor, they are finally led to the external circuit. At the cathode, the electrons are transported to the holes in the photoanode and the circuit is completed. The optimization and compatibility of the constituents is important for improving efficiency (Adedokun et al., 2016).

2.3 Dye for DSSCs

Dyes or sensitizers can be divided into synthetic and natural dyes. The sensitizer mainly functions to harvest light, generate positive (holes) and negative (electrons) charges. Finally, the electrons are injected to the MOS conduction band in order to generate electricity. Dyes adhere to the walls of the pores in the semiconductor. Characteristics of a good dye or photosensitizer are as follows (Haque et al., 2005; Mehmood et al., 2014; Rho et al., 2015):

- absorbs intensely between 400 and 700 nm of the electromagnetic spectrum.
- have a surface-anchoring group such as -COOH so that can strongly bond or anchor on the semiconductor surface to minimize interfacial resistance and prevent loss of electrons via recombination.
- have good stability in oxidized form so that it can be reduced when it receives electrons from the I^- ions.
- the LUMO of the dye must be more positive than the TiO_2 conduction band edge so that electrons can be transferred efficiently.
- the HOMO of the dye must be lower than the redox level to facilitate dye regeneration.

The long term stability and excellent energy conversion in DSSCs have been accomplished by utilization of ruthenium (Ru) based dyes viz., N3 and N719 developed by the Grätzel group. These dyes are superb light harvesters and are durable. The fast charge transfer rate enables the electrons to leave the external circuit before the possibility of electron recombination with the oxidized dye molecule (Ryan, 2009). However, due to their environmental unfriendliness and expensive cost (Reijnders, 2010), it is necessary to look for green or natural dyes as alternative photosensitizers.

2.3.1 Natural Dyes

Since ruthenium complexes are not eco-friendly, efforts were geared to develop synthetic ruthenium-free dyes to be used as sensitizer in DSSCs. In fact, the synthesis of the synthetic dyes takes much time and is a laborious task. Hence, there may be a need for natural dyes such as pigments used in the manufacturing of certain types of foods for use in DSSCs. Natural dyes could be obtained from fruits, flowers and leaves of plants, which exhibit various colours and contain various types of pigments. These are easily acquired using simple procedure and applied as sensitizer in DSSC fabrication (Chang & Lo, 2010). Natural pigments are cheap, easy to prepare, relatively abundant, biodegradable, non-toxic and environmental friendly since it does not contain heavy metals like ruthenium (Kishiomoto et al., 2005; Sinha et al., 2012; Nishantha et al., 2012). These floral colourants display electronic configuration when in contact with light. The pigment and specific colour are described by the maximum absorption wavelength (λ_{max}) as perceived by the viewers (Davies, 2004). The DSSC cell performance sensitized using natural dye sensitizer can be assessed in terms of open circuit voltage (V_{oc}), short circuit current, (J_{sc}), fill factor (FF) and efficiency of light conversion (η) (Huizhi et al., 2011). Numerous natural dye sources have been investigated as sensitizers in DSSCs such as chlorophyll (Hao et al., 2006; Kumara et al., 2006), carotenoid (Kishiomoto et al., 2005; Rühle et al., 2010; Gomez-Ortiz et al., 2010) and anthocyanin (Chang & Lo, 2010; Alhamed et al., 2012). Figure 2.3 shows the classification of common natural pigment. However, we restrict ourselves next to the anthocyanin dyes.

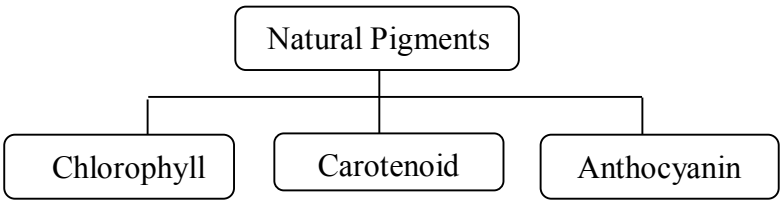

Figure 2.3: Classification of plant pigments.

Anthocyanins are flavonoids that impart flowers and fruits with blue and red colours (Delgado-Vargas et al., 2000; Andersen & Jordheim, 2006; Chang & Lo, 2010). Flowers and fruits can contain many types of anthocyanins. The colours of strawberry for example, is due to different type of anthocyanins (Delgado-Vargas et al., 2000). Anthocyanin can be obtained from other plant organs too. These include tubers, roots, and stems (Patrocínio et al., 2009). Anthocyanins can dissolve in water (Castaneda et al., 2009).

2.3.2 Structure of Anthocyanin

The flavylium cation that is the core of anthocyanins comprises an aromatic ring (A) bonded to a heterocyclic ring (C). The heterocyclic ring contains an electron deficient oxygen, O^+ that is linked by a C–C bond to another aromatic ring (B) (Delgado-Vargas et al., 2000; Calogero et al., 2013; Paliwal et al., 2016; Pervaiz et al., 2017). Anthocyanins are derived from anthocyanidins which consist of at least one pendant sugar moiety (glycoside form). When the anthocyanidins are found in their glycoside form (bonded to a sugar moiety) they are known as anthocyanins. Anthocyanins are formed by glycosylation of the base pigment anthocyanidins. Glycoslyation of -OH groups and the position of their attachment, acylation of aliphatic and aromatic group, glycosyl units nature and the substitution pattern determined the anthocyanin type (Andersen & Jordheim, 2006). Basic anthocyanin molecules are shown in Figure 2.4.

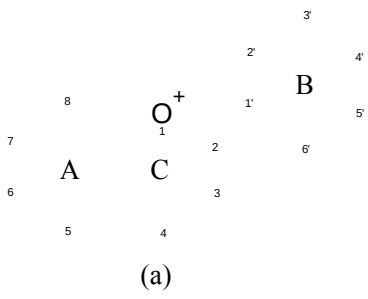

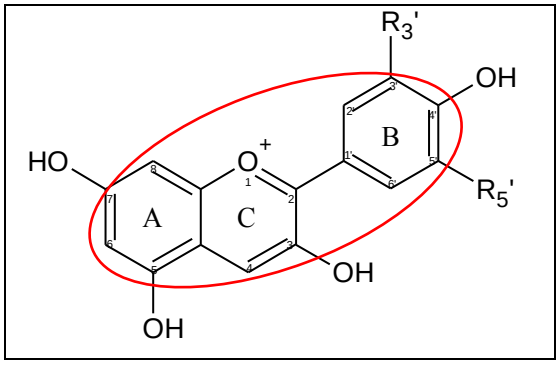

Figure 2.4: Structure of anthocyanidin. The red circle indicate the flavylium cation.

There are six common anthocyanins which are cyanidin, pelargonidin, delphinidin, peonidin, petunidin and malvidin (Khoo et al., 2017; Pervaiz et al., 2017) as in Figure 2.5. The chemical structure of these anthocyanins differ in the number and position of hydroxyl groups and/or methyl groups at the 3' and 5' positions of the B-ring. In acidic form, anthocyanins are intense red or orange, bluish in alkaline form while colourless at higher pH. The intensity and colour type are influenced by the number of -CH_3 and -OH groups attached. The bluish shade colour is due to more -OH groups while increased in redness if more -CH_3 groups (Heredia et al., 1998; Delgado-Vargas & Paredes-López, 2003).

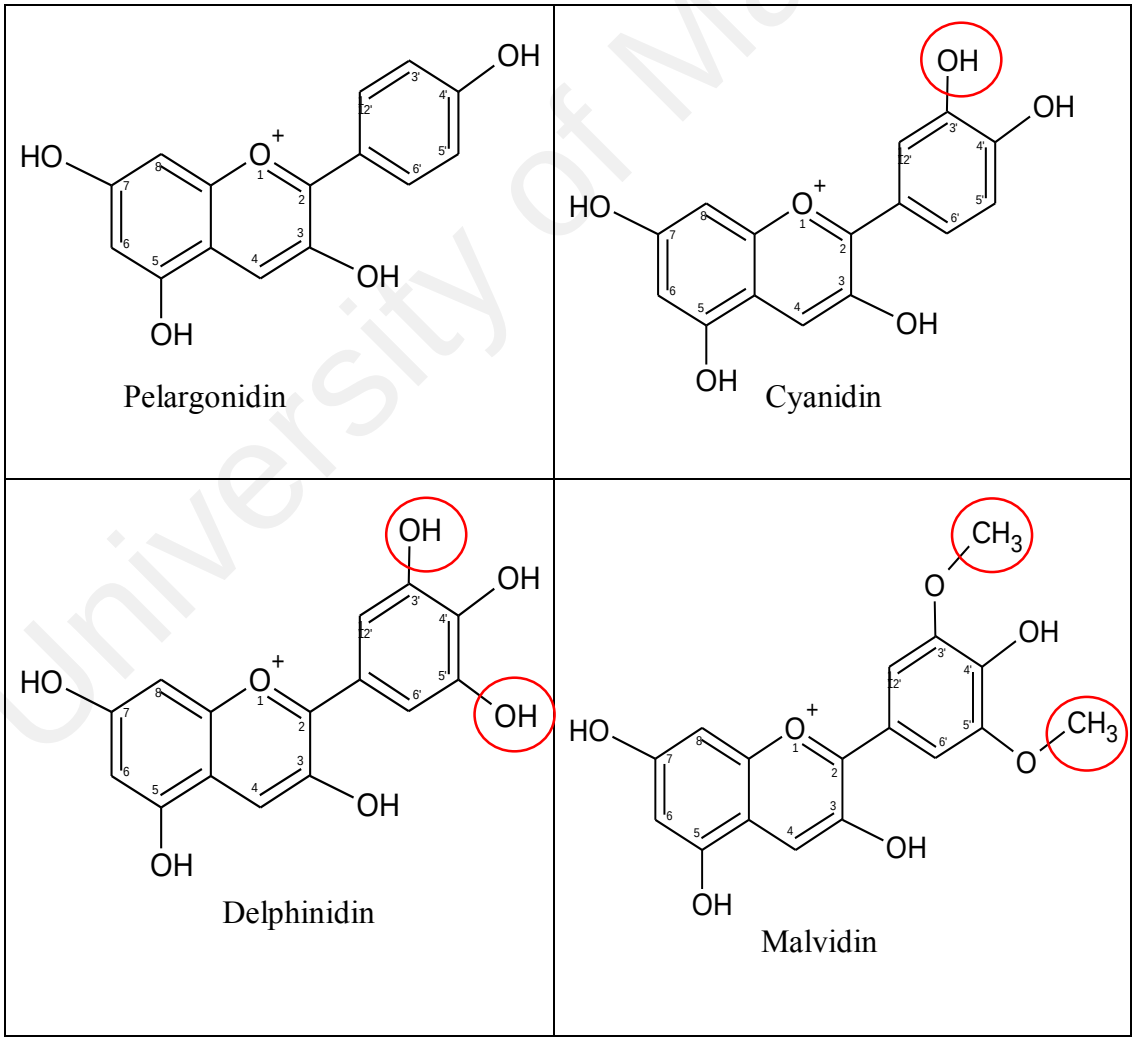

Figure 2.5: Structure of common occurring anthocyanin. The red circle indicate the differences between anthocyanin structure.

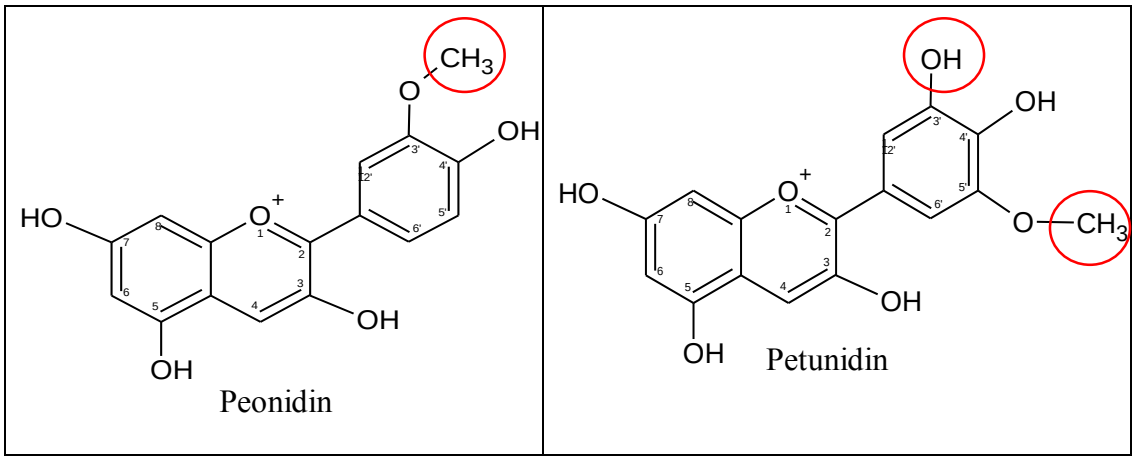

Figure 2.5, continued.

2.3.3 Compatibility of Anthocyanin in DSSC Application

Anthocyanin dyes have captured attention as sensitizer in DSSC applications due to their ability to absorb light and convert it into electrons in a natural and efficient way (Hao et al., 2006). The anthocyanin molecule will absorb ultraviolet-visible wavelengths differently depend upon the type of anthocyanidin, the sugar attached and where the sugar is located on the anthocyanin molecule structure. Ordinarily, the anthocyanin molecule absorbs light in the wavelength ranging from 450 to 600 nm, which impart the colours of blue, purple and red in plants (Hao et al., 2006). Anthocyanin dyes are often used in sensitizing wide band gap semiconductors in DSSCs. The joining of nanoparticles to the anthocyanin dye can potentially broaden the absorption spectra, that will enhance the efficiency of solar cell (Furukawa et al., 2009). Anthocyanin molecules have carbonyl and hydroxyl groups that can adhere to the TiO_2 surface. These groups help in the excitation of the anthocyanin molecule and electron administration in the mesoporous TiO_2 conduction band from the LUMO of the sensitizer molecules (Hao et al., 2006; Ludin et al., 2014). Anthocyanin pigment occurs in the quinoidal form, which is acidic or flavilium form which is basic in nature (Fernando & Senadeera, 2008). The complexation studies on anthocyanin pigments have shown that the pigment chelates with metal ions of titanium, chromium, aluminum and iron as displayed in Figure 2.6

(Cherapy et al., 1997; Garcia et al., 2003; Calogero & Di Marco, 2008). The metallic ions will interact with the anthocyanin and shift the dyes equilibrium from quinoidal to flavilium state. The shift between the two chemical states resembles the shift in absorption peak towards longer wavelengths, observable from the absorption spectrum (Wongcharee et al., 2007; Fernando & Senadeera, 2008). Similar shift has been observed in blue-violet anthocyanin extracts from *Calafate* (Polo & Iha, 2006). This is due to the alcoholic bound proton in the –OH group that condensed on the surface of nanostructured TiO_2 film and stabilized the excited state of the dye (Hao et al., 2006; Wongcharee et al., 2007; Fernando & Senadeera, 2008). Thus, the adhesion and interaction between the sensitizer (dye) and semiconductor (TiO_2 film) is important in increasing DSSC efficiency. Anthocyanin from different plants provides different sensitizing performance. Other examples of anthocyanin dye used as photosensitizer are listed in Table 2.1. We restrict to DSSCs with efficiency greater than 1%.

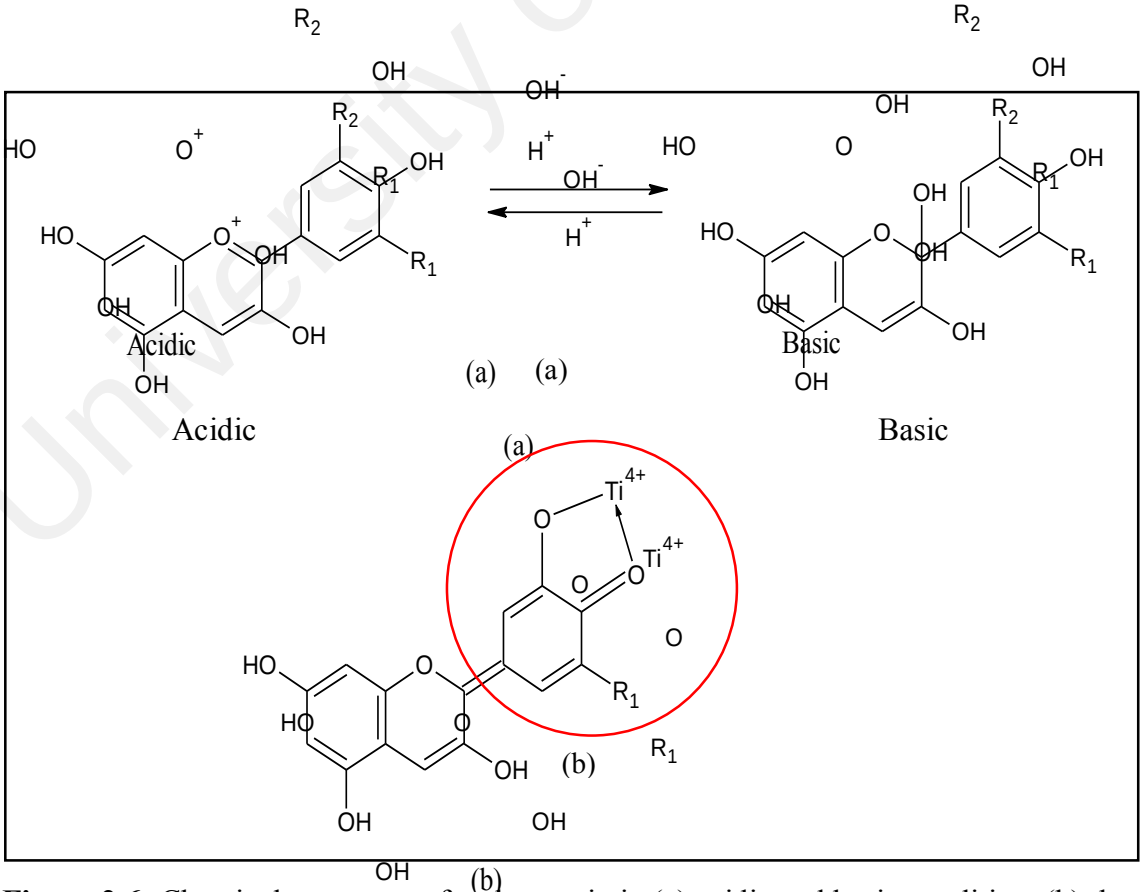

Figure 2.6: Chemical structures of anthocyanin in (a) acidic and basic condition, (b) the red circle indicate the binding between anthocyanin molecule and TiO_2 particles.

Table 2.1: Characteristics of anthocyanins dyes in DSSCs.

Dye solution	J_{sc} ($mAcm^{-2}$)	V_{oc} (V)	FF	η (%)	Ref.
Roselle (*Hibiscus sabdariffa*)	3.55	0.66	0.68	1.60	Hernández-Martínez et al., 2012
Hibiscus surattensis	5.45	0.39	0.54	1.14	Wongcharee et al., 2007
Hibiscus rosasinensis	4.04	0.4	0.63	1.02	Fernando & Senadeera, 2008
Red cabbage (*Brassica oleracea var. capitata f. rubra*)	3.47	0.59	0.69	1.42	Chien & Hsu, 2013
	11.2	0.59	0.43	2.91	Li et al., 2013
Red Sicilian orange (*Citrus Sinensis*)	5.13	0.33	0.59	1.01	Calogero & Di Marco, 2008
Blackberries	10.6	0.33	0.42	1.46	Zhu et al., 2008
	5.85	0.32	0.57	1.07	Calogero & Di Marco, 2008
Raspberries	0.27	0.43	0.65	1.50	Alhamed et al., 2012
Black rice (*Oryzasativa L. indica*)	5.73	0.54	0.73	2.26	Prima et al., 2016
Punica granatum peel	3.34	0.72	0.78	1.86	Hernández-Martínez et al., 2012
Sumac/Rhus	0.93	0.39	0.41	1.50	Suhaimi et al., 2015
Mangosteen pericarp	2.92	0.611	0.626	1.12	Huizhi et al., 2011

2.3.4 Extraction of Anthocyanin

In this work, *Ixora siamensis* was chosen as the source of anthocyanin sensitizer for DSSCs fabrication. Its local name is "jejarum". It is from the Rubiaceae family (Fosberg & Sachet, 1989). It is plentiful in Malaysia. The *Ixora* genus is famous as an ornamental plant (Figure 2.7 (a)), with colourful flowers that include pink, red and yellow (De Block, 1998). The fruits (Figure 2.7 (b)) can be eaten and the flowers used as a flavouring agent. The utilization of this fruit are overlooked and yet to be explored. The fruit pericarp of *Ixora siamensis* which is underutilized were solvent extracted and used as natural sensitizer. Natural dyes from *Ixora* species contained anthocyanin (Patil & Datar, 2015). Extraction parameters can influence the anthocyanin dye properties. Anthocyanins have been extracted using alcohol solutions that are acidified, water and acetone/alcohol/water mixtures. Extracts rich in anthocyanins were usually extracted using solutions of alcohols with small amount of acid to prevent degradation of the nonacylated compounds. In the

recovery of materials (pigments) from plants, extraction is a crucial step (Spigno et al., 2007). In an attempt to improve the dye performance, optimization of extraction parameters were performed prior to utilization in DSSC cells. The extraction process is to provide the maximum yield of pigment (in this case) with the best quality and high concentration (Spigno et al., 2007). Many aspects influence the quality and yield of the extract. This include the solvent type, solvent composition, time for extraction, temperature and particle size of plant material (Cacace & Mazza, 2003; Rajha et al., 2014). The nature of solvent affects dye absorption or concentration and binding between dye and surface of semiconductor (Aduloju et al., 2011). Hence, the optimization of these extraction parameters is important for this study. Although there are several methods to optimize the extraction parameters such as the classical single factor experiments or one-to-one factor experiments and the second is the response surface methodology (RSM) (Tan et al., 2013). We restrict ourselves to the response surface methodology (RSM).

Figure 2.7: (a) Flower and (b) fruits of *Ixora siamensis.*

2.3.5 Response Surface Methodology (RSM)

For the one-to-one factor approach, there is only one factor or parameter that is varied at a time while other parameters are kept constant. However, there are some drawbacks. These include time-consuming, expensive, not being able to evaluate interaction between parameters and conclusions can be misleading (Bas & Boyaci, 2007; Bezerra et al., 2008). RSM optimization method is a statistical technique which is commonly used in

optimizing complex process since it is able to predict the complete effects of variables, determine interactions between several parameters, reduce process time and number of experimental trials (Hosseinpour et al., 2014). The mathematical and statistical techniques involved analyze the effect of a few parameters on a particular response and finally optimize the process. These theoretical aspects of RSM have been reviewed by Bas & Boyaci (2007) and Myers et al. (2009). Compared to one-to-one method, RSM is far better since in RSM several parameters can interact simultaneously with each other. RSM can be used to evaluate the interaction between these factors. It can investigate the interactive consequence of operating parameters and to establish a mathematical model, which explains accurately the complete operation (Maran & Manikandan, 2012). In RSM method, series of tests designed to achieve an optimum output. This technique has been widely used in different fields such as agriculture, biology and chemistry to predict the optimal conditions of the systems (Liyana-Pathirana and Shahidi, 2005; Cacace & Mazza, 2003). Extraction of anthocyanin are affected by various process parameters which can have a significant influence in the extraction process (Cacace & Mazza, 2003; Liyana-Pathirana & Shahidi, 2005).

RSM is a commonly used procedure for optimizing the natural pigment extraction (Fan et al., 2008; Thirunavukkarasu & Nithya, 2011). The steps presented in Figure 2.8 need to be followed in order to apply the RSM method satisfactorily (Aydar, 2019). The aim in RSM experiments is to predict the value of an output or responses called the dependent variables, based on the controlled values of input or experimental factors called the independent variables. The RSM established the relationship between the output and input parameters. It also determines the optimum operating requirements for a system being studied (Pishgar-Komleh et al., 2012; Farooq et al., 2013). Two experimental designs commonly used in RSM are central composite design (CCD) and

Box-Behnken designs (BBD) (Koç, 2009; Aydar, 2019). The experimental data are assessed to fit either a Linear, Quadratic, Cubic or 2FI (two factor interactions) statistical model. The independent variables are designated as A, B and C. AB, AC and BC are terms representing interactions of independent variables. A^2 , B^2 and C^2 represent interactions between the same independent variables. Regression (R^2), adjusted regression (Adj-R^2) and adequate precision are applied to determine the model adequacies. A model is considered adequate or suitable if p value < 0.05, if lack of fit p value > 0.05, R^2 > 0.9 and Adeq Precision > 4. Differences between means can be tested for statistical significance using analysis of variance (ANOVA) (Aydar et al., 2017). In this study, the RSM method with BBD design was employed for optimization of anthocyanin extraction from *Ixora siamensis* in order to forecast the best anthocyanin removal requirements in terms of solvent composition, time for extraction and temperature to maximize the anthocyanin yield as well as to quantify the extracted colour properties. This work also provides a chance to determine the prospect of *Ixora siamensis* as a sensitizer in DSSCs.

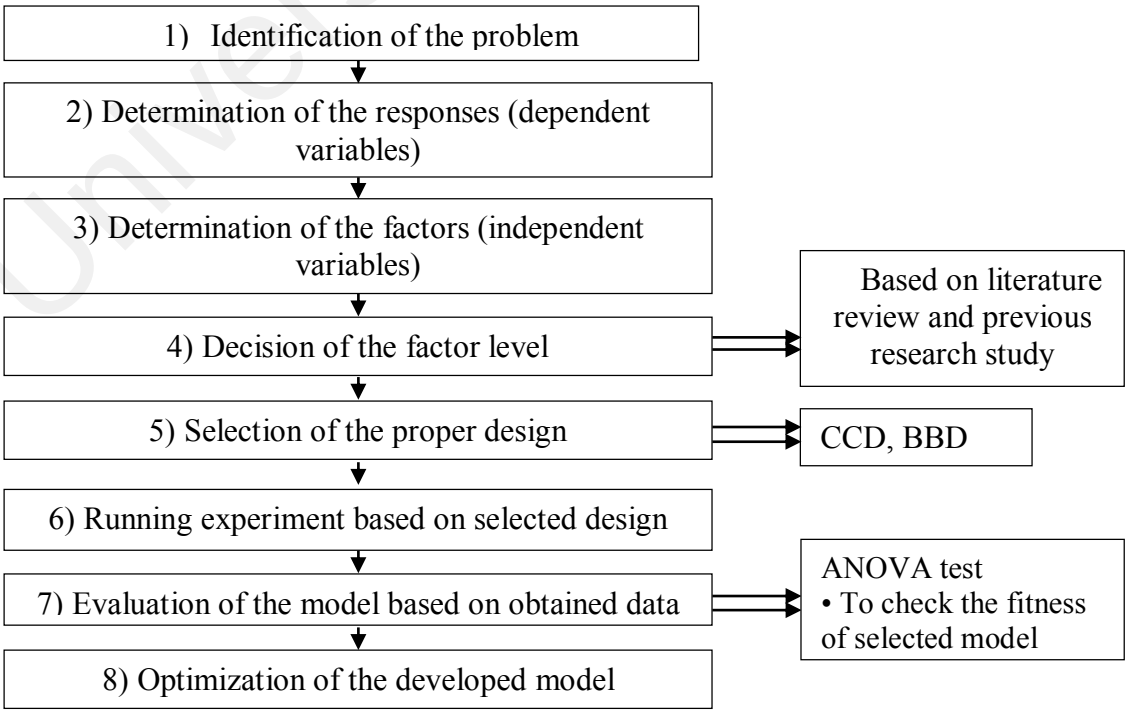

Figure 2.8: Steps involve in RSM analysis.

2.4 Semiconductor Photoelectrode

The photoelectrode in a DSSC system consists of nanostructured semiconductor oxide materials deposited onto the transparent oxide (TCO) glass. Oxides of titanium (TiO_2) (Ito et al., 2007), zinc (ZnO) (Lupan et al., 2010) and stannic (SnO_2) (Han et al., 2009) have been investigated as the component materials in the photoanodes (Shalini et al., 2015). However, the use of ZnO and SnO_2 as the MOS material in DSSC fabrication yields a lower energy conversion efficiency in comparison to nanocrystalline TiO_2 (Bauer et al., 2002; Fukai et al., 2007; Han et al., 2009). The need for semiconductor material that can absorb more light has become the driving force in the development of DSSC systems (Narayan, 2012; Bakhshayesh & Mohammadi, 2013).

According to Hoffman et al. (1995); Karruppuchamy et al. (2006); Zhang et al. (2009) and Narayan (2012), the ideal semiconductor material for DSSC is TiO_2 NPs. It is because of its photoactivity, non-toxicity, biocompatibility, photodurability, low cost, inert, posses oxidizing ability, good corrosive resistance, stability, has suitable band gap and has good optical properties. The conduction band edge of TiO_2 lies slightly below the LUMO of many dyes. This is one of the requirements for excellent electron injection (Li et al., 2005). Apart from DSSCs, TiO_2 is a versatile compound that are widely used in various applications such as white paint, toothpaste, sunscreen, optical filters, microelectronic devices, chemical sensors, photoluminescense and catalytic devices (Watthanaarun et al., 2005; Song et al., 2005; Fujihara et al., 2007; Nakata & Fujishima, 2007; Elayappan et al., 2015).

2.4.1 TiO_2 Nanoparticles (NPs)

The fourth most abundant element in the earth is TiO_2 or titanium white. Its melting and boiling points are 1843 ℃ and 2972 ℃, respectively. Its three crystalline forms are

the tetragonal anatase, tetragonal rutile and orthorhombic brookite. Rutile structure is the most thermodynamically stable phase. The other two are metastable. The anatase band gap is 3.2 eV. For the rutile and brookite phases, the band gaps are 3.0 and 1.9 eV respectively (Zallen & Moret, 2006; Tabaei et al., 2012). Of the three crystalline forms of TiO_2, anatase form is preferred as semiconductor phase because of its wide band gap. Hence, it has better photo-activity performance and suitable for DSSC application (Na-Phattalung et al., 2006). The higher anatase conduction band edge leads to a higher Fermi level. The wide band gap of TiO_2 will not absorb the incoming light. The light will be absorbed by the dye molecules. The anatase is also a more photoactive phase due to its slower recombination velocity of photogenerated charges in its structure (Caratão et al., 2014). The anatase-based DSSC has a short circuit photocurrent that is 30% more than that of the rutile-based DSSC with the same film thickness. Due to smaller surface area to volume ratio, the rutile phase adsorbs less dye, thereby provides low efficiency yield. The high packing density of rutile TiO_2 hinders and makes the electron transport slower compared to anatase TiO_2 (Park et al., 2000; Sima et al., 2010). The highest efficiency is given by the TiO_2 due to its higher surface area to volume ratio, porosity, pore diameter, transparency and film thickness.

TiO_2 NPs have been used to make semiconductor photoelectrode for DSSC application since it is able to adsorb a larger number of dye molecules. Once the MOS receives the electrons generated from the excited dye molecules, the TiO_2 NPs transfer the electrons rapidly to the load. If the generated electrons spend more time in MOS, they are more likely to recombine with the holes in dye molecules or involved in reducing the triiodide ions in the electrolyte. Hence, highly porous electrode could provide a large surface area for accommodating more loading of dye molecules to generate a large amount of electrons.

There are three types of porosity; microporosity, mesoporosity and macroporosity. In micropores the pore diameter is up to 2 nm. In mesopores, pores have diameter from 2 to 50 nm. Pores greater than 50 nm are macropores. Mesoporous TiO_2 nanoparticles are being employed in DSSC fabrication for dye molecules anchorage to the TiO_2 surface to enhance photoabsorption (Grätzel, 2004). Mesoporous TiO_2 has more surface area due to the pore walls for the dye to adhere. Such structures will provide reaction sites to facilitate mass propagation through internal pathways (O'regan & Grätzel, 1991). Normally, mesoporous films with thickness between 10 and 12 μm, 50% porosity and 20 nm diameter particles can absorb all the incoming light and exhibit efficiency to 11.4%. Screen printing and doctor blade techniques are used to deposit the films. Sintering is commonly performed at temperatures between 450 and 500 ℃ (Adedokun et al*.*, 2016). The first DSSCs using mesoporous nanocrystalline TiO_2 films been reported by O'Regan & Grätzel (1991) have become extraordinary breakthrough. Until now, the mosoporous film is widely used as a MOS in DSSCs. The mesoporous TiO_2 film have unique characteristics compared to compact analogs, which are: (i) very low inherent film conductivity and (ii) no built-in electrical field due to the small nanocrystalline particles (Grätzel, 2003; Gong et al*.*, 2012).

The additional surface area in mesoporous TiO_2 film enables a larger amount of dye uptake. However, it is also not without any drawbacks (Karthikeyan et al*.*, 2006; Gong et al*.*, 2012). This is because if the electrolyte is liquid, electrical shorts between the electrolyte and the conducting FTO/ITO layer may occur (Karthikeyan et al*.*, 2006). The dynamis of electron transport is also affected by film morphology and the pore network (Saito et al*.*, 2004). Again, if liquid electrolytes are used, they can flood the pathways due to the mesopores to the FTO layer and back electron transfer will occur diminishing the efficiency of the cell (Longo & de Paoli, 2003; Kong et al*.*, 2007; Gong et al*.*, 2012).

This drawback may be overcome using solid or gel polymer electrolyte. These drawbacks can also be minimized by employing a blocking layer (Karthikeyan et al., 2006; Longo & de Paoli, 2003) onto the surface of the FTO substrate. There are different MOS blocking and insulating layers e.g. TiO_2, niobium pentoxide (Nb_2O_5), zinc oxide (ZnO), calcium carbonate ($CaCO_3$) and barium carbonate ($BaCO_3$). These insulating layers retard the charge recombination and reduce interaction between the injected electrons and the liquid electrolyte (Palomares et al., 2003). TiO_2 is the most appropriate material since it can provide a bigger TiO_2/FTO contact area to enhance electron transfer (Cameron & Peter, 2003; Zhang et al., 2009). Cameron & Peter (2003) have studied the impact of TiO_2 blocking layers on electron and to triiodide ion recombination in the electrolyte.

2.4.2 TiO_2 Nanorods (NRs)

TiO_2 NPs is often used in photoanode, but with limitations. Due to their smaller sizes compared to the wavelength of the incident light, a dye-coated TiO_2 NPs shows less light absorption by the dye. Inefficient scattering of visible light and trapped charges at grain boundaries result in a substantial loss of incoming light. Insufficient electron diffusion coefficient and decrease in electron mobility and lifetime lead to slow transport rate and reduction in the generated power (Lee et al., 2011; Nair et al., 2011; Chen et al., 2013; Lee et al., 2014; Anjusree et al., 2013; Mali et al., 2014; Sugathan et al., 2015; Lu et al., 2015). TiO_2 NPs size is another key parameter for good DSSC performance since the electron diffusion coefficient increases with increasing of particle size. This is due to reduced surface area and grain boundary structure. Also, electron recombination time decreases with increase in particle size (Martison et al., 2007). Unfortunately, efficiency is reduced with particle size decrease due to the reduced diffusion length. Hence, particle size optimization is required (Martison et al., 2007).

To overcome TiO_2 NPs limitations, research is geared towards making structures that can facilitate pore diffusion (Grätzel, 2003). One-dimensional (1-D) nanostructured materials e.g. nanofibers, nanorods, nanowhiskers, nanowires, and nanotubes have also attracted much attention all over the world with respect to their application in DSSCs (Park et al., 2013; Elayappan et al., 2015). One-dimensional nanostructures (1-D) exhibit good light scattering and electron transport properties (Lee et al., 2014; Anjusree et al., 2013; Wang et al., 2015), hence improve the electrical and optical properties in the photoelectrodes of the DSSCs (Cozzoli et al., 2003). These 1-D nanostructures also have high surface area to provide a direct electron pathways, maintain sufficient dye adsorption sites and reduce electron recombination (Manna et al., 2002; Enache-Pommer et al., 2007; Ramakrishna et al., 2010; Lee et al., 2014; Anjusree et al., 2013; Wang et al., 2015). The TiO_2 layer packed with random orientation of 1-D nanorods helps the electrolyte penetration into the photoelectrode due to porosity (Park et al., 2000). Furthermore, 1-D nanostructured TiO_2 can scatter light and enable incident light to stay longer in the cell that can lead to the enhancement of the solar energy conversion efficiency (Cuangchote et al., 2008).

Many metal oxide nanofibers and nanotubes, including the oxides of silica, titanium, cobalt oxide, nickel oxide, zirconium, zinc and palladium have been prepared effectively by electrospinning method (Li et al., 2006). Among the methods for fabricating TiO_2 fibrous materials, electrospinning technique is a common method to prepare inorganic oxide nanofibers since the electrospun fiber microstructure can be control by optimizing the electrospinning parameters or the properties of the precursor solution (Chen et al., 2013). One-dimensional (1-D) TiO_2 porous nanofibers can be developed via sol-gel synthesis and electrospinning technique in order to achieve superior charge transport properties in the semiconductor metal oxide. By sintering the obtained nanofibers at

certain temperature followed with mechanical grinding of the TiO_2 nanofiber, 1-D TiO_2 nanorods can be produced.

2.4.3 Sol-gel Synthesis

The sol-gel method was used first to synthesize the TiO_2 solution while the electrospinning techniques was further employed to produce one dimensional (1-D) TiO_2 nanofibers. The sol-gel is the commonly used as the simple method to synthesize metal oxide that involved two distinct phases which are solution and gelation. The sol-gel method is chemical process in which solution are prepared into the gel form (Levy & Zayat, 2015; Pradeep & Dubey, 2017). It is prepared through the formation of a colloidal suspension or a solution from the hydrolysis and polymerization reactions of the precursors (Wang et al., 2014). It is a simple and low cost process that able to produce good nano-materials with higher yield. The size of nano-materials are depend on the precursor, solvent, polymer concentration and period of aging (Pradeep & Dubey, 2017). The combination method of sol-gel and electrospinning technique have been reported by Watthanaarun et al. (2005). By using sol-gel synthesis technique, high molecular weight of polymer was added into the solvent in order to form polymeric solution before proceed to electrospinning process. The advantages of this combine method are ease control of concentration and viscosity of the polymer solution. There was also the possibility of control over the physico–chemical properties of the resulting compounds (Esposito, 2019).

2.4.4 Electrospinning

As mentioned before, electrospinning is an efficient and easy-to-use technique to fabricate nanofibers (Frenot & Chronakis, 2003; Yarin, 2011; Bellan & Craighead, 2011; Dalton et al., 2013; Ghorani & Tucker, 2015). The electrospinning process seems to be

a suitable method to develop continuous nanofibers from several polymers since other methods are time comsuming (Asagoe et al., 2007). The fiber diameters ranging from 2 nm to several micrometers using natural and synthetic polymer solutions can be produced through electrospinning process (Ahn et al., 2006; Renekar & Yarin, 2008) which utilizes the electrical forces to produce polymer fibers. The diameter fiber produced are thinner with larger surface area than those obtained from the conventional spinning process (Li & Xia, 2004).

The word electrospinning is derived from the term "electrostatic spinning" which uses a polymeric solution for the fabrication of 1-D nanostructures such as nanofibers, nanorods, nanotubes, nanoflowers and even some non-conventional nanostructures at nanometric scale (Thavasi et al., 2008; Kumar et al., 2012, Cavaliere et al., 2013). These nanostructures contain remarkable characteristics such as flexibility, mechanical functionalities i.e. stiffness and tensile strength that make them a superior candidate in a number of devices (Thavasi et al., 2008, Huang et al., 2003). The setup for electrospinning is illustrated in Figure 2.9, which comprises three parts, a high voltage power supply, a capillary tube containing a small diameter needle also called a spinneret and a grounded metal collector.

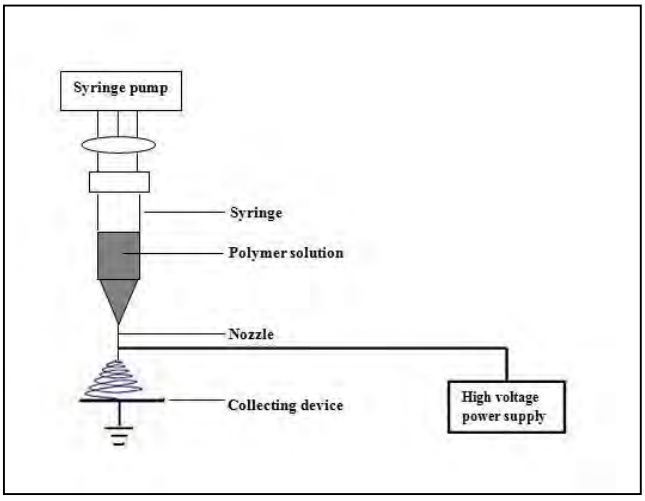

Figure 2.9: Schematic diagram of electrospinning setup.

2.4.5 Factors Affecting Electrospinning Process

For the formation of nanofibers, a high voltage is required between the tip of the needle and the grounded conductor to create electrically charge polymeric solution out of the needle towards the collector. The polymeric solution becomes highly charged at such a high voltage-so that the solution droplet at the tip of the needle experiences two major forces i.e. surface tension and electrostatic force. As the high voltage leads to increase in electric field intensity, the semi-spherical surface at the tip of the syringe elongates toward the collector in the form of a cone called the "Taylor cone". On reaching a critical electric field value, the electrostatic force is greater than the surface tension of the Taylor cone and the polymer solution from the needle tip, which will be collected at the grounded electrode in the form of 1-D nanofibers (Huang et al*.,* 2003, McCann et al*.,* 2005, Sawicka & Gouma, 2006; Sun et al*.,* 2014). The factors effects electrospinning process and morphology of fibers can be categorized into solution, process and ambient parameters. Polymer concentration, viscosity of solution and molecular weight are solution parameters. Process parameters encompass tip to collector distance, flow rate and electric field applied. By changing these parameters, the nanofibers with preferred diameters and morphology can be obtained (Chong et al*.,* 2007). Relative humidity and temperature are environmental or ambient parameters. These also influence the diameter and morphology of the electrospun nanofibers (Li & Xia, 2004). The parameters are taken into account during the electrospinning process including: (Li & Xia, 2004; Rutledge & Fridrikh, 2007; Inagaki et al*.,* 2012).

2.4.6 Solution Parameters

2.4.6.1 Concentration

Jet stretching is significantly affected by polymer solution concentration. In electrospinning, it is required to have a minimum solution concentration to form the

fibers. Beads and fibers will be form if the solution concentration is low (Deitzel et al., 2001; Haider et al., 2018). This is because, at sufficiently low concentration the applied electric field and surface tension can make the polymer chains to shred before reaching the collector (Haider et al., 2013; Pillay et al., 2013; Haider et al., 2018). If the concentrations increased, the bead shape changes. The bead shape changes from spherical-like to spindle-like. At the optimum solution concentrations, uniform fibers with bigger diameters will form due to the higher viscosity resistance (Deitzel et al., 2001; Haider et al., 2018). Solution viscosity and concentration are related. Low solution concentration will give low solution viscosity. Increasing the polymer solution concentration to an optimized value results in viscosity increase. Viscosity increase can entangle polymer chains. The chain entanglements overcome the surface tension, cause the solution to discharge and lead to the formation of uniform beadless electrospun nanofibers (Haider et al., 2018). If the concentration is too high which is beyond the optimal value, continuous fibers are not formed as this hinders the solutions flow through the syringe. This is because the polymer solution will dry at the tip and blocks it thus resulted in beaded fibers (Haider et al., 2018). There are also possible formation of larger fibers (Sukigara et al., 2003). The correlation between solution concentration and diameter of fibers can be summarized, as increasing the solution concentration lead to an increase in diameter of fibers (Deitzel et al., 2001). Solution viscosity and concentration are related. Low solution concentration will give low solution viscosity.

2.4.6.2 Molecular Weight

Molecular weight of the polymer has an impact on the electrical and rheology properties such as conductivity, dielectric strength, viscosity and surface tension (Haider et al., 2018). Hence, this parameter influences the electrospun fiber morphology. With the use of high molecular weight of polymers the desired viscosity are provided for fiber

formation. Eventually, at low molecular weight polymers beads will form rather than fibers. At high molecular weight of polymer fibers with large average diameters formed due to more entanglements of polymer chains will lead to increased in solution viscosity (Ki et al*.*, 2005).

2.4.7 Processing Parameters

2.4.7.1 Flow rate

The flow rate of the polymer solution influences jet velocity and mass transfer rate, and hence affects morphology. A lower flow rate is better as there will be sufficient time for the solvent to "dry up". Via critical flow rate that can be tuned with the polymer solution concentration, uniform beadles electrospun nanofibers will form. Beyond the critical value of flow rate leads to increase pore size and fiber diameter. Beads are also formed. This is due to inadequate drying of the nanofiber when the jet reaches the collector (Megelskiet al*.*, 2002). For polystyrene, when the flow rate was increased to 0.10 mL/min, beads are formed but when decreased to 0.07 mL/min, beadless nanofibers were formed. Therefore, a minimal flow rate must accompany the spinning solution to keep the steadiness between the leaving jet and the following jet that forms (Megelski et al., 2002).

2.4.7.2 Tip-to-collector Distance (TCD)

TCD is another crucial part that will influence the electrospun nanofiber morphology. This is because it is related to time for deposition, rate of evaporation and the instability interval (Matabola & Moutloali, 2013). The effects differs with the polymer system. A minimal distance is needed for the fibers to dry before reaching the collector. Insufficient for drying will result in beads to be observed. Hence, there are necessary for critical distance in order to form uniform and smooth nanofibers (Bhardwaj & Kundu, 2010).

Other researchers (Matabola & Moutloali, 2013; Wang & Kumar, 2006) have concluded that there will be a large and defective nanofibers formed when the distance is small while the diameter reduces as the distance was increased.

2.4.7.3 Applied Voltage

The voltage applied to the solution is crucial. Fibers are formed only after obtaining a threshold voltage. This charge up the solution and together with the electric field starts electrospinning that cause a spherical droplet to deform into a Taylor cone and finally the ultrafine nanofibers will form at a critical voltage (Laudenslager & Sigmund, 2012). This effects different depending on the types of polymers. The initial drop changes shape with flow rate, voltage and viscosity. Nanofibers with smaller diameters formed when the applied voltage increased which assigned to the stretching of the polymer solution in association with the charge repulsion within the polymer jet (Sill & von Recum, 2008). However, at higher voltages and beyond the critical voltage, beads or beaded nanofibers can form easily. This is due to the decreased size of the Taylor cone and increased jet velocity within the same flow rate. This phenomena have been reported by Deitzel et al. (2001) with the used of poly(ethylene oxide) (PEO)/water as the beads formed when the applied voltage increased. It can be expected that more polymer will be ejected at higher applied voltage. This will also result in fibers with larger diameters to form.

2.4.8 Application of Electrospun Nanostructures

Electrospinning technology is one of the most efficient techniques used for the fabrication of nanofibers. Fibers produced by electrospinning are smooth with solid-core cross-section and are used in different applications such as biomedical, protective clothing, filtration, catalysis, energy devices, biosensors, tissue engineering field, etc. Fibers that are hollow and porous have advantage for application in energy devices.

Porous fibers with large surface area to volume ratio are already produced using the electrospinning method (Zhang et al., 2006; Cao et al., 2010). The porous structure of nanofibers fabricated through electrospinning is due to fast evaporation of the solvent that make the polymer solidifies rapidly (Bognitzki et al., 2001; Han et al., 2005). Porous fibers can also be produced by electrospinning polymer blends, followed by selective removal of one of the components (Bognitzki et al., 2001). There is a prospect to implement this electrospinning technique in the development of photovoltaic systems, as the structures produced through this technique have nanoscale dimension. Small device lengths are possible without sacrificing charge collection efficiency. An increase in charge collection will enhance the efficiency of the devices. Nevertheless, the simple fabrication technique may reduce the cost and ease of scale-up. The good potentials of 1-D nanostructure materials have been described by Fujihara et al. (2007) as the utilization of electrospun nanorods semiconductor photoanode resulted in the high efficiency of 4.58%.

In this work, commercial TiO_2 P90 nanoparticles was used as the compact or blocking layer. This layer was spin-coated on the FTO substrate. The mesoporous commercial TiO_2 P25 layer was deposited on top of the compact layer using the doctor-blade method before proceed for DSSCs characterization. Doctor-blade method is simple and inexpensive to prepare a crack free TiO_2 film with thickness that can be controlled (Chen et al., 2007; Singh et al., 2008). Although 1-D nanostructures have good light scattering and electrical property, their use is also not without problems. This is because the internal surface areas of these 1-D materials are lower than that of the nanoparticles resulting in inefficient uptake of dye molecules, which can lower the device efficiency (Cozzoli et al., 2003; Anjusree et al., 2013; Wang et al., 2015). In an attempt to increase the efficiency of the DSSC, the strategy of composite films as the second layer was

introduced in this study which combined the advantages of P25 TiO_2 nanoparticles and 1-D TiO_2 nanorods. This composite film was applied as the second layer to replace the previous used of P25 mesoporous layer. This is hoped to produce good light scattering and efficient dye loading. Such a composite photoanode has been shown to enhance the DSSC performance (Kim et al., 2014). These authors use synthetic dyes and it is our interest to see how much efficiency can be obtained with natural dyes.

2.5 Transparent Conductive Oxide Substrate (TCO)

In DSSCs, conductive glass is used as the substrate to enhance electronic conductivity and transmittance of light in the visible (Ludin et al., 2014; Adedokun et al., 2016). The electrical conductivity of the TCO substrate should be high with low electrical resistivity so that electrons will be transferred to the external circuit efficiently and reduce energy loss (Hara & Arakawa, 2003; Gong et al., 2012; Adedokun et al., 2016). Typically, indium tin oxide (ITO) and fluorine tin oxide (FTO) are deposited on the glass substrate in DSSC application. FTO glass transmittance in the visible spectrum is 75%, the transmittance. That of ITO is >80%, but the FTO glass sheet resistance is only 8.5 Ω/cm^2 compared to 18 Ω/cm^2 for ITO glass (Gong et al., 2012; Mehmood et al., 2014). Sima et al. (2010) compared ITO and FTO based DSSCs by sintering the photoanode on both glasses at 450 ℃ for 2 h in oxygen. It was found that FTO sheet resistance remained constant with overall efficiency *(η)* of 9.4%, while that for ITO increased to 52 Ω/cm^2 with η = 2.4% upon heating. These indicated the instability of the ITO substrate on heating. Hence, FTO has better thermal stability (Kawashima et al., 2004).

2.6 Electrolyte

The electrolyte is the essential part in the DSSC cell. Electrolytes provide the internal ion diffusion between the holes in the photoanode and counter electrode. It is known

that the electrolyte has high ionic conductivity and is important for DSSC performance (Wang et al., 2009). Hence, electrolyte helps dye regeneration. Generally, electrolytes for DSSC consist of salt, solvent and redox mediator. Electrolytes for DSSCs can be in the form of liquid, solid or quasi solid state (Wu et al., 2008; Adedokun et al., 2016). Liquid electrolytes contain organic solvents. Each electrolyte component affects DSSC performance. Organic solvent in the electrolyte is responsible for ion diffusion and dissolution (Wu et al., 2008). However, liquid electrolytes have several disadvantages such as volatilization and leakage. However, solid state electrolyte exhibits low ionic conductivity and DSSCs with solid state electrolyte exhibit low efficiency due to poor intimate contact and high rate of recombination (Mehmood et al., 2014). Therefore, efforts have been directed towards the use of gel polymer electrolytes.

The main drawbacks for solid state electrolyte related to the weak contact between the mesoporous semiconductor photoanode and the electrolyte itself. Thus, quasi solid state electrolytes is the alternative to solve this problem. Gel polymer electrolytes comprise liquid electrolyte which can be either organic solvent based or ionic liquid based and entrapped in a polymer (Song et al., 1999; Mohmeyer et al., 2004). In GPEs, the liquid electrolyte is entrapped by the gel nets (Lan et al., 2007). GPEs also do not penetrate fully into the pores of mesoporous TiO_2 and hence reduces recombination of electrons (De Freitas et al., 2009). GPEs offer advantages of low vapor pressure, good contact with electrodes and exhibit better ionic conductivity compared to solid polymer electrolytes (Wang, 2009). GPEs based on ionic liquids and polymers can also overcome the volatilization and leakage problems that restrict the effective performance of the DSSCs (Wang et al., 2012; Bai et al., 2013; Achari, et al., 2013). This type of electrolyte also exhibits better stability, good contact with the electrodes and low ionic resistivity (Song

et al., 1999; Mohmeyer et al., 2004). For DSSC application, the GPE must also contain a redox couple.

In this study, the redox couple is the iodide/triiodide (I^-/I_3^-) couple. The I_3^- will be formed on interaction with I^- from the salt(s) with iodine (I_2) crystals. The redox couple (I^-/I_3^-) has a potential appropriate for reduction of oxidized dyes. The redox couple also has good kinetic properties for DSSCs (Longo & de Paoli, 2003; Lan et al., 2008; Boschloo & Hagfeldt, 2009). The recombination kinetics between injected electrons and the triiodide component of the mediator are sufficiently slow for longer electron lifetimes (Boschloo & Hagfeldt, 2009).

In the present study, polyacrylonitrile (PAN) based GPEs with ternary iodides (lithium iodides, tetrapropylammonium iodide and 1-butyl-3-methylimidazolium iodide) was used as the electrolyte for DSSC fabrication which has been optimized by Bandara et al. (2015). The PAN based GPEs with ternary iodides is ionic in nature. The DSSC with this GPE exhibits efficiency, η of 5.41%, displaying J_{sc} of 20.6 mA cm^{-2}. The difference between the present work and that of Bandara et al. (2015) is the natural dye sensitizer that we used and the N3 dye used by Bandara and co-workers. The main advantage of PAN-based GPEs is their high ionic conductivity, ~10^{-3} S cm^{-1} at at room temperature (25 ℃). The multiple cation effect in GPEs has attracted a lot of attention. The use of iodides containing small alkaline cations such as Li^+ (Nakade et al., 2001; Agarwala & Thummalakunta, 2011; Aziz et al., 2014) and incorporating molten salts (BMII) with larger cations have boosted efficiency of DSSCs (Agarwala & Thummalakunta, 2011; Bandara et al., 2013). Intermediate-sized cations such as tetrapropylammonium ions can also increase the efficiency of DSSCs with GPEs. Tetrapropylammonium iodide or Pr_4NI are used widely as the dopant salts. Since the

cations are bulky, they are less mobile. Thus, the electrolyte has a higher iodide transference number. Small-sized cations such as Li^+ have high charge density. They will be able to get adsorbed on the TiO_2 semiconductor surface and this will result in faster electron transfer at the dye-TiO_2 boundary (Dissanayake et al., 2013; Wanninayake et al., 2016).

2.7 Counter Electrode (CE)

As mentioned before, the counter electrode (CE) is an essential component used for dye regeneration and reduction of triiodide ions in the electrolyte. The triiodide ion accepts electrons that have been reduced through the CE. Hence, the CE must conduct efficiently and show a low over-voltage for redox couple reduction (Mehmood et al., 2014; Adedokun et al., 2016). A catalytic material, coated on TCO layer is required to accelerate the reduction reaction since the rate of reaction is slow for TCO glass substrate without adherence of catalyst coating (Yen et al., 2009; Mehmood et al., 2014).

Platinum (Pt) is a preferred catalyst due to its high exchange current density, transparent and act as a good catalytic (Kim et al., 2006; Mehmood et al., 2014). Pt can be deposited on counter electrode by thermal decomposition (Papageorgiou et al., 1997), electrodeposition (Tsekouras et al., 2008), sputtering (Fang et al., 2004), vapor deposition and screen printing (Khelashvili et al., 2006). The utilization of platinum as catalyst is very compatible with the use of I^-/I_3^- as redox couple. Pt catalyst can reduce triiodide, I_3^- ion efficiently that will eventually lead to faster dye regeneration (Calandra et al., 2010). Platinum can also reduce the overpotential for the triiodide/iodide reduction and hence, reduces the loss of energy (Yoon et al., 2008). Until now, researchers (Kushwaha et al., 2013; Jonathan et al., 2016; Maurya et al., 2016) still report the used of platinum and I^-/I_3^- as counter electrode and redox couple, respectively. There are also

other counter electrodes reported in the literature such as carbon nanotubes, conductive polymers and graphene (Kim et al., 2006; Cruz et al., 2012). In this study, platinum was the catalyst chosen for coating on the FTO glass substrate.

2.8 Additives

The performance of DSSCs can be improved by incorporating additives in the natural dye solution. Additives are materials added in small quantities to improve the photovoltaic cell performance. In this study, chenodeoxycholic acid (CDCA) and ferulic acid (FA) were used as additives or co-adsorbents to help increase the performance of the DSSCs based anthocyanin. Co-adsorbents can prevent dye aggregation on the semiconductor surface. Their presence can reduce charge recombinations of photoelectrons between the semiconductor and electrolyte (Chien & Hsu, 2014; Ismail et al., 2018). CDCA and FA can increase the amount of carboxyl and hydroxyl groups within photosensitizer in order to improve the co-absorbance properties and chemical structure (Ismail et al., 2018). There are conjugated double bonds in the FA structure that make it easier for the electron to move by reduce the fermi level between TiO_2 and ferulic acid.

2.9 Summary

In this chapter, the structure of DSSC and its working principles, as well as the choice of DSSC components have been explained. The types of semiconductor and dyes have also been discussed. The choice of DSSCs components are:

- Anthocyanin dye extraction from underutilized fruit pericarp of *Ixora siamensis.*
- TiO_2 nanoparticles (NPs) with efficient dye loading and TiO_2 nanorods (NRs) with good light scattering.

- Gel polymer electrolyte of different salts, PAN-TPAI-LI-BMII with iodide/triiodide (I^-/I_3^-) ions as redox mediator in order to get the advantages of mixed cation.
- Platinum as counter electrode due to good catalytic performance.

The next chapter presents the materials used, sample preparation and experimental technique employed in this study.

CHAPTER 3: EXPERIMENTAL METHODS

3.1 Introduction

In this work, the experimental and preparation method were divided into three parts. The first part presents the preparation for identification of natural dyes from fruit pericarps of *Ixora siamensis* using UPLC-ESI-MS/MS in order to prove and confirm the presence of anthocyanin content. Results from this experiment indicated the presence of three types of anthocyanin which are cyanidin-3-rutinoside, delphinidin glucoside and peonidin-3-glucoside. Hence, we considered that the natural dye from fruit pericarp of *Ixora siamensis* consist of anthocyanin compound. These extracts were also subjected to absorption spectroscopy which exhibited a peak at 522 nm. According to Hao et al. (2006), the absorption peak of anthocyanin range within 450 to 600 nm and our findings for anthocyanin absorption is within the range stated in th reference. Hence, in this work, we designate the natural dye from fruit pericarp of *Ixora siamensis* as anthocyanin and the highest colourant content were attribute to the anthocyanin content. This part also presents the detailed preparation on the optimization parameters that will produce the highest anthocyanin extraction yield from fruit pericarps of *Ixora siamensis* by response surface methodology (RSM). The anthocyanin content was determined by following the visible spectrophotometric pH differential method (Lee et al*.,* 2005). The optimized conditions that produced the highest anthocyanin yield was used to extract anthocyanin from the *Ixora siamensis* plant for application as sensitizer in DSSC.

The second part comprises of preparation and characterization of TiO_2 nanostructures. The TiO_2 nanofibers were synthesized using the combined sol-gel and electrospinning methods. Effect of solution concentration and applied voltage were investigated in order to produce uniform beadless TiO_2 nanofibers. Further calcined and mechanical grinding of TiO_2 nanofibers produced TiO_2 nanorods (NRs). Investigation on the effects of

different calcination temperature were also performed. The characterization on surface morphology, elemental and structural analysis of TiO_2 nanostructures via FESEM, EDX and XRD were also carried out.

The third part of this experimental method consists of the preparation of different types of semiconductor photoanode and preparation of electrolyte for DSSC applications. The commercial P90 and P25 TiO_2 nanoparticles (NPs) were used as the MOS in the first DSSC system in order to evaluate the effects of anthocyanin concentration on the efficiency performance. The anthocyanin was extracted following the optimized parameters which have been determined by RSM method. In the second DSSC system, the mesoporous layer consists of a mixture of commercial P25 TiO_2 NPs and TiO_2 nanorods (NRs) at various ratios in order to determine the suitable NP:NR ratio that gives good DSSC performance. FESEM were carried out to observe the surface morphology of the composite mesoporous. The second system will use the anthocyanin concentration that exhibited the highest efficiency in the first system. The third DSSC system will use the composite NPs-NRs ratio that exhibited the highest efficiency, but the anthocyanin extract was added with chenodeoxycholic acid (CDCA) and ferulic acid (FA) and used as the sensitizer. For the electrolyte preparation, the optimized GPE from the work of Bandara et al. (2015) was employed. PAN was used as the polymer host. The polymer and doping salts were dissolved in EC and PC, which at the same time act as plasticizers. LiI and tetrapropylammonium iodide (TPAI) were the doping salts in the PAN-based GPE. These salts provide the iodide ions in the electrolyte. The electrolyte also contained 1-butyl-3-methylimidazolium iodide (BMII) ionic liquid (IL) to increase the supply of iodide ions. In order to create I_3^- to form the I^-/I_3^- redox mediator or redox couple iodine (I_2) crystals were added. The third part also included characterization of the three DSSCs systems in order to investigate the performance. These characterizations were (i) visible

spectroscopy, (ii) electrical *J-V* characterizations, (iii) incident photon to current efficiency (IPCE) and (iv) electrochemical impedance spectroscopy (EIS) analysis.

3.2 Optimization of Anthocyanin Extraction from Fruit Pericarps of *Ixora siamensis* by Response Surface Methodology (RSM)

3.2.1 Materials

Ixora siamensis is also known by its local name of "jejarum". It was used as the anthocyanin source. The colourant was extracted using solvent. The solvents were a mixture of methanol from Systerm and trifluoroacetic acid (TFA) from Merck. These were mixed in the ratio to be determined via RSM for optimized yield. Potassium chloride (KCl) and sodium acetate (CH_3CO_2Na) were the chemical reagents used in the analysis process. They were of analytical grade and obtained from Sigma Aldrich. The fruits of *Ixora siamensis* were obtained from Banting, in the state of Selangor, Malaysia. Fresh fruit pericarps of *Ixora siamensis* were skinned before they were freeze-dried. These freeze-dried fruit pericarps were powdered with a commercial grinder and sieved to get particles of ≤ 250 μm in size. Samples were stored in amber bottles at -20 ℃ and sealed until further analysis.

3.2.2 Experimental Design by Response Surface Methodology (RSM) Approach

Quite often, the model to relate factors or variables to control a response or output is either unavailable or complex. For such cases, information that can explain "input-output" relation need to be explained in an empirically. Box and Wilson has introduced the response surface methodology (RSM) that can relate the dependent and independent from a collection of empirical data. RSM can evaluate not only independent variables, but is able to evaluate the effect of the interaction of several independent variables on the responses. In this work, the RSM was used to design the best condition for anthocyanin

removal from fruit pericarp of *Ixora siamensis*. The independent variables or factors in this study were the trifluoroacetic acid (TFA) to be added to methanol (coded as A), soaking time (coded as B) and extraction temperature (coded as C). The analysis was performed using Design-Expert software (version 6.0.8, Stat Ease Inc., Minneapolis, MN, USA). A three-level (-1, 0, 1) three-factor design was used to evaluate the combined effect of these three parameters. The minimum (-1) and maximum (1) ranges for TFA content were set at 0.5 and 3%, with 60 and 180 min soaking times and temperatures of 30 and 80 ℃, as displayed in Table 3.1. For this study, there were 7 responses (CIE colour indices and anthocyanin content) to be evaluated experimentally in order to achieved the set objective. The CIE colour indices were evaluated in terms of lightness denoted as L*, redness and greenness represent as a*/-a* while b*/-b* indicates the yellowness and blueness, chromaticity (C), hue angle (H°) and colour saturation (s). The response function (Y) was separated into linear (A, B and C), quadratic (A^2, B^2 and C^2) and interactive (AB, AC and BC) (Fan et al*.,* 2008) components. The experimental sequence was randomized. In order to develop an empirical model which correlated the responses to the independent factors, experimental data obtained were fitted to the second-order regression equation. The response equation is (Carley et al*.,* 2004):

$$Y = b_0 + b_1 A + b_2 B + b_3 C + b_{11} A^2 + b_{22} B^2 + b_{33} C^2 + b_{12} AB + b_{13} AC + b_{23} BC \quad (3.1)$$

where b_0 is the intercept at the Y axis; b_1, b_2, and b_3 are linear coefficients; b_{11}, b_{22}, and b_{33} are squared coefficients; b_{12}, b_{13}, and b_{23} are interaction coefficients. Analysis of variance (ANOVA) tables were then generated and the effect of individual, linear, quadratic and interaction terms were examine in order to evaluate the significance of the selected model. Figure 3.1 summarizes the steps involved in RSM optimization for this study.

Table 3.1: Independent variables and their coded and actual values used for optimization.

Independent factor	Unit	Symbol	Code level		
			-1	0	1
TFA content	%	A	0.5	1.75	3
Soaking time	min	B	60	120	180
Extraction temperature	℃	C	30	55	80

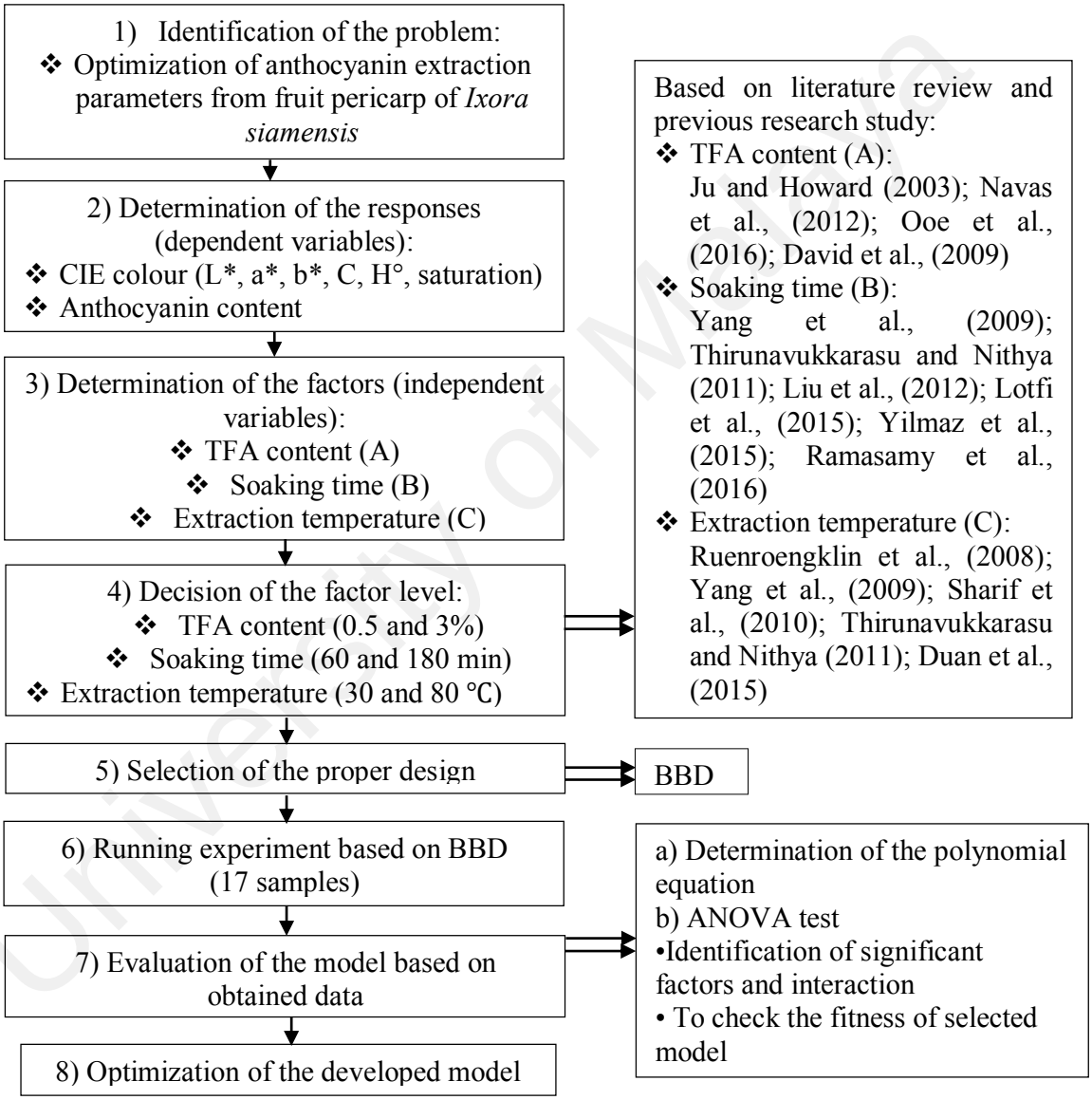

Figure 3.1: Steps in RSM optimization for anthocyanin extraction in this study.

3.2.3 Anthocyanin Colourant Extractions from *Ixora siamensis* by BBD

The Box-Behnken Design (BBD) was chosen to design the experiments to be performed using the independent variables (TFA content, soaking time and extraction

temperature) values generated. From the input variables, BBD generated 17 combination extraction parameters for optimization process. Anthocyanins are soluble in polar solvents. Usually, anthocyanin was extracted from the plant parts using methanol added with trifluoroacetic acid (TFA). For the extraction, 0.03 g of the powdered fruit pericarp and 16 mL of TFA-methanol solvent were added together. The trifluoroacetic acid (TFA) content in methanol were 0.5, 1.75 and 3%. The solutions were then stirred and heated at temperatures of 30, 55 and 80 ℃ and soaking times of 60, 120 and 180 min. 17 samples were prepared according to combination parameter generated by BBD as in Table 3.2.

Table 3.2: BBD sample arrangements.

	Factor 1	Factor 2	Factor 3
Sample	A:TFA content (%)	B:Soaking time (min)	C:Extraction temperature (℃)
1	0.5	60	55
2	3	60	55
3	0.5	180	55
4	3	180	55
5	0.5	120	30
6	3	120	30
7	0.5	120	80
8	3	120	80
9	1.75	60	30
10	1.75	180	30
11	1.75	60	80
12	1.75	180	80
13	1.75	120	55
14	1.75	120	55
15	1.75	120	55
16	1.75	120	55
17	1.75	120	55

After extraction of the natural colourant using various acidified methanol mixture for the different soaking times and temperatures, the solutions were centrifuged at 5000 rpm for 15 min. This was for removal of balanced residues. The supernatant was filtered to

remove any traces of residue. The 17 prepared samples were then subjected to visible spectroscopy to calculate the total anthocyanin content and measured the CIE colour analysis in terms of L*, a*, b*, C, H° and saturation.

3.2.4 Total Anthocyanin Content Measurement

The total amount of anthocyanin was evaluated by following the spectrophotometric pH differential method (Lee et al., 2005). Samples were diluted separately with 0.025 M potassium chloride (KCl) buffer pH 1 (procured from Sigma Aldrich) and 0.4 M sodium acetate (CH_3CO_2Na) buffer pH 4.5 (procured from Sigma Aldrich). The absorbance (A) of the mixture was measured at $A_{\lambda vis\text{-}max}$ and at 700 nm using visible spectrophotometer. The absorbance was calculated as:

$$A = [(A_{\lambda vis\text{-}max} - A_{700})_{pH1.0} - (A_{\lambda vis\text{-}max} - A_{700})_{pH4.5}] \quad (3.2)$$

The total anthocyanin content was calculated using equation (Wrolstad et al., 2005):

$$\text{Anthocyanin content } \left(\frac{\text{mg}}{\text{L}}\right) = \frac{\text{A} \times \text{MW} \times \text{DF} \times \text{V} \times 1000}{\varepsilon \times \text{l} \times \text{c}} \quad (3.3)$$

Here A is the absorbance from equation (3.2). DF being dilution factor and for this work DF=6. MW is 449.2 g/mol, the molecular weight of cyanidin-3-glucoside. V is volume of sample stock solution. l is the cell path length (cm) and c is the sample concentration while ε is the molar absorptivity (26,900).

3.2.5 CIELab Analysis for obtaining L*, a*, b*, C, H° and Saturation Responses

Colour originates from the absorption of a particular wavelength in the visible by the pigment. In this work, the L*, a*, b*, C and H° values for the natural dye from fruit pericarp of *Ixora siamensis* were obtained using the Avantes (AvaSoft 7.6) visible spectrophotometer and analyzed using the CIE colour system. Spectral curves were

recorded in the dark, from 380 to 780 nm. The colour measurement of L*, a*, b*, C, H° and saturation of the "jejarum extract" was evaluated according to the Commission Internationale de l'Éclairage (CIE), or The International Commission on Illumination) colour system. CIE is the main international organization concerned with colour and colour measurement (Loughrey, 2002). CIELab colour system evaluates colour of the natural dye using CIELab colour co-ordinates (Gonnet, 1998; Loughrey, 2002; Birse, 2007). The values of L*, a*, b*, C and H° are the variables in the CIELAB colour space (Figure 3.2). The vertical axis, is the lightness axis, L*. L* expresses the distinction between the condition of light (L* = 100) and dark (L* = 0). Chromaticity (C) concerns with intensity of colour brightness. On the chromaticity circle in Figure 3.2, the hue angle values are from h_{ab} 0° to 360° (magenta-red) stepped counterclockwise across a continuously fading hue circle. Other values of h_{ab} are 90° (yellow), 180° (bluish-green) and 270° (blue) (Gonnet, 1998). In the horizontal plane depicted in Figure 3.2, a* is a measure of redness (or –a* of greenness and b* is a measure of yellowness (or –b* of blueness) (Birse, 2007; Velmurugan et al., 2009). Other additional values derived from CIE colour coordinates is saturation (s) using equation (3.4). Saturation (s) is chromaticity to lightness ratio (Birse, 2007).

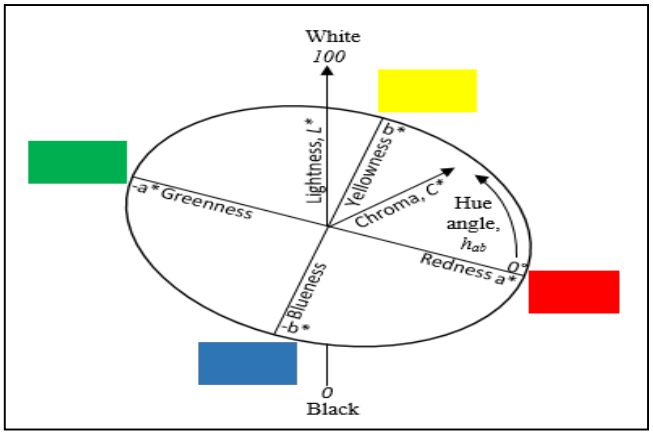

Figure 3.2: CIELab colour space.

$$\boldsymbol{s = C*/L*} \tag{3.4}$$

After completion of the procedures from sub-sections 3.2.4 and 3.2.5, we have obtained the experiment results. 17 combination results obtained were included into the BBD table (Table 3.3) to investigate the relationship between the responses (CIE colour analysis and anthocyanin content) and extraction parameters (TFA content, soaking time and extraction temperature). Several evaluation step which displayed in Figure 3.2 were performed in order to determine the optimize combination extraction parameter of anthocyanin extraction.

Sequential model sum of squares, model summary statistics and ANOVA analysis were done to examine and develop the suitable polynomial equation that can represent the relationship between input (CIE colour and anthocyanin content) and output responses (TFA content, soaking time and extraction temperature). These evaluation steps offers comparison between models showing the statistical significance. A small p-value (Prob>F) indicates that adding interaction terms improved the model. The model that has a p-value less than 0.05 will be the model to describe the process. Models with significant lack of fit of probability value 0.05 or smaller should be avoided while high regression analysis were chosen. Upon determining the appropriate polynomial equations, validation steps were performed to investigates the experimental errors of the developed models. Response surface model generated by Design Expert software were examined to evaluate the input and output process variables. The numerical optimizations of the multiple responses were performed in which to generate optimum combination of factor levels that meet the specific goals. The combination of optimized extraction parameters i.e. TFA content, soaking time, extraction temperature will be used for the anthocyanin natural colourant extraction for application as sensitizer in the DSSCs.

Table 3.3: BBD tables of 17 experimental results of different combination parameters with responses of L*, a*, b*, C, H°, saturation and anthocyanin content responses.

	Factor 1	Factor 2	Factor 3	Response 1	Response 2	Response 3	Response 4	Response 5	Response 6	Response 7
Sample	A:TFA content (%)	B:Soaking time (min)	C:Extraction temperature (℃)	L*	a*	b*	C	H°	Saturation (s)	Anthocyanin content (mg/L)
1	0.5	60	55							
2	3	60	55							
3	0.5	180	55							
4	3	180	55							
5	0.5	120	30							
6	3	120	30							
7	0.5	120	80							
8	3	120	80							
9	1.75	60	30							
10	1.75	180	30							
11	1.75	60	80							
12	1.75	180	80							
13	1.75	120	55							
14	1.75	120	55							
15	1.75	120	55							
16	1.75	120	55							
17	1.75	120	55							

3.3 Analytical Ultra Performance Liquid Chromatography with Electrospray Ionization Tandem Mass Spectrometry (UC-ESI-MS/MS)

An analytical ultra performance liquid chromatography with electrospray ionization tandem mass spectrometry, UPLC-ESI-MS/MS (Perkin Elmer FX15) was used to prove and identify the anthocyanin content in the fruit pericarps of *Ixora siamensis*. The samples were dissolved in acidified methanol. The anthocyanin fractions were examined using the AB Sciex 3200Q Trap, equipped with Phenomenex Aqua C18 reverse-phase column (50 mm × 2.0 mm × 5 μM). Elution was performed with a gradient of mobile phase A (water with 0.1% formic acid and 5 mM ammonium formate) and mobile phase B (acetonitrile with 0.1% formic acid and 5 mM ammonium formate) with rapid screening at 15 min run time. The following subsequent gradient was used for all samples: 0.01 to 8 min, from 10% to 90% B, held for 3 min and back to 10% A in 0.1 min and re-equilibrated for 5 min. The samples were filtered through a nylon filter of 0.22 μM. The ion source used for the interface was a Turbo V source run in negative and positive electrospray ionization (ESI) modes. The following MS conditions were set: full scan, i.e. between 100 and 1200 m/z, MS/MS scan at 50 and 1200 m/z, source temperature of 400 ℃, nebulizer N_2 purified gas 40 psi and capillary voltages +5500 V and −4500 V. Acquisition and processing of the mass fragmentations were performed based on journal references and ACD/Labs advanced chemometrics mass fragmentation predictive software.

3.4 Synthesis of TiO_2 Nanostructure for Semiconductor Photoelectrode

3.4.1 Materials

Titanium (IV) isopropoxide TTIP, [$Ti(OCH(CH_3)_2)_4$, 98%] was purchased from Sigma–Aldrich. TTIP was used as precursor in the electrospinning procedure. Polyvinylpyrrolidone (PVP) (MW: 1,300,000, Aldrich) was the binder for the electrospinning solution. The PVP was dissolved in ethanol (95.0%, Aldrich). N,N-

dimethylformamide (DMF, 99.0%, Aldrich) was also added to help make the fibers continuous. Acetyl acetone (99.0%, Aldrich) was the catalyst in order to extend the solidification time of the TiO_2 gel solution. The solidification time can be extended due to the formation of a stable ligand structure between the TTIP and the acetyl acetone (Park et al., 2013). In this study, the fabrication of TiO_2 nanofibers involve combination of two steps which are sol-gel methods and electrospinning process. The sol-gel method was employed to produce the precursor for TiO_2 which will be used in the electrospinning solution. After obtaining the nanofibers from electrospinning, the nanofibers were sintered to get pure TiO_2 nanofibers. Nanorod will be obtained after mechanical grinding.

3.4.2 Preparation of TiO_2 Solution by Sol-gel Synthesis

Here, the details of chemicals and processes are as follows. 0.44 g of PVP was dissolved in 3 mL ethanol in a glass bottle and continuously stirred until dissolved. In order to optimize and study the effect of the polymer concentration for nanofiber formation, different amounts of PVP polymer, 0.44, 0.50, 0.56, 0.62 and 0.68 g which correspond to 9.2, 10.2, 11.2, 12.2 and 13.2 wt.% of PVP were used to prepare the sol-gel solution. To ensure stable and continuous electrospun nanofibers, 1 mL of DMF which is polar organic solvent was added to the ethanolic solution of PVP. Subsequently, a polymerization catalyst of 1.2 mL acetyl acetone was then added to the solution. Finally, 0.6 mL of Titanium (IV) isopropoxide (TTIP) was added into the sol-gel system and the TTIP added sol-gel solution was stirred for 1 h until homogeneity was achieved. Similar procedure with the optimized amount of polymer concentration was used to prepare the TiO_2 sol-gel solution in order to optimize fiber formation and study the effect of electric field towards nanofiber formation. The above procedure was conducted in a controlled environment in order to avoid moisture.

3.4.3 TiO_2 Nanofiber Preparation by Electrospinning

The electrospinning process was further used to prepare TiO_2 nanofibers by using the solution prepared in sol-gel synthesis. It is an efficient method for small diameter and high surface-to-volume ratio fiber production. The electrospinning setup (Figure 3.3) consisted of a 1 mL/h syringe, syringe pump, a high-voltage power supply and aluminum foil as the collector. During the experiments, the TiO_2 precursor solution from sol-gel synthesis was loaded in a syringe with vertically attached electrospinning device. The TiO_2 solution were electrospun using the electrical potential (voltage) which was supplied by a high-voltage power supply and applied between the needle tip and collector. A syringe pump was used to control the flow rate of the spinning solution.

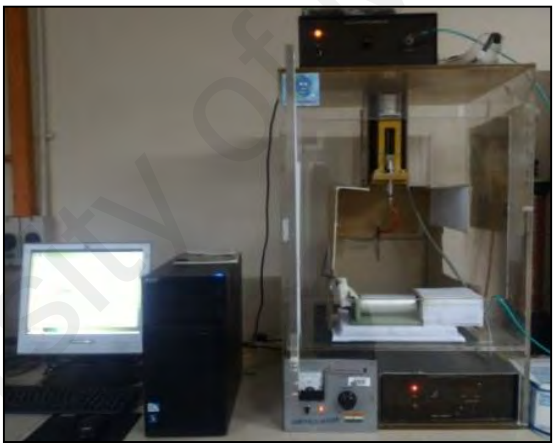

Figure 3.3: Electrospinning setup.

3.4.4 Effect of Polymer Concentration on TiO_2 Nanofiber Formation

In electrospinning, the polymer solution concentration plays an important role in fiber formation. The different polymer concentrations involved in the preparation of sol-gel solution influences the nanofiber formation. Polymer concentration is an important factor that controls the diameter of the fibers (Fridrikh et al., 2003; Inai et al., 2005; Patra et al., 2009). In this study, the effect of polymer concentration towards formation of beadless electrospun nanofiber will be investigated. The bead and fiber diameter

relationship with polymer concentration will also be examined. For the effect of polymer concentration on TiO_2 nanofiber formation, the rate of solution emission (flow rate), the needle tip-to-collector distance (TCD) and applied voltage were set constant for all different polymer concentrations in the electrospinning process. This is done to ensure that only the polymer concentration was being varied and the electric field defined as the applied voltage divided by the TCD (Chowdury & Stylios, 2010) are the same for all samples. Table 3.4 displays the experimental requirements to prepare the TiO_2 solution with regards to the effect of different polymer concentrations. The samples are denoted as NF1, NF2, NF3, NF4 and NF5 (9.2, 10.2, 11.2, 12.2 and 13.2 wt% PVP). During the experiments, the applied voltage was fixed at 18 kV. The flow rate of the spinning solution was set to 1 mL/h while TCD was set at 14 cm. The optimized wt.% of PVP was then subjected to further studies.

Table 3.4: Effect of polymer concentration on nanofiber formation.

Designation	PVP (wt.%)	PVP (g)	TTIP (mL)	Ethanol (mL)	DMF (mL)	Acetyl acetone (mL)
NF1	9.2	0.44	0.6	3	1	1.2
NF2	10.2	0.50	0.6	3	1	1.2
NF3	11.2	0.56	0.6	3	1	1.2
NF4	12.2	0.62	0.6	3	1	1.2
NF5	13.2	0.68	0.6	3	1	1.2

3.4.5 Effect of Applied Voltage on TiO_2 Nanofiber Formation

Applied voltage is another key factor for formation of electrospun nanofibers. Fibers will form only when a minimal voltage has been obtained. This minimal or threshold or offset voltage is required to produce the solution jet, which will finally be collected on the collector as nanofibres. The jet motion is influenced by the electric field. Thus, the nanofiber surface structure and fiber diameter will be affected (Jin et al., 2018). Thus, further investigation on applied voltage used in electrospinning process were performed

in order to intensively study how electric field manipulation can affect bead and fiber formation. The electric field distribution can be manipulated by changing the applied voltage although TCD was kept fixed.

To investigate the effect of electric field to the fiber formation, different voltages (16, 17, 18, 19, 20, 21 and 22 kV), were set for the optimized polymer concentration; hence creating a different electric field in electrospinning setup which can influence the nanofiber formation. The working distance from tip-to-collector (TCD) were fixed at 14 cm and the solution flow rate fixed at 1 mL/h. Table 3.5 lists the required experimental parameters for the effect of electric field on TiO_2 nanofiber formation for optimized polymer concentration, denoted as NF5 sample with 13.2 wt% PVP. The optimized polymer concentration and electrospinning parameter that resulted in continuous nanofiber formation without beads was used for the TiO_2 nanorod production.

Table 3.5: Effect of electric field on nanofiber formations using optimized polymer concentration of 13.2 wt.% (NF5).

Designation	Distance (cm)	Voltage (kV)	Electric field (kV/cm)
NF5-1	14	16	1.14
NF5-2	14	17	1.21
NF5-3	14	18	1.29
NF5-4	14	19	1.36
NF5-5	14	20	1.43
NF5-6	14	21	1.50
NF5-7	14	22	1.57

A thick white electrospun film of PVP-TiO_2 composite was collected on a grounded aluminium (Al) foil that was wrapped on the rotating drum. The sheet was peeled-off from the Al foil and and further characterized for morphological properties using FESEM. The sheet membrane was then calcined at different temperatures of 400, 500,

600 ℃, respectively for 5 h, at 2 ℃/min heating rate. This is to determine the suitable temperature to obtain TiO_2 nanofibers with anatase crystallite form since anatase is the most suitable structure for good DSSC efficiency. This structure can be determined from the x-ray diffraction (XRD) analysis. By heating the composite at the thermal decomposition temperature, the PVP polymer will be degraded and removed leaving the TiO_2 nanofiber product behind. These TiO_2 nanofibers were ground mechanically to produce TiO_2 nanorods and further characterized for morphological analysis (Chen et al., 2007). Figure 3.4 shows the TiO_2 nanofibers formed.

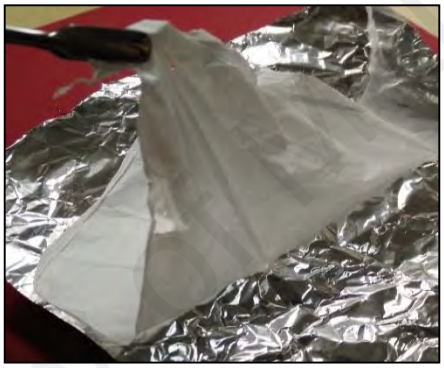

Figure 3.4: Photograph of TiO_2 nanofibers produced from electrospinning process.

3.5 Characterization of TiO_2 Nanostructures

3.5.1 Field Emission Scanning Electron Microscope (FESEM)

FESEM was used to investigate the surface of a solid material at the nanoscale range and in this study is to evaluate nanofiber formation. This technique offers higher resolution and large depth focus compared to an optical microscope. FESEM capable of detecting fiber diameters and morphologies of nanomaterials. In this study, surface morphology and fiber formation of electrospinning nanofibers and the photoanode films were investigated using FESEM (Hitachi SU8220). To investigate the surface morphology of nanofibers from electrospinning, membrane samples were used, while nanorods and nanoparticle samples were in powder form. For FESEM, all sample studied

were sputtered to coat them with a thin layer of platinum to make them conducting and to avoid any possible charging effect during FESEM analysis. This is to ensure that the samples are electrically conductive especially at high magnification. The morphology of the samples were then evaluated using Image J in order to measure the diameter and particle size.

3.5.2 Energy Dispersive Analysis of X-Rays (EDX)

EDX is an x-ray technique that can identify elemental composition in materials. The EDX systems is attached to the FESEM instrument. In EDX, an electron beam excites atoms in a sample and X-rays with energy characteristic of the atoms and a spectrum is obtained (Cushing et al*.,* 2004). EDX provides a spectrum that depicts peaks signifying the elements making up sample being analysed. Elemental mapping of a sample and image analysis are also possible. In this study, the synthesized nanorods (NRs) of TiO_2 was characterized using EDX (Hitachi) analysis in order to determine elemental composition that exist in the NRs.

3.5.3 X-Ray Diffraction (XRD)

XRD is a useful tool that can characterize solid crystalline materials, ceramics and inorganic compounds. This analysis is a nondestructive and rapid technique that can be used to determine crystal structure, phase identification, strain and average crystallite size (McCusker & Baerlocher, 2013). High intensity x-rays was used to determine the material structure. The experiment was performed when an x-ray beam with a wavelength λ at a scattering angle θ hit the target material which leads to interference between the scattered radiation. The diffraction occurs when the rays are reflected from successive planes. The diffraction pattern is related to the distribution of atoms in a material and atomic spacing. The diffraction condition follows Bragg's law ($n\lambda=2d \sin$

θ), where d is lattice atomic spacing, θ is the scattering angle (Bragg's angle), n is reflection order and λ is x-ray wavelength. In the present study, XRD analysis was used to identify the nature of the nanostructured materials calcined at different temperatures of 400, 500 and 600 ℃ in order to confirm their phase structure. The XRD analysis was performed using the Olympus BTX Benchtop XRD Diffractometer. The data were collected using Cu-$K\alpha$ x-radiation at diffraction angles of 2θ = 5° to 55° with X-ray wavelength = 1.5406 Å. For the XRD measurements, the nanostructured materials were prepared in powder form. XRD patterns were analyzed using Origin 9.0 software. The XRD peaks were indexed by comparing with the similar diffraction patterns reported in the literature. The aim is to produce the anatase TiO_2 nanostructures to be use in DSSC fabrication. The percentages of anatase was calculated based on following equation:

$$\% \text{ of anatase} = \frac{area\ of\ anatase}{area\ of\ anatase + area\ of\ rutile} \times 100\% \quad (3.5)$$

3.6 Preparation of Materials for DSSC Applications

3.6.1 Fluorine-doped Tin Oxide (FTO) Glass Cleaning Process

The 1 cm x 2 cm FTO glass was used as the electrode substrate. FTO was chosen due to its transparency and low resistivity. Cleaning of the FTO substrate surface is vital to remove any contaminants. It was first washed with detergent to remove marks and dirt before being rinsed twice with distilled water to remove the detergent. The FTO was then rinsed again with acetone. The dried and cleaned FTO glass was immersed in propan-2-ol until boiling (353 K) to eliminate remaining organic impurities on the FTO surface. The conducting glasses were dried again and then kept in a petri dish and sealed with parafilm to be used later.

3.6.2 Preparation of the Commercial Photoelectrode for DSSC

Two layers of TiO_2, one being the blocking or compact layer was coated on the pre-cleaned FTO glass and the second is a porous layer coated on the compact layer. P90 commercial TiO_2 nanoparticles (~15 nm size) and P25 commercial TiO_2 (<25 nm size) purchased from Sigma Aldrich were used in preparing the photoanode. For the compact layer, 0.5 g of P90 TiO_2 powder was added to 2 mL of nitric acid, HNO_3 of pH 1 and ground for 30 min using a mortar and pestle. HNO_3 was added to improve TiO_2 nanoparticle adhesion to the FTO substrate. This blocking or compact layer is to help prevent the electrolyte from being in contact with the FTO glass which may cause shorting. The TiO_2 paste was spin-coated (Figure 3.5 (a)) on the conducting FTO substrate at 2350 rpm for one min before sintering for 30 min at 723 K and then cooled to room temperature. During the coating process, an adhesive tape was used to cover a part of the FTO glass for electrical contacts.

For the second porous layer, 0.5 g of P25 TiO_2 powder was mixed with 2 mL of HNO_3 solution at pH 1 and ground for 30 min using a mortar and pestle. Poly(ethylene glycol) (PEG) of mass 0.25 g and several drops of Triton X-100 surfactant (Sigma) were added to the TiO_2 slurry and ground again to get a homogeneous paste. PEG (Sigma-Aldrich) was added to create pores in the TiO_2 mesoporous layer when the PEG evaporated on heating the TiO_2 film. The surfactant ensured wetting of the solution onto the FTO glass (Yusuf et al., 2014). The solution paste can then be applied on the compact layer by the doctor blade technique (Figure 3.5(b)). The mesoporous layer was sintered again for 30 min at 723 K and then cooled to room temperature. The porous layer gives more surface area for the dye to adsorb onto the TiO_2 surface. The FTO/compact layer/mesoporous layer assembly was then immersed in the anthocyanin solution for 24 h. The white TiO_2 layer will change colour when the dye is adsorbed (Figure 3.5(c)). Before use in DSSC,

the dyed assembly was cleaned with ethanol. Figure 3.5 shows the TiO_2 photoanode before and after being immersed in the anthocyanin solution.

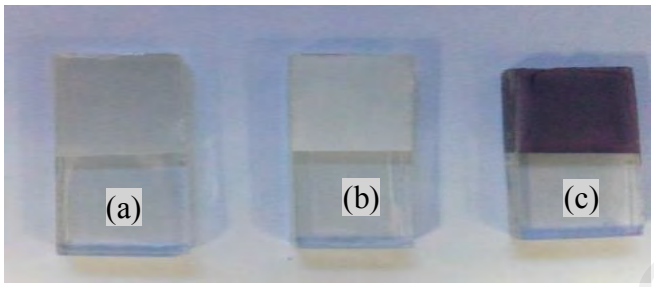

Figure 3.5: TiO_2 photoanode after (a) first layer, (b) second layer and (c) after immersed into anthocyanin dye solutions.

3.6.3 Preparation of the Composite Photoanode for DSSC

In the present study, the TiO_2 nanorods that have potential to be used in the photoelectrode for DSSC application were made by grinding mechanically the sintered electrospun TiO_2 nanofibers. For the preparation of compact layer which using the P90 TiO_2, similar procedure used in the preparation commercial photoanode were followed. The mesoporous layer is a composite layer containing commercial P25 TiO_2 NPs and TiO_2 NRs. Different ratios of TiO_2 nanorods (NRs) (10, 20, 30, 40 and 50 wt.%) which produced via electrospinning process were added into the commercial P25 TiO_2 NPs separately, as presented in Table 3.6. These electrodes were labelled as CP1, CP2, CP3, CP4 and CP5. The P25 commercial TiO_2 NP powder and TiO_2 NRs were mixed with 2 mL solution of nitric acid, HNO_3 of pH 1 and ground for 30 min using a mortar and pestle. PEG of 0.25 g followed with several drops of Triton X-100 surfactant were added to the composite TiO_2 slurry and ground again to get a homogeneous paste. The solution paste was coated onto the compact layer by the doctor blade technique. The compact layer have been firstly spin coated on the FTO glass substrate. The composite photoanode was then sintered again for 30 min at 723 K. The TiO_2 NP-NR composite electrodes were then characterized for the morphology using FESEM analysis. The prepared composite

TiO_2 assembly were then immersed for 24 h in the optimized anthocyanin dye solution that gives good efficiency for the commercial nanoparticles (NPs) DSSC system. The weight percentage of nanorods that results in highest power conversion efficiency will be immersed in different anthocyanin-additive solutions (CDCA and FA) at different percentages (1, 2, 3, 4 and 5 wt.%). Three to four replicates were evaluated for each composition. Figure 3.6 shows the photograph of the composite electrode prior for FESEM analysis.

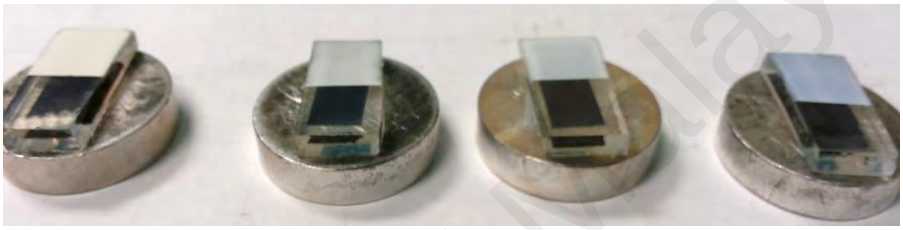

Figure 3.6: Photograph of composite TiO_2 photoanode.

Table 3.6: Different composition of commercial P25 TiO_2 NPs and TiO_2 NRs mixture for composite DSSCs photoanode.

Designation	Commercial TiO_2 NPs (wt.%)	TiO_2 NRs (wt.%)	Commercial TiO_2 NPs (g)	TiO_2 NRs (g)
CP1	90	10	0.45	0.05
CP2	80	20	0.40	0.10
CP3	70	30	0.35	0.15
CP4	60	40	0.30	0.20
CP5	50	50	0.25	0.25

3.6.4 Preparation of Platinum (Pt) Counter Electrode

For the platinum counter electrode, a commercial paste containing platinum solution, plastisol (Solaronix) was deposited dropwise on the conducting side of the cleaned FTO substrate until the substrate surface turned opaque. The Pt coated FTO electrode was then heated for 30 min at 723 K in a furnace. Figure 3.7 depicts the prepared platinum cathode.

Figure 3.7: Platinum counter electrode.

3.6.5 Gel Polymer Electrolyte Preparation (GPE)

In the present work, PAN-based GPEs with ternary iodide salts that have been optimized by Bandara et al. (2015) were used in this study. Polyacrylonitrile (PAN) (MW =150,000g/mol), propylene carbonate (PC), ethylene carbonate (EC), tetrapropylammonium iodide (Pr_4NI or TPAI), lithium iodide (LiI), 1-butyl-3-methylimidazolium iodide (BMII) and iodine (I_2) from Sigma Aldrich were used to prepare the GPE. In preparing the PAN-based GPE system with ternary iodide, 1.245 g of EC was mixed with 1.155 g of PC and stirred until dissolved. The solvents were the mixture of EC and PC. An amount of 0.1329 g of TPAI was added into the solvent, followed with 0.1323 g of LiI and 0.0376 g of BMII. The mixture was stirred until all the added salts have completely dissolved.

The polymer PAN of mass 0.3 g was mixed with the homogenous solution and then stirred at 110 ℃ to form a homogeneous gel. Once the gel has cooled down, 0.039 g of I_2 crystals as redox mediator were added into the gel form. Stirring was continued until the iodine has completely diffused in the GPE. Figure 3.8 shows the PAN-based GPE prepared. The composition of the optimized GPE was 9.86 wt.% PAN, 40.93 wt.% ethylene carbonate, 37.97 wt.% propylene carbonate, 4.37 wt.% tetrapropylammonium iodide, 1.24 wt.% 1-butyl-3- methylimidazolium iodide, 4.35 wt.% lithium iodide and 1.28 wt.% iodine.

Figure 3.8: PAN-based GPEs.

3.6.6 Preparation of Anthocyanin Extraction from *Ixora siamensis* as Dye Sensitizer for DSSC

In this study, the extraction parameter which is the crucial step have already been optimized using RSM. Freeze-dried fruit pericarp powder of *Ixora siamensis* (Figure 3.9 (a)) that contained anthocyanin pigments was used as the anthocyanin source. After extracting for highest anthocyanin content, it was used as the DSSC's photosensitizer. In the first DSSC system using P25 TiO_2 NPs as the mesoporous layer, five different compositions (1, 2, 3, 4 and 5 wt.%) of anthocyanin dye powder were used in order to investigate the dye-solvent composition that can give the highest energy conversion efficiency (η).

For the 1 wt.% composition, a mass of 0.1 g freeze-dried powder was solvent extracted in a tightly closed container with 9.9 g of methanol that contained 0.5% trifluoroacetic acid, soaked for 119 min at extraction temperature of 80 ºC. These combination extraction parameters were obtained from the RSM optimization. The extractions were then centrifuged at 5,000 rpm for 15 min to remove remaining residues (Figure 3.9 (b)). Similar procedure were repeated for other dye composition. The weight percentage of anthocyanin dyes powders which exhibited the highest efficiency performances was further used for composite photoanode system. In the second DSSC system, in which the mesoporous layer comprised of composite NPs-NRs at different nanorods percentage

ratio (10, 20, 30, 40 and 50 wt.%), 3 wt.% of dyes powder which exhibited the highest efficiency in the first DSSC systems was used as the optimized photosensitizer concentration. In the third DSSC systems with optimized nanorod content (10 wt.%), the optimized 3 wt.% of dyes solution were added with additives at different percentages.

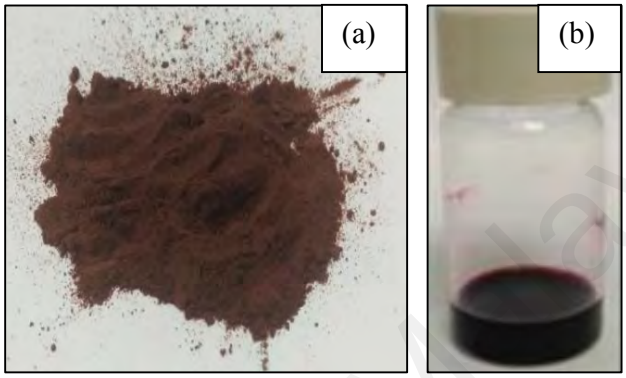

Figure 3.9: (a) Freeze-dried dye powder and (b) dyes extraction.

3.6.7 Additives

The presence of additives such as chenodeoxycholic acid (CDCA) and ferulic acid (FA) are essential for enhancing the efficiency performance of composite DSSCs systems with optimum nanorod content (10 wt.%). The additives at different percentages (1, 2, 3, 4 and 5 wt%) were added into the optimized anthocyanin extract separately.

3.6.8 Fabrication of Dye-sensitized Solar Cells (DSSCs)

DSSCs were fabricated using the anthocyanin natural dye from fruit pericarp of *Ixora siamensis*. The active area was 0.196 cm^2. The prepared GPE was placed between the photoanode and the platinum (Pt) counter electrode, as displayed in Figure 3.10. The Pt electrode was placed with its conductive side on top of the electrolyte layer. The optimized gel polymer electrolyte of PAN-TPAI-LiI-BMII with I^-/I_3^- redox mediator with composition of 9.86 wt.% PAN, 40.93 wt.% ethylene carbonate, 37.97 wt.% propylene carbonate, 4.37 wt.% tetrapropylammonium iodide, 1.24 wt.% 1-butyl-3-

methylimidazolium iodide, 4.35 wt.% lithium iodide and 1.28 wt.% iodine was the medium to transport the charges. In the present study, there were three DSSCs systems. The configurations were as follows:

1) glass/FTO/TiO_2(P90NPs)/TiO_2(P25NPs)/anthocyanin/electrolyte/Pt/FTO/glass immersed into different dye percentages (1, 2, 3, 4 and 5 wt.%).
2) glass/FTO/TiO_2(P90NPs)/TiO_2(P25NPs)+TiO_2NRs/anthocyanin/electrolyte/Pt/FTO/glass. Five different percentages (10, 20, 30, 40 and 50 wt.%) of TiO_2 NRs were mixed with TiO_2 P25 NPs, respectively to prepare composite photoanode. All composite samples were immersed into 3 wt.% of optimized dyes content obtained in (1).
3) glass/FTO/TiO_2(P90NPs)/TiO_2(P25NPs)+10wt.%TiO_2NRs/anthocyanin/electrolyte/Pt/FTO/glass immersed into additives (FA and CDCA) at different percentages (1, 2, 3, 4 and 5 wt.%).

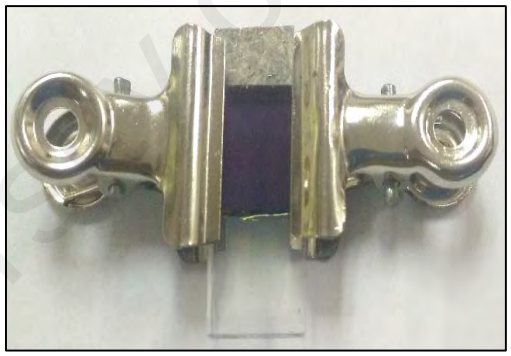

Figure 3.10: Fabrication of DSSC.

3.7 Characterizations in DSSC Applications

The samples that were subjected to FESEM analysis in this study were:

- The composite photoanode (NPs-NRs) made up of P25 commercial TiO_2 nanoparticles and various TiO_2 nanorod percentages (10, 20, 30, 40 and 50 wt.%) which were performed to investigate the morphology properties.

The samples that were subjected to visible spectroscopy (wavelength range between 400 and 800 nm) in this study were:

- Different percentages (1, 2, 3, 4 and 5 wt.%) of anthocyanin extraction from *Ixora siamensis* which were performed in order to examine the effects of different dye concentrations towards the maximum absorption.

The samples that were subjected to visible spectroscopy (wavelength range between 400 and 800 nm), *J-V*, IPCE and EIS characterization in this study were:

- The photoanode prepared from the commercial TiO_2 that have been immersed into different percentages (1, 2, 3, 4 and 5 wt.%) of anthocyanin extraction in order to obtain the optimized dye composition. Samples designated as D1, D2, D3, D4 and D5, respectively.
- The composite photoanode (NPs-NRs) made up of P25 commercial TiO_2 nanoparticles and various TiO_2 nanorod percentages (10, 20, 30, 40 and 50 wt.%), respectively which have been immersed into the 3 wt.% anthocyanin extract (optimized anthocyanin percentage with highest efficiency achieved in the first DSSC system) in order to find the optimal amount of TiO_2 NR that adequately improves the DSSC efficiency. Samples designated as CP1, CP2, CP3, CP4 and CP5, respectively.
- The composite photoanode (NPs-NRs) made up of P25 commercial TiO_2 with 10 wt.% TiO_2 nanorod (optimized nanorod percentage with highest efficiency) which have been immersed into the 3 wt.% anthocyanin extraction mixed with different additives (FA and CDCA) at different percentages (1, 2, 3, 4 and 5 wt.%) in order to obtained the optimize additives percentages. Samples for CDCA designated as C1, C2, C3, C4 and C5, respectively while samples for FA designated as F1, F2, F3, F4 and F5, respectively.

3.7.1 Visible Spectroscopy

Absorption spectroscopy measures absorption of electromagnetic radiation, as a function of radiation wavelength on interaction with sample. The sample absorbs energy from the radiating field. Absorption intensity varies with wavelength and variation of absorbtion in a specified range of the electromagnetic radiation is the absorption spectrum. The electromagnetic spectrum begins from a low energy with long wavelengths and has the potential to turn into a high level energy at shorter wavelengths. Most organic molecules are transparent to some regions of the electromagnetic spectrum. This may be the ultraviolet (UV), wavelength between 190 and 399 nm and visible (VIS), wavelengths between 400 and 800 nm. Absorption spectroscopy, in this work was performed within visible wavelength. The absorbance of dye solution and dye-TiO_2 photoanode were measured between 400 and 800 nm wavelength using UV-Visible spectrophotometer of Jasco V-730 model.

3.7.2 *J-V* Analysis

The DSSC photocurrent density-photovoltage or (*J-V*) characteristics were measured with the Autolab potentiostat-galvanostat instrument under the exposure of light illumination (1000 W m^{-2}) with 0.196 cm^2 active area. The TiO_2 photoanode acts as the counter/reference electrode. The Pt cathode acts as the working electrode. The two electrodes were then connected to the Autolab potentiostat-galvanostat. Figure 3.11 shows the normal *J-V* curve in DSSC measurements (Jinchu et al., 2014). There are several important parameters that can be obtained from the *J-V* curves. These are the photocurrent density (J_{sc}) and photovoltage (V_{oc}). Others are the fill factor (*FF*). *FF* is essentially a measure of quality of the solar cell. From these values, the efficiency (η) can be calculated. Series resistance (R_s) and shunt resistance (R_{sh}) can also be obtained from the *J-V* characteristics. R_s and R_{sh} affects *FF*.

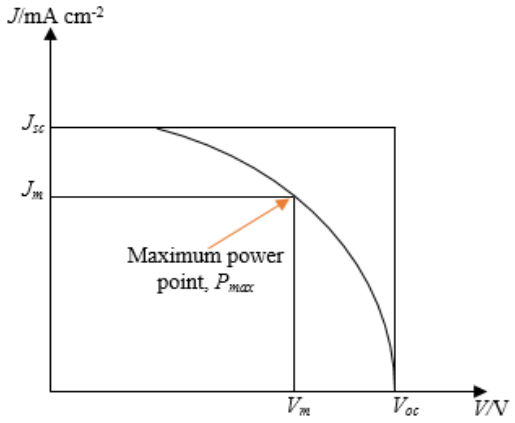

Figure 3.11: *J-V* curve plot in DSSCs.

3.7.3 Short-circuit Current (J_{sc})

J_{sc} is the photocurrent per unit area (in units of mA/cm^2) where the external output voltage is equal to zero ($V = 0$). In other words when the load resistance is zero. It is related to the IPCE. J_{sc} depends on light absorption, light intensity, injection efficiency, regeneration of the oxidized dye and the efficiency of charge transport in the TiO_2 film to the counter electrode.

3.7.4 Open-Circuit Voltage (V_{oc})

V_{oc} is the maximum voltage that can be obtained from a solar cell when no current flows through the cell. In other words, the circuit is open with no external load connected. V_{oc} depends on the semiconductor bandgap and charge recombination in the cell. The theoretical V_{oc} is the difference in energy between the semiconductor Fermi level and the electrolyte redox potential.

3.7.5 Fill Factor (*FF*)

FF indicates the maximum density of power output of the solar cell. It is normally described as a measure of the "squareness" of the *J-V* curve and is defined as the ratio of

the maximum power (V_mJ_m) to the product of V_{oc} and J_{sc} as referred to Figure 3.11 mentioned before. *FF* is given by the equation:

$$FF = \frac{V_{\mathrm{m}} \times J_m}{V_{oc} \times J_{sc}} \tag{3.6}$$

where, V_m is the voltage at P_{max} of the DSSC and J_m is the maximum photocurrent obtainable at maximum power point. Fill factor has no units. Fill factor can also be qualitatively described by the shunt and series resistances of the photovoltaic cell. *FF* reflects the extent of electrical and electrochemical losses during cell operation. To obtain higher fill factor improvement of the shunt resistance and decrement of the series resistance, with reduction of the overvoltage for diffusion and charge transfer is required.

3.7.6 Series Resistance (R_s)

Series resistance, R_s is due to contact and charge transfer resistances in the TiO_2 semiconductor material. Series resistance lowers the *FF* and influences the maximum power output. Very high *FF* can also reduce the J_{sc} value. V_{oc} is not affected since the total current flow through cell itself and hence through the series resistance is zero.

3.7.7 Shunt Resistance (R_{sh})

Significant power losses caused by the presence of a shunt resistance, R_{sh}, are typically due to manufacturing defects, rather than poor solar cell design. Low R_{sh} can provide an alternative path for the light generated current and results in power loss which decreases the *FF*. The shunt resistance (R_{sh}) is attributed to slow back electron transfer rate from TiO_2 to electrolyte in TiO_2/dye/ electrolyte interface. Low R_{sh} reduces *FF* while lower the V_{oc} and affects the maximum power output. The short-circuit voltage is not affected unless for a very low value, since at J_{sc} the total current flows through the outer path and hence through the R_{sh} is low. An approximation of the R_{sh} can be calculated from the

slope of the *JV* curve at the short circuit current point. Figure 3.12 present the solar cell equivalent circuit that shows the series (R_s) and shunt resistance (R_{sh}).

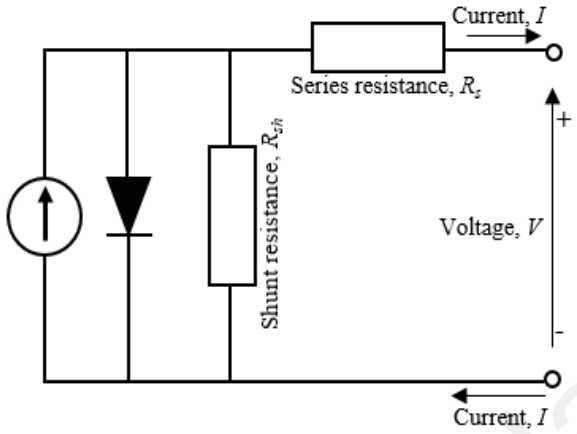

Figure 3.12: Solar cell equivalent circuit that shows the series (R_s) and shunt resistant (R_{sh}).

3.7.8 Efficiency (η)

The efficiency (η) is the key parameter of the photovoltaic cell. Efficiency is a measure of how many photons is converted into electricity. Mathematically, it is the ratio of maximum energy output to the energy input from the sun as represented by the following expression:

$$\eta(\%) = \frac{J_{sc}V_{oc}FF}{P_{in}} \times 100\% \tag{3.7}$$

where, P_{in} correspond to the input power density from the sun. Efficiency is generally expressed as a percentage.

3.7.9 Incident Photon to Current Efficiency (IPCE)

The spectral response of the DSSCs is dependent on how light absorbing is the dye. IPCE is also called quantum efficiency (QE) (Shaheen et al., 2001). IPCE indicates how solar cell respond to the incident wavelengths. It measures how efficiently the percentage

of incident photons converted into current at a specific wavelength. The measurement of IPCE is important for the understanding of the light to electricity conversion efficiency as a function of the wavelength of the light incident on the cell. The analysis involved the effects of optical losses such as transmission through and reflection of light away from the cell. In this study, the Newport Oriel setup was used to measure the photocurrent action spectrum for all complete DSSCs cells.

$$IPCE\ (\lambda) = \frac{1240\ \times J_{sc}}{\lambda \times \phi} \tag{3.8}$$

where J_{sc} is the short circuit current (mA/cm^2), λ is the wavelength (nm) and ϕ is the incident radiative light flux (W/m^2).

3.7.10 Electrochemical Impedance Spectroscopy (EIS)

The *J-V* curves do not directly tell the physical reasons why a cell works efficiently or otherwise. EIS characterization was used to examine the charge transport behavior in DSSCs. To obtain a better understanding of the processes that occur in the cell, the device is modelled with an equivalent electrical circuit comprising different electrical elements such as resistors and constant phase elements. These elements can be related to chemical or physical processes occurring in the device. In this study, the AUT 85988 advanced electrochemical system (Metrohm Autolab B.V. PGSTAT 128N Netherlands) was used in the measurement of DSSC impedance under AM 1.5 sun (1000 W m^{-2}) illumination with the frequency range from 10 mHz to 100 kHz at room temperature. The potential of each DSSC cell in this study was set at their V_{oc}, respectively. The impedance of an equivalent circuit was fitted using the Nova 1.11 to the experimental impedance data of the DSSC. It is common to observe three semicircles in the impedance spectroscopy obtained. The first semicircle, R_1 in Nyquist plot represent the charge transfer resistance at the Pt counter electrode while the second semicircle R_2, correspond to the charge

transfer resistance at the TiO_2/dye/electrolyte interface. The third semicircle, R_3 is denote as the ionic diffusion resistance in the electrolyte (Sarker et al., 2014).

3.8 Summary

In this chapter, the RSM technique was used for optimization of anthocyanin extract from fruit pericarp of *Ixora siamensis*. The aim was to investigate the potential of optimized extraction to be used as the light harvester in DSSC application with commercial P25 TiO_2 nanoparticles. The investigation also included the suitability of synthesized TiO_2 nanorods from electrospinning to be used in the mixed photoanode (NPs-NRs). The characteristics of TiO_2 nanostructures used in this study were analyzed using FESEM, EDX and XRD. The fabricated DSSC samples were examined using visible spectroscopy, *J-V* analysis, IPCE and EIS. This chapter has presented the details preparation and characterization employed in this study.

CHAPTER 4: RESULTS FOR IDENTIFICATION AND OPTIMIZATION OF ANTHOCYANIN EXTRACTION FROM FRUIT PERICARPS OF *IXORA SIAMENSIS* BY RESPONSE SURFACE METHODOLOGY (RSM)

4.1 Introduction

This chapter provides a detailed analysis on the identification of anthocyanin compound from the fruit pericarp of *Ixora siamensis* and optimization conditions or requirements of anthocyanin extraction parameter using Response Surface Methodology (RSM). This chapter begins with identification and confirmation of the major anthocyanin type from fruit pericarp of *Ixora siamensis* using UPLC-ESI-MS/MS mass spectrometry. RSM was used in this study in order to investigate the optimization of anthocyanin extraction from fruit pericarp of *Ixora siamensis*.

The three-level-three factor Box Behnken Design (BBD) was used for designing the experiments to determine the optimization conditions for anthocyanin extraction. The three independent variables for extraction were TFA% in methanol (A), soaking time (B) and temperature of extraction (C) while the response variables were the CIE visual colour measurement of lightness, (L*), redness (a*), blueness (b*), chromaticity (C), hue angle (H°), saturation and anthocyanin content. The relationship between the input variables (TFA%, soaking time and extraction temperature) and output variables (CIE colour parameters and anthocyanin content) were determined using the RSM modelling approach which justify the polynomial equations that best represent the relationship. Determination of potential interactions between process variables and all response values were done by carrying out analysis of variance (ANOVA). The desirability function method generated from Design expert software was employed to define the ideal optimized extraction conditions for anthocyanin extraction from fruit pericarp of *Ixora siamensis*.

4.2 Identification of Anthocyanin Extraction by UPLC-ESI-MS/MS

Figure 4.1 shows the mass spectra for identification of anthocyanins compound from fruit pericarps of *Ixora siamensis* using the UPLC-ESI-MS/MS. It can be confirmed that the extraction contained anthocyanin compound. The mass spectra detected three main anthocyanin compounds with different retention times (t_R) that were recognized as (a) cyanidin-3-rutinoside, (b) delphinidin glucoside and (c) peonidin-3-glucoside. The assignments of these anthocyanin types based on ACD/Labs advanced chemometrics mass fragmentation predictive software.

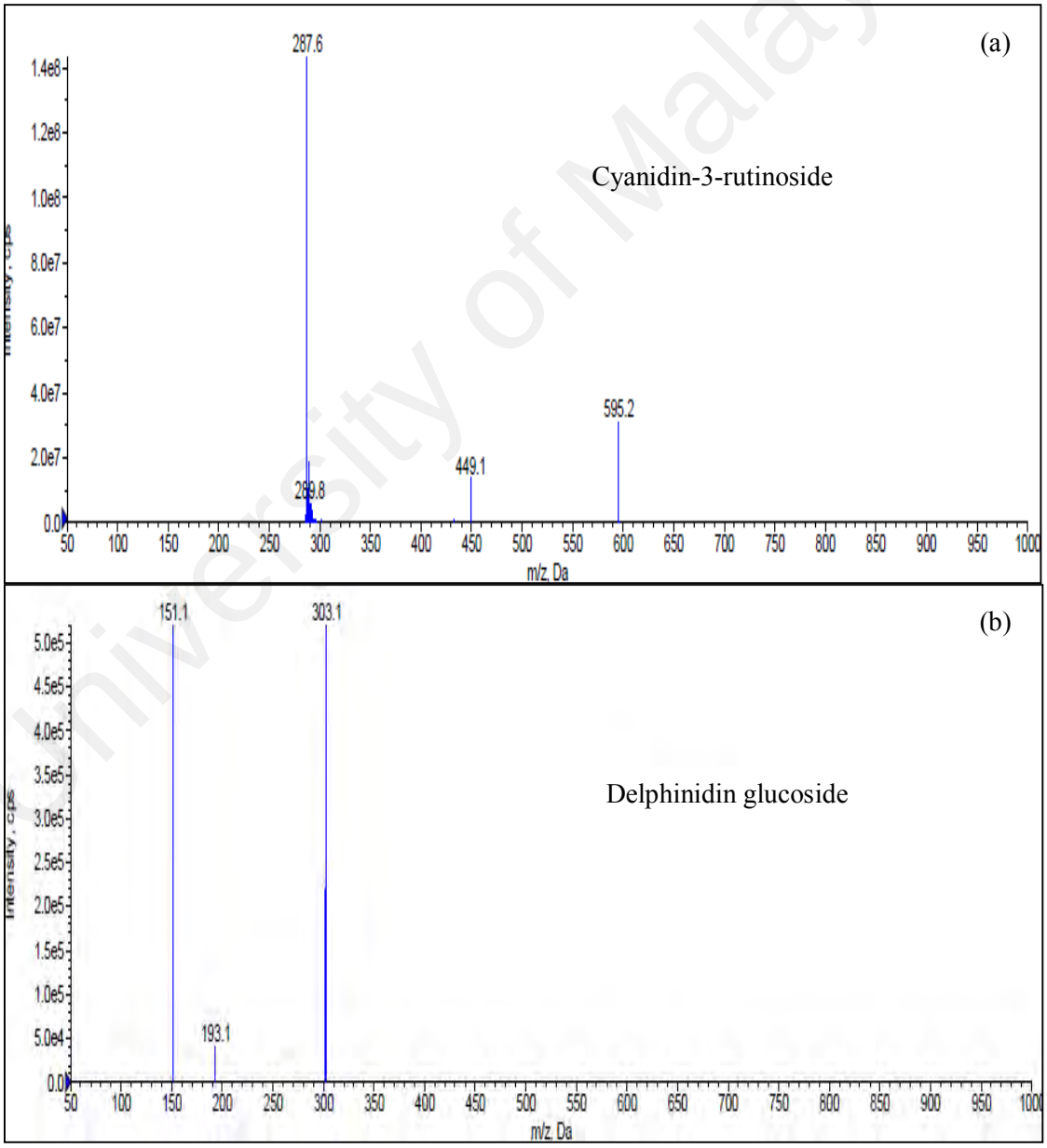

Figure 4.1: Mass spectra of identified anthocyanin from fruit pericarps of *Ixora siamensis.*

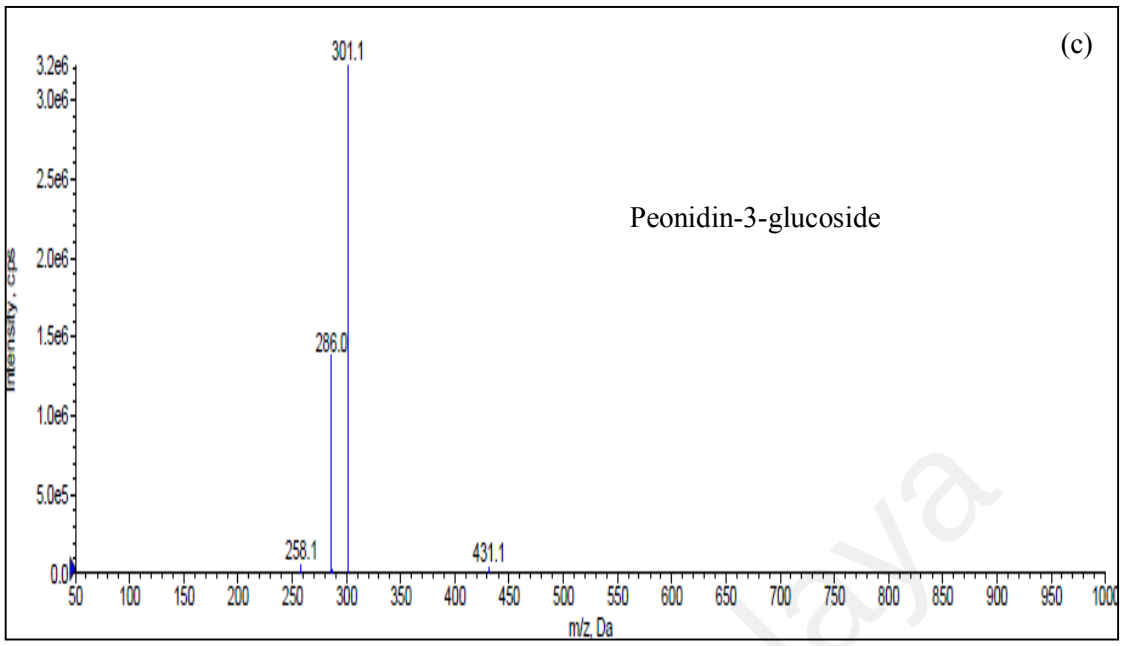

Figure 4.1, continued.

4.3 RSM Analysis

4.3.1 Box Behnken Design (BBD) Analysis of L*, a*, b*, C, H°, Saturation and Anthocyanin Content

There are various factors that affects anthocyanin extraction and colour variation. As mentioned before, we restrict ourselves and set the factors to the composition of extracting solvent (TFA content (%)), time and temperature of extraction to determine the parameters that can result in the maximum extraction yield. Box Behnken design (BBD) which is based on RSM was chosen as the experimental design for evaluating this objective. A three-level (-1, 0, 1) three-factor was applied to investigate the combination effect of TFA content (%), designated as A, soaking period or time (min) designated as B and extraction temperature (°C), designated as C. The minimum level of these factors was set at -1 and the maximum level at 1. The center or midpoint level (0) were automatically included by BBD. The decision of factor level (TFA content (%), time of extraction and temperature) were done based on literature review and previous research study.

The range of TFA content was set between 0.5 and 3%, soaking time was set between 60 and 180 min and temperature of extraction were between 30 and 80 ℃. The factor level decided for TFA content were 0.5% for minimum and 3% for maximum, while the center or midpoint level 1.75% were included by BBD. The ranges between 0.5 to 3% were recommended for efficient extraction as reported by Ju & Howard (2003), Navas et al. (2012), Ooe et al. (2016) and David et al. (2009). The factor level decided for soaking time were 60 min for minimum and 180 min for maximum, while the midpoint level were 55 ℃. The soaking time were also used by other researchers (Yang et al., 2009; Thirunavukkarasu & Nithya, 2011; Liu et al., 2012; Lotfi et al., 2015; Yilmaz et al., 2015; Ramasamy et al., 2016).

The factor level decided for extraction temperatures were 30 ℃ for minimum and 80 ℃ for maximum, while the midpoint level were 55 ℃. The chosen temperatures were also used by other researchers (Ruenroengklin et al., 2008; Yang et al., 2009; Sharif et al., 2010; Thirunavukkarasu & Nithya, 2011; Duan et al., 2015). From this order input, the BBD generated 17 experiments including centre points with different combination factors at different level for examining the effects of extraction parameters on the visual colour and anthocyanin field, as listed in Table 4.1. Centre point was included by BBD to determine the experiment error. The responses being investigated in this work were L*, a*, b*, C, H°, saturation and anthocyanin content. The responses value for visual colour (L*, a*, b*, C, H°, saturation) were analysed using the CIE system and the anthocyanin content using spectrophotometric method as mentioned in Chapter 3.

In order to optimizes the extraction parameter which are known influenced by various factors, 17 samples being prepared according to combination extraction condition being generated by the BBD and tested for CIE visual colour and anthocyanin content. The

experimental results obtained were included into the BBD table design as tabulated in Table 4.1.

Based on Table 4.1, it can be clear noticed that the different combination extraction parameter (TFA %, soaking time and temperature of extraction) influenced visual colour variation of L*, a*, b*, C, H°, saturation and anthocyanin content significantly since different combination extraction parameters resulted in different responses value. The BBD analysis was performed to examine the effects of different extraction parameters (factors) on the studied responses (L*, a*, b*, C, H°, saturation and anthocyanin content). Several evaluation steps were done before the relationship between input (extraction parameters) and output (CIE colour analysis and anthocyanin content) can be defined.

4.3.2 Statistical Analysis for Determination of Appropriate Polynomial Equation to Represent RSM Model for L*, a*, b*, C, H°, Saturation and Anthocyanin Content Responses

Four analytical steps were performed to determine the optimize conditions for the responses which are (1) adequacy of various model test (sequential model sum of squares and model summary statistics), (2) analysis of variance (ANOVA), (3) the response surface analysis and the last step was (4) goal setting for optimization.

The obtained experimental data from 17 experiment runs on seven responses (L*, a*, b*, C, H°, saturation and anthocyanin content) were analyzed and fitted to the polynomial models which are linear, two factor interaction (2FI), quadratic and cubic models in order to obtain the regression equations.

Table 4.1: Experimental runs of BBD design and the responses of L*, a*, b*, C, H°, saturation (s) and anthocyanin content.

	Factor 1	Factor 2	Factor 3	Response 1	Response 2	Response 3	Response 4	Response 5	Response 6	Response 7
Sample	A:TFA content (%)	B:Soaking time (min)	C:Extraction temperature (℃)	L*	a*	b*	C	H°	Saturation (s)	Anthocyanin content (mg/L)
1	0.5	60	55	76.67	44.89	-4.52	45.12	353.67	0.5885	3770.82
2	3	60	55	72.91	54.11	-6.1	54.45	359.67	0.7468	4074.95
3	0.5	180	55	72.22	55.32	-3.98	55.46	357.96	0.7679	4000.00
4	3	180	55	74.44	52.87	-4.42	53.05	355.22	0.7127	4786.00
5	0.5	120	30	71.37	47.99	-3.92	48.15	352.87	0.6747	4234.00
6	3	120	30	70.31	52.88	-3.87	53.02	358.81	0.7541	5045.00
7	**0.5**	**120**	**80**	**72.00**	**58.88**	**-1.65**	**58.9**	**359.65**	**0.8181**	**5791.70**
8	3	120	80	70.34	55.39	-4.4	55.56	357.34	0.7899	5124.98
9	1.75	60	30	76.56	45.79	-4.59	46.02	353.27	0.6011	3821.96
10	1.75	180	30	74.02	50.71	-4.3	50.89	354.75	0.6875	3693.90
11	1.75	60	80	75.56	49.15	-4.17	49.33	355.15	0.6529	3946.68
12	1.75	180	80	73.70	56.72	-2.63	56.78	357.19	0.7704	5045.00
13	1.75	120	55	72.56	58.75	-4.18	58.9	355.39	0.8117	4897.00
14	1.75	120	55	73.50	54.41	-3.98	54.56	355.81	0.7423	4121.70
15	1.75	120	55	73.35	53.72	-4.3	53.89	355.01	0.7347	4026.41
16	1.75	120	55	72.54	55.38	-4.53	55.56	354.96	0.7659	4007.73
17	1.75	120	55	73.65	50.89	-3.92	51.04	351.59	0.6930	4254.35

4.3.2.1 Sequential Model Sum of Squares (SMSS)

Experimental data obtained were first evaluated by using SMSS in order to choose the appropriate model to represent the responses. At a 95% confidence level, if the F value is close to unity (larger F-value) and p value<0.05, the model/factor is significantly affect the output response (Wen et al., 2015). Table 4.2 (a) to (g) showed the SMSS tested output for all responses of L*, a*, b*, C, H°, saturation and anthocyanin content. It can be clearly indicated that the cubic model was found to be aliased for all responses and cannot be used for further modeling and representing experimental data. The quadratic models were suggested as the appropriate model for responses of L*, a*, b*, H°, saturation and anthocyanin content since the p-value is lowest indicating strength of significance. The p-values for L*, a*, b*, H°, saturation and anthocyanin content responses were p<0.0001, p=0.0003, p=0.0004, p=0.0771, p=0.0375 and p=0.0109, respectively as displayed in Table 4.2 (a), (b), (c), (e), (f) and (g). For the C response as in Table 4.2 (d), the linear and quadratic model were suggested, since both models were significant with lower p-value, p=0.0297 and p=0.1385, respectively. **To further verify and confirm that the suggested model is suitable for all responses, model summary statistics (MSS) was done.**

Table 4.2: Sequential model sum of squares (SMSS) analysis for (a) L*, (b) a*, (c) b*, (d) C, (e) H°, (f) saturation and (g) anthocyanin content.

(a) Sequential Model Sum of Squares for L*

Source	Sum of Squares	DF	Mean Square	F Value	Prob	
Mean	91280.5	1	91280.5			
Linear	9.02	3	3.01	0.85	0.4891	
2FI	9.15	3	3.05	0.83	0.5060	
Quadratic	34.55	3	11.52	39.02	<0.0001	Suggested
Cubic	0.94	3	0.31	1.11	0.4436	Aliased
Residual	1.13	4	0.28			
Total	91335.29	17	5372.66			

Table 4.2, continued.

(b) Sequential Model Sum of Squares for a*

Source	Sum of Squares	DF	Mean Square	F Value	Prob	
Mean	46226.28	1	46226.28			
Linear	135.01	3	45.00	3.10	0.0639	
2FI	102.19	3	34.06	3.94	0.0431	
Quadratic	79.72	3	26.57	27.21	0.0003	Suggested
Cubic	3.20	3	1.07	1.18	0.4233	Aliased
Residual	3.63	4	0.91			
Total	46550.04	17	2738.24			

(c) Sequential Model Sum of Squares for b*

Source	Sum of Squares	DF	Mean Square	F Value	Prob	
Mean	283.81	1	283.81			
Linear	6.67	3	2.22	4.43	0.0236	
2FI	2.68	3	0.89	2.32	0.1374	
Quadratic	3.51	3	1.17	24.34	0.0004	Suggested
Cubic	0.09	3	0.03	0.50	0.7008	Aliased
Residual	0.24	4	0.06			
Total	297.00	17	17.47			

(d) Sequential Model Sum of Squares for C

Source	Sum of Squares	DF	Mean Square	F Value	Prob	
Mean	47719.09	1	47719.09			
Linear	128.65	3	42.88	4.10	0.0297	Suggested
2FI	52.97	3	17.66	2.13	0.1598	
Quadratic	43.31	3	14.44	2.55	0.1385	Suggested
Cubic	7.15	3	2.38	0.29	0.8287	Aliased
Residual	32.41	4	8.10			
Total	47983.58	17	2822.56			

(e) Sequential Model Sum of Squares for H°

Source	Sum of Squares	DF	Mean Square	F Value	Prob	
Mean	2.15E+06	1	2.15E+06	1.18		
Linear	18.94	3	6.31	3.62	0.3551	
2FI	36.19	3	12.06	3.52	0.0529	
Quadratic	20.03	3	6.68	0.21	0.0771	Suggested
Cubic	1.83	3	0.61	1.18	0.8823	Aliased
Residual	11.43	4	2.86	3.62		
Total	2.15E+06	17	1.27E+05	3.52		

Table 4.2, continued.

(f) Sequential Model Sum of Squares for saturation

Source	Sum of Squares	DF	Mean Square	F Value	Prob > F	
Mean	8.92	1	8.92			
Linear	0.031	3	0.010	3.19	0.0594	
2FI	0.015	3	4.85E-03	1.80	0.2104	
Quadratic	0.018	3	6.37E-03	4.95	0.0375	Suggested
Cubic	1.01E-03	3	3.38E-04	0.18	0.9063	Aliased
Residual	9.74E-03	4	2.44E-03			
Total	8.99	17	0.53			

(g) Sequential Model Sum of Squares for anthocyanin content

Source	Sum of Squares	DF	Mean Square	F Value	Prob > F	
Mean	3.28E+08	1	3.28E+08			
Linear	1.86E+06	3	6.20E+05	2.04	0.1582	
2FI	9.80E+05	3	3.27E+05	1.10	0.3939	
Quadratic	2.31E+06	3	7.71E+05	8.19	0.0109	Suggested
Cubic	1.15E+05	3	38405.53	0.28	0.8362	Aliased
Residual	5.43E+05	4	1.36E+05			
Total	3.34E+08	17	1.96E+07			

4.3.2.2 Model Summary Statistics (MSS)

The suggested models were further examined using the model summary statistics (MSS) for all responses of L*, a*, b*, C, H°, saturation and anthocyanin content. The R^2 value indicates how well a regression line represents the data and how accurately a regression line of the suggested model can predict the future outcomes. Based on model summary statistics output in Table 4.3 (a) to (g), it can be revealed that the quadratic model resulted in the highest values for R^2, adjusted R^2 and predicted R^2 compared to other models (linear and 2FI). These similar results pattern were observed for responses of L*, a*, b*, C, H°, saturation and anthocyanin content.

For the L* response as in Table 4.3 (a), the quadratic models showed R^2=0.9623, adjusted R^2=0.9138 and predicted R^2=0.6939. The values of R^2, adjusted R^2 and

predicted R^2 for quadratic model of a* response were 0.9789, 0.9517 and 0.8241, respectively as listed in Table 4.3 (b). Based on Table 4.3 (c), for the b* response, R^2 is equal to 0.9745 while the adjusted R^2 is equal to 0.9417 and 0.8593 for predicted R^2, which can be observed for the quadratic model. As in Table 4.3 (d) for C response showed the highest values for the R^2=0.8504, adjusted R^2=0.6581 and predicted R^2=0.3760, respectively. The highest values for R^2 (0.8500), adjusted R^2(0.6571) and predicted R^2 (0.4664) were obtained by the quadratic model for response of H°, displayed in Table 4.3 (e).

The quadratic model of saturation response, as displayed in Table 4.3 (f) showed the maximum values of R^2 equal to 0.8803, adjusted R^2 equal to 0.7263 and predicted R^2 equal to 0.6096. As can be deduced from Table 4.3 (g), quadratic model of anthocyanin content response contributed to the highest values in terms of R^2=0.8867, adjusted R^2= 0.7409 and predicted R^2= 0.5365 compared to the linear and 2FI model. In contrast, the cubic model were disregarded for all responses since it is aliased and not favorable for further modeling of the experimental data. These analyses suggested that the relationship between factors (TFA content, soaking time and temperature of extraction) and resultant responses (L*, a*, b*, C, H°, saturation and anthocyanin content) can be modelled and explained using the quadratic equations.

The quadratic models for all responses were not only found to have maximum R^2, adjusted R^2, predicted R^2, but also exhibited low p-values. Hence, the quadratic model was chosen for further analysis of responses of L*, a*, b*, C, H°, saturation and anthocyanin content. **In order to more improve the suggested model, ANOVA was carried out next to determine the significant of each input parameters. The**

insignificant factors will be eliminated. After performing the ANOVA test the best polynomial equation that described the responses were obtained.

Table 4.3: Model summary statistics analysis for (a) L*, (b) a*, (c) b*, (d) C, (e) H°, (f) saturation and (g) anthocyanin content.

(a)Model Summary Statistics for L*					
Source	Std. Dev.	R-Squared	Adjusted R-Squared	Predicted R-Squared	
Linear	1.88	0.1647	-0.0281	-0.7266	
2FI	1.91	0.3316	-0.0695	-2.3426	
Quadratic	0.54	0.9623	0.9138	0.6939	Suggested
Cubic	0.53	0.9794	0.9176		Aliased
(b) Model Summary Statistics for a*					
Source	Std. Dev.	R-Squared	Adjusted R-Squared	Predicted R-Squared	
Linear	3.81	0.4170	0.2825	-0.1675	
2FI	2.94	0.7326	0.5722	-0.1539	
Quadratic	0.99	0.9789	0.9517	0.8241	Suggested
Cubic	0.95	0.9888	0.9551		Aliased
(c) Model Summary Statistics for b*					
Source	Std. Dev.	R-Squared	Adjusted R-Squared	Predicted R-Squared	
Linear	0.71	0.5055	0.3914	-0.0138	
2FI	0.62	0.7083	0.5334	-0.4101	
Quadratic	0.22	0.9745	0.9417	0.8593	Suggested
Cubic	0.25	0.9815	0.9259		Aliased
(d) Model Summary Statistics for C					
Source	Std. Dev.	R-Squared	Adjusted R-Squared	Predicted R-Squared	
Linear	3.23	0.4864	0.3679	0.1027	
2FI	2.88	0.6867	0.4987	0.1294	
Quadratic	2.38	0.8504	0.6581	0.3760	Suggested
Cubic	2.85	0.8775	0.5098		Aliased
(e) Model Summary Statistics for H°					
Source	Std. Dev.	R-Squared	Adjusted R-Squared	Predicted R-Squared	
Linear	2.31	0.2142	0.0328	-0.4377	
2FI	1.82	0.6234	0.3975	-0.0730	
Quadratic	1.38	0.8500	0.6571	0.4664	Suggested
Cubic	1.69	0.8707	0.4828		Aliased

Table 4.3, continued.

(f) Model Summary Statistics for saturation					
Source	Std. Dev.	R-Squared	Adjusted R-Squared	Predicted R-Squared	
Linear	0.056	0.4242	0.2913	-0.0605	
2FI	0.052	0.6262	0.4020	-0.3186	
Quadratic	0.035	0.8803	0.7263	0.6096	Suggested
Cubic	0.044	0.8943	0.5774		Aliased
(g) Model Summary Statistics for anthocyanin content					
Source	Std. Dev.	R-Squared	Adjusted R-Squared	Predicted R-Squared	
Linear	551.22	0.3200	0.1630	-0.3195	
2FI	544.98	0.4887	0.1819	-1.1946	
Quadratic	306.67	0.8867	0.7409	0.5365	Suggested
Cubic	368.48	0.9065	0.6260		Aliased

4.3.2.3 ANOVA of Selected Model for L*, a*, b*, C, H°, Saturation and Anthocyanin Content Responses

To ensure that the selected polynomial equation best represents the model for each responses, analysis of variance approach (ANOVA) were done. In this method approach, the regression model, individual model coefficient and lack of fit were test for its significance. ANOVA were performed on the selected quadratic polynomial model of all responses L*, a*, b*, C, H°, saturation and anthocyanin content which were used to check the adequacy and fitness of the developed models. The quadratic model was suggested based on the SMSS and MSS results. This step is important in order to improve the quadratic polynomial model chosen by eliminating the terms factor that are not significant and acknowledged as reduce quadratic polynomial model. The significance of linear (A, B and C), quadratic (A^2, B^2 and C^2) and interactive model (AB, AC and BC) terms were determined by p-value or Fisher's F-test. If there are many insignificant model terms (not counting those required to support hierarchy), model reduction may improve the developed model.

The overall model developed from ANOVA for L* response were highly significant, as displayed in Table 4.4, since $p<0.0001$. The "Model F-value" of 29.72 implies significance of the model. The accuracy of this model is also supported by the "Lack of Fit" analysis. The "Lack of Fit F-value" or the variation existence designates model inadequacy. If a model fails the lack of fit, then the model is inadequate to describe the functional relationship between the input variables and the output responses. This means that the model is still unfit to predict the response investigated eventhough the test is statistically significant (if $p<0.05$) (Rezaee et al., 2014). The "Lack of Fit F-value" of 0.81 implies that the lack of fit is not significant relative to the pure error. Therefore, the models adequately explain the variation in the responses. With regards to Table 4.4, insignificant lack of fit test value, $p=0.5970$ (p-value > 0.05) relative to the pure error also shows good relationship between the independent variables and output responses of L*. Based on the significant p-value of less than 0.05, TFA content (A) ($p=0.0150$), soaking time (B) ($p=0.0006$), TFA content quadratic term (A^2) ($p=0.0002$), soaking time quadratic term (B^2) ($p<0.0001$), extraction temperature quadratic term (C^2) ($p=0.0349$) and interaction between TFA content and soaking time (AB) ($p=0.0002$) were the significant influencing factors of the resultant L* values. These justifies that the developed models successfully describes most variation in the L* response. p-values greater than 0.05 designates the insignificant of terms in the model with reference to extraction temperature (C), since $p=0.6534$. This insignificant model term was not reduced since the extraction temperature term are needed to support the hierarchy of the quadratic model. Other model terms AC (interaction between TFA content and temperature of extraction) and BC (interaction between soaking time and temperature of extraction) have been reduced to improve the developed model. ANOVA analysis of L* is summarized in Table 4.4.

Table 4.4: ANOVA analysis of the reduced quadratic model for L*.

ANOVA for Response Surface Reduced Quadratic Model						
Analysis of variance table [Partial sum of squares]						
Source	Sum of Squares	DF	Mean Square	F Value	Prob	
Model	52.51	7	7.50	29.72	< 0.0001	significant
A-TFA content	2.27	1	2.27	8.99	0.0150	
B-Soaking time	6.70	1	6.70	26.54	0.0006	
C-Extraction temperature	0.054	1	0.054	0.22	0.6534	
A^2	9.57	1	9.57	37.91	0.0002	
B^2	25.22	1	25.22	99.92	< 0.0001	
C^2	1.55	1	1.55	6.16	0.0349	
AB	8.94	1	8.94	35.42	0.0002	
Residual	2.27	9	0.25			
Lack of Fit	1.14	5	0.23	0.81	0.5970	not significant
Pure Error	1.13	4	0.28			
Cor Total	54.79	16				

Adequacy of the developed models for all responses were tested by regression analysis (R^2), adjusted R^2 and predicted R^2. The R^2 is the proportion of the variability in the data explained by the ANOVA which is defined as the ratio of sum of squares due to regression to the total sum of squares. The further the line is away from the points, the less accurate is the particular regression line, the R^2 value will be small. A good model fit should $R^2 \geq 0.8$ (Qiu et al., 2014). A high R^2 regression coefficient certifies that the predicted model are satisfactorily adjusted to the experimental data (Maran et al., 2013). The high R^2 values infer only less than 5% of experimental data cannot be explained by the model. Predicted R^2 helps to determine whether there is any overfitting of the regression model. An overfit model includes an excessive number of terms and it begins to fit the random noise in the sample. The differences between predicted R^2 and adjusted R^2 should not be more than 0.2 (Maran & Manikandan, 2012).

For L* response, the relatively high values R^2=0.958 which closer to 1, thus implies that most of the experimental data can be explained by the reduced model. The high values of adjusted R^2=0.9263, deduce a high correlation between the observed and the

predicted values. There were reasonably agreement of the predicted R^2 =0.8353 with the adjusted R^2 of 0.9263, since the differences between both measurement are not more than 0.2. Meanwhile, the adequate precision measures the signal (responses) to noise (deviation) ratio. The ratio of 19.186 indicates an adequate signal confirmed that the developed model can be used to navigate the design space, since a ratio greater than 4 is desirable (Maran et al*.,* 2013). Therefore, this model can be accepted and used to represent the experiment results for L* response.

The overall model developed from ANOVA for a* response were highly significant, since $p<0.0001$ as can be observed in Table 4.5. The insignificant "Lack of Fit F-value" of 1.18, with p=0.4233 (p-value > 0.05) indicates that the lack of fit is not significant relative to the pure error. This implies that the relationship between the independent variables and process responses of a* is good. Based on the significant p-value of less than 0.05, TFA content (A) (p=0.0028), soaking time (B) (p=0.0009), extraction temperature (C) ($p<0.0001$), TFA content quadratic term (A^2) ($p<0.0001$), soaking time quadratic term (B^2) (p=0.0314), interaction between TFA content and soaking time (AB) (p=0.0002), interaction between TFA content and extraction temperature (AC) (p=0.0005) and interaction between soaking time and extraction temperature (BC) (p=0.0061) were the significant influencing factors of the resultant a* values. These justifies that the developed models satisfactorily describes most of the variation in the a* response. p-values greater than 0.05 indicates that the model terms are not significant with reference to extraction temperature quadratic term (C^2), since p=0.1667. This insignificant model term was not being reduced since the extraction temperature quadratic term are needed to improve the developed model. ANOVA analysis of a* is summarized in Table 4.5.

Table 4.5: ANOVA analysis of the quadratic model for a*.

ANOVA for Response Surface Quadratic Model						
Analysis of variance table [Partial sum of squares]						
Source	Sum of Squares	DF	Mean Square	F Value	Prob	
Model	316.93	9	35.21	36.06	< 0.0001	significant
A-TFA content	19.72	1	19.72	20.19	0.0028	
B-Soaking time	29.88	1	29.88	30.59	0.0009	
C-Extraction temperature	85.41	1	85.41	87.46	< 0.0001	
A^2	71.41	1	71.41	73.12	< 0.0001	
B^2	7.03	1	7.03	7.19	0.0314	
C^2	2.33	1	2.33	2.38	0.1667	
AB	51.62	1	51.62	52.86	0.0002	
AC	35.94	1	35.94	36.80	0.0005	
BC	14.63	1	14.63	14.98	0.0061	
Residual	6.84	7	0.99			
Lack of Fit	3.20	3	1.07	1.18	0.4233	not significant
Pure Error	3.63	4	0.91			
Cor Total	323.76	16				

The relatively high R^2 values with 0.9789 which is close to 1, implies that more than 95% of experiment results for the a* response can be explained by the model. The high values of adjusted R^2 was 0.9517, indicates a high correlation between the experimental and the predicted values. There were reasonably agreement of the predicted R^2=0.8241 with the adjusted R^2 of 0.9517, since the differences between both measurement are not more than 0.2. The adequate precision ratio of 18.24 which is greater than 4 shows an adequate signal, established that this model can be used to navigate the design space. Therefore, this model can be established and applied to represent the experiment results for a* response.

The overall model developed from ANOVA for b* response were highly significant, as can be displayed in Table 4.6, since p<0.0001. The "Lack of Fit F-value" of 0.43 with p=0.7835 (p-value > 0.05) implies that the lack of fit is not significant, hence indicates good relationship between the input variables and output responses of b*. Based on the

significant p-value of less than 0.05, TFA content (A) ($p<0.0001$), soaking time (B) ($p=0.0001$), extraction temperature (C) ($p=0.0002$), soaking time quadratic term (B^2) ($p=0.0009$), extraction temperature quadratic term (C^2) ($p<0.0001$), interaction between TFA content and soaking time (AB) ($p=0.0260$), interaction between TFA content and extraction temperature (AC) ($p=0.0002$) and interaction between soaking time and extraction temperature (BC) ($p=0.0173$) were the significant influencing factors of the resultant b* values. These implies that the developed models satisfactorily describes most of the variation in the b* response. In contrast, the TFA content quadratic term (A^2) have been reduced to improve the developed model. The ANOVA analysis of b* is summarized in Table 4.6.

Table 4.6: ANOVA analysis of the reduced quadratic model for b*.

ANOVA for Response Surface Reduced Quadratic Model						
Analysis of variance table [Partial sum of squares]						
Source	Sum of Squares	DF	Mean Square	F Value	Prob	
Model	12.84	8	1.61	36.75	< 0.0001	significant
A-TFA content	2.78	1	2.78	63.75	< 0.0001	
B-Soaking time	2.05	1	2.05	46.94	0.0001	
C-Extraction temperature	1.83	1	1.83	41.98	0.0002	
B^2	1.14	1	1.14	26.20	0.0009	
C^2	2.53	1	2.53	57.96	< 0.0001	
AB	0.32	1	0.32	7.44	0.0260	
AC	1.96	1	1.96	44.87	0.0002	
BC	0.39	1	0.39	8.94	0.0173	
Residual	0.35	8	0.044			
Lack of Fit	0.10	4	0.026	0.43	0.7835	not significant
Pure Error	0.24	4	0.061			
Cor Total	13.19	16				

The values close to 1 of $R^2=0.9735$, is relatively high values which justifies that more than 95% of experiment results for the b* response can be explained by the model. The high values of adjusted $R^2=0.9470$, indicates a high correlation between the experimental and the predicted values. There were reasonably agreement of predicted $R^2=0.8958$ with

the adjusted R^2 of 0.9735, since the differences between both measurement are not greater than 0.2. The adequate precision ratio of 29.23 indicates an adequate signal since the values is not more than 4, established that this model can be used to navigate the design space. Therefore, this model can be accepted and used to represent the experiment results for b* response.

The overall model developed from ANOVA for C response were highly significant, as presented in Table 4.7, since p=0.0025. The insignificant "Lack of Fit F-value" of 0.28 with p=0.9179 (P value > 0.05) indicates good relationship between the independent variables and process responses of C. Based on the significant p-value of less than 0.05, soaking time (B) (p=0.0057), extraction temperature (C) (p=0.0041), soaking time quadratic term (B^2) (p=0.0163) and interaction between TFA content and soaking time (AB) (p=0.0211) were the significant influencing factors of the resultant C values. These indicates that the developed models successfully describes most of the variation in the C response.

The p-values greater than 0.05 indicates that the model terms are not significant with reference to TFA content (A) with p=0.1945. This insignificant model term was not being reduced since TFA content term are needed to support the hierarchy of the quadratic model. For better modelling equation, the non significant model term of interaction between TFA content and extraction temperature (AC) (p=0.0851) was not being excluded. In contrast, other model terms A^2 (TFA content quadratic term), C^2 (extraction temperature quadratic term) and BC (interaction between soaking time and extraction temperature) have been reduced to improve the developed model. The ANOVA analysis of the reduced quadratic model for C is summarized in Table 4.7.

Table 4.7: ANOVA analysis of the reduced quadratic model for C.

ANOVA for Response Surface Reduced Quadratic Model						
Analysis of variance table [Partial sum of squares]						
Source	Sum of Squares	DF	Mean Square	F Value	Prob	
Model	218.34	6	36.39	7.88	0.0025	significant
A-TFA content	8.93	1	8.93	1.93	0.1945	
B-Soaking time	56.50	1	56.50	12.24	0.0057	
C-Extraction temperature	63.23	1	63.23	13.70	0.0041	
B^2	38.38	1	38.38	8.32	0.0163	
AB	34.46	1	34.46	7.47	0.0211	
AC	16.85	1	16.85	3.65	0.0851	
Residual	46.16	10	4.62			
Lack of Fit	13.75	6	2.29	0.28	0.9179	not significant
Pure Error	32.41	4	8.10			
Cor Total	264.49	16				

For the C response, the values of R^2 was 0.8255, which imply that more than 95% of experiment results can be explained by the model. The values of adjusted R^2=0.7208, designate a good correlation between the experimental and the predicted values. There were reasonably agreement of the predicted R^2=0.5860 with the adjusted R^2 of 0.9735, since the differences between both measurement are not more than 0.2. The adequate precision ratio of 9.768 which is more than 4, indicates an adequate signal. This confirmed that the developed model can be used to navigate the design space. Therefore, this model can be accepted and used to represent the experiment results for C response.

The overall model developed from ANOVA for H° response were highly significant as can be observed in Table 4.8, since p=0.0042. The insignificant "Lack of Fit F-value" of 0.13 with p=0.9756 (P value > 0.05) indicates that the relationship between the input variables and output responses of H° is good. Based on the significant p-value of less than 0.05, extraction temperature (C) (p=0.0208), TFA content quadratic term (A^2) (p=0.0067) interaction between TFA content and soaking time (AB) (p=0.0059), interaction between TFA content and extraction temperature (AC) (p=0.0080) and were

the significant influencing factors of the resultant H° values. These indicates that the developed models successfully describes most of the variation in the H° response. p-values greater than 0.05 indicates that the model terms are not significant with reference to TFA content (A) and extraction temperature (C) since p=0.0765 and p=0.3548 respectively. These insignificant model terms were not being reduced since both were needed to support the hierarchy of the quadratic model. For better modelling equation, the non significant extraction temperature quadratic model term (C^2) (p=0.3878) was not being excluded. In contrast, other model terms BC (interaction between soaking time and extraction temperature) and B^2 (soaking time quadratic term) have been reduced to improve the developed model. ANOVA analysis of the reduced quadratic model for H° is summarized in Table 4.8.

Table 4.8: ANOVA analysis of the reduced quadratic model for H°.

ANOVA for Response Surface Reduced Quadratic Model						
Analysis of variance table [Partial sum of squares]						
Source	Sum of Squares	DF	Mean Square	F Value	Prob	
Model	75.08	7	10.73	7.23	0.0042	significant
A-TFA content	5.93	1	5.93	4.00	0.0765	
B-Soaking time	1.41	1	1.41	0.95	0.3548	
C-Extraction temperature	11.59	1	11.59	7.82	0.0208	
A^2	18.23	1	18.23	12.29	0.0067	
C^2	1.22	1	1.22	0.82	0.3878	
AB	19.10	1	19.10	12.88	0.0059	
AC	17.02	1	17.02	11.48	0.0080	
Residual	13.35	9	1.48			
Lack of Fit	1.91	5	0.38	0.13	0.9756	not significant
Pure Error	11.43	4	2.86			
Cor Total	88.43	16				

The values of R^2 was 0.8491, imply that more than 95% of experiment results for the H° response can be explained by the model. The values of adjusted R^2 was 0.7317, shows a good correlation between the experimental and the predicted values. There were

reasonably agreement of the predicted R^2=0.6780 with the adjusted R^2 of 0.7317, since the differences between both values are not more than 0.2. The adequate precision ratio of 7.82 which is greater than 4 indicates an adequate signal. This confirmed that the developed model can be used to navigate the design space. Therefore, this model can be accepted and used to represent the experiment results for H° response.

The overall model developed from ANOVA for saturation response were highly significant as can be observed in Table 4.9, since p=0.0059. The insignificant "Lack of Fit F-value" of 0.17 with p=0.9454 (P value > 0.05) implies good correlation between the input variables and output responses of saturation. Based on the significant p-value of less than 0.05, soaking time (B) (p=0.0060), extraction temperature (C) (p=0.0103), soaking time quadratic term (B^2) (p=0.0045) and interaction between TFA content and soaking time (AB) (p=0.0124) were the significant influencing factors of the resultant saturation values. These shows that the developed models satisfactorily describes most of the variation in the saturation response.

The p-values greater than 0.05 indicates that the model terms are not significant with reference to TFA content (A) with p=0.1398. This insignificant terms was not being reduced since the model terms was needed to support the hierarchy of the quadratic model. For better modelling equation, the non significant model terms of interaction between TFA content and extraction temperature (AC) (p=0.1446), TFA content quadratic term (A^2) (p=0.3040) and extraction temperature quadratic term (C^2) (p=0.6275) were not being excluded. In contrast, interaction between soaking time and extraction temperature term (BC) has been reduced to improve the developed model. The analysis of the reduced quadratic model for saturation is summarized in Table 4.9.

Table 4.9: ANOVA analysis of the reduced quadratic model for saturation.

ANOVA for Response Surface Reduced Quadratic Model						
Analysis of variance table [Partial sum of squares]						
Source	Sum of Squares	DF	Mean Square	F Value	Prob	
Model	0.063	8	7.89E-03	7.12	0.0059	significant
A-TFA content	2.98E-03	1	2.98E-03	2.69	0.1398	
B-Soaking time	0.015	1	0.015	13.76	0.0060	
C-Extraction temperature	0.012	1	0.012	11.12	0.0103	
A^2	1.34E-03	1	1.34E-03	1.21	0.3040	
B^2	0.017	1	0.017	15.27	0.0045	
C^2	2.82E-04	1	2.82E-04	0.25	0.6275	
AB	0.011	1	0.011	10.3	0.0124	
AC	2.90E-03	1	2.90E-03	2.61	0.1446	
Residual	8.86E-03	8	1.11E-03			
Lack of Fit	1.26E-03	4	3.14E-04	0.17	0.9454	not significant
Pure Error	7.61E-03	4	1.90E-03			
Cor Total	0.072	16				

The R^2 values of 0.8769 indicates that more than 95% of experiment results for the saturation response can be explained by the model. The values of adjusted R^2 was 0.7538, implies a good correlation between the experimental and the predicted values. There were reasonably agreement of the predicted R^2=0.6527 with the adjusted R^2 of 0.7538, since the differences between both values are not more than 0.2. The adequate precision ratio of 9.018 which is more than 4 indicates an adequate signal. This confirmed that the developed model can be used to navigate the design space. Therefore, this model can be accepted and used to represent the experiment results for saturation response.

The overall model developed from ANOVA for anthocyanin content response were highly significant as displayed in Table 4.10, since p=0.0059. The insignificant "Lack of Fit F-value" of 0.32 with p=0.8528 (P value > 0.05) indicates good relationship between the input variables and output responses of anthocyanin content. Based on the significant p-value of less than 0.05, extraction temperature (C) (p=0.0062), TFA content quadratic

term (A^2) (p=0.0230), soaking time quadratic term (B^2) (p=0.0079) and extraction temperature quadratic term (C^2) (p=0.0319) and interaction between TFA content and extraction temperature (AC) (p=0.0388) were the significant influencing factors of the resultant anthocyanin content values. These shows that the developed models satisfactorily explained most of variation in the anthocyanin content response. The p-values greater than 0.05 indicates that the model terms are not significant with reference to TFA content (A) and soaking time (B) with p=0.1828 and p=0.0540 respectively. These insignificant model terms were not being reduced since both were needed to support the hierarchy of the quadratic model. For better modelling equation, the non significant interaction between soaking time and extraction temperature term (p=0.0746) was not being excluded. In contrast, interaction between TFA content and soaking time term has been reduced to improve the developed model. ANOVA analysis of anthocyanin content is summarized in Table 4.10.

Table 4.10: ANOVA analysis of the reduced quadratic model for anthocyanin content.

ANOVA for Response Surface Reduced Quadratic Model						
Analysis of variance table [Partial sum of squares]						
Source	Sum of Squares	DF	Mean Square	F Value	Prob	
Model	5.09E+06	8	6.37E+05	7.11	0.0059	significant
A-TFA content	1.91E+05	1	1.91E+05	2.13	0.1828	
B-Soaking time	4.56E+05	1	4.56E+05	5.09	0.0540	
C-Extraction temperature	1.21E+06	1	1.21E+06	13.53	0.0062	
A^2	7.05E+05	1	7.05E+05	7.88	0.0230	
B^2	1.11E+06	1	1.11E+06	12.36	0.0079	
C^2	6.02E+05	1	6.02E+05	6.73	0.0319	
AC	5.46E+05	1	5.46E+05	6.1	0.0388	
BC	3.76E+05	1	3.76E+05	4.2	0.0746	
Residual	7.16E+05	8	89548.52			
Lack of Fit	1.73E+05	4	43316.56	0.32	0.8528	not significant
Pure Error	5.43E+05	4	1.36E+05			
Cor Total	5.81E+06	16				

The R^2 values of 0.8767 indicates that more than 95% of experiment results for the anthocyanin content response can be explained by the model. The values of adjusted R^2 was 0.7533, showed a good relationship between the experimental and the predicted values. There were reasonably agreement of the predicted R^2=0.6122 with the adjusted R^2 of 0.8767, since the differences between both values are not more than 0.2. The adequate precision ratio of 9.109, which is greater than 4 indicates an adequate signal. This confirmed that the developed model can be used to navigate the design space. Therefore, this model can be accepted and used to represent the experiment results for anthocyanin content response.

4.3.2.4 Polynomial Equations Developed for Predicted Responses of L*, a*, b*, C, H°, Saturation and Anthocyanin Content

The developed polynomial equation to represent the selected quadratic model for L*, a*, b*, C, H°, saturation and anthocyanin content responses are displays in equation (4.1) to (4.7). Herein, A, B and C are TFA%, soaking time and extraction temperature. These equations were used to calculate the predicted values in order to optimize the response model. The predicted values were further evaluated and compared with the experimental results to estimate the experimental error.

$$L^* = 73.12 - 0.53A - 0.91B - 0.082C - 1.51A^2 + 2.45B^2 - 0.61C^2 + 1.49AB - 0.15AC + 0.17BC \quad (4.1)$$

$$a^* = 50.47 + 1.57A + 1.93B + 3.27C + 4.12A^2 - 1.29B^2 + 0.74C^2 - 3.59AB - 3AC + 1.91BC \quad (4.2)$$

$$b^* = -4.21 - 0.59A + 0.51B + 0.48C - 0.52B^2 + 0.77C^2 + 0.29AB - 0.7AC + 0.31BC \quad (4.3)$$

$$C = 54.4 + 1.06A + 2.66B + 2.81C - 3.01B^2 - 2.94AB - 2.05AC \quad (4.4)$$

$$H° = 354.55 + 0.86A + 0.42B + 1.2C + 2.08A^2 + 0.54C^2 - 2.19AB - 2.06AC \quad (4.5)$$

$$\text{Saturation} = 0.75 + 0.019A + 0.044B + 0.039C + 0.018A^2 - 0.063B^2 - 8.18E - 3C^2 - 0.053AB - 0.027AC \quad (4.6)$$

$$\text{Anthocyanin content} = 4261.44 + 154.3A + 238.81B + 389.19C + 409.27A^2 - 512.77B^2 + 378.21C^2 - 369.43AC + 306.6BC \quad (4.7)$$

4.4 Validation of the Developed Models for Responses of L*, a*, b*, C, H°, Saturation and Anthocyanin Content

The results of the fitted response surface models may be misleading, unless the model shows a good fit. Therefore it is important to examine the validation of the reduced models. The obtained data from the experiments were further examined to check the residuals. Residuals are defined as the difference between the experimental data of a measured response and the predicted value from the theorized model that relate to the experimental error estimation. For evaluating the normality of the residuals, the normal probability plot of residuals were generated which represents the normal distribution of the residuals. In order to evaluate correlation and satisfactory of the developed model, normal percentage probability versus studentized residuals were constructed (Maran et al., 2013).

Figure 4.2 (a) until (g) presents the generated normal probability plots of residuals for L*, a*, b*, C, H°, saturation and anthocyanin content responses. From the figures, it can be noticed that the residuals followed the normal distribution well since majority of the data points are reasonably closer to a straight line. This inferred good relationship between the experimental results and values predicted by the statistical model. This also shows the successfull of the generated model since it capable to predict closely the experimental data outcome (Maran et al., 2013; Qiu et al., 2014). The error terms are

considered normally distributed since the data points is close to the straight line. There were no obvious obvious S-shape pattern noticed in Figure 4.3. The S-shape pattern are not preferred because it can indicates that there are abnormalities in the obtained experiment data. The graph plotted in Figure 4.2 shows the values were low (value between -3 and 3) and the residual appear to be randomly distributed. This suggested that for all responses value the observation variance is constant. If the value of the studentized residual exceeds ±3, the experiment data have to examine for checking errors (Shafi'i et al., 2013). It is favored to obtain smaller residual value since this will shows the degree of deviation from the predicted model. Hence, this confirmed that the reduced models generated for responses of L*, a*, b*, C, H°, saturation and anthocyanin content were theoretically validated.

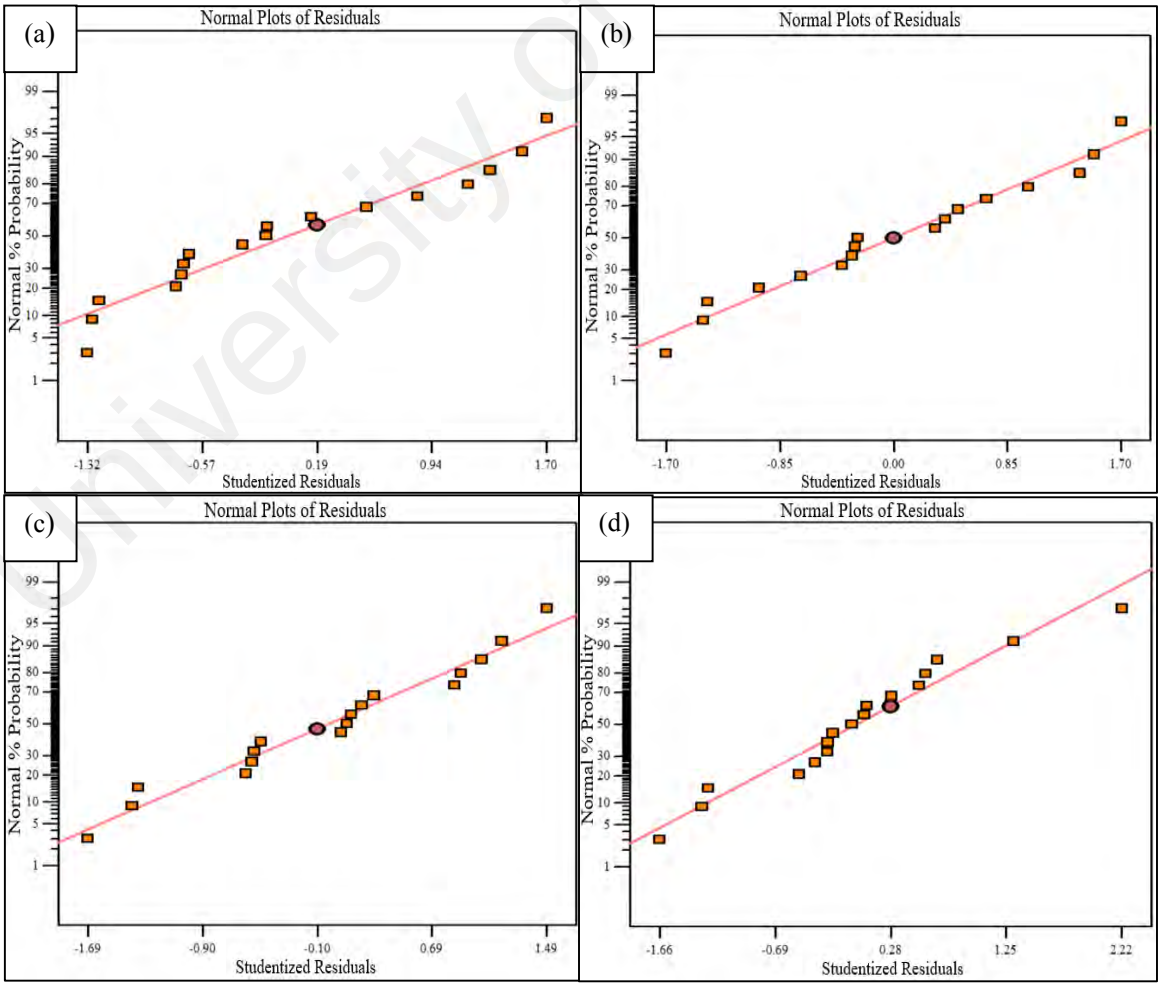

Figure 4.2: Normal probability plots of residuals for responses of (a) L*, (b) a*, (c) b*, (d) C, (e) H°, (f) saturation, (g) anthocyanin content.

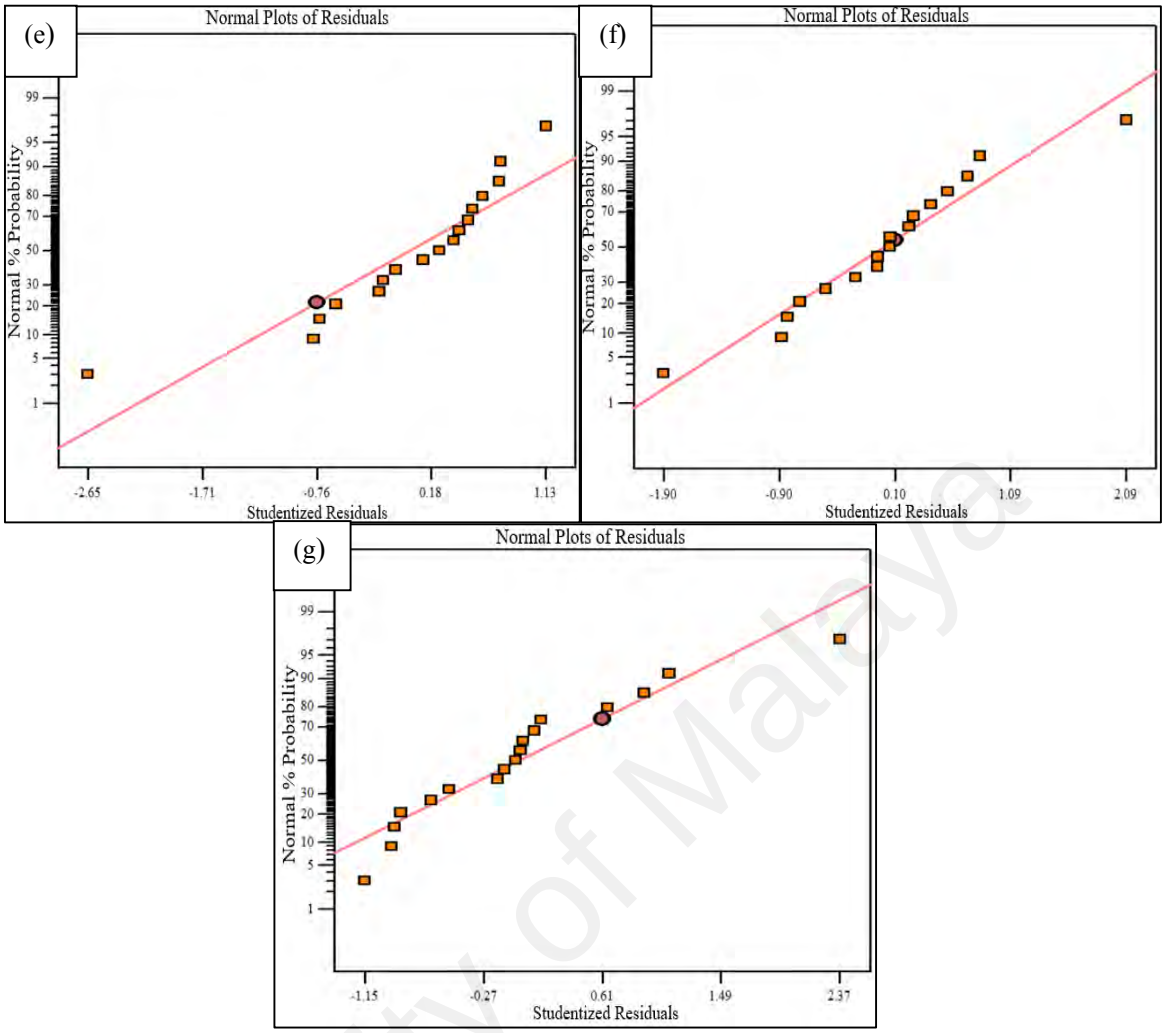

Figure 4.2, continued.

4.5 Response Surface Analysis of L*, a*, b*, C, H°, Saturation and Anthocyanin Content

In this work, BBD design of three factors at three level were used to investigate the influence of process variables which were addition of TFA content in methanol, soaking time and extraction temperature on the CIE colour analysis and anthocyanin content responses. The effect of independent and combination variables on these responses can be further analysis by using response model graph generated by Design Expert Software. The cube graph and three dimensional (3D) surface response plots were constructed from the developed models for each responses. The 3D surface response plot shows the effect of varying two parameters while holding the other parameter constant. These graphs are

graphical representations of a regression equation that show the main and interactive effects of independent variables on responses variable of L*, a*, b*, C, H°, saturation and anthocyanin content.

4.5.1 Response model graph on lightness (L*)

The cube graph shown in Figure 4.3 (a) describes how the independent variables affect lightness (L*) response. A- and A+ represent the lower and upper limit of TFA content which were 0.5% and 3%, respectively. B- and B+ represent the lower and upper limit of soaking time which were 60 and 180 min respectively. C- and C+ represent the lower and upper limit of extraction temperature which were 30 and 80 ℃, respectively. Based on this figure, it can be clearly noticed that lightness for sample with 0.5% TFA content, resulted in the decreasing of L* value to from 76.31 to 71.49 with increasing of soaking time up till 180 min at 80 ℃. At 30 ℃, lightness (L*) values L*=72.42 slightly decreased with increased of extraction temperature to 80 ℃, L*=72.26. At low temperature of 30 ℃, the increase in TFA content from 0.5% to 3% for 60 min soaking time resulted in the decrease L* value from 76.48 to 72.42. Nevertheless, at 3% TFA content the L* value increased up to 73.58 when the soaking time increased to 180 min.

The relationship between independent and L* response can also be represented graphically by 3D surface response plots. Each plot shows the effect of varying two parameters while holding the other parameter constant. Figure 4.3 (b) showed the interaction between TFA content and soaking time at holding temperature of 80 ℃ for L* response. It can be seen that at 0.5% TFA, lightness (L*) values decreased until 120 soaking time before start to increase continuously until soaking time of 180 min. Again, at 3% TFA, the L* value decreased with increasing soaking time until 120 min. At greater than 120 min, the L* value increased.

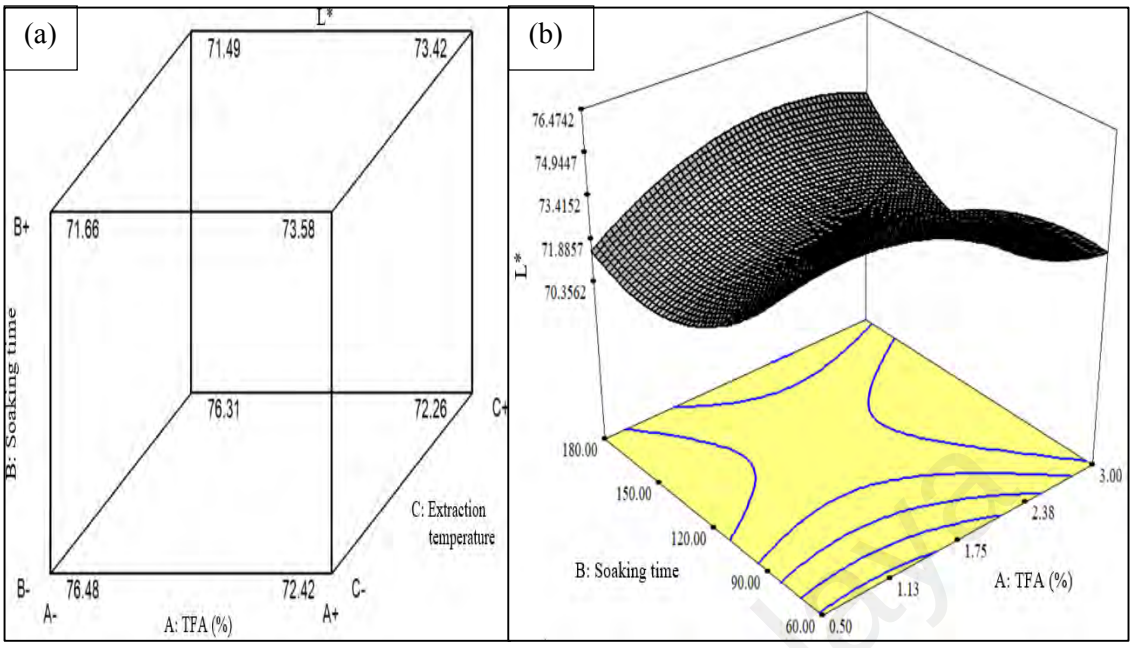

Figure 4.3: (a) Cube graph, (b) 3D response surface model at holding temperature 80 ℃ for lightness (L*) response of anthocyanin extraction from fruit pericarps of *Ixora siamensis.*

4.5.2 Response model graph on redness, a* response

Based on Figure 4.4 (a), it can be observed that for sample with 0.5% TFA content, redness, a* value increased to from 51.29 to 66.17 with increasing of soaking time up till 180 min at 80 ℃. The results also showed that a* value (a*=66.17) decreased with decreased in extraction temperature as at low temperature (30 ℃) a* value was 49.81. It is also can be noticed that with increasing of TFA content from 0.5 to 3% at 60 min soaking time and 30 ℃, the a* value increased from 42.59 to 58.91. In contrast, at 3% TFA content the a* value decreased to 51.76 as the soaking time increased up to 180 min. Figure 4.4 (b) showed the interaction between TFA content and soaking time at holding temperature of 80 ℃ for a* response. It can be noticed that at 0.5% until 1.75% TFA, a* values increased continuously until 180 soaking time. Beyond 1.75% TFA, the a* value decreased with increasing soaking time until 180 min.

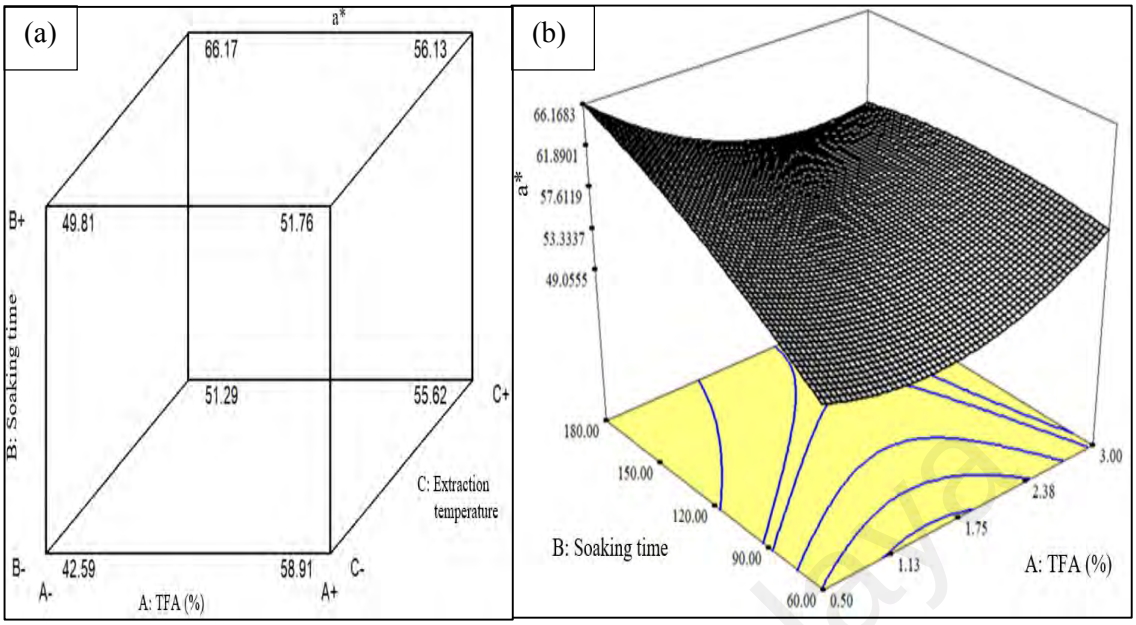

Figure 4.4: (a) Cube graph, (b) 3D response surface model at holding temperature 80 ℃ for redness (a*) response of anthocyanin extraction from fruit pericarps of *Ixora siamensis.*

4.5.3 Response model graph on blueness, b* response

Based on Figure 4.5 (a), it can be shown that at 0.5% TFA content, b* value decreased from -2.72 to -1.65 with increasing of soaking time up till 180 min at 80 ℃. b* value increased with decreased in extraction temperature. At low temperature of 30 ℃, b* value was -4.63. It can also be summarized that with increasing of TFA content from 0.5 to 3% at 60 min soaking time and 30 ℃, the b* value showed slightly increased -4.45 to -4.80. Nevertheless, at 3% TFA content the b* value decreased to -3.84 as the soaking time increased up to 180 min. Figure 4.5 (b) showed the interaction between TFA content and soaking time at holding temperature of 80 ℃ for b* response. It can be observed that at 0.5% TFA, b* values increased until around 120 soaking time before start to decrease continuously until soaking time of 180 min. At 60 min soaking time, the b* value decreased continuously with increasing TFA content up to 3%.

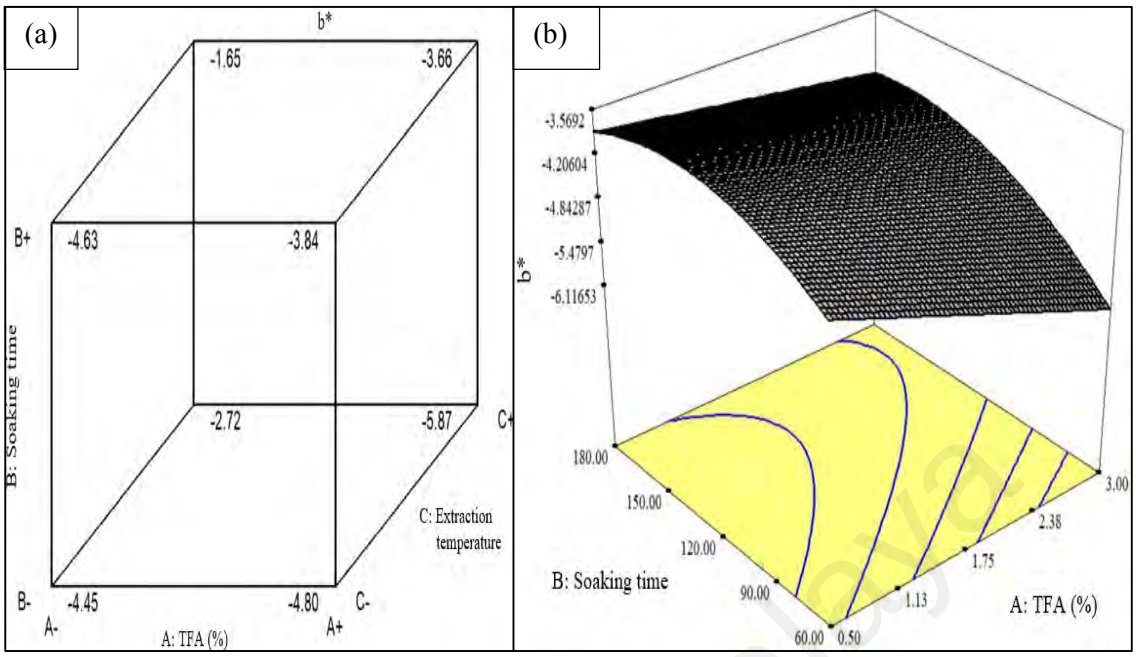

Figure 4.5: (a) Cube graph, (b) 3D response surface model at holding temperature 80 ℃ for blueness (b*) response of anthocyanin extraction from fruit pericarps of *Ixora siamensis.*

4.5.4 Response model graph on chromaticity (C) response

Based on Figure 4.6 (a), it can be clear noticed that for sample with 0.5% TFA content, C value increased from 49.60 to 60.79 when soaking time increased up to 180 min at 80 ℃ extraction temperature. C value decreased with decreased in extraction temperature. At low temperature (30 ℃), the C value was 51.06. In addition, at 60 min soaking time and 30 ℃, increasing of TFA content from 0.5 to 3% resulted in the increased of C value increased from 39.86 to 51.96. Figure 4.6 (b) showed the interaction between TFA content and soaking time at holding temperature of 80 ℃ for C response. It can be observed that at 0.5% TFA, chromaticity (C) values increased continuously with increasing soaking time up to 180 min. At 60 min soaking time, the C value increased continuously with increasing TFA content up to 3%. Nevertheless, at 3% TFA, the C values increased when increased the soaking time until near to 120 min soaking time. Beyond 120 min soaking time, the C decreased.

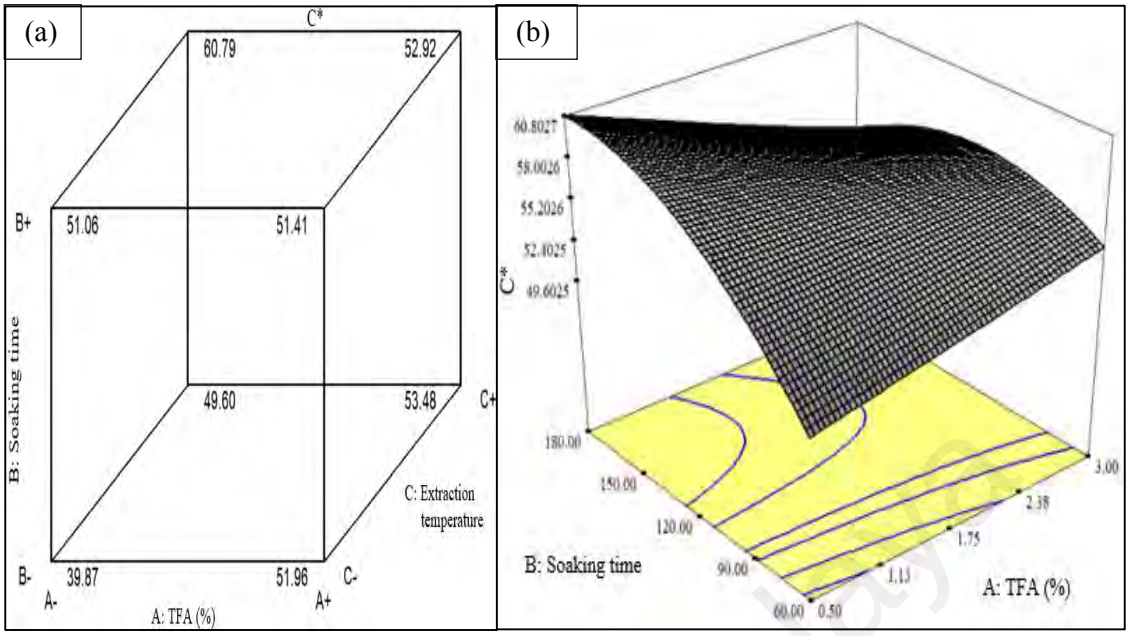

Figure 4.6: (a) Cube graph, (b) 3D response surface model at holding temperature 80 ℃ for chromaticity (C) response of anthocyanin extraction from fruit pericarps of *Ixora siamensis.*

4.5.5 Response model graph on hue angle (H°) response

Based on Figure 4.7 (a), it can be clear noticed that for sample with 0.5% TFA content, H° value increased from 356.97 to 362.18° with increasing of soaking time up to 180 min at 80 ℃. The results also showed that H° value decreased with decreased in extraction temperature to 30 ℃ as H° value was 355.65°. By increasing of TFA content from 0.5 to 3%, at 60 min soaking time and 30 ℃, the H° value increased from 350.44 to 360.65°. H° value decreased to 357.12° as the soaking time increased up to 180 min. Figure 4.7 (b) showed the interaction between TFA content and soaking time at holding temperature of 80 ℃ for H° response. It can be observed that at 0.5% TFA, H° values increased continuously with increasing soaking time up to 180 min. At 60 min soaking time, the H° value decreased when increasing TFA content before start to increase continuously up to 3%.

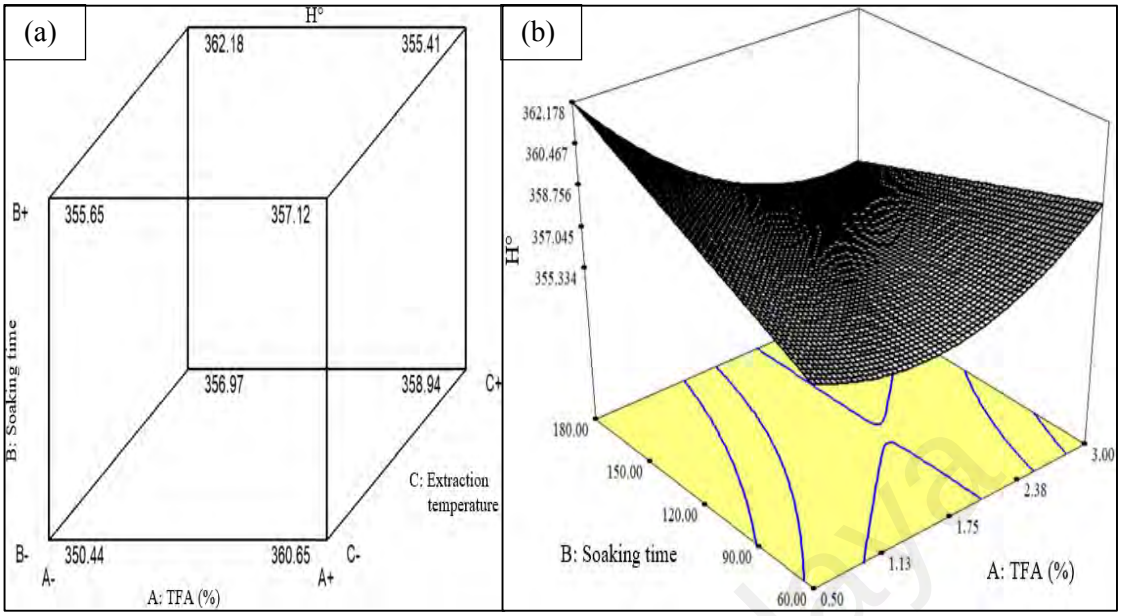

Figure 4.7: (a) Cube graph, (b) 3D response surface model at holding temperature 80 ℃ for hue angle (H°) response of anthocyanin extraction from fruit pericarps of *Ixora siamensis.*

4.5.6 Response model graph on saturation (s) response

Based on Figure 4.8 (a), it can be clearly noticed that, at 80 ℃ the saturation value of sample with 0.5% TFA content increased from 0.646 to 0.840 with increasing of soaking time up till 180 min. Saturation response decreased with decrease in extraction temperature as at 30 ℃, the saturation value was 0.707. The saturation values increased with increasing of TFA content from 0.5% to 3% TFA for 60 min soaking time from 0.513 to 0.712. Nevertheless, at 3% TFA content and at low temperature of 30 ℃, saturation decreased to 0.693 when increased the soaking time to 180 min. Figure 4.8 (b) showed the interaction between TFA content and soaking time at holding temperature of 80 ℃ for saturation response. It can be observed that at 0.5% TFA, saturation values increased continuously with increasing soaking time up to 180 min. At 60 min soaking time, the saturation value increased continuously when increasing TFA content up to 3%. Nevertheless, at 3% TFA, the saturation values increased when increased the soaking time until near to 120 min soaking time. Beyond 120 min soaking time, the saturation values decreased.

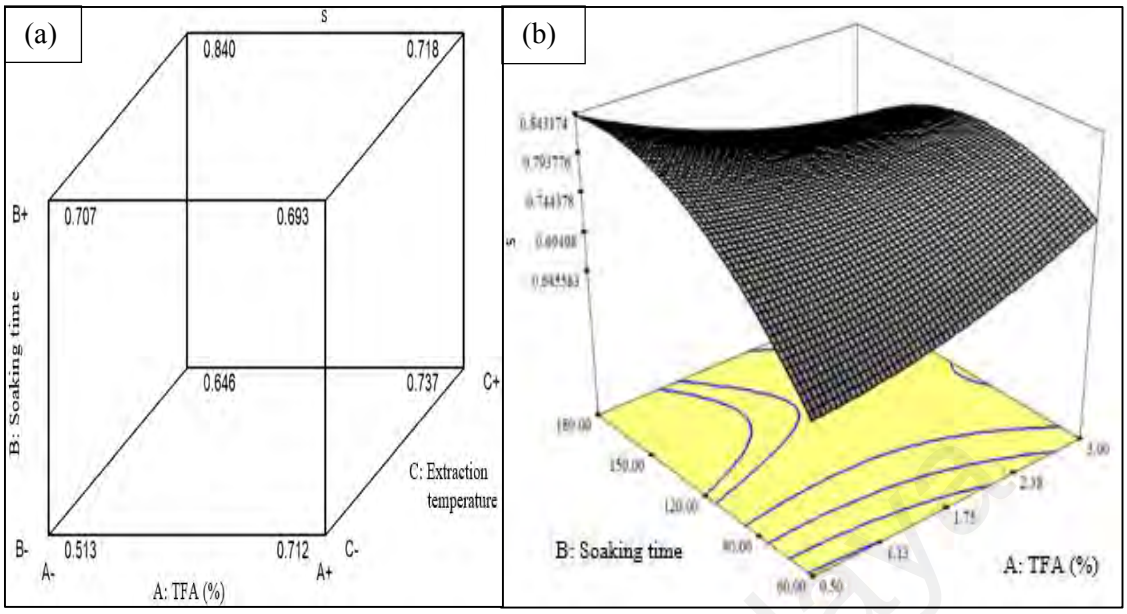

Figure 4.8: (a) Cube graph, (b) 3D response surface model at holding temperature 80 ℃ for saturation (s) response of anthocyanin extraction from fruit pericarps of *Ixora siamensis*.

4.5.7 Response model graph on anthocyanin content response

Based on Figure 4.9 (a), it can be clearly deduced that, at 80 ℃, the anthocyanin content value of sample with 0.5% TFA content increased rapidly from 4595.06 to 5685.88 mg/L with increasing of soaking time up to 180 min. Anthocyanin content response decreased drastically with decrease in extraction temperature to 30 ℃, which the anthocyanin value was 3555.45 mg/L. The anthocyanin content also increased with increasing of TFA content from 0.5% to 3% TFA for 60 min soaking time from 3691.02 to 4738.48 mg/L. Nevertheless, at 3% TFA content and at low temperature of 30 ℃, anthocyanin content decreased to 4602.91 mg/L when increased the soaking time to 180 min. Figure 4.9 (b) showed the interaction between TFA content and soaking time at holding temperature of 80 ℃ for anthocyanin content response. It can be observed that at 0.5% TFA, anthocyanin values increased continuously with increasing soaking time up to 180 min. At 60 min soaking time, the anthocyanin content value decreased when

increased soaking time until 1.75%. Beyond 1.75% TFA, anthocyanin content values increased.

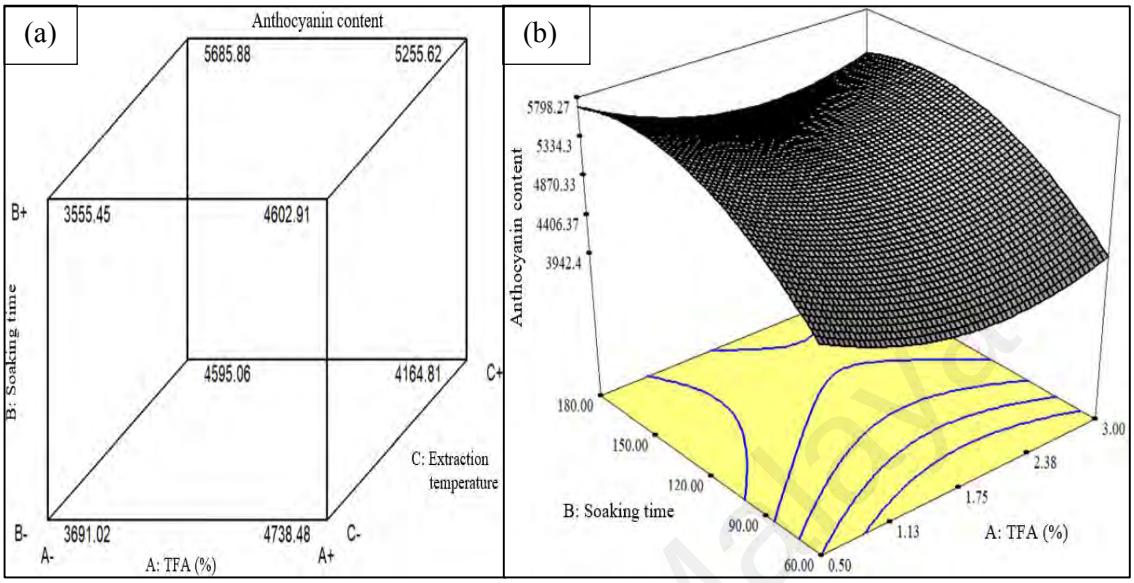

Figure 4.9: (a) Cube graph, (b) 3D response surface model at holding temperature 80 ℃ for anthocyanin content response of anthocyanin extraction from fruit pericarps of *Ixora siamensis*.

4.6 Optimization of the Models for L*, a*, b*, C, H°, Saturation and Anthocyanin Content

The optimization of anthocyanin extraction from fruit pericarps *Ixora siamensis* was accomplished using the numerical optimization based on Design-Expert software which search for factor level combinations that satisfy simultaneously the needs or requirements or for each factors and responses. The simultaneous optimizations of the multiple responses were performed using desirability function method in which to generate optimum conditions that meet specific goals. The goals for the variables and response were set either none, maximum, minimum, target, or in range which will then be combined into one desirability functions.

The desirability procedure includes two phases: first, finding the independent variables levels that simultaneously produce the most desired predicted responses on the

dependent variables and second, maximize the overall desirability with respect to the controllable factors (Mourabet et al., 2017). In this study, to find a good set of conditions that achieve the specific goals, the three independent variables (i) TFA content (0.5 and 3%), (ii) soaking time (60 and 180 min), (iii) extraction temperature (30 and 80 ℃) were set within range. The CIE colour visual of L*, a*, b*, C, H° and saturation responses were also set within range while anthocyanin content was set at maximum as stated in Table 4.11. The "importance" of goals (option 1-5) for all variables and responses was considered to be equally important in a setting of 3. Design-Expert software will optimized the best combination condition for anthocyanin extraction using this desirability target. The desirability profiles for the suggested optimum conditions are shown in Table 4.12. The optimization combination was selected based on the desirability value of each solution suggested. For this study, the selected optimized condition were 0.5% TFA content, 119 min soaking time and extraction temperature of 80 ℃ with highest desirability of 0.928. Hence, this independent variable were further used as the optimization parameter for anthocyanin extraction from fruit pericarps of *Ixora siamensis.*

Table 4.11: Settings for multi-criteria optimization for desirability goal of L*, a*, b*, C, H°, saturation and anthocyanin content.

Factor/Response	Goal	Lower Limit	Upper Limit	Importance
TFA (%)	is in range	0.5	3	3
Soaking time (min)	is in range	60	180	3
Extraction temperature (℃)	is in range	30	80	3
L*	is in range	70.31	76.67	3
a*	is in range	45.79	59.87	3
b*	is in range	-6.1	-1.65	3
C	is in range	45.12	58.9	3
H°	is in range	351.59	359.67	3
Saturation	is in range	0.5885	0.81806	3
Anthocyanin content	maximize	3693.9	5791.7	3

Table 4.12: Recommended solution for optimal anthocyanin extraction from fruit pericarp of *Ixora siamensis.*

No	TFA (%)	Soaking time (min)	Extraction temperature (°C)	L*	a*	b*	C	H°	s	Anthocyanin content (mg/L)	Desirability	
1	**0.5**	**119**	**80**	**71.50**	**59.87**	**-1.67**	**58.10**	**359.52**	**0.80**	**5641.36**	**0.928**	**Selected**
2	0.51	119.39	79.98	71.50	59.87	-1.68	58.14	359.50	0.80	5638.96	0.927	
3	0.5	120.42	79.34	71.47	59.87	-1.73	58.12	359.48	0.81	5617.25	0.917	
4	3	152.21	80	71.41	56.94	-3.80	55.20	356.22	0.77	5367.99	0.798	
5	3	116.01	30	70.53	56.86	-3.83	54.70	359.01	0.77	5185.7	0.711	
6	3	118	30	70.54	56.75	-3.82	54.70	358.95	0.77	5185.15	0.711	
7	3	128.32	30	70.68	56.11	-3.74	54.60	358.64	0.76	5164.21	0.701	

4.7 Identifying colour differences (ΔE*) using L*, a* and b* coordinates

The 17 extraction samples from fruit pericarps of *Ixora siamensis* with different extraction parameter combination were then calculated for the colour differences (ΔE*) based on L*, a* and b* colour coordinate. The colour differences that vary between the sample of extraction are calculated in comparison with the sample with highest anthocyanin content (sample 7) using equation (4.8):

$$\Delta E^* = \sqrt{(L_2^* - L_1^*)^2 + (a_2^* - a_1^*)^2 + (b_2^* - b_1^*)^2} \quad (4.8)$$

Table 4.13 lists the anthocyanin content in mg/L with the colour differences (ΔE*). Figure 4.10 shows the relationship between anthocyanin content and the sample of extractions while Figure 4.11 present the relationship between colour difference (ΔE*) and sample of extractions. Based on Figure 4.10 and 4.11 the relationship between anthocyanin content with sample of extractions and colour difference with sample of extractions, if assumed linear has a regression (R^2) of 0.8785 and 0.5955, respectively.

Table 4.13: Anthocyanin content and colour differences (ΔE*) for different extraction parameters.

Sample	Anthocyanin content (mg/L)	Colour differences (ΔE*)
1	3770.82	14.4
2	4074.95	5.3
3	4000.00	4.1
4	4786.00	7.9
5	4234.00	12.1
6	5045.00	4.2
7	**5791.70**	**0.0**
8	5124.98	4.5
9	3821.96	15.1
10	3693.90	13.4
11	3946.68	11.6
12	5045.00	2.8
13	4897.00	8.5
14	4121.70	10.0
15	4026.41	11.1
16	4007.73	10.1
17	4254.35	9.4

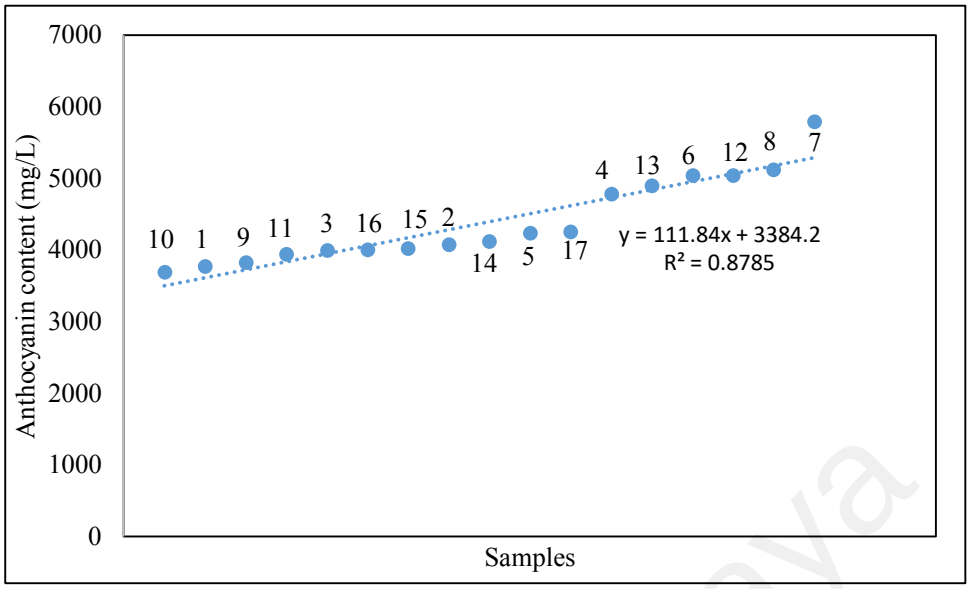

Figure 4.10: Relationship between anthocyanin content with different sample of extractions.

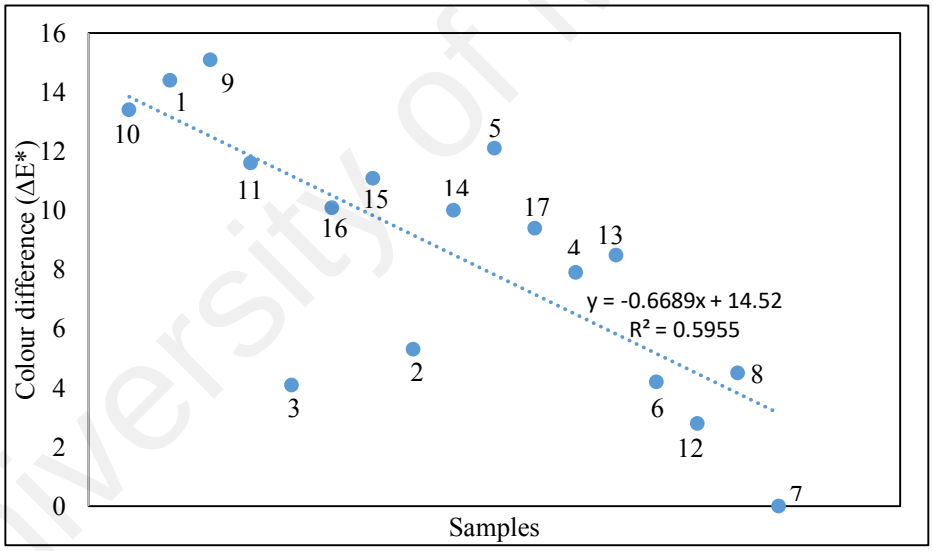

Figure 4.11: Relationship between colour difference (ΔE*) with different sample of extractions.

4.8 Summary

In summary, for optimized extraction of anthocyanin from *Ixora siamensis* the conditions are 0.5% TFA content, 119 min soaking time and extraction temperature of 80 ºC which have been successfully optimized by RSM. Further extraction for DSSCs application will use these parameters.

CHAPTER 5: RESULTS FOR SYNTHESIS AND CHARACTERIZATION OF TiO_2 NANOSTRUCTURES

5.1 Introduction

Chapter 5 provides the analyses on the synthesis and characterization of TiO_2 structures from the combination of sol-gel and electrospinning methods. This chapter presents results on the morphology investigation of the PVP-TiO_2 nanofibers obtained from the electrospinning process. Solution concentration and electrospinning processing parameters affects the surface structure or morphology of the PVP-TiO_2 nanofibers. These were studied using FESEM (Hitachi SU8220). To examine solution concentration effect on nanofiber morphology, five different PVP polymer concentrations (9.2, 10.2, 11.2, 12.2 and 13.2 wt.%) were used in the preparation of the nanofibers or fibrous mats. To study the effect of electrospinning processing parameters, seven voltages (16, 17, 18, 19, 20, 21 and 22 kV) were applied during electrospinning process and the surface morphology of the nanofibers formed were studied using FESEM. The distributions of average fiber and bead diameters were determined with the image J software. The successfully beadless nanofibers obtained were subjected to different calcination temperatures. The sintered samples were ground to obtain the TiO_2 nanorod powders. The influence of calcination temperature on the production of TiO_2 nanorods were examined via morphological analysis and the average nanorod diameter distributions were evaluated for the corresponding temperature. EDX was performed for the elemental analysis of the TiO_2 nanorods produced. The phase of the electrospun TiO_2 nanorods whether anatase, rutile or brookite with respect to the different calcination temperatures was examined by XRD. The data were collected using Cu-$K\alpha$ x-ray-radiation at diffraction angles of $2\theta = 5°$ to $55°$. XRD patterns were analyzed using Origin 9.0 software. Nanorods with dominant anatase structure were used to fabricate the composite photoanode that consists of nanoparticles and nanorods (NPs-NRs). Investigation on the

surface morphology for composite photoanode at various nanorod ratios were also studied using FESEM. All samples were coated with platinum for FESEM analysis.

5.2 Morphological Studies on Electrospun TiO_2 Nanofibers Obtained from Combined Method of Sol-Gel and Electrospinning

5.2.1 Effect of Polymer Concentration on Nanofiber Morphology

The electrospun PVP-TiO_2 nanofibers were prepared from the combination of sol-gel method and electrospinning process. The electrospun PVP-TiO_2 nanofibers were observed under FESEM and analyzed for fiber and bead diameters. To investigate the effects of polymer concentrations on formation of PVP-TiO_2 nanofibers, the applied voltage and working distance from the tip-to-collector were set constant at 18 kV and 14 cm, respectively. The flow rate of the spinning solutions was fixed at 1 mL/h. Figure 5.1 illustrates the FESEM images of PVP-TiO_2 nanofibers produced from electrospinning technique with different PVP concentrations of (a) 9.2, (b) 10.2, (c) 11.2, (d) 12.2 and (e) 13.2 wt.% designated as NF1, NF2, NF3, NF4 and NF5 at the magnification of x1000. Based on these images, it can be observed that at PVP concentrations of 9.2 and 10.2 wt.%, Figure 5.1 (a) and (b), cylindrical fibers were not formed and there were a flat fiber observed in inset image. Cylindrical fibers were only start to observed for 11.2 wt.% PVP, Figure 5.1 (c). It can also be noticed that many beads were also present. On increasing the PVP concentration to NF4 sample with 12.2 wt.% PVP as seen in Figure 5.1 (d), fibers with less beads were formed and the bead shape changed from spherical-like to spindle or rod-like. Finally, with increased PVP concentration in NF5 sample with 13.2 wt.% PVP, more uniform cylindrical fibers with smaller beads were obtained as displayed in Figure 5.1 (e). It can be examined that increasing the PVP concentration led to an increase in fiber diameters with decreased bead diameters. Polymer concentration therefore, is an important factor that affects the fiber morphology.

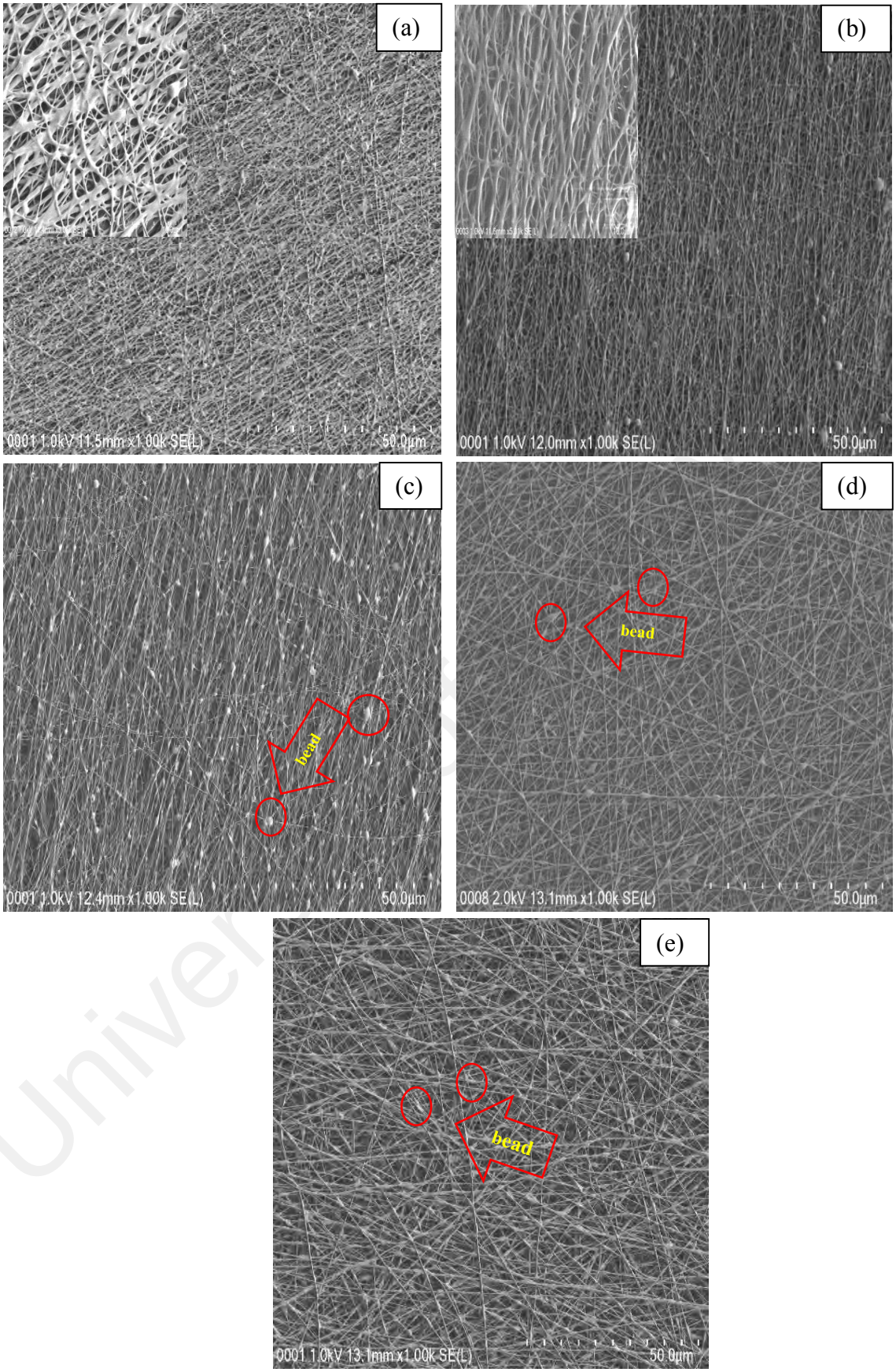

Figure 5.1: FESEM images of PVP-TiO_2 electrospun fibers at different PVP concentrations (a) 9.2 (NF1), (b) 10.2 (NF2), (c) 11.2 (NF3), (d) 12.2 (NF4) and (e) 13.2 wt.% (NF5).

To study the influence of PVP concentrations towards the resultant fiber diameter, Image J software was used to measure fiber diameters for PVP concentrations ranging from 11.2 to 13.2 wt.%. Results on the fiber diameter are presented in Figure 5.2. Within the limits of the same voltage and working distance (18 kV and 14 cm), increasing PVP concentration from 11.2 to 13.2 wt.% saw the increase in average diameter of the electrospun PVP-TiO_2 fibers as presented in histogram distributions in Figure 5.2 (a) until (c). The diameter of fibers increased as the PVP concentration increased under the same electric field. For the PVP concentrations of 11.2 wt.% designated as NF3, the fiber diameter averaged between 95 and 202 nm with the highest number of fibers having average diameter of 132 nm.

At PVP concentration of 12.2 wt.% designated as NF4, the average fiber diameter increased to the range between 120 and 307 nm, with most fibers having diameter of 255 nm. At PVP concentration of 13.2 wt.% designated as NF5, average fiber diameter continued to increase between 201 to 452 nm in size and the majority had an average of 301 nm. For the 11.2 wt.% of PVP polymer concentration, a lot of beads were observed. On increasing the PVP concentration from NF4 to NF5, less beads were observed. Hence, sample with PVP concentration of 13.2 wt.% designated as NF5, was selected as an optimal concentration for PVP concentration. It is realized that least beads were observed at 13.2 wt.% PVP concentration, hence other electrospinning parameters should be studied and PVP concentration was fixed at 13.2 wt.%. To further improve the quality of the fibrous mats, the effects of applied voltage on the fibrous mat morphologies were made at NF5 concentration.

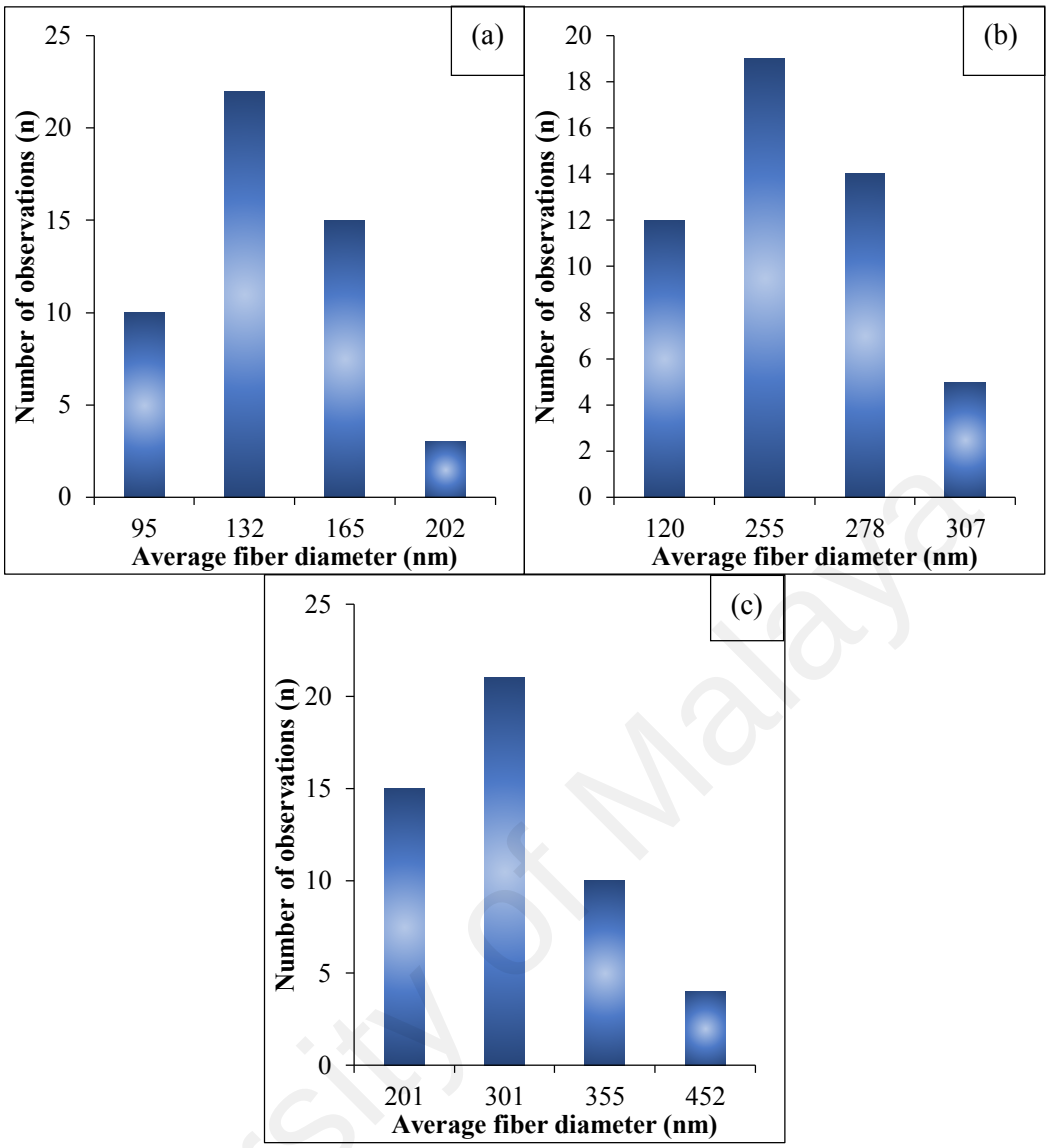

Figure 5.2: Histogram showing the size distribution of average fiber diameter for PVP-TiO_2 electrospun fibers as function of different PVP concentration (a) 11.2 (NF3), (b) 12.2 (NF4) and (c) 13.2 wt.% (NF5).

Further investigation on the bead diameters were performed by randomly calculating beads diameter distribution using image J software. The respective bead diameter histogram is displayed in Figure 5.3 for three different polymer concentrations of 11.2, 12.2 and 13.2 wt.% PVP since at these concentrations, cylindrical nanofibers were really formed. However, beads were also formed within the limits of the voltage and working distance (18 kV and 14 cm). Increasing PVP concentration from 11.2 to 13.2 wt.% the average bead diameter of the electrospun PVP decreased as displayed in Figure 5.3 (a) until (c). For PVP concentration of 11.2 wt.% designated as NF3, the average bead

diameter was in the range between 0.63 and 1.57 µm with most beads have diameters of 1.26 µm. On increasing the PVP to 12.2 wt.% designated as NF4, the average bead diameter decreased and the range was from 0.45 to 1.22 µm, with the highest number of beads have diameter of 0.84 µm. At 13.2 wt.% PVP designated as NF5, average diameters of the bead-like structures continued to decrease within the range between 0.33 and 0.47 µm in size. The maximum number of beads have an average of 0.40 µm. No observation on bead diameter recorded for NF1 and NF2 samples.

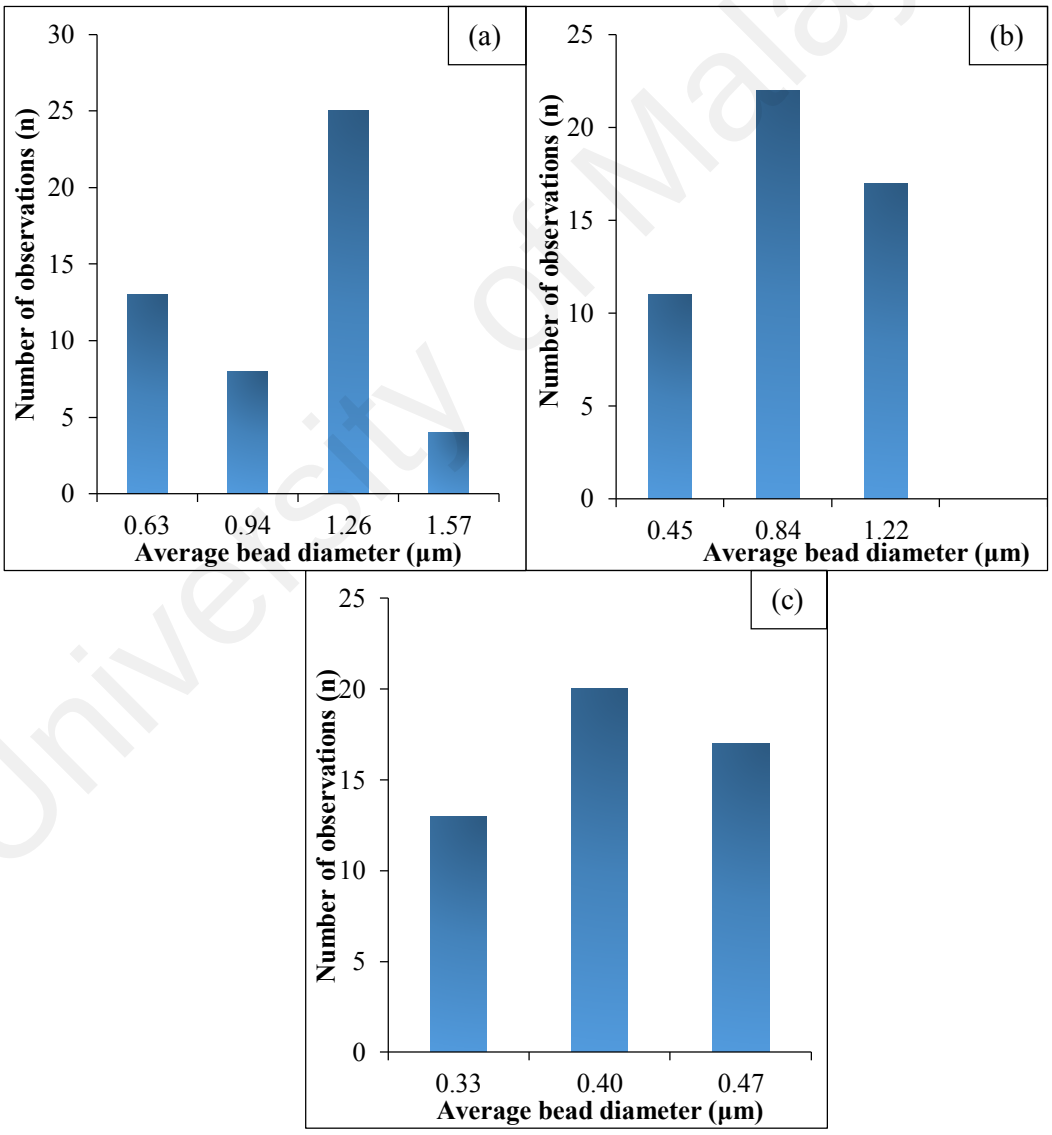

Figure 5.3: Histogram showing the size distribution of average bead diameter for PVP-TiO_2 electrospun fibers as function of different PVP concentration (a) 11.2 (NF3), (b) 12.2 (NF4) and (c) 13.2 wt.% (NF5).

Table 5.1 summarizes the relationships between average fiber and bead diameters with respect to PVP concentration. It can be justified that PVP content has significant impact on the morphology of the electrospun nanofibers in terms of fiber and bead diameters. The results show that increasing PVP content from 11.2 to 13.2 wt.% resulted in significantly increased average fiber diameter which most fibers have diameter values from 132 to 301 nm, respectively. Eventhough the average fiber diameter increased with increasing in PVP content, there were still bead formations. It can be observed that on increasing the PVP content from 11.2 to 13.2 wt.%, the average bead diameter decreased with most beads had diameters from 1.26 to 0.40 μm. These showed that sufficient PVP was needed to form more uniform fibers with less formation of beads. It is not possible to increase more PVP content as it will results in larger fiber diameter. In an attempt to produce non-beaded nanofibers, another parameter, which is the applied voltage will be varied.

Table 5.1: Experimental results on the effects of different weight percentage (wt. %) of PVP on fiber morphology.

Designation	PVP concentrations (wt.%)	Average diameter with highest number of observations		Fiber Morphology
		Fiber (nm)	Bead (μm)	
NF1	9.2	-	-	Flat fiber
NF2	10.2	-	-	Flat fiber
NF3	11.2	132	1.26	Beaded fiber
NF4	12.2	255	0.84	Beaded fiber
NF5	13.2	301	0.40	Beaded fiber

5.2.2 Effect of Applied Voltage on Nanofiber Morphology

FESEM image of electrospun nanofibers were analyzed to get a thorough look at the resultant fiber morphology and to measure the fiber and bead diameters with respect to

the applied voltage. In order to explore the effect of applied voltage on morphology of PVP-TiO_2 nanofibers formed, the applied voltage was varied from 16 kV to 22 kV while the flow rate of spinning solution and working distance were fixed at 1 mL/h and 14 cm, respectively. In this experiments, the PVP concentration of 13.2 wt.% assigned for NF5 sample was chosen since the morphology showed smallest bead formed. To remove the beads in NF5 sample, the applied voltage was varied. Figure 5.4 showed the FESEM images of 13.2 wt.% of PVP sample (NF5) at x1000 magnification produced from electrospinning technique at applied voltages (a) 16 kV, (b) 17 kV, (c) 18 kV, (d) 19 kV, (e) 20 kV, (f) 21 kV, (g) 22 kV. Based on FESEM images in Figure 5.4, it is evident that electrospun PVP-TiO_2 showed morphology transition from beaded nanofibers to the successfully beadless uniform continuous cylindrical nanofiber morphology. As depicted in Figure 5.4 (a), there were signs of fiber formation at 16 kV (NF5-1) but these were flat fibers which are different from the well-known cylindrical fibers (Sohrabi et al*.*, 2013), since they are flatter. When increased the applied voltage to 17 kV (NF5-2) as observed in Figure 5.4 (b), the morphology of fiber mat change from flat to cylindrical fibers but there were still spherical beads observed.

Continued increase in voltage to 18 kV (NF5-3), showed that cylindrical fibers formed and bead shape changes to more spindle-like as seen in Figure 5.4 (c). More uniform cylindrical fibers with less bead formations were observed for electrospun PVP-TiO_2 at 19 kV (NF5-4), Figure 5.4 (d). Finally, on reaching 20 kV (NF5-5), uniform cylindrical fibers with almost bead free mats were successfully formed as presented in Figure 5.4 (e). For better understanding on effect of applied voltage on fiber morphologies, the higher applied voltages of 21 and 22 kV were included as the investigated parameter. It can be noticed that beads have started to form again at voltages of 21kV (NF5-6) and 22

kV (NF5-7). From these results, it is evident that the applied voltage is also one of the driving forces in the electrospinning process.

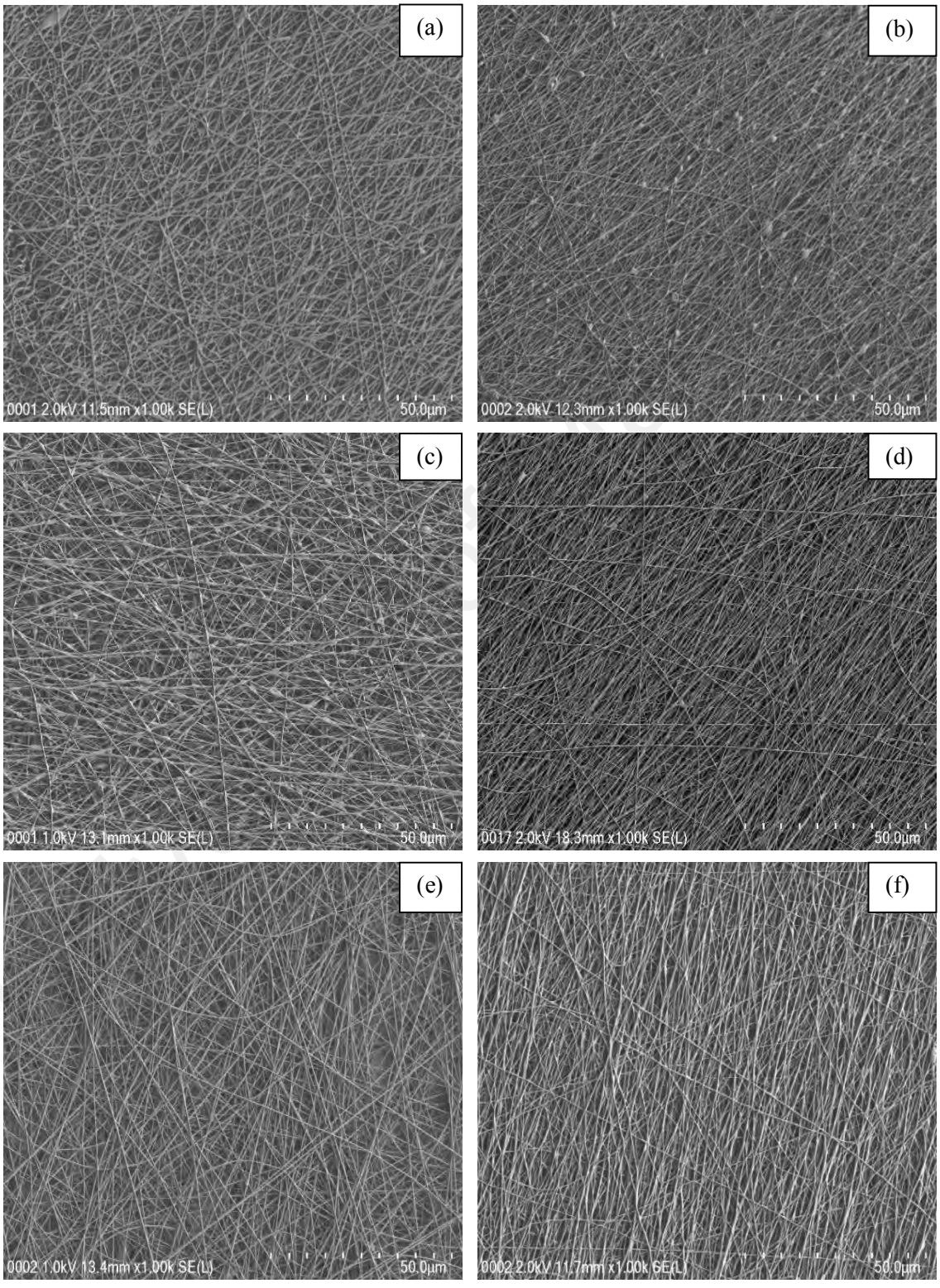

Figure 5.4: FESEM images of PVP-TiO_2 electrospun fibers at different applied voltage (a) 16, (b) 17, (c) 18, (d) 19, (e) 20, (f) 21 and (g) 22 kV.

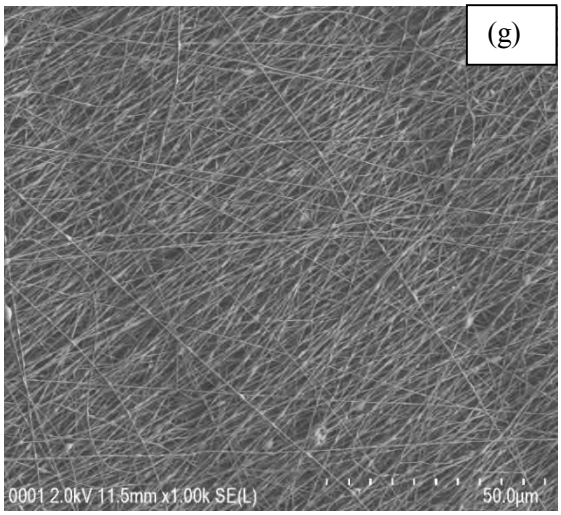

Figure 5.4, continued.

More observations on fiber morphologies were performed on the effects of different applied voltages towards the resultant fiber diameter and randomly calculating using image J software. Results on respective fiber diameter histogram distributions were depicted in Figure 5.5 (a) until (f) for six different applied voltages of 17 to 22 kV with 13.2 wt.% PVP concentration. It can be observed in Figure 5.5 (a) that average fiber diameter of fiber electrospun at 17 kV (NF5-2) was in the range between 120 to 289 nm with the highest number of fibers having average diameter of 167 nm. At 18 kV (NF5-3), the average fiber diameter increased to the range between 201 to 452 nm, with the highest number of fibers having average diameter of 301 nm as displayed in Figure 5.5 (b).

In contrast, as seen in Figure 5.5 (c) there was a decrease in average fiber diameter at 19 kV (NF5-4) with diameter range from 153 to 407 nm and most fibers had a diameter of 283 nm. Continued increase in applied voltage to 20 kV (NF5-5), Figure 5.5 (d) resulted in further decrease in average diameter of cylindrical fibers. The NF5-5 samples electrospun at 20 kV had the average fiber diameter between 131 to 349 nm. The histogram of Figure 5.5 (d) indicates that most of the fibers produced at 20 kV are

nanofibers having average diameter of 177 nm. On increasing the applied voltages beyond 20 kV (NF5-6 and NF5-7 samples), the average fiber diameter increased as can be seen in Figure 5.5 (e) and (f). These results showed that the applied voltage was also a significant factor that determined the morphology of the electrospinning nanofibers.

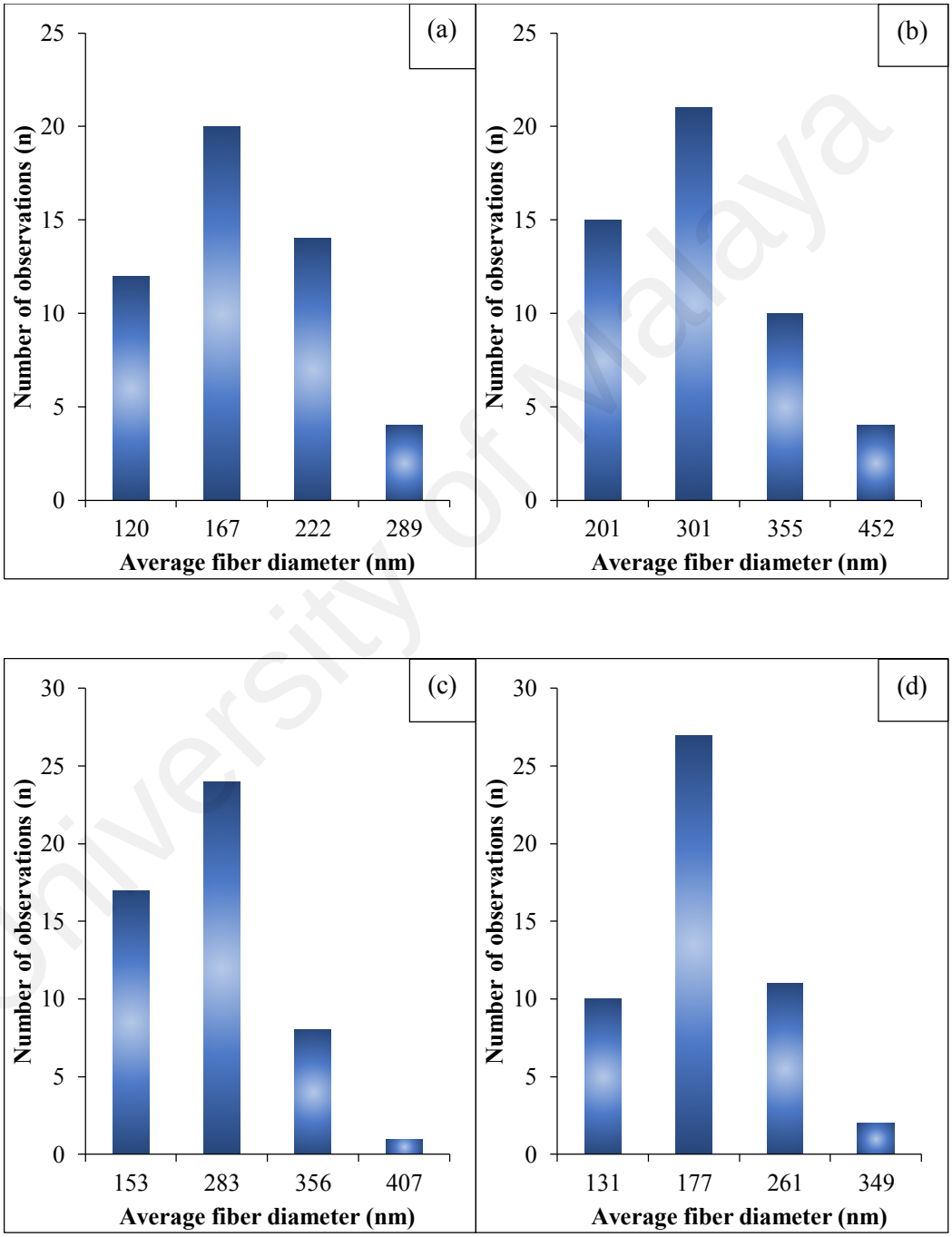

Figure 5.5: Histogram showing the size distribution of average fiber diameter for PVP-TiO_2 electrospun fibers as function of different applied voltages (a) 17 kV (NF5-2), (b) 18 kV (NF5-3), (c) 19 kV (NF5-4), (d) 20 kV (NF5-5), (e) 21 kV (NF5-6) and (f) 22 kV (NF5-7).

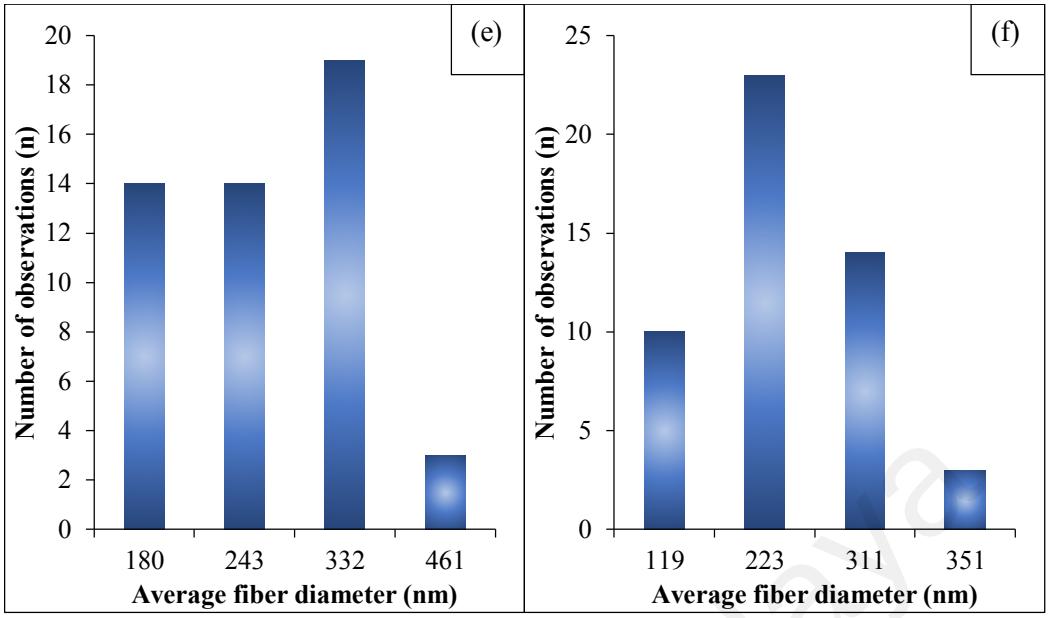

Figure 5.5, continued.

Further exploration on the bead diameters was performed by randomly calculating using the image J software. The respective bead diameter distributions was plotted as a histogram and displayed in Figure 5.6 (a) to (e) for five different applied voltages 17, 18, 19, 21 and 22 kV. Within the fixed of 13.2 wt.% PVP, distance of 14 cm and flow rate of 1 mL/h, the results showed that the bead formation appear for sample electrospun at 17 kV until 19 kV and beyond 20 kV. As can be seen in Figure 5.6 (a), the large average beads diameter observed at 17 kV (NF5-2) ranging from 0.33 to 1.34 μm with majority having diameter of 0.66 μm. On increasing the voltage to 18 kV (NF5-3) as in Figure 5.6 (b), the average bead diameter decreased to within the range of 0.33 to 0.47 μm, with diameter of the majority beads at 0.40 μm. The decreasing trend in average bead diameter continued when applied voltage was increased up to 19 kV, assigned as NF5-4 samples as seen in Figure 5.6 (c). The average bead diameter were in the range from 0.14 to 0.24 μm and most fibers have diameter of 0.19 μm. It can be clearly observed that there was no bead formation for sample electrospun at 20 kV (NF5-5) as continuous cylindrical fibers are formed. It can be noticed in Figure 5.6 (d) that the average bead diameter

distributions at 21 kV (NF5-6) were between 0.09 and 0.61 µm with majority having average diameter of 0.44 µm. Further increase of the voltage to 22 kV (NF5-7), resulted in bigger average bead diameter between 0.38 to 0.97 µm with most beads having diameter of 0.77 µm, as displayed in Figure 5.6 (e).

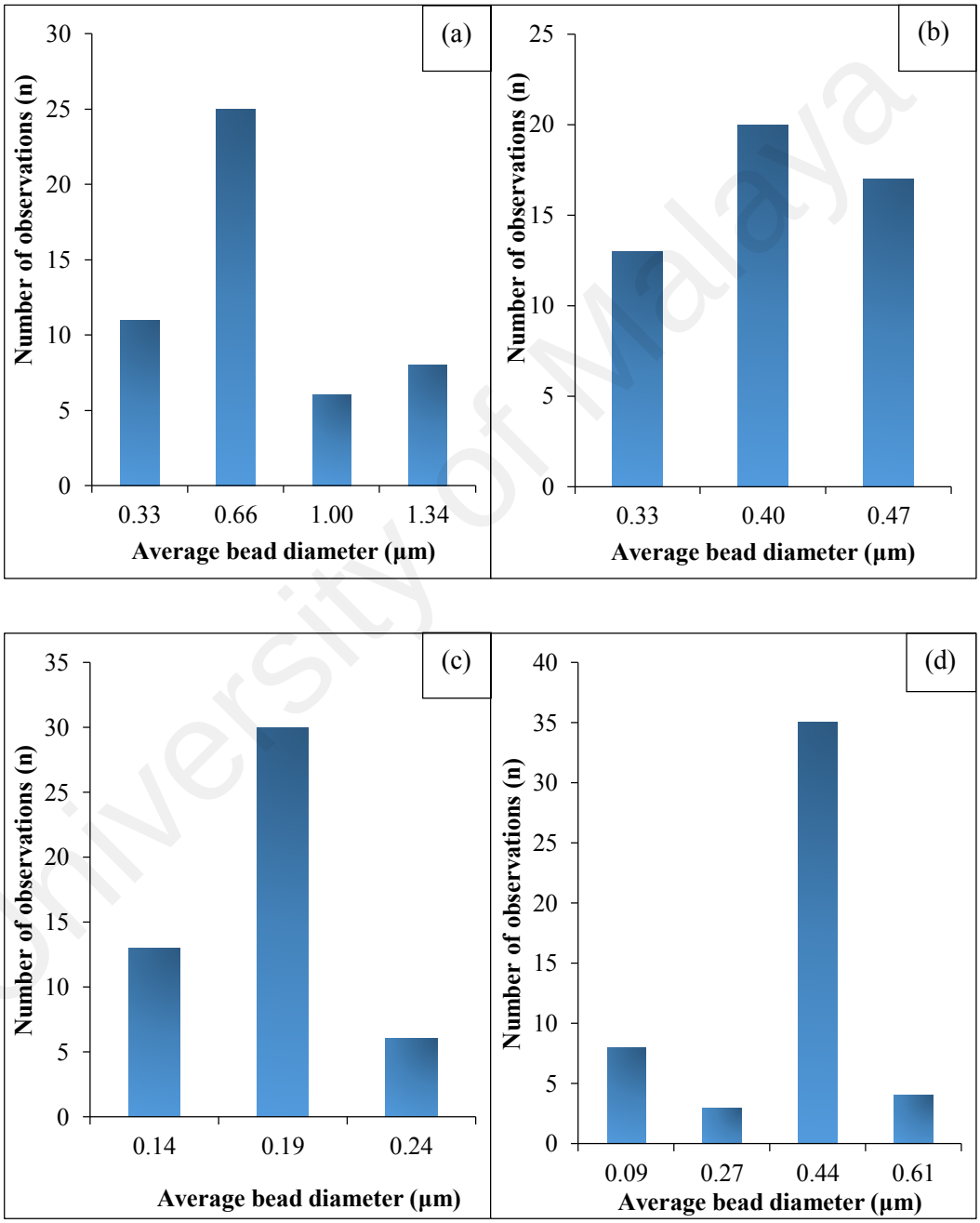

Figure 5.6: Histogram showing the size distribution of average bead diameter for PVP-TiO_2 electrospun fibers as function of different applied voltages (a) 17 kV (NF5-2), (b) 18 kV (NF5-3), (c) 19 kV (NF5-4), (d) 21 kV (NF5-6) and (e) 22kV (NF5-7).

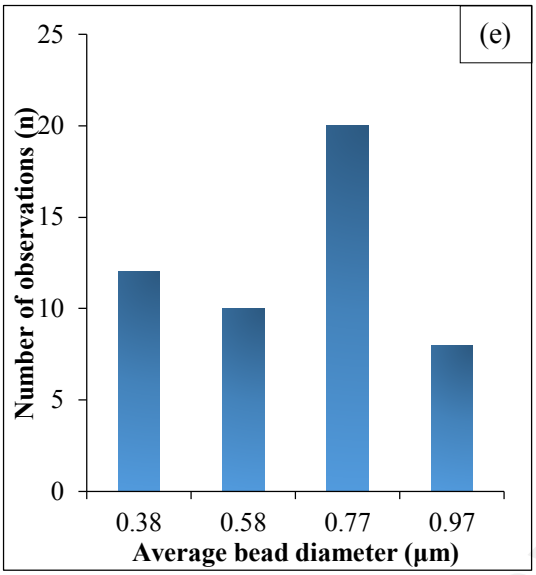

Figure 5.6, continued.

Table 5.2 summarizes the relationships between average fiber and bead diameters of the PVP-TiO_2 with respect to applied voltage and electric field. Different voltages were applied which were 16, 17, 18, 19, 20, 21 and 22 kV with fixed 14 cm distance. This gives an electric field between 1.14, 1.21, 1.29, 1.36, 1.43, 1.50 and 1.57 kV/cm. From the Table 5.2, it can be justified that applied voltage significantly influenced the electrospun fiber morphologies in terms of fiber and bead diameters. At lower applied voltage of 16 kV with electric field of 1.14 kV/cm, flat fibers were formed. The appearance of this structure is disregarded. By increasing the voltage to 17 kV (electric field of 1.21 kV/cm), the fiber morphology significantly changed from flat fiber to more cylindrical fibers with bead formations. The average fiber and bead diameters were 167 nm and 0.66 µm, respectively. Increased the voltage to 18 kV, the average fiber diameters increased to 301 nm and average bead diameters of 0.40 µm.

Further increased of voltage up to 19 kV with 1.36 kV/cm electric field, resulted in decreased in average fiber and bead diameters of 283 nm and 0.19 µm, repectively. Finally, at optimum voltage of 20 kV (electric field of 1.43 kV/cm), the bead-free uniform cylindrical nanofibers were successfully formed with fiber diameter of 177 nm.

On further increase of applied voltage to 22 kV with 1.57 kV/cm electric field, resulted in more fibers having average fiber diameters of 223 nm and bigger beads of 0.77 μm. It can be summarized that increasing applied voltage resulted in decreased fiber and bead diameters. The applied voltage of 20 kV (1.43 kV/cm), designated as NF5-5 sample was selected as the best option for further electrospinning process since electrospun fibers at this applied voltage successfully produced non-beaded membranes with uniform cylindrical fibers. These electrospun mat was further calcined to form TiO_2 nanorods.

Table 5.2: Experimental results on the effects of different applied voltages (kV) and electric field on fiber morphology.

Designation	Applied voltage (kV)	Electric field (kV/cm)	Average diameter with highest number of observations		Fiber Morphology
			Fiber (nm)	Bead (μm)	
NF5-1	16	1.14	-	-	Flat fiber
NF5-2	17	1.21	167	0.66	Beaded fiber
NF5-3	18	1.29	301	0.40	Beaded fiber
NF5-4	19	1.36	283	0.19	Beaded fiber
NF5-5	20	1.43	177	-	Beadless cylindrical fiber
NF5-6	21	1.50	332	0.44	Beaded fiber
NF5-7	22	1.57	223	0.77	Beaded fiber

5.3 Morphological Studies On Electrospun TiO_2 Nanorods

In the subsequent procedure, the bead free uniform cylindrical PVP-TiO_2 nanofiber membranes obtained using 13.2 wt.% PVP concentration, electrospun at 20 kV voltage with 14 cm working distance (1.43 kV/cm electric field) and 1 mL/h flow rate were further subjected to different calcination temperatures in order to produce anatase TiO_2 nanorods. The anatase TiO_2 nanorods were used as semiconductor material with commercial TiO_2 nanoparticles for production of composite electrode in DSSC application. The calcination temperature is another important parameter to affect the

morphologies and size distribution of the TiO_2 nanorods. The TiO_2 nanorods were obtained by mechanically grinding the calcined TiO_2 nanofibers. In this study, different calcination temperatures of 400, 500 and 600 ℃ at 2 ℃/min heating rate for 5 h duration were used in order to analyze the effects of calcination temperatures on the morphology of the TiO_2 nanorods. The morphology of TiO_2 nanorods were examined using FESEM. Figure 5.7 (a) displays the FESEM images of P25 commercial TiO_2 nanoparticles. Figure 5.7 (b) until (d) depict FESEM morphologies of TiO_2 nanorods obtained from calcination temperatures of 400, 500 and 600 ℃. Based on FESEM figures, the P25 commercial TiO_2 nanoparticles showed small spherical shapes. The morphology of electrospun TiO_2 nanorods after calcined at different temperatures of 400 to 600 ℃ followed by mechanical grinding showed rod-like structures with no significant change in shape. It could also be observed that the agglomeration of nanorods occurred. The nanorods calcined at 500 ℃ exhibited well-distinguished nearly uniform rod-like structure with narrow size distribution. It can also be noted that there were changes in diameter of nanorods with different calcination temperature. Further morphologies observations were performed on the resultant nanorod diameter by randomly calculating the diameter using image J software.

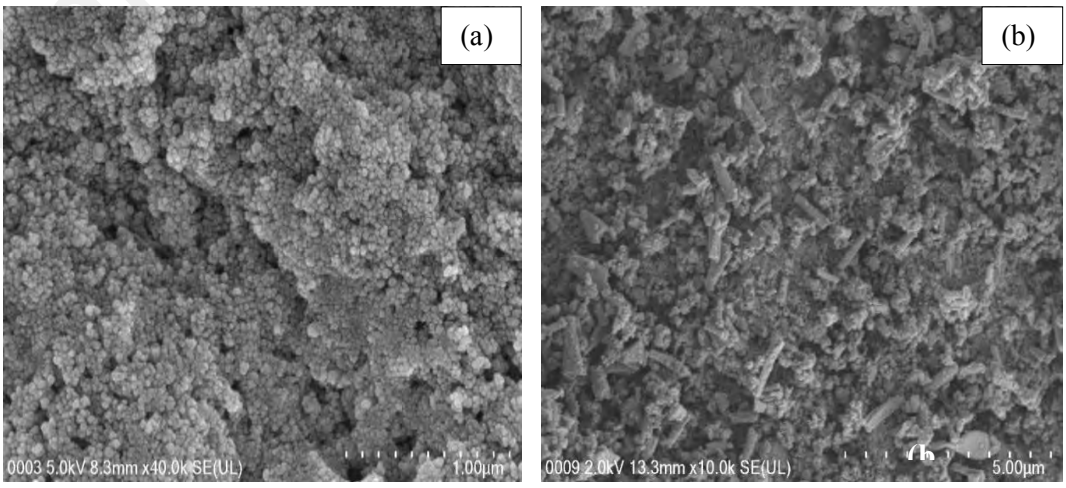

Figure 5.7: FESEM images of (a) commercial TiO_2 nanoparticles and TiO_2 nanorods after calcination at (b) 400, (c) 500 and (d) 600 ℃.

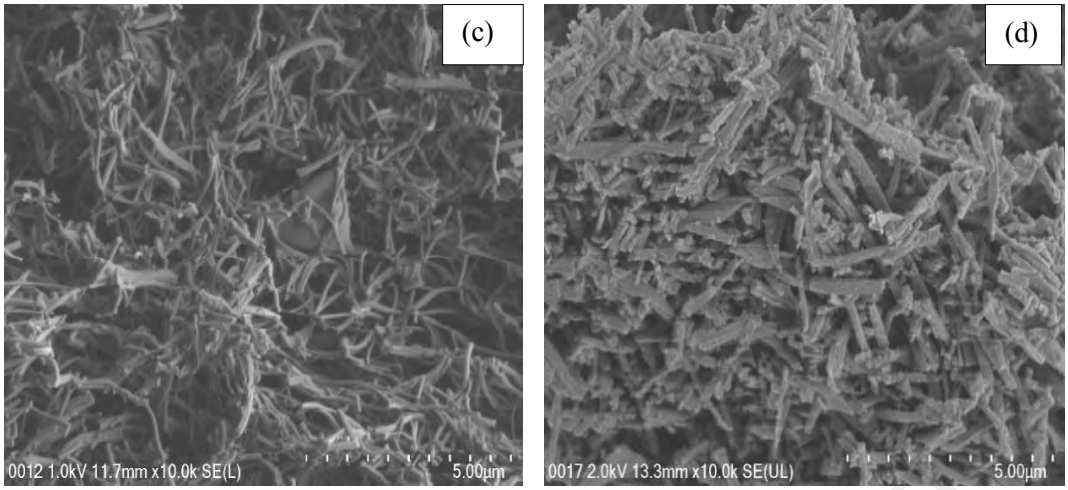

Figure 5.7, continued.

The respective nanorod diameter was plotted in a histogram format shown in Figure 5.8 (a) until (c). Within the same heating rate of 2 ℃/min, the average diameter distributions were calculated for three different temperatures. For the nanorods calcined at 400 ℃, the average nanorod diameter was in the range of 80 to 291 nm with most of nanorods having average diameter of 130 nm as can be observed in Figure 5.8 (a). It can be noticed in Figure 5.8 (b) that the average nanorods diameter calcined at 500 ℃, ranged between 58 and 286 nm. Majority of the nanorods had average diameter of 90 nm.

Figure 5.8 (c) showed the average nanorod diameter after calcined at 600 ℃ with highest number of nanorods having average diameter of 135 nm. The range was from 96 to 300 nm. As reported earlier, the highest average diameter of electropinning PVP-TiO_2 nanofiber before calcinations was 177 nm. After calcination, the average diameter of TiO_2 nanorods have decreased to 130, 90 and 135 nm as displayed in Figure 5.8 for applied temperature of (a) 400, (b) 500 and (c) 600 ℃.

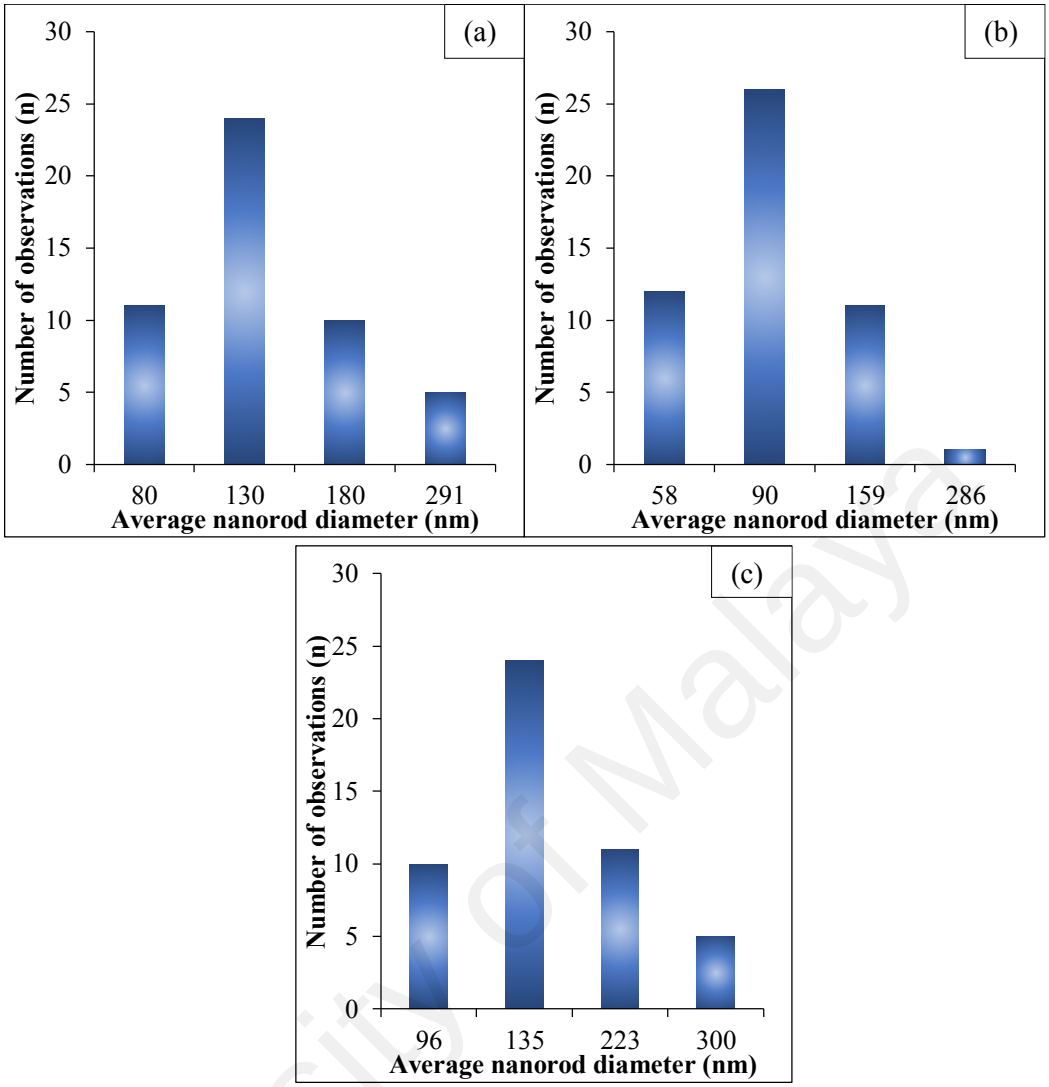

Figure 5.8: Histogram showing the size distribution of nanorod diameter for different calcination temperature (a) 400 (b) 500 and (c) 600 ℃ at heating rate of 2 ℃/min.

5.4 Elemental Analysis of TiO_2 Nanorods

Figure 5.9 shows the energy-dispersive analysis of x-rays (EDX) of the calcined TiO_2 nanorods. The EDX spectra was recorded as a function of binding energy from 0 to 20 keV as shown in Figure 5.9. The EDX data of TiO_2 nanorods showed several peaks around 0.4, 0.5, 4.5 and 4.9 keV attributed to Ti and O. There was no traces of impurities within the detection limit of the EDX instrument, indicating that the final product of calcined TiO_2 nanorods is pure TiO_2 compound. The peak around 0.1 keV is the baseline peaks while peak around 2.1 keV attributed to the platinum (Pt) since the nanorod

samples were sputtered with Pt to avoid any possible charging effect during EDX analysis.

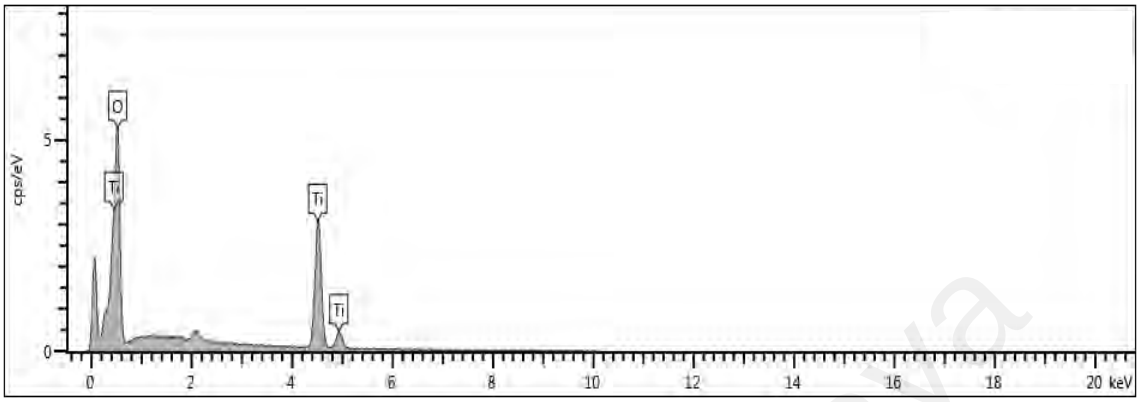

Figure 5.9: Energy dispersive x-ray (EDX) spectra of TiO_2 nanorods.

5.5 X-Ray Diffraction (XRD) Analysis of Electrospun TiO_2 Nanorods

TiO_2 can be divided into phases of anatase, brookite and rutile. TiO_2 nanofibers produced via electrospinning technique were calcined at different temperatures followed with grinding in order to obtain TiO_2 nanorods. Anatase dominant TiO_2 nanorods will be use to form composite electrode on mixing with P25 commercial TiO_2 nanoparticles for DSSCs. XRD patterns were analyzed using Origin 9.0 software. Figure 5.10 depicts the XRD patterns of TiO_2 nanorods which were calcined at 400, 500 and 600 ℃ for 5 h at heating rate of 2 ℃/min. XRD results indicate well-defined diffraction peaks of electrospun TiO_2 nanorods consisting mixed anatase and rutile phases. In the XRD spectra based on Figure 5.10, peaks noted as A and R are assigned to the anatase and the rutile phase, respectively. The brookite phase was not detected. Based on Figure 5.10, the anatase peaks (JCPDS Card No.21-1272) were inferred to originate from the lattice planes at 2θ angles of 25.5, 37.2, 37.9, 38.8, 48.2 and 54° representing the planes of (101), (103), (004), (200) (112) and (211), respectively. For the rutile phase (JCPDS Card No.21-1276), peaks were detected at 2θ angles of 27.6, 36.1, 41.2, 44 and 54.3°. These represent the reflection planes of (110), (101), (111) and (210), respectively. The

diffraction peak with the highest intensity was at 2θ = 25.5° of the (101) plane corresponding to the TiO_2 anatase phase, as can be evidently deduced from Figure 5.10 (a), (b) and (c). To further confirm the phase of TiO_2 nanorods, the percentages of anatase and rutile phase for each temperature were calculated and listed in Table 5.3. TiO_2 nanorods calcined at 500 ℃ containing highest anatase percentages ~91.97% while ~8.03% of rutile, followed with nanorods calcined at 400 ℃ which contained almost 88.68 and 11.32% of anatase and rutile, respectively. TiO_2 nanorods calcined at 600 ℃ exhibited to the lowest percentage of anatase ~73.20% while ~26.8% of rutile. Thus, by controlling the calcination temperature at 500 ℃ for 5 h, it is possible to obtain crystalline phases with dominant anatase structures. This calcination temperature was selected for the production of electrospun TiO_2 nanorods that served as semiconductor material in composite photoanode for DSSC application. DSSC results will be discussed in the next chapter.

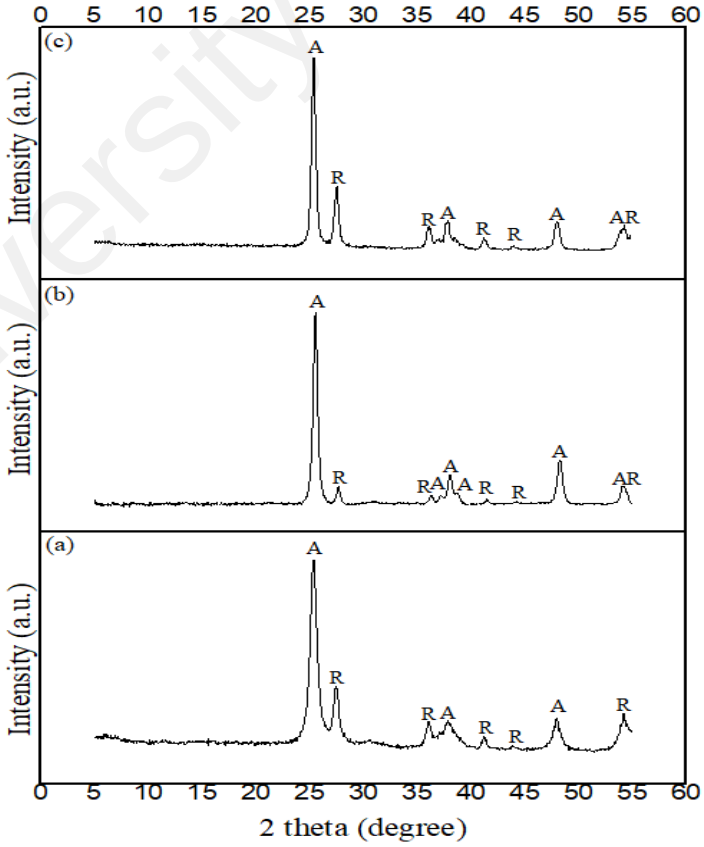

Figure 5.10: X-ray diffraction patterns of TiO_2 nanorods after calcination temperatures of (a) 400, (b) 500 and (c) 600 ℃ at 2 ℃/min heating rate for 5 h.

Table 5.3: Percentages of anatase and rutile phase for the TiO_2 nanorods prepared at different calcination temperatures.

Calcination temperature (°C)	Anatase (%)	Rutile (%)
400	88.68	11.32
500	91.97	8.03
600	73.20	26.80

5.6 Morphology Studies on Composite of TiO_2 Nanoparticles (NPs) With Nanorods (NRs)

Two different TiO_2 forms, P25 commercial nanoparticles (NPs) and nanorod (NRs) were used for preparing five TiO_2 composite electrodes (NP-NR). Different addition of TiO_2 NRs (10, 20, 30, 40 and 50 wt.%) produced from electrospinning method were incorporated into the P25 commercial NPs for preparation of TiO_2 slurry, respectively and were coated onto the FTO glass (which was already spin-coated with P90 commercial TiO_2 NP) using the doctor blade technique. These composite electrodes were labelled as CP1, CP2, CP3, CP4 and CP5. Figure 5.11 shows the FESEM morphology of TiO_2 films prepared using P25 commercial TiO_2 nanoparticles and TiO_2 nanorods at different magnifications. Clearly, a spherical particle-like surface in the film is prepared using commercial TiO_2 NPs versus a nanorod-shape surface in the film prepared by our NRs. Figure 5.11 (a) shows the FESEM image of (a) CP1, (b) CP2, (c) CP3, (d) CP4 and (e) CP5 electrodes. As depicted by the FESEM images of composite electrodes, it can be observed that there were increased in distribution of TiO_2 nanorods from CP1 (10 wt.%) to CP5 (50 wt.%) and the nanorods were quite evenly dispersed. It is obvious that CP4 and CP5 composite electrodes clearly detected TiO_2 nanorods. There were few voids and porous structure noticed for all composite electrodes.

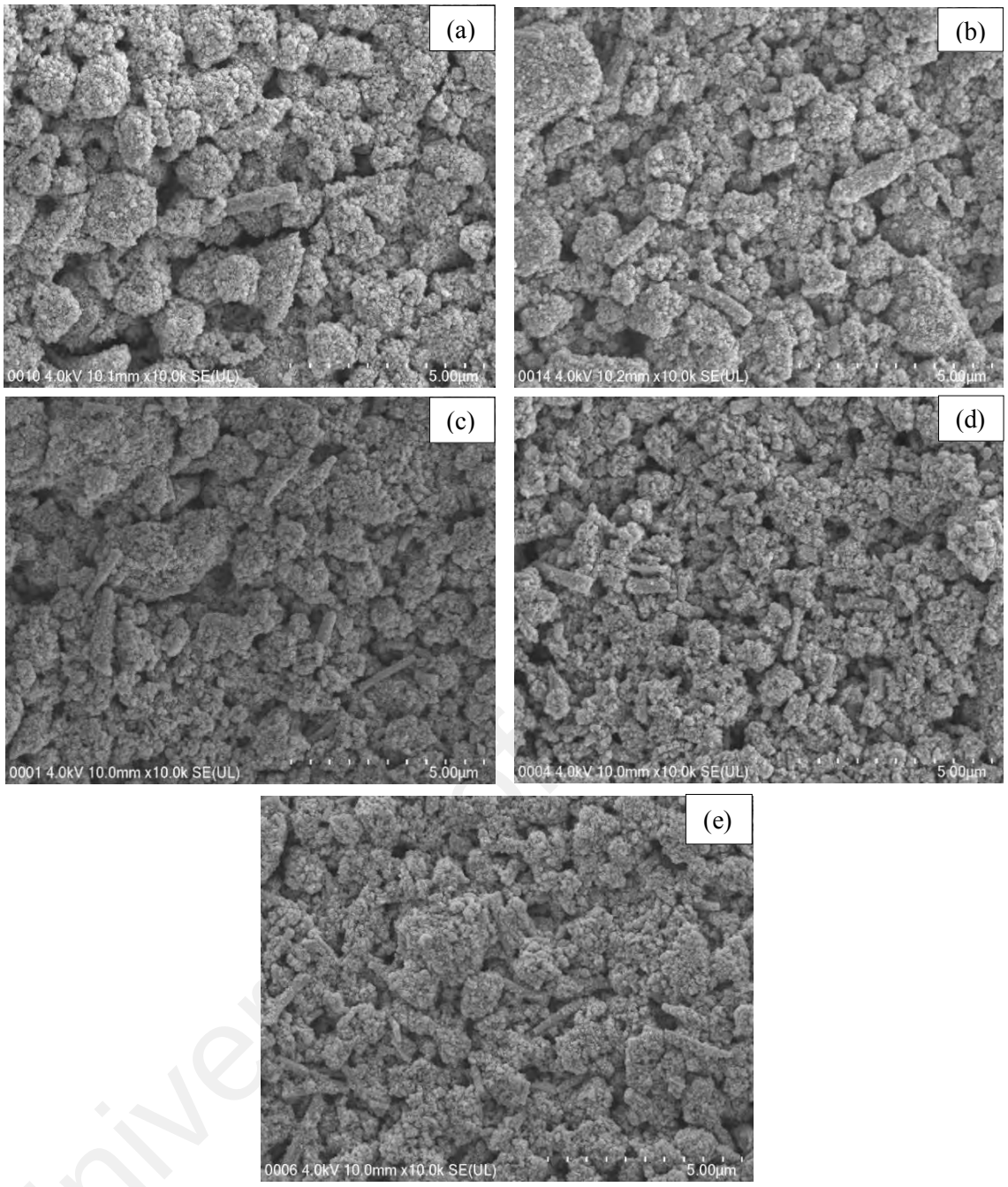

Figure 5.11: FESEM images of composite electrode with different nanorod compositions (a) 10 wt.% NR (CP1), (b) 20 wt.% NR (CP2), (c) 30 wt.% NR (CP3), (d) 40 wt.% NR (CP4) and (e) 50 wt.% NR (CP5).

5.7 Summary

In this chapter, the surface morphology of the synthesized TiO_2 nanofibers from electrospinning process were determined using FESEM. The effects of polymer concentration and applied voltage on the formation of nanofibers were determined. TiO_2 nanofibers designated as NF5-5 with 13.2 wt.% PVP and electrospun at 20 kV exhibited

non-beads uniform cylindrical nanofibers. Further sintering and grinding process produced the morphology of TiO_2 nanorods. Sintering temperature at 500 ℃ with 2 ℃/min heating rate was considered as the suitable temperature to obtain the TiO_2 anatase phase as proven from EDX and XRD analysis. The different morphology for composite photoanodes of TiO_2 nanoparticles-nanorods (NPs-NRs) were observed using FESEM for different composition of NRs.

CHAPTER 6: RESULTS FOR DSSCS APPLICATIONS

6.1 Introduction

The optimized extraction parameters from RSM analysis that exhibited the highest yield of anthocyanin content have been used to extract anthocyanin dyes as the source of natural sensitizer. 1-D TiO_2 nanorods obtained from combining sol-gel and electrospinning method followed with sintering and grinding process were mixed with TiO_2 nanoparticles (P25) and used to form the mesoporous layer in the composite photoanode DSSC system. The properties of these natural sensitizer and semiconductor materials have been analyzed in the previous chapters. The composite DSSCs system were fabricated to improve performance of the DSSC utilizing only P25 TiO_2 as the photoanode mesoporous layer. To determine if the performance can be further improved, chenodeoxycholic acid (CDCA) and ferulic acid (FA) as additives were added to the anthocyanin dye solution. In this chapter, three types of DSSC systems have been fabricated and investigated: 1) DSSC system with P25 TiO_2 photoanode containing different anthocyanin dye contents, 2) composite DSSC with photoanode containing different ratios of TiO_2 nanorods (NRs) and P25 TiO_2 nanoparticles (NPs) with optimized dye percentage and 3) composite DSSC with different additive contents.

6.2 Effect of *Ixora siamensis* Anthocyanin Dye Concentration on Commercial (NPs) DSSCs System

6.2.1 Visible spectroscopy studies for different concentration of anthocyanin dye extract

Figure 6.1 shows the visible spectroscopy of five different percentages (1, 2, 3, 4 and 5 wt.%) of the anthocyanin extract from *Ixora siamensis*. The absorption spectrum of anthocyanin for fruit pericarp of *Ixora siamensis* anthocyanin extraction displayed a broad absorption in the visible light from 400 to 600 nm, with a maximum peak at

wavelength, λ= 522 nm. It can be clearly noticed that the maximum absorption peak of the anthocyanin solution increased from 0.72 to 0.98 with increasing of weight percentage dyes from 1 wt.% until 3 wt.%, respectively. However, beyond 3 wt.%, the maximum absorption decreased from 0.67 to 0.56 observed for 4 and 5 wt.%, respectively. 3 wt.% of anthocyanin content exhibited the highest absorption peak of 0.98 at wavelength 522 nm hence indicates higher visible absorption.

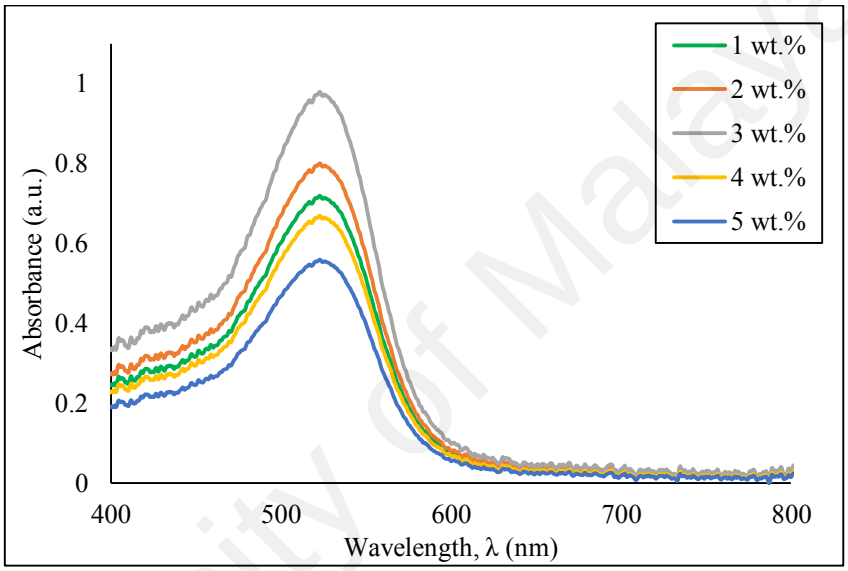

Figure 6.1: The absorption spectra of anthocyanin extract from *Ixora siamensis* at different weight percentages (1, 2, 3, 4 and 5 wt.%).

The prepared P25 TiO_2 electrodes were immersed into a solution containing different weight percentages (1, 2, 3, 4 and 5 wt.%) of anthocyanin extract, designated as D1, D2, D3, D4 and D5. Figure 6.2 shows the absorption spectra of anthocyanin adsorbed onto the TiO_2 electrode surface after immersion into each dye solution. It can be seen that the absorption spectra of anthocyanin dyes increased from 0.48 to 0.66 with increasing dye concentration from 1 (D1) until 3 wt.% (D3) before decreasing at D4 with 4 wt.% (0.43) up to D5 with 5 wt.% (0.39). The intensity of absorbance at wavelength 525 nm for the pigmented TiO_2 electrodes were highest at 0.66 (D3) after immersion into 3 wt.% of anthocyanin dye solution. A shift of anthocyanin/TiO_2 electrode absorption band towards

higher wavelength compared to anthocyanin extract solution from 522 to 525 nm was also observed.

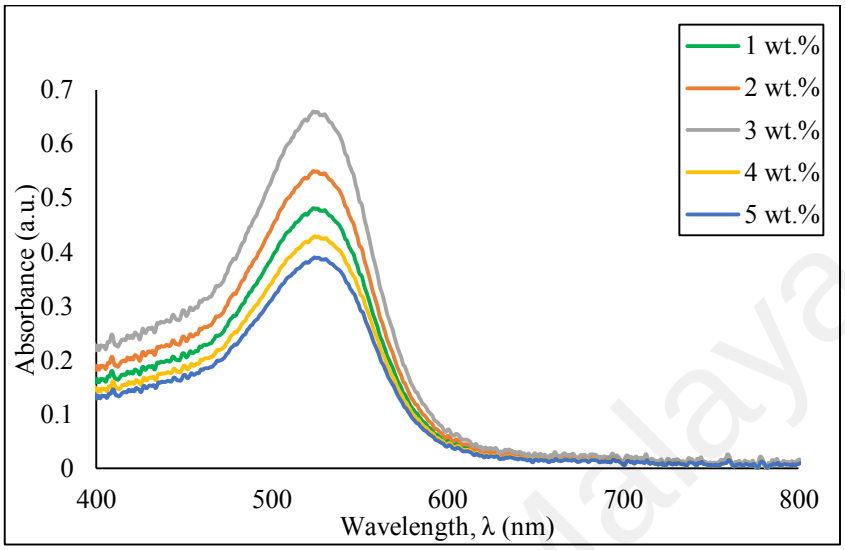

Figure 6.2: The absorption spectra of pigmented TiO_2 electrodes at different weight percentages (1, 2, 3, 4 and 5 wt.%) of anthocyanin dyes.

6.2.2 *J-V* characterization of DSSCs sensitized at different weight percentages of anthocyanin dye extract

Photocurrent density versus cell potential (*J-V*) analysis was used to characterize the DSSCs after immersed for 24 h at different anthocyanin contents. *J-V* characteristics of FTO/P25 TiO_2 nanoparticles (NPs) sensitized at different percentages (1, 2, 3, 4 and 5 wt.%) of anthocyanin sensitizer are illustrated in Figure 6.3. The DSSCs were illuminated under 1000 Wm^{-2} or 1 sun at room temperature. The purpose of this study is to study the relationship between dye concentration and the efficiency performance. Using the *J-V* characteristic curves shown in Figure 6.3, the short-circuit current density (J_{sc}), open-circuit voltage (V_{oc}), fill factor (FF), power conversion efficiency (η), series resistance (R_s) and shunt resistance (R_{sh}) were calculated for all the DSSCs and the values with standard deviation were listed in Table 6.1. Based on the result, the solar conversion efficiency of DSSCs based anthocyanin increased with increasing anthocyanin dye

content from 1 (D1) to 3 wt.% (D3) before efficiency decreased until 5 wt.% (D5). DSSCs with 3 wt.% (D3) anthocyanin dye exhibited a maximum solar conversion efficiency of (1.076 ± 0.042)% while the lowest efficiency was exhibited by the DSSC with 5 wt.% (D5) anthocyanin with efficiency value of (0.563 ± 0.073)%. It can be observed that the short circuit density, J_{sc} increased accordingly with an increased in efficiency as in Table 6.1. J_{sc} value from (3.713 ± 0.081) mA cm^{-2} at 1 wt.% increased to a maximum of (4.456 ± 0.101) mA cm^{-2} at 3 wt.% dye. Beyond 3 wt.% of dye, the J_{sc} decreased to (2.660 ± 0.136) mA cm^{-2}, assigned for sample with 5 wt.% anthocyanin. R_s and R_{sh} control the *FF* of DSSC. R_{sh} also increased accordingly with efficiency. R_{sh} increased from (1.643 ± 0.014) Ω-cm^2 to a maximum of (1.904 ± 0.040) Ω-cm^2 at 3 wt.%. Beyond 3 wt.% of dye, the R_{sh} values decreased to (1.480 ± 0.026) Ω-cm^2 at 5 wt.%. In contrast, R_s decreased from (0.028 ± 0.005) Ω-cm^2 to (0.024 ± 0.003) Ω-cm^2 at 3 wt.% of dye. Beyond 3 wt.% of dye, R_s values increased to (0.042 ± 0.003) Ω-cm^2 as observed for 5 wt.% of dyes. It can also be seen that the DSSC based anthocyanin of highest efficiency at 3 wt.% anthocyanin showed the highest R_{sh} values with lowest R_s values.

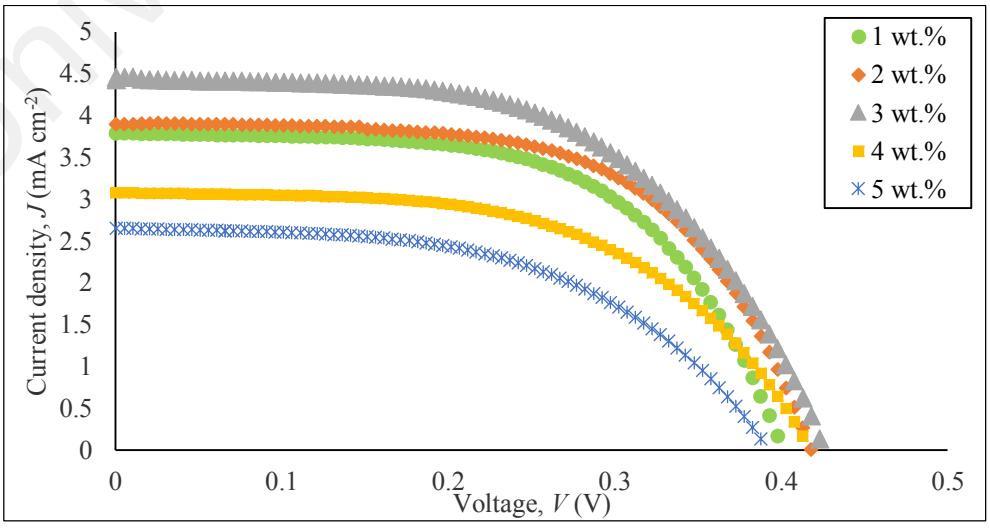

Figure 6.3: *J-V* curve for DSSCs sensitized at different weight percentages (1, 2, 3, 4 and 5 wt.%) of anthocyanin dyes.

Table 6.1: Values of J_{sc}, V_{oc}, FF, η, R_s and R_{sh} for DSSCs sensitized at different weight percentages (1, 2, 3, 4 and 5 wt.%) of anthocyanin dyes.

Wt. (%)	J_{sc} (mA cm^{-2})	V_{oc} (V)	FF	η (%)	R_s (Ω-cm^2)	R_{sh} (Ω-cm^2)
1	3.713 ± 0.081	0.393 ± 0.006	0.564 ± 0.020	0.823 ± 0.020	0.028 ± 0.005	1.643 ± 0.014
2	3.897 ± 0.059	0.418 ± 0.005	0.565 ± 0.012	0.920 ± 0.032	0.025 ± 0.003	1.795 ± 0.019
3	4.456 ± 0.101	0.423 ± 0.006	0.571 ± 0.008	1.076 ± 0.042	0.024 ± 0.003	1.904 ± 0.040
4	3.075 ± 0.088	0.413 ± 0.012	0.570 ± 0.016	0.724 ± 0.036	0.035 ± 0.004	1.529 ± 0.022
5	2.660 ± 0.136	0.388 ± 0.028	0.546 ± 0.015	0.563 ± 0.073	0.042 ± 0.003	1.480 ± 0.026

6.2.3 Incident photon-to-current conversion efficiency (IPCE) characterization at different weight percentages of anthocyanin dye

After *J-V* characterization, the DSSCs were further evaluated with IPCE characterictics. Figure 6.4 depicts the photo-action spectra of the DSSC sensitized with anthocyanin dyes at different weight percentages (1, 2, 3, 4 and 5 wt.%), designated as D1, D2, D3, D4 and D5. It can be revealed that the IPCE plot exhibits a maximum of 20% at 580 nm with 3 wt.% (D3) extract for pigment-sensitized solar cell. The trend followed with samples sensitized with 1 (D1) and 2 wt.% (D2) with IPCE peaks of 12 and 17%, respectively. The IPCE peaks of 4 (D4) and 5 wt.% (D5) pigment-sensitized solar cells showed IPCE peaks of 10 and 9%, respectively. For the *Ixora siamensis* anthocyanin dyes sensitized solar cells, the spectral response showed a shift due to the electronic coupling between anthocyanin dye and TiO_2 structures. Within the light visible range from 500 to 600 nm, the DSSCs sensitized by the anthocyanin dye have better ability to transform light energy into electrical energy. Moreover, the results from the IPCE data are consistent with the results from the visible spectroscopy curves which showed that anthocyanin dye has similar absorption visible light range. The IPCE of the DSSC depends on the incident light harvesting and light scattering (Wang et al*.,* 2004).

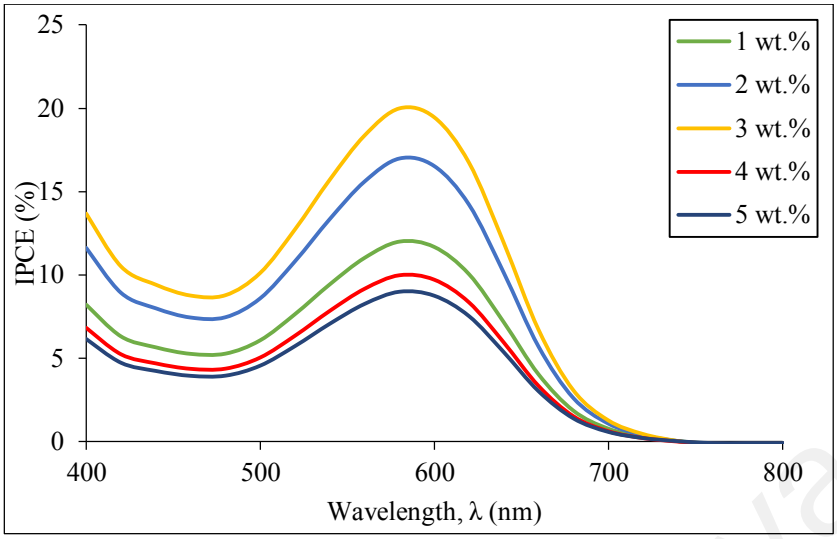

Figure 6.4: IPCE curves for DSSCs sensitized at different weight percentages (1, 2, 3, 4 and 5 wt.%) of anthocyanin dyes.

6.2.4 Electrochemical impedance spectroscopy (EIS) characterization at different weight percentages of anthocyanin dye

Further characterization of DSSCs based anthocyanin at different dye percentages were performed with the electrochemical impedance spectroscopy (EIS) measurement under 1000 Wm^{-2} illumination. The EIS results were fitted based on the equivalent circuit as in Figure 6.5. Typically, three semicircles can be observed in the Nyquist plot. As mentioned in Chapter 3, R_s is the ohmic serial resistance. The first semicircle, R_1 is the resistance of charge transfer at the Pt counter electrode, the second semicircle, R_2 is the resistance of charge transfer at the TiO_2/dye/electrolyte interface and the third semicircle, R_3 is ionic diffusion resistance in the electrolyte (Sarker et al., 2014). Figure 6.6 shows the EIS analysis in the DSSCs system of TiO_2 nanoparticles sensitized with different anthocyanin dye percentages (1, 2, 3, 4 and 5 wt.%). The fitted graph also included for each graph as displayed in Figure 6.6. The R_s, R_1, R_2, R_3 values calculated for the DSSCs based anthocyanin at different percentages with standard deviation are tabulated in Table 6.2. Since other resistances are not affected by the use of different dye percentages, we focused on the differences in R_2 which represented as the second semicircle. Increasing

the dye percentages from 1 (D1) to 3 wt.% (D3) directly decreased R_2 values from (90.00 ± 0.12) Ω to (66.50 ± 0.12) Ω, respectively before decreased up to 5 wt.% (D5). The decrement is almost 26%. The R_2 values of (66.50 ± 0.12) Ω for the cell with 3 wt.% of anthocyanin dyes is the lowest while cell with 5 wt.% of anthocyanin dyes exhibited the maximum R_2 values of (97.20 ± 0.14) Ω. R_2 influenced the overall DSSC cell performance. As predicted, the lowest R_2 correlated with highest efficiency performance. The highest efficiency solar cell with lowest R_2 that corresponded to the DSSC with 3 wt.% dye (D3) was chosen to further enhance the DSSC performance by incorporating TiO_2 nanorods in the mesoporous TiO_2 nanoparticles.

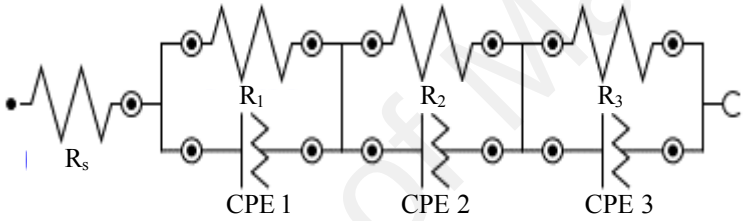

Figure 6.5: Equivalent circuit for experimental data fitting.

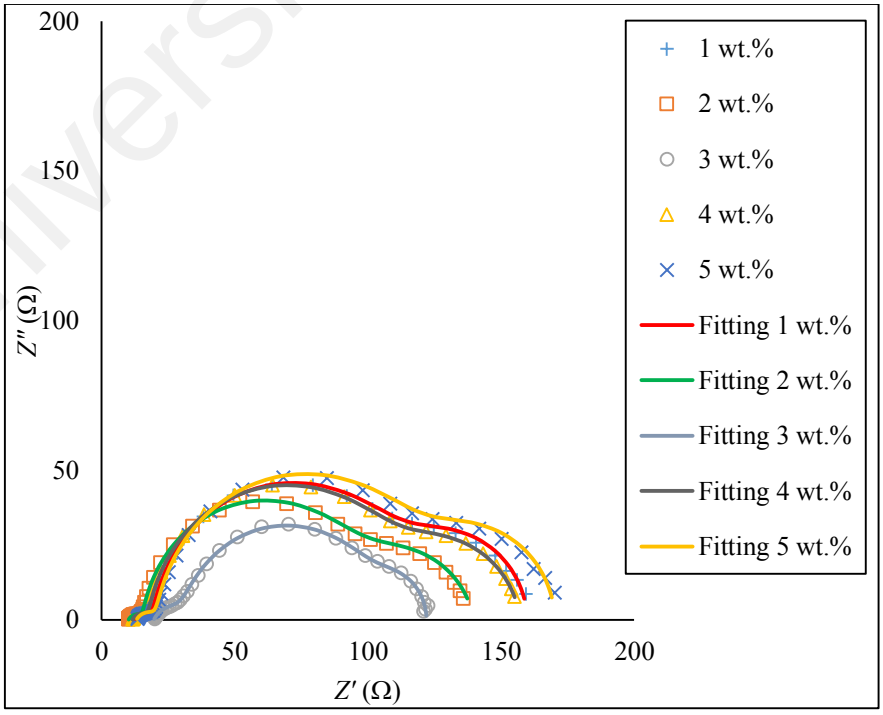

Figure 6.6: EIS for DSSCs based anthocyanin sensitized at different weight percentages (1, 2, 3, 4 and 5 wt.%) of dyes.

Table 6.2: R_s, R_1, R_2, R_3 values for DSSCs based anthocyanin sensitized at different weight percentages (1, 2, 3, 4 and 5 wt.%) of dyes.

Wt.%	R_s (Ω)	R_1 (Ω)	R_2 (Ω)	R_3 (Ω)
1	12.46 ± 0.10	7.08 ± 0.08	90.00 ± 0.12	50.00 ± 0.07
2	10.12 ± 0.07	10.25 ± 0.08	81.58 ± 0.10	22.40 ± 0.06
3	19.85 ± 0.07	10.85 ± 0.07	66.50 ± 0.12	22.40 ± 0.06
4	11.71 ± 0.09	6.14 ± 0.11	85.00 ± 0.13	38.40 ± 0.12
5	13.00 ± 0.12	8.00 ± 0.09	97.20 ± 0.14	53.0 ± 0.09

6.3 Effect of Different Percentage of TiO_2 Nanorods on Composite (NPs-NRs) DSSCs System

6.3.1 Visible spectroscopy studies for different weight percentages of TiO_2 nanorods (NPs-NRs)

For the second DSSC systems, five different amounts of TiO_2 nanorod (NR) (10, 20, 30, 40 and 50 wt.%) were incorporated into the mesoporous TiO_2 nanoparticles (NPs) to form composite electrode of TiO_2 NPs-NRs, designated as CP1, CP2, CP3, CP4 and CP5. As mentioned before, 3 wt.% of anthocyanin dyes were used as sensitizer in second DSSC systems since it exhibited the highest efficiency of (1.076 ± 0.042)% in the first DSSC systems. Figure 6.7 shows the absorption spectra of anthocyanin adsorbed onto the TiO_2 composite electrode after immersion into the dye solution. The absorption spectrum for pigmented composite electrode with anthocyanin extract from fruit pericarp of *Ixora siamensis* showed a peak at wavelength, λ= 525 nm. From the figure, it can be observed that the highest absorption of pigmented composite electrodes achieved by CP1 samples with 10 wt.% addition of NRs. This composite electrode showed a slight increase in absorption intensity of 0.72 compared to the DSSC with P25 TiO_2 in the photoanode (0.66), i.e. ~9% increment. This means that the composite electrode can absorb more anthocyanin dye compared to P25 electrode. However, as the NR percentage increased from 20 to 50 wt.% represented by CP2, CP3, CP4 and CP5, the absorption intensity continuously decreased.

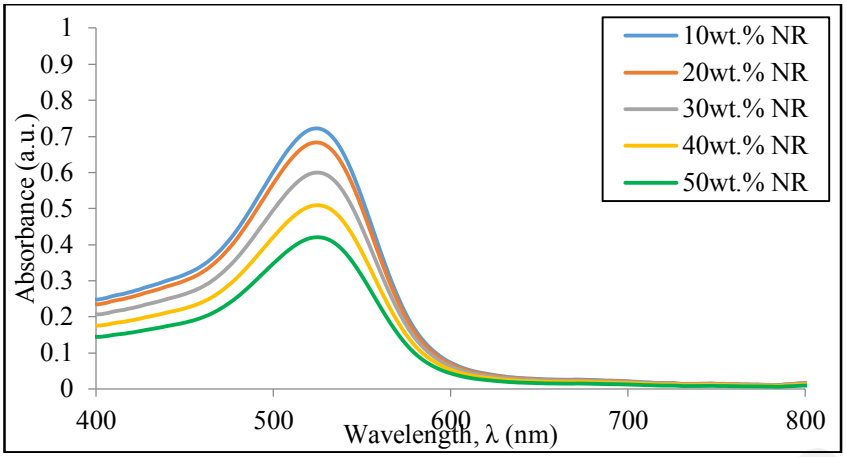

Figure 6.7: The absorption spectra of composite electrodes based on different percentages (10, 20, 30, 40 and 50 wt.%) of TiO_2 nanorods sensitized at 3 wt.% of anthocyanin dyes.

6.3.2 *J-V* characterization of DSSCs containing different weight percentages of TiO_2 nanorods

DSSCs with various percentages of TiO_2 NRs (10, 20, 30, 40 and 50 wt.%) that were immersed for 24 h into the 3 wt.% anthocyanin dye were illuminated under 1000 W m^{-2} at room temperature. The aim of this study was to investigate the effect of adding TiO_2 nanorods on the DSSC efficiency. *J-V* curves of the second system are plotted in Figure 6.8. The J_{sc}, V_{oc}, FF, η, R_s and R_{sh} values are tabulated in Table 6.3. There were significant enhancement observed for J_{sc} and η values owing to incorporation of TiO_2 nanorods. The DSSC made using the composite with 10 wt.% NR addition, designated as CP1 exhibited the highest J_{sc} of (4.808 ± 0.105) mA cm^{-2} and efficiency (η) of (1.317 ± 0.035)%. The R_{sh} value observed also increased to (2.179 ± 0.042) Ω-cm^2 with lower R_s values at (0.019 ± 0.002) Ω-cm^2 as seen in Figure 6.8 and Table 6.3. However, when increasing the percentages of TiO_2 nanorods from 20 (CP2) to 50 wt.% (CP5), the J_{sc}, η and R_{sh} values decreased continuously, as seen in Table 6.3. In contrast, the R_s value is observed to increase continuously from sample CP2 to CP5. The DSSC made using the commercial TiO_2 NPs in previous results had J_{sc}, η values of (4.456 ± 0.101) mA cm^{-2}

and (1.076 ± 0.042)%, respectively. As compared to DSSC with 10 wt.% NR, there were ~8% improvement in J_{sc} value while ~22% increase in η values. The result revealed that inclusion of 10 wt.% NR is sufficient to improve the second DSSC systems.

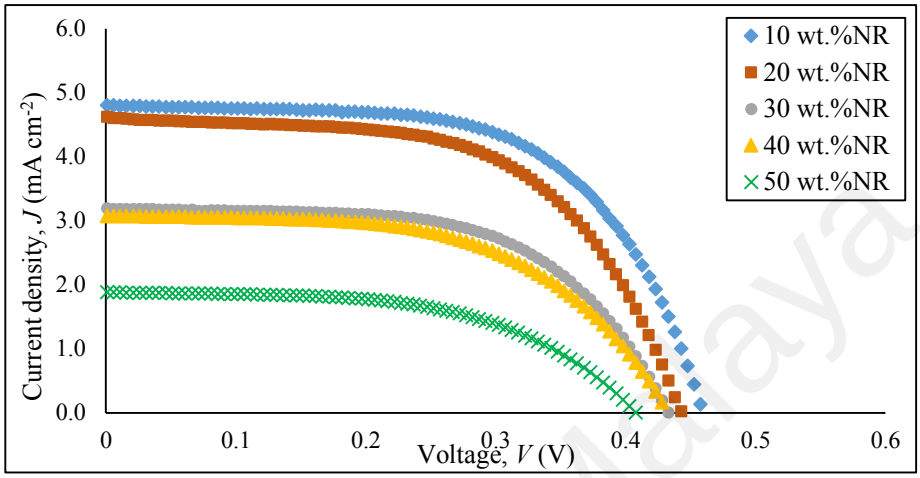

Figure 6.8: *J-V* curve for composite DSSCs fabricated from TiO_2 nanoparticle-nanorod samples with nanorod percentages of 10, 20, 30, 40 and 50 wt.% sensitized at 3 wt.% anthocyanin dyes.

Table 6.3: J_{sc}, V_{oc}, *FF*, η, R_s and R_{sh} values for composite DSSCs fabricated from TiO_2 nanoparticle-nanorod samples with nanorod percentages of 10, 20, 30, 40 and 50 wt.% sensitized at 3 wt.% anthocyanin dyes.

Wt. (%)	J_{sc} (mA cm^{-2})	V_{oc} (*V*)	*FF*	η (%)	R_s (Ω-cm^2)	R_{sh} (Ω-cm^2)
10	4.808 ± 0.105	0.458 ± 0.003	0.599 ± 0.005	1.317 ± 0.035	0.019 ± 0.002	2.179 ± 0.042
20	4.548 ± 0.095	0.443 ± 0.006	0.550 ± 0.005	1.108 ± 0.019	0.022 ± 0.001	1.587 ± 0.021
30	3.198 ± 0.102	0.438 ± 0.008	0.546 ± 0.006	0.765 ± 0.032	0.033 ± 0.001	1.458 ± 0.022
40	3.080 ± 0.096	0.437 ± 0.021	0.534 ± 0.019	0.719 ± 0.034	0.034 ± 0.002	1.388 ± 0.030
50	1.890 ± 0.131	0.408 ± 0.028	0.533 ± 0.015	0.411 ± 0.048	0.046 ± 0.002	1.292 ± 0.012

6.3.3 Incident photon-to-current conversion efficiency (IPCE) characterization at different weight percentages of TiO_2 nanorods

Further investigation on the effects of TiO_2 nanorods were performed by carrying the incident photon to current conversion efficiency (IPCE) analysis after *J-V*

characterization. The IPCE spectra of the composite photoanode made up of different percentages of TiO_2 nanorods (NRs) (10, 20, 30, 40 and 50 wt.%), designated as CP1, CP2, CP3, CP4 and CP5 are shown in Figure 6.9. These composite photoanodes were sensitized with dye percentage of 3 wt.%. Previously, the IPCE of commercial DSSC system sensitized with 3 wt.% of anthocyanin dye exhibited a maximum of 20% at 580 nm. The NP-NR composite photoanode revealed higher IPCE values compared to DSSC with P25 TiO_2. This is compatible with the J_{sc} value obtained by photocurrent-voltage measurement. In order to estimate the light scattering effect, the NP-NR composite electrode showed higher IPCE values in the long wavelength region around 600-700 nm, suggesting that the NP-NR composite electrode provided an appreciable light scattering effect (Hong et al., 2014). The IPCE peak for the CP1 electrode with 10 wt% of NRs showed the highest photon to current conversion efficiency of 25% at higher wavelength 600 nm. This value is much higher than that obtained for commercial sample without NR composite (NPs electrode), a ~25% increment. The IPCE peak for other composite electrodes continuously decreased with increasing of nanorod percentages in which the values were 18%, 14%, 10%, 7%, achieved by the CP2 (20 wt.%), CP3 (30 wt.%), CP4 (40 wt.%) and CP5 (50 wt.%) samples, respectively.

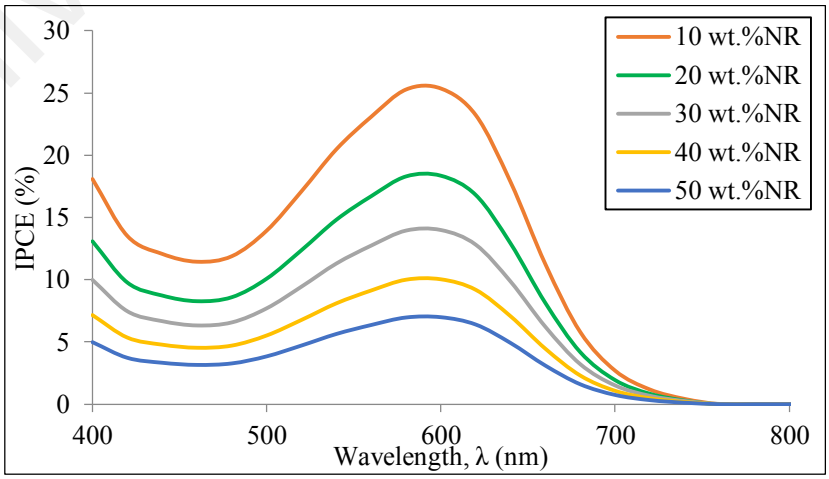

Figure 6.9: IPCE curves for composite DSSCs fabricated from TiO_2 nanoparticle-nanorod samples with nanorod percentages of 10, 20, 30, 40 and 50 wt.% sensitized at 3 wt.% anthocyanin dyes.

6.3.4 Electrochemical impedance spectroscopy (EIS) characterization at different weight percentages of TiO_2 nanorods

The EIS studies were performed when illuminated under 1000 Wm^{-2} to examine whether different amounts of TiO_2 nanorods (NRs) incorporated into conventional P25 TiO_2 nanoparticles may enhance the charge transport properties. Figure 6.10 displays the Nyquist and fitting plots of the fabricated composite DSSCs at various nanorods weight ratios (10, 20, 30, 40 and 50 wt.%) sensitized with 3 wt.% anthocyanin dye. R_s, R_1, R_2, R_3 were calculated for the composite DSSCs and the results are presented in Table 6.4. Again, focus was on the R_2 variations as other resistances are not able to justify the use of different nanorod percentages. R_2 values of (63.00 ± 0.13) Ω, is observed to be lowest for the cell with 10 wt.% nanorods, assigned for CP1 sample. When increasing the NR percentages from CP2 (20 wt.%) to CP5 (50 wt.%), the R_2 increased continuously, with the highest R_2 of (99.00 ± 0.19) Ω exhibited by the CP5 DSSC. This can be correlated with *J-V* analysis study in which CP5 with 50 wt.% NR resulted in lowest DSSC efficiency.

As expected, R_2 value affects the DSSCs performance whereby the highest efficiency was associated with DSSC that possessed the lowest R_2 value. DSSCs with TiO_2 assembly soaked in 3 wt.% anthocyanin dye showed enhanced cell performance with photoanode modification. In an attempt to further maximize the performance of DSSCs, a third system was designed to take advantage of additives contribution. The cell with highest efficiency and lowest R_2 value represented by composite DSSC with 10 wt.% nanorods, CP1 was selected for this attempt. To accomplish this motivation, two types of additives were used, chenodeoxycholic acid (CDCA) and ferulic acid (FA).

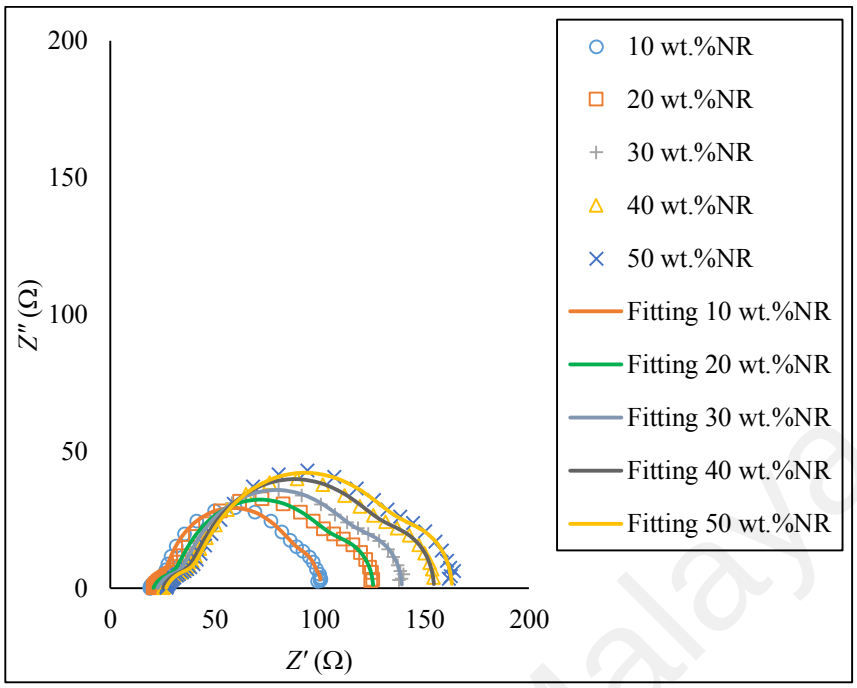

Figure 6.10: EIS for composite DSSCs fabricated from TiO_2 nanoparticle-nanorod samples with nanorod percentages of 10, 20, 30, 40 and 50 wt.% sensitized at 3 wt.% anthocyanin dyes.

Table 6.4: R_s, R_1, R_2, R_3 values for composite DSSCs fabricated from TiO_2 nanoparticle-nanorod samples with nanorod percentages of 10, 20, 30, 40 and 50 wt.% sensitized at 3 wt.% anthocyanin dyes.

Wt.%	R_s (Ω)	R_1 (Ω)	R_2 (Ω)	R_3 (Ω)
10	19.40 ± 0.06	10.00 ± 0.06	63.00 ± 0.13	21.40 ± 0.06
20	20.45 ± 0.09	16.90 ± 0.07	72.00 ± 0.12	17.00 ± 0.06
30	22.68 ± 0.07	11.00 ± 0.07	82.00 ± 0.13	21.00 ± 0.07
40	25.98 ± 0.06	16.00 ± 0.08	87.00 ± 0.18	21.60 ± 0.09
50	26.56 ± 0.07	14.60 ± 0.10	99.00 ± 0.19	21.60 ± 0.15

6.4 Effect of Different Additives Addition on Composite (NPs-NRs) DSSCs System

6.4.1 Visible spectroscopy studies at different weight percentages of additives

The composite photoanode of 10 wt.% NR (CP1) were soaked in the optimized 3 wt.% anthocyanin dye added with additives at different weight percentages (1, 2, 3, 4 and 5 wt.%) separately. The CP1 composite electrode was immersed into the anthocyanin-

additives solutions. Figure 6.11 displays the absorption spectra of anthocyanin adsorbed onto the TiO_2 composite electrode after immersion into the anthocyanin-CDCA solution (designated as C1, C2, C3, C4 and C5) and Figure 6.12 shows the absorption spectra for sample immersed into anthocyanin-FA solutions (designated as F1, F2, F3, F4 and F5).

The absorption spectrum for pigmented composite electrode sensitized with anthocyanin-CDCA at different percentages (1, 2, 3, 4 and 5 wt.%) showed a peak at wavelength, λ= 525 nm. From the figures, it can be observed that the highest absorption of pigmented composite electrodes for CDCA added samples was achieved by adding 1 wt.% CDCA (C1) with intensity of 0.74. For anthocyanin-FA cells a peak was observed at 528 nm for sample added with 1 wt.% FA additive (F1). This peak shifted to 532 nm for 3 wt.% FA (F3) which exhibited intensity of 1.

The composites added with CDCA additives showed a slight increase in absorption compared to CP1 composite without additives (0.72) i.e. 0.74, a ~3% increment while there was a prominent increase for the composite added with FA, ~39%. This means that by adding the 1 wt.% CDCA (C1) and 3 wt.% FA (F3) additives, the composite electrode can absorb more anthocyanin dye especially for composite added with FA. Hence this can possibly give good impact for conversion efficiency in DSSC application. However, as the CDCA percentage increased from 2 to 5 wt.% the absorption intensity decreased. The absorption intensity for FA added dye increased from 1 to 3 wt.% and decreased beyond 3 wt.%. This shows that FA is a more suitable additive for anthocyanin sensitized solar cell compared to CDCA.

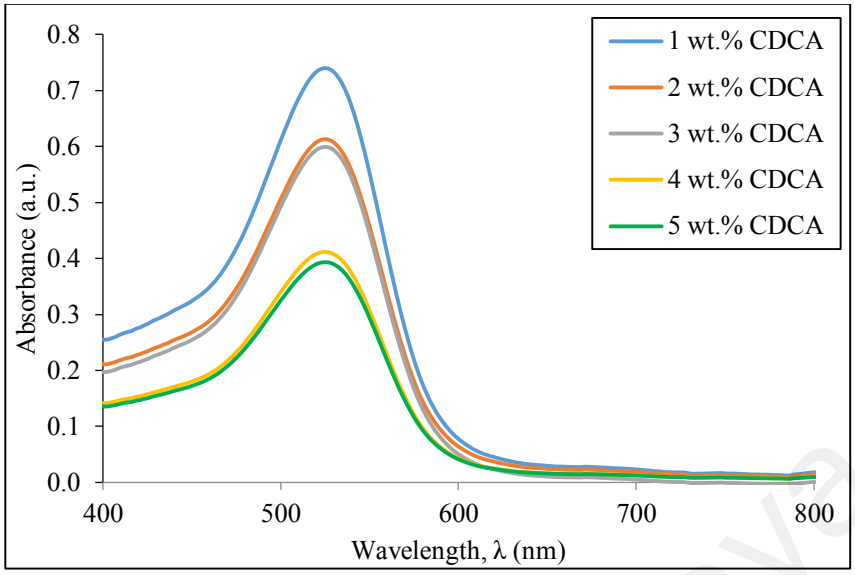

Figure 6.11: The absorption spectra of anthocyanin-pigmented TiO_2 composite electrodes with 10 wt.% TiO_2 NRs at different weight percentages (1, 2, 3, 4 and 5 wt.%) of CDCA additive.

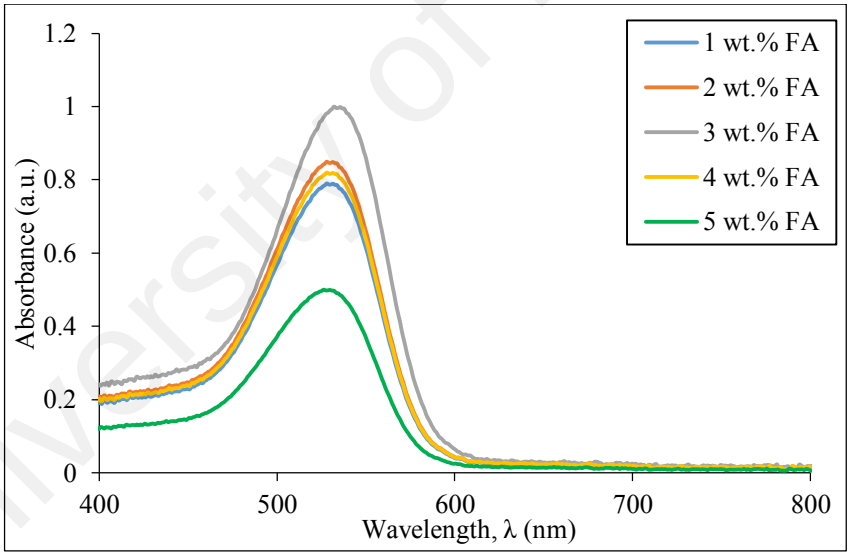

Figure 6.12: The absorption spectra of anthocyanin-pigmented TiO_2 composite electrodes with 10 wt.% TiO_2 NRs at different weight percentages (1, 2, 3, 4 and 5 wt.% of additives) of FA additive.

6.4.2 *J-V* characterization of DSSCs sensitized at different weight percentages of additives

DSSCs of photoanode with 10 wt.% NRs were immersed for 24 h into anthocyanin-CDCA and anthocyanin-FA solutions at five different percentages (1, 2, 3, 4 and 5 wt.%),

respectively and measured under 1000 W m^{-2} at room temperature. The aim of this study was to examine the additive effects on the efficiency and optimize the additives percentage. Figure 6.13 presents the *J-V* curves of DSSC samples immersed in anthocyanin-CDCA solutions and Figure 6.14 illustrated the *J-V* curves of DSSC samples immersed in anthocyanin-FA solutions. The J_{sc}, V_{oc}, *FF*, η, R_s and R_{sh} values are given in Tables 6.5 and 6.6. For comparison, the previous results for composite DSSC of 10 wt.% NR (CP1) without additive addition using optimized 3 wt.% anthocyanin solution on J_{sc} and η were (4.808 ± 0.105) mA cm^{-2} and (1.317 ± 0.035)%, respectively. It can be noticed that there were slight increment in J_{sc} and η values for 1 wt.% of CDCA (C1), which the values were (4.835 ± 0.095) mA cm^{-2} and (1.393 ± 0.039)%, respectively as seen in Figure 6.11 (a) and Table 6.5.

Beyond 1 wt.% CDCA, the DSSCs performance decreased. In contrast, there were significant enhancements observed for J_{sc} and η values owing to inclusion of FA additives. The highest efficiency for the FA series was exhibited by the 3 wt.% FA addition (F3) with J_{sc} of (6.178 ± 0.128) mA cm^{-2} and η of (1.917 ± 0.045)%. These results showed a huge increment of ~28% and ~46% for J_{sc} and η values, respectively when compared to the DSSC system without additives. The R_{sh} value was also higher at (2.505 ± 0.050) Ω-cm^2 with lowest R_s value at (0.014 ± 0.004) Ω-cm^2 as seen in Figure 6.14 and Table 6.6. Beyond 3 wt.% until 5 wt.% of FA addition, the J_{sc} and η values decreased. These results showed that composite DSSC sample of 10 wt.% NR sensitized with anthocyanin from *Ixora siamensis* added with 3 wt.% of FA significantly improved the DSSC performance.

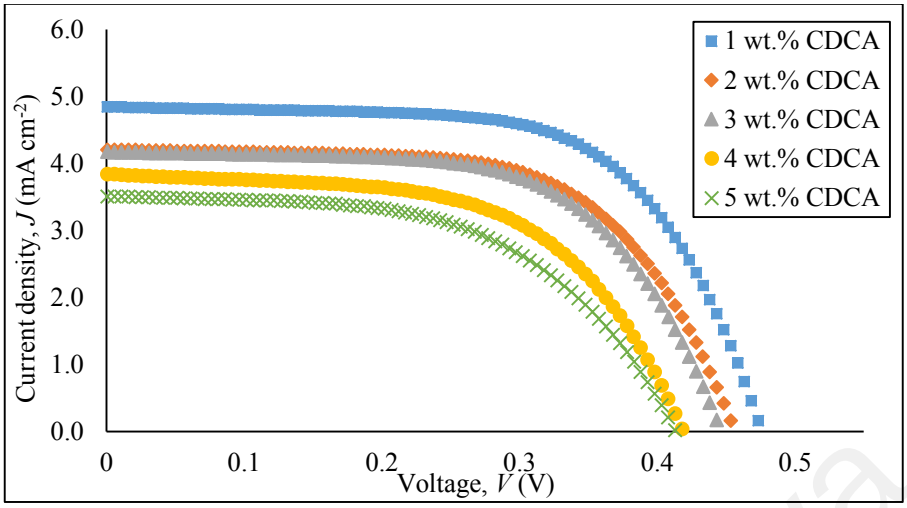

Figure 6.13: *J-V* curve for composite DSSCs fabricated with 10 wt.% TiO_2 NRs at different weight percentages (1, 2, 3, 4 and 5 wt.%) of CDCA additive.

Table 6.5: J_{sc}, V_{oc}, *FF*, η, R_s and R_{sh} values for composite DSSCs fabricated with 10 wt.% TiO_2 NRs at different weight percentages (1, 2, 3, 4 and 5 wt.%) of CDCA.

Wt. (%)	J_{sc} (mA cm^{-2})	V_{oc} (*V*)	*FF*	η (%)	R_s (Ω-cm^2)	R_{sh} (Ω-cm^2)
1	4.835 ± 0.095	0.458 ± 0.006	0.629 ± 0.010	1.393 ± 0.039	0.018 ± 0.005	2.285 ± 0.035
2	4.207 ± 0.059	0.453 ± 0.005	0.629 ± 0.012	1.200 ± 0.032	0.023 ± 0.003	2.169 ± 0.021
3	4.174 ± 0.131	0.443± 0.006	0.611 ± 0.008	1.130 ± 0.053	0.024 ± 0.003	2.082 ± 0.030
4	3.829 ± 0.207	0.418 ± 0.012	0.580 ± 0.016	0.928 ± 0.069	0.026 ± 0.004	1.217 ± 0.026
5	3.515 ± 0.193	0.413 ± 0.028	0.562 ± 0.015	0.816 ± 0.087	0.030 ± 0.003	1.171 ± 0.040

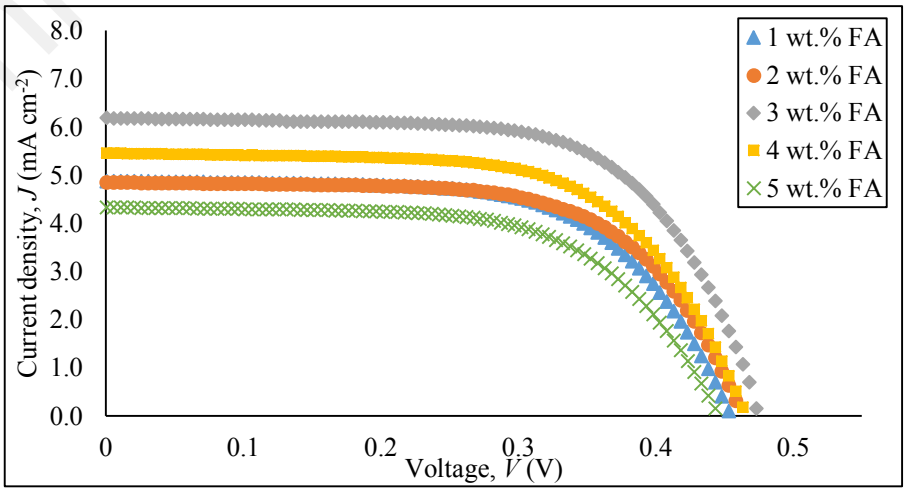

Figure 6.14: *J-V* curve for composite DSSCs fabricated with 10 wt.% TiO_2 NRs at different weight percentages (1, 2, 3, 4 and 5 wt.%) of FA additive.

Table 6.6: J_{sc}, V_{oc}, *FF*, η, R_s and R_{sh} values for composite DSSCs fabricated with 10 wt.% TiO_2 NRs at different weight percentages (1, 2, 3, 4 and 5 wt.%) of FA.

Wt. (%)	J_{sc} (mA cm^{-2})	V_{oc} (*V*)	*FF*	η (%)	R_s (Ω-cm^2)	R_{sh} (Ω-cm^2)
1	4.716 ± 0.101	0.453 ± 0.008	0.634 ± 0.005	1.354 ± 0.068	0.019 ± 0.005	2.184 ± 0.052
2	4.844 ± 0.092	0.458 ± 0.014	0.649 ± 0.004	1.440 ± 0.073	0.018 ± 0.003	2.257 ± 0.058
3	6.178 ± 0.128	0.473± 0.009	0.656 ± 0.010	1.917 ± 0.045	0.014 ± 0.004	2.505 ± 0.050
4	5.458 ± 0.153	0.463 ± 0.009	0.638 ± 0.020	1.612 ± 0.028	0.017 ± 0.009	2.356 ± 0.072
5	4.207 ± 0.147	0.453 ± 0.013	0.629 ± 0.013	1.200 ± 0.091	0.022 ± 0.009	2.067 ± 0.081

6.4.3 Incident photon-to-current conversion efficiency (IPCE) characterization at different weight percentages of additives

IPCE analysis were done for further investigation on the effects of additives on the DSSC performance after *J-V* characterization. The IPCE spectra of the composite photoanode with 10 wt.% NRs sensitized at 3 wt.%. anthocyanin percentages with incorporation of CDCA and FA additives are shown in Figure 6.15 and Figure 6.16. Previously, the IPCE of composite DSSC with 10 wt.% NR (CP1) without additives exhibited a maximum of 25% at 600 nm.

The composite DSSCs with additives addition revealed higher IPCE values which was compatible with the J_{sc} value obtained by photocurrent-voltage measurement. The CDCA added samples showed the highest IPCE peak at 580 nm with 28%, exhibited by the DSSC with 1 wt.% CDCA (C1) while 3 wt.% FA (F3) resulted in highest IPCE peak of 36% at 580 nm, which showed an increment from DSSC system without additives of almost 12% and 44%, respectively.

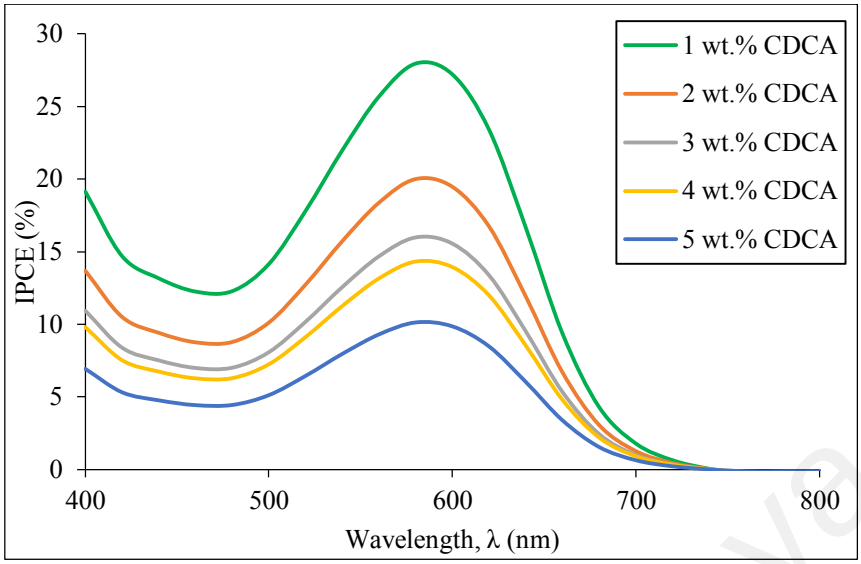

Figure 6.15: IPCE curves for composite DSSCs fabricated with 10 wt.% TiO_2 NRs at different weight percentages (1, 2, 3, 4 and 5 wt.%) of CDCA additive.

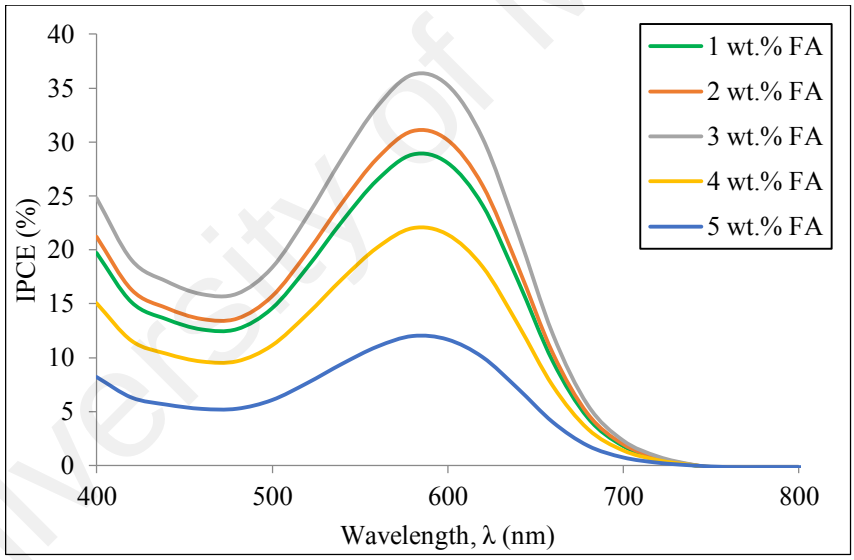

Figure 6.16: IPCE curves for composite DSSCs fabricated with 10 wt.% TiO_2 NRs at different weight percentages (1, 2, 3, 4 and 5 wt.%) of FA additive.

6.4.4 Electrochemical impedance spectroscopy (EIS) characterization at different weight percentages of additives

In order to explain more on the good sides of additives on DSSCs performance, EIS analysis were conducted when illuminated under 1000 Wm^{-2} which provided information about the electron transport and recombination in DSSCs. The aim also was to evaluate

the best percentage that can enhance the efficiency. Figure 6.17 illustrates the Nyquist and fitting plots of the fabricated composite DSSCs with 10 wt.% NRs, assigned for CP1 photoanode sensitized at 3 wt.% anthocyanin dyes and different CDCA additive content and Figure 6.18 displayed the Nyquist plot for DSSC samples of anthocyanin-FA solution. The calculated values of R_s, R_1, R_2, R_3 for the DSSCs are presented in Tables 6.7 and 6.8. As mentioned earlier, we only focusing on the R_2 variations. The R_2 is calculated after fitted the nyquist plot based on the equivalent circuit mentioned before. For the CDCA added samples, the lowest R_2 value of (61.20 ± 0.15) Ω was observed for the cell with 1 wt.%, but the values reduced on increased percentage up to 5 wt.% with R_2 of (110.00 ± 0.15) Ω , as seen in Figure 6.17. In contrast, for the FA added samples, the cell with 3 wt.% FA exhibited the lowest R_2 value of (39.78 ± 0.17) Ω, which increased when the FA percentage increased as displayed in Figure 6.18. Thus, this results are in agreement with highest efficiency performance associated with lowest R_2 values since the cell with 3 wt. FA also achieved highest efficiency (η) (1.917 ± 0.045)% values.

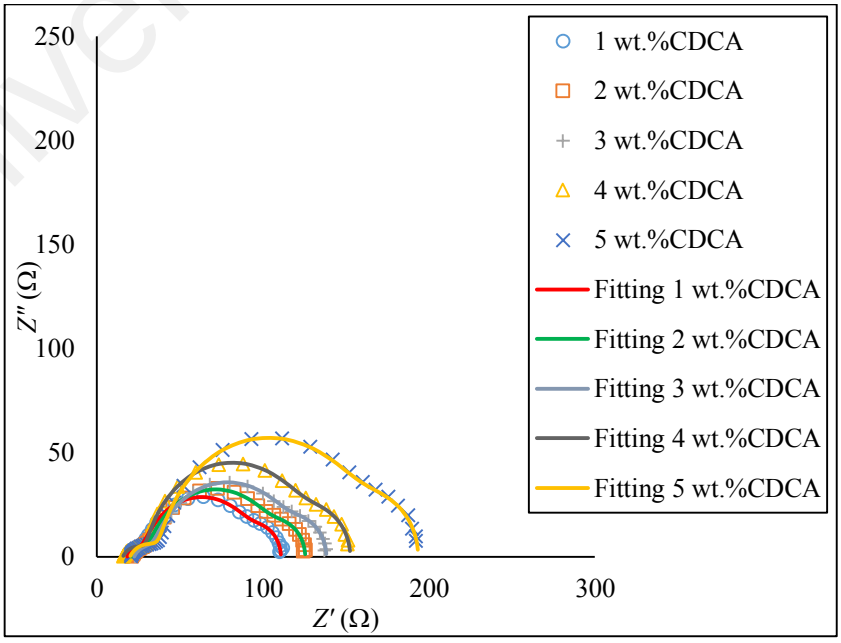

Figure 6.17: EIS for composite DSSCs fabricated with 10 wt.% TiO_2 NRs at different weight percentages (1, 2, 3, 4 and 5 wt.%) of CDCA additive.

Table 6.7: The R_s, R_1, R_2, R_3 values for composite DSSCs fabricated with 10 wt.% TiO_2 NRs at different weight percentages (1, 2, 3, 4 and 5 wt.%) of CDCA.

Wt.%	R_s (Ω)	R_1 (Ω)	R_2 (Ω)	R_3 (Ω)
1	18.10 ± 0.08	7.20 ± 0.08	61.20 ± 0.15	21.90 ± 0.07
2	20.42 ± 0.09	8.40 ± 0.10	70.00 ± 0.10	25.55 ± 0.06
3	23.20 ± 0.05	10.80 ± 0.10	80.00 ± 0.12	23.60 ± 0.09
4	16.65 ± 0.09	13.05 ± 0.10	90.00 ± 0.12	29.25 ± 0.04
5	20.35 ± 0.10	13.75 ± 0.10	110.00 ± 0.15	35.20 ± 0.05

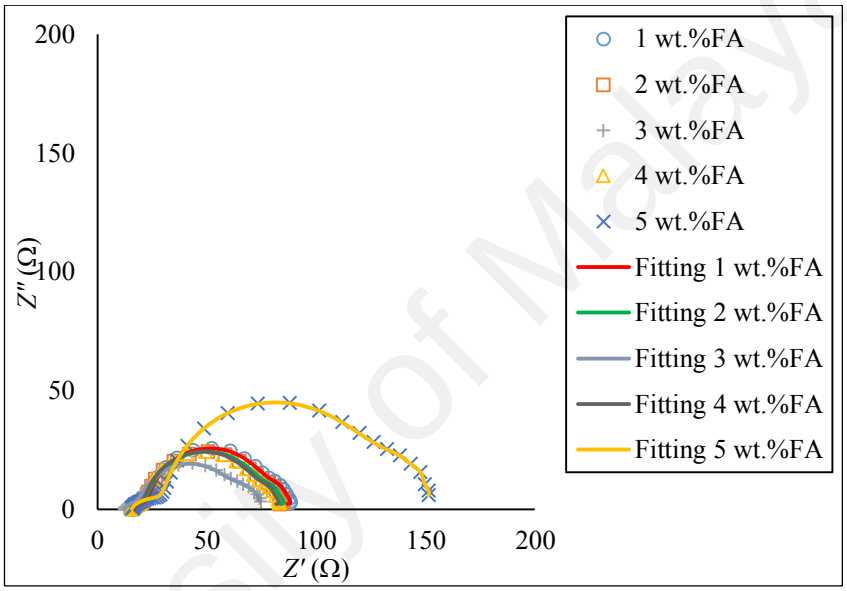

Figure 6.18: EIS for composite DSSCs fabricated with 10 wt.% TiO_2 NRs at different weight percentages (1, 2, 3, 4 and 5 wt.%) of FA additive.

Table 6.8: The R_s, R_1, R_2, R_3 values for composite DSSCs fabricated with 10 wt.% TiO_2 NRs at different weight percentages (1, 2, 3, 4 and 5 wt.%) of FA.

Wt.%	R_s (Ω)	R_1 (Ω)	R_2 (Ω)	R_3 (Ω)
1	17.21 ± 0.06	5.00 ± 0.06	55.76 ± 0.11	10.76 ± 0.09
2	16.00 ± 0.07	4.08 ± 0.07	50.87 ± 0.13	10.00 ± 0.10
3	11.80 ± 0.06	5.00 ± 0.08	39.78 ± 0.17	11.40 ± 0.08
4	15.50 ± 0.07	5.00 ± 0.08	50.45 ± 0.15	11.40 ± 0.05
5	15.66 ± 0.10	14.58 ± 0.10	93.00 ± 0.19	27.0 ± 0.09

Figure 6.19 summarized the DSSC performance in terms of (a) J_{sc}, (b) η, (c) R_s, (d) R_{sh} and (e) R_2 for different sample types. Sample number 1 correspond to DSSC of the

commercial P25 TiO_2 with 3 wt.% anthocyanin dyes (D3), sample number 2 correspond to DSSC of the NPs-NRs composite mesoporous with 10 wt.% nanorods sensitized at 3 wt.% anthocyanin dyes (CP1) while sample number 3 and 4 correspond to DSSC of the composite NPs-NRs (with 10 wt.% NR) sensitized with 3 wt.% of dyes added with 1 wt.% of CDCA (C1) and 3 wt.% of FA (F3), respectively. The commercial P25 with 3 wt.% anthocyanin dyes (D3) exhibited the lowest J_{sc}, η and R_{sh} values while highest R_s and R_2 values. The composite NPs-NRs added with 10 wt.% NRs sensitized with optimized (3 wt.%) anthocyanin dyes with addition of 3 wt.% FA (F3) resulted in highest J_{sc}, η and R_{sh} values while lowest R_s and R_2 values.

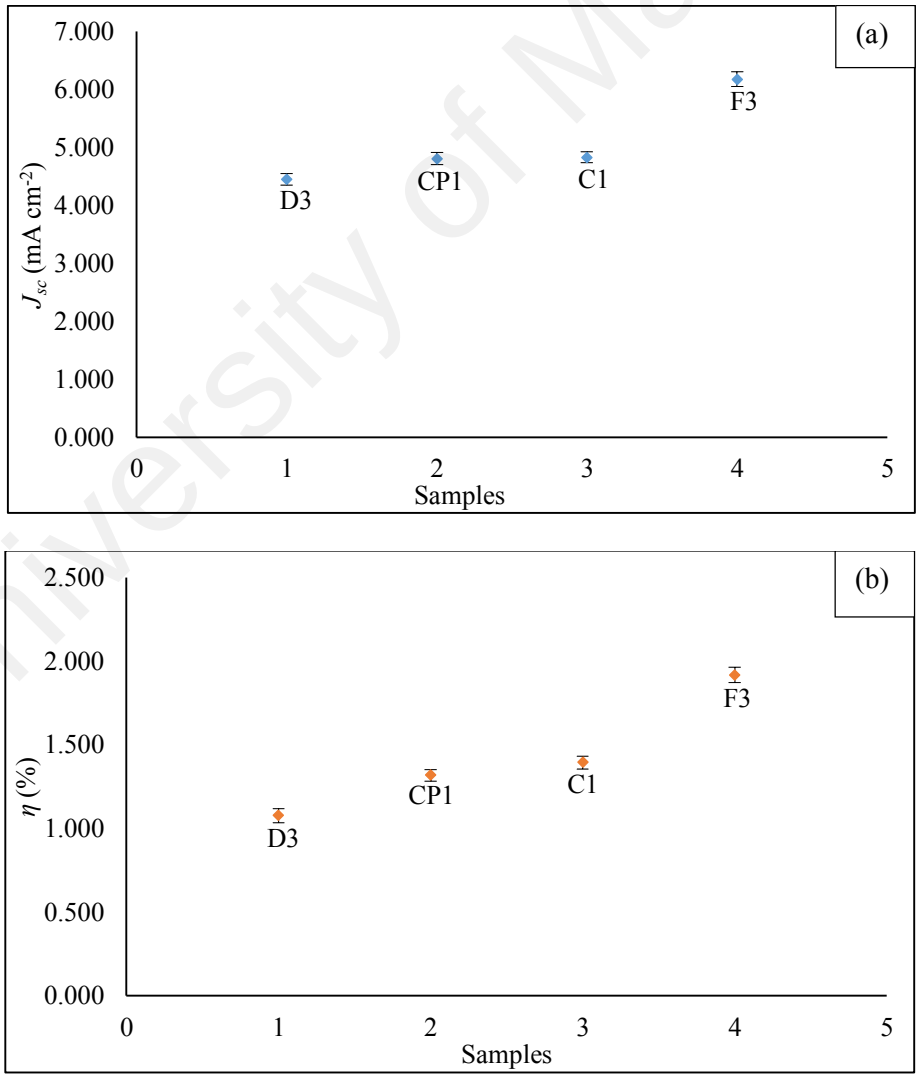

Figure 6.19: DSSC performance in terms of (a) J_{sc}, (b) η, (c) R_s, (d) R_{sh}, (e) R_2 for different sample types.

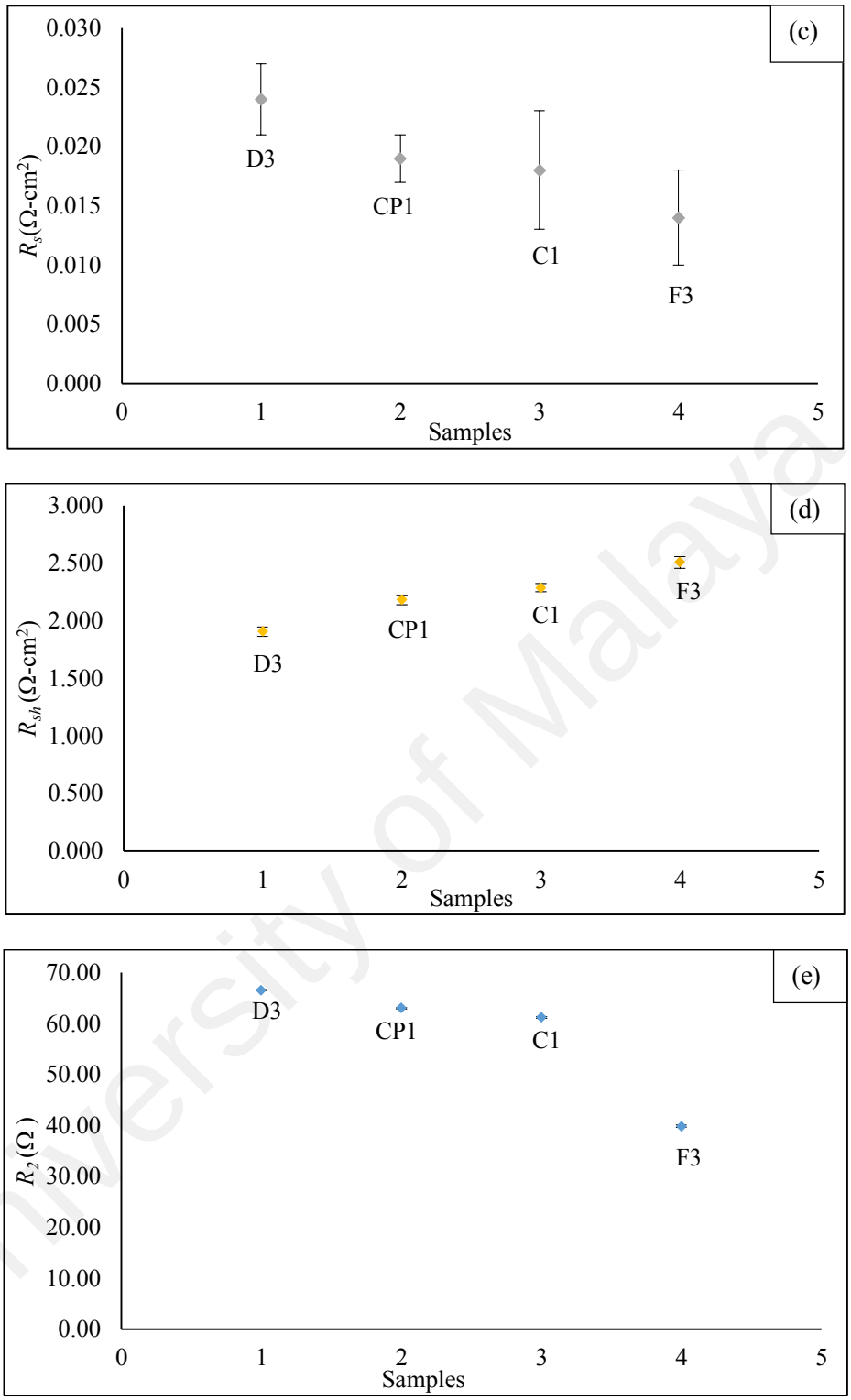

Figure 6.19, continued.

6.5 Summary

DSSCs using anthocyanin based sensitizer extracted from fruit pericarp of *Ixora siamensis* were fabricated. To determine the amount of dye needed to be included, effects

towards dye concentration on the commercial DSSCs systems was the preliminary investigation in these studies. Since there are no report on the utilization of anthocyanin sources from fruit pericarp of *Ixora siamensis* as natural sensitizer. This investigation showed positive feedback as the efficiency managed to achieve (1.076 ± 0.042)% efficiency (D3). To improve the DSSCs performance, modification on the mesoporous layer were done by incorporating the TiO_2 nanorods (which have been produced through the electrospinning method) into the TiO_2 nanoparticles, hence it forms the composite mesoporous layer. The DSSC performance of 10 wt.% added NRs (CP1) sensitized at 3 wt.% dye (optimized dye percentage) was further improved with efficiency of (1.317 ± 0.035)%. The addition of 1 wt.% CDCA (C1) only give slight improvement with (1.393 ± 0.039)% efficiency whereas addition of 3 wt.% FA (F3) as additives in the anthocyanin dye succeeded in enhancing the performance of composite DSSC with efficiency of (1.917 ± 0.045)%.

CHAPTER 7: DISSCUSSIONS

Plant phenolics have captured the attention of the scientist community. It is also known that for obtaining the maximum yield of an interested pigment from plant, the extraction parameters must be optimized. It is not an easy task to determine the method that gives higher yield of extraction since the anthocyanin content may differ from plant to plant. According to Sarkis et al. (2013) the choice of extraction method depends on the purpose of extraction and the prospective use of the final extract. In this study, the source of anthocyanin pigment was the fruit pericarp of *Ixora siamensis.* The fruit pericarps of *Ixora siamensis* were firstly freeze-dried in order to obtain particle powder of size ≤ 250 μm. Silva et al. (2017) reported that a good approach is to turn the source of pigment into powder. This will lead to the increase in contact surface area with solvent, hence promoting solid particle diffusion into the solvent. The smaller the particle, the shorter the diffusion path from the powdered fruit pericarp to the solvent (Hojnik et al., 2008; Cissé et al., 2012). According to Cissé et al. (2012), the anthocyanin content in the extract is more when the particle size is smaller. To the best of the author's knowledge, there is limited report on the extraction of natural pigment from the fruit pericarp of *Ixora siamensis* and the use of the extract as a natural colourant especially in DSSCs. Hence, the starting point of this study was to identify that this species contained anthocyanin pigment.

By using the UPLC-ESI-MS/MS, the mass spectra illustrated in Figure 4.1 was obtained. It was found that the fruit pericarp extract of *Ixora siamensis* consists of anthocyanin pigment. There are three major anthocyanin types detected which were cyanidin-3-rutinoside, delphinidin glucoside and peonidin-3-glucoside. The compounds were identified by comparing individual retention times with reference compounds and ACD/Labs fragmentation. These types of anthocyanin compounds were also detected by

other researchers (Dias et al., 2012; Gouvêa et al., 2012) for their sample species. Therefore, *Ixora siamensis* was proven to contain anthocyanin. Thus, anthocyanin was extracted from the powdered fruit pericarp of *Ixora siamensis* and were proceeded for extraction optimization in order to be used as natural colourant. Extraction is a crucial step. A good extraction process must maximize the anthocyanin yield and ensures that degradation of the product is negligible. Typical extraction process uses organic aqueous solvent (water with alcoholic solvent) that is made acidic for efficient transfer of the polar anthocyanin pigments into the solvent. Anthocyanin is obtained via solvent-extraction. As mentioned in Chapter 2, the key extraction parameters are dependent on the type of solvent and its concentration, liquid-to-solid ratio, extraction temperature and time. Hence, these parameters need to be optimized (Cacace & Mazza, 2003; Barnes et al., 2009; Rajha et al., 2014; Bridgers et al., 2010).

In our research work, we only focused on the influence of three parameters. These are (i) TFA content in methanol, (ii) soaking time and (iii) temperature of extraction. The different extraction parameters will give varied results on CIE colour and anthocyanin yield as can be observed from the BBD results, Table 4.1. Therefore, the aim was to obtain the optimal extraction conditions through RSM optimization, in order to achieve maximum extraction yield of anthocyanin for use as natural sensitizer in DSSCs. The DSSCs performance depends on several factors. These include sensitizer type, photoelectrode and electrolyte (Lee et al., 2009). In this study, we restrict our investigation to the sensitizer and photoelectrode. In order to obtain the appropriate model to represent the responses of CIE colour and anthocyanin content, several evaluation tests were done as mentioned in Chapter 4. RSM generated the model to represent the responses based on results from the experiments suggested by the BBD. The selected polynomial model for all responses were evaluated using ANOVA. Based

on Tables 4.4 until 4.10, the results showed that the reduced quadratic polynomial model were the best model since it significantly influenced the responces of L*, a*, b*, C, H°, saturation and anthocyanin content. The appropriate polynomial equations generated from the selected quadratic models are displayed in equations (4.1) to (4.7). These equations were used to calculate the predicted values of L*, a*, b*, C, H°, saturation and anthocyanin content responses. There was good relationship between the experiment and predicted values as depicted in Figure 4.2 since most of data point can be considered to lie in a straight line. It can be noticed that no obvious S-shape pattern was observed which can relate to the abnormalities of the experiment data (Shafi'i et al., 2013). This also proved the success of all generated models since they are capable to closely predict the outcome of the experimental data. The relationship and influence of solvent composition, soaking time and extraction temperature on the CIE colour indices and anthocyanin content can be deduced from the response model graphs in Figure 4.3 until Figure 4.9. It is proven that three combination parameters (different percentages of added TFA, different soaking times and different extraction temperatures) affect significantly the anthocyanin extraction. From the optimization data of developed model displayed in Table 4.12, the optimized conditions for anthocyanin extraction from fruit pericarp of *Ixora siamensis* generated by RSM were 0.5% TFA content, 119 min soaking time and extraction temperature of 80 ºC. The optimized conditions will be used to obtain anthocyanin from the powdered fruit pericarp of *Ixora siamensis* for use as natural sensitizer in DSSCs.

The optimized 0.5% TFA content was sufficient to promote the efficiency of anthocyanin extraction in this study. Most extraction procedures use acidic solvents, which denatured the cellular membranes and facilitated solubilization of anthocyanins (Jackman, 1987). David et al. (2009) also used methanol containing 0.5% TFA for

anthocyanin extraction from *Vaccinium Myrtillus L.* Anthocyanin yield improved compared to extraction using purely methanol. This also explained the requirement of an acidic medium in most extraction protocols for anthocyanin recovery. Literature have shown that for better extraction, trifluoroacetic acid (TFA) (0.5-3.0%) and hydrochloric acid (HCl) (<1.0%) (Ju & Howard, 2003; Navas et al., 2012; Silva et al., 2017; Ooe et al., 2016 and David et al., 2009) can be used. Revilla et al. (1998) also stated that the addition of weaker and volatile organic acids e.g. TFA from the range of 0.5% to 3% into to the alcohol solvents can minimize the anthocyanin degradation. The presence of acids is able to stabilize the anthocyanins in the solvent since acidity is required to obtain the most stable flavylium cation. The acids can also alter the original form of the anthocyanins during extraction. However, the amount of acid addition cannot exceed the amount needed since solvents that are strongly acidic may hydrolyse the glycoside bonds (Ju & Howard, 2003; Silva et al., 2017). Acidification of solvent has been shown to improve yield of extraction. According to Barnes et al. (2009) the TFA addition has increased anthocyanin yield significantly for all solvents except acetone. Hence, the addition of optimized 0.5% TFA in this study was sufficient to improve the anthocyanin extraction.

The results also showed that soaking or extraction time played an important role in achieving better extraction yield since different extraction times resulted in different CIE colour properties and anthocyanin content. The extraction or soaking time is also crucial for recovery of phenolic compounds. Soaking time can vary from as short as a few minutes to very long and extending up to 24 hours (Salar et al., 2016). In our study, 119 min was the optimized soaking time adequate to obtain highest anthocyanin yield. Rajha et al. (2014) also obtained the optimal extraction time of 119 minutes for optimized anthocyanin content. According to Silva et al. (2017), with longer time of contact

between tissue and solvent, solid to liquid diffusion will be more complete until an equilibrium is reached. The time for equilibrium depends on several factors such as temperature and type of solvent. Therefore, the soaking time has to be determined (Cacace & Mazza, 2003). Observations on soaking time were also reported by other researchers (Yang et al., 2009; Thirunavukkarasu & Nithya, 2011; Liu et al., 2012; Lotfi et al., 2015; Yilmaz et al., 2015; Ramasamy et al., 2016). Soaking times ranging 20 to 180 min were used by Lotfi et al. (2015) to extract anthocyanin from saffron *(Crocus sativus L.)* tepal. Longer extraction time can cause hydration and swelling of anthocyanin. As a result, the solvent will diffuse into the plant (Steytler, 1996). Hence, too long an extraction time is prohibited for extraction process. Moreover, Fick's second law of diffusion states that an equilibrium of solute concentration between solid matrix (plant matrix) and solvent occurs after a particular reaction time. Therefore, prolonging soaking time does not prove useful (Silva et al., 2017). Also, lengthening the time of extraction can decompose and oxidize the anthocyanin due to long exposure to light or oxygen (Naczk & Shahidi, 2004; Salar et al., 2016).

Anthocyanin extraction is dependent also on temperature (Silva et al., 2017). The optimized extraction temperature obtained for this study was 80 ℃ which resulted in highest anthocyanin content (5791.70 mg/L). The temperature to extract anthocyanin from *Ixora siamensis* is in agreement with the study conducted by Thirunavukkarasu & Nithya (2011) who obtained the ideal extraction temperature of 76.5 ℃ for anthocyanin extraction from *Solanum melongena*. Other researchers (Ruenroengklin et al., 2008; Yang et al., 2009; Sharif et al., 2010; Thirunavukkarasu & Nithya, 2011; Duan et al., 2015) also investigated the effects of temperature on the extraction process. Sharif et al. (2010) reported the highest absorption of anthocyanin extract from onion (*Allium cepa)* using acidified methanol at 80 ℃. Duan et al. (2015) obtained the optimal extraction

temperature for anthocyanin from Chinese bayberry, *Myrica rubra Sieb. & Zucc.* at 80 ℃. Decomposition of plant cell walls at high temperatures makes removal of anthocyanins from plant tissues easier since the bonds of the bound phenolic compounds (phenol-protein or phenol-polysaccharide) was hydrolyzed. This enhanced the phenolics solubility and led to more phenolics transferred into the solvent. Also, the softening and swelling of the plant tissues would speed up at high temperatures making extraction easier (Shi et al., 2003; Cacace & Mazza, 2003; Khazaei et al., 2016; Salar et al., 2016). However, too long exposure at high temperatures would be detrimental to the desired compound as it would undergo the process of oxidation and polymerization (Shi et al., 2003). Thus, optimized soaking time of 119 min at high temperature was adequate to enhance extraction process.

Other than sensitizer, the semiconductor photoanode is also an important component and have a prominent role in DSSCs. Photoelectrode morphology also influenced photocurrent production. One-dimensional (1-D) TiO_2 nanostructures have preferred morphology for DSSC photoelectrodes. The higher photocurrent production with 1-D TiO_2 nanostructures is due to the reduction in grain boundaries, higher dye loadings and slower recombination rates (Lee et al., 2009). Hence, the improvement in the properties of TiO_2 semiconductor in the photoanode was also the ultimate goal in this study. 1-D TiO_2 nanorods have been successfully produced in this study by combining sol-gel synthesis and electrospinning method followed with sintering and grinding processes. Similar procedure was also performed by other researchers (Jose et al., 2008; Fujihara et al., 2007; Lee et al., 2009; Huang et al., 2012; Park et al., 2013; Chen et al., 2013; Chen et al., 2014; Hong et al., 2014; Rezvani et al., 2016) in order to obtain 1-D TiO_2 nanorods. These were combined with TiO_2 nanoparticles and further used in the preparation of composite photoanode for DSSCs. Various parameters influenced the electrospinning

process for preparing the TiO_2 nanofibers, which have been discussed in detail in Chapter 2. The solution and process parameters influenced nanofiber properties. Two parameters that were observed and being investigated in this study were the effect of polymer concentration and effect of applied voltages on the morphology of TiO_2 nanofiber formations. The influence of different polymer concentrations with varied PVP content (9.2, 10.2, 11.2, 12.2 and 13.2 wt.% PVP) can be observed from the FESEM image as depicted in Figure 5.1. Increasing the PVP concentration have a positive impact since at more dilute concentrations i.e. 9.2 and 10.2 wt.% PVP, designated as NF1 and NF2, there were no cylindrical fiber observed (flat fiber formed) but when the polymer concentration was increased from 11.2 until 13.2 wt.%, designated as NF3 to NF5, cylindrical fibers were observed, though beads still exist. The formation of more cylindrical fibers was expected due to sufficient polymer chain entanglement. At 13.2 wt.% PVP containing sample, which is the optimized polymer concentration, the solution was expected to have higher polymer chain entanglement and resulted in more cylindrical fibers as compared to fibers at lower concentrations (Deitzel et al*.,* 2001). The average fiber diameter 301 nm of electrospun TiO_2 at the optimized 13.2 wt.% PVP as displayed in Figure 5.2 was slightly larger due to greater resistance towards thinning of the jets (Deitzel et al*.,* 2001; Haghi & Akbari, 2007). In contrast, the average bead diameter of 0.40 μm for 13.2 wt% PVP (NF5), displayed in Figure 5.3 was the smallest. This showed that the bead diameter decreased with increased polymer concentration. Bead formation at low PVP concentrations and wider fiber diameter at higher polymer concentrations were attributed to the polymer solution viscosity.

As mentioned earlier in Chapter 2, solution viscosity influenced the polymer chain complexity inside the solution (Deitzel et al*.,* 2001; Tarus et al., 2016; Haider et al., 2018). Increased entanglement of the polymer chains led to viscosity increase

(Tungprapa et al., 2007; Tarus et al., 2016; Haider et al., 2018). Low solution viscosity results in low viscoelastic force during electrospinning process. The low viscoelastic force is unable to match the electrostatic and Coulumbic repulsive forces. As a result, the electrospinning jet will be stretched and breaks up. A mixture of flat fiber and larger beads occur due to the low viscosity at low PVP concentrations of 9.2 (NF1) and 10.2 wt.% PVP (NF2) compared to higher percentages. When solution concentration was increased from 11.2 (NF3) to 13.2 wt.% PVP (NF5), viscoelastic force increased. This prevented the jet from break up. The bead diameter decreased from 11.2 wt.% (average bead diameter of 1.26 μm) with increasing polymer concentrations to 13.2 wt.% (average bead diameter of 0.40 μm) as depicted in Figure 5.3. The beads change shape from ball-like to rod-like when the solution concentration keeps increasing. The increasing entanglement of polymer chain with increasing PVP concentration also enabled distribution of solvent molecules over the entangled polymer chains resulting in the formation of smooth, uniform and beadless nanofibers (Mit-uppatham, 2007; Haider et al., 2018). The fiber diameter increased with increasing of polymer concentrations from 11.2 wt.% with average fiber diameter of 132 nm to 13.2 wt.% with average fiber diameter of 301 nm as can be observed in Figure 5.2. Thicker fiber and thinner bead diameters are listed in Table 5.1. These results can be attributed to the increasing viscoelastic force that restricts stretching of the jets by the Coulumbic repulsive and electrostatic forces. Further increased in polymer concentration is not necessary because it will result in increase of solution viscosity and eventually led to fibers with bigger diameter formed. Since the 13.2 wt.% PVP was able to produce fibers with less beads, the concentration was chosen as the optimized polymer concentration for use in further investigation on the effects of different applied voltages in order to produce beadless fibers.

Figure 5.4 revealed the FESEM images of TiO_2 nanofiber morphology produced as a result of applying different applied voltages from 16 to 22 kV. There was transformation from beaded nanofibers to successfully uniform continuous nanofibers. The voltage applied has to exceed a certain threshold for discharge of the polymeric solution out of the needle tip to begin the electrospinning operation (Arof et al., 2017; Someswararao et al., 2018). In order to understand diameter changes with voltage variation, there are few forces need to be considered which are gravitational force, electrostatic force that accelerates the jet to the collector and Coulombic force that stretches the jet. Others include viscoelastic force and surface tension that prevent the charge jet from being stretched. The effect of applied voltages on the TiO_2 fiber diameters are depicted in Figure 5.5. The corresponding values are listed in Table 5.2. The relationships between Coulombic, viscoelastic forces and surface tension can be used to explain the influence of applied voltage on the nanofiber diameters (Kim et al., 2018). At lower voltage of 16 kV corresponding to 1.14 kV/cm electric field (sample NF5-1), the cylindrical fiber was not formed. On increasing the voltage from 17 to 18 kV (NF5-3), nanofibers with large diameters (average fiber diameter of 301 nm) are formed. These implied that the Coulombic force is less compared to viscoelastic force and surface tension. At moderate voltages of 19 to 20 kV, all three forces are in equilibrium, resulting in the thinning of nanofibers. At 20 kV (electric field of 1.43 kV/cm) (NF5-5) uniform cylindrical nanofibers without beads with average fiber diameter of 177 nm were formed. On further increase of high applied voltages from 21 (NF5-6) to 22 kV (NF5-7) with electric field of 1.50 to 1.57 kV/cm, the Coulombic force was bigger than both viscoelastic force and surface tension. The jet reached the collector faster due to the greater acceleration. Due to this, the solvent does not have enough time to evaporate and nanofibers with large diameters (average fiber diameter of 223 nm) are formed. The larger nanofiber diameters in this study were also due to transverse stretching that exceeded the longitudinal

stretching. The effects of applied voltage towards bead diameter can be observed in Figure 5.6. Bead diameters decreased as applied voltage increased until beadless nanofibers were formed at 20 kV (NF5-5). It should be noted that when the applied voltage is low, beads appear. This is because at low voltage the viscoelastic force is also low. Surface tension of the solution will cause the solution to form spherical particles and this will be responsible for the formation of beads (Haider et al., 2018; Kim et al., 2018). Since electrospinning at 20 kV (NF5-5) is capable of producing uniform cylindrical nanofibers without beads, applied voltage was optimized at 20 kV. Hence, the optimized electrospinning parameter for further production of TiO_2 nanorods will be 13.2 wt.% PVP content, 20 kV applied voltages, 14 cm working distance and 1 mL/h flow rate.

FESEM images in Figure 5.7 showed the morphology of the rod-like structure of TiO_2 nanorods (NRs) at different calcination temperatures of 400, 500 and 600 ℃. The average nanorod diameters (Figure 5.8) at these temperatures were 130, 90 and 135 nm, respectively. The average nanofiber diameter before calcination was 177 nm. There were reduced in size of the nanofibers before and after calcination which could assigned to the further loss of PVP from the nanofibers and the crystallization of TiO_2 (Li & Xia, 2003; Lee, 2006; Nuansing et al., 2006; Kumar et al., 2007). Elemental analysis in Figure 5.9 confirmed the removal of PVP polymer and proved that the final product was pure TiO_2 materials. XRD patterns in Figure 5.10 and Table 5.3 confirmed that calcination at 500 ℃ yielded TiO_2 nanorods having dominant anatase structure (91.97%) with the strongest peak being at 25.5° (Huang et al., 2012). PVP is reported to be thermally degraded at around 420 ℃ (Chrissafis et al., 2008; Shibaev et al., 2008; Lau & Mi, 2002). As reported by Jung et al. (2012), in order to produce DSSCs of high efficiency, anatase TiO_2 that must be used. The anatase phase offers higher quantum yields and phototransformation

efficiencies. Upon confirmation of anatase phase, the TiO_2 nanorods were mixed with commercial P25 TiO_2 nanoparticles in order to produce composite mesoporous layer. FESEM micrographs in Figure 5.11 revealed the morphologies of the composite mesoporous layer with different nanorod contents of 10, 20, 30, 40 and 50 wt.%. The micrographs revealed the presence of randomly oriented nanorods. Closer observation on the FESEM micrograph of as-prepared composite film revealed that there were still interspaces and few large voids appeared. These voids and interspaces will make dye loading easier (Huang et al., 2012; Hong et al., 2014). These composite photoanode systems were used in the fabrication of DSSCs.

In Chapter 6, characterization of dyes extracted from fruit pericarp of *Ixora siamensis* via visible spectroscopy studies showed a distinguished peak at λ=522 nm which can be ascribed to the anthocyanin components, Figure 6.1. The wavelength is comparable with the reported research by Hao et al. (2006) and Ludin et al. (2014) who stated that the absorbance peak of anthocyanin extraction ranged from 450 to 600 nm. There were shifts observed in absorption band of anthocyanin/TiO_2 NPs electrode towards lower energy as can be seen in Figure 6.2. The absorption shift can be attributed to the complexation that has taken place between anthocyanin and metal ions, Ti^{4+} (Cherapy et al., 1997; Garcia et al., 2003; Calogero & Di Marco, 2008). The hydroxyl groups (-OH) present in the anthocyanin of natural dye molecule can be bound easily to the surface of the porous TiO_2 film and stabilized the excited state of the dye (Hao et al., 2006; Wongcharee et al., 2007; Fernando & Senadeera, 2008). The chemical adsorption of these anthocyanin dyes takes place due to condensation of alcoholic-bound protons with -OH groups on the TiO_2 nanostructured surface. These chemical attachments affect the energy levels of the highest occupied molecular orbital (HOMO) and lowest unoccupied molecular orbital (LUMO) of the anthocyanin pigment. This eventually affects the band gaps and shift the

absorption peak towards higher wavelength or lower energy of the absorption spectra (λ shifted from 522 to 525 nm) (Hao et al., 2006; Fernando & Senadeera, 2008). Evidently, the absorption maxima shift in our study, could be prominently due to attachment of the anthocyanin molecules onto the TiO_2 surface. These –OH groups can help in the excitation of the anthocyanin molecule and electron administration in the mesoporous TiO_2 conduction band from the LUMO of the sensitizer molecules (Hao et al., 2006; Fernando & Senadeera, 2008; Ludin et al., 2014). Based on Figures 6.1, 6.2 and 6.3, it can be shown that increasing the anthocyanin dye concentration above 3 wt.% resulted in decreased maximum absorption as well as decreased in efficiency performance. This could be explained due to anthocyanin molecules that are easily self-aggregate (Chien & Hsu, 2014). Anthocyanin is a planar molecule with aromatic rings that are prone to π–π stacking interactions with themselves (self-association) and organizing into aggregations to form complex aggregates (Hoshino, 1991; Houbiers et al., 1998; Leydet et al., 2012). Hence, increasing the anthocyanin content beyond 3 wt.% has increased the dye aggregation due to the presence of more hydroxyl groups in the anthocyanin extraction that can interact and aggregate with one another through hydrogen bonds (Spillmann and Burger, 1996). Dye aggregation will result in decrease of maximum absorption in the visible, which means that less adsorbed dye molecule to harvest the light (Yang et al., 2014). This implied that the concentration of sensitizer significantly affects the DSSC performance.

It was found that the dye concentration greatly influenced the dye adsorption and the resultant overall light conversion efficiency of the DSSCs. The results from the IPCE data in Figure 6.4 are also comparable with the results from the *J-V* curves. Wang et al. (2004) also agreed that the shift observed from spectral response is attributed to the electronic coupling between anthocyanin dye and TiO_2 structures. Figure 6.3 showed that

DSSCs sensitized with 3 wt.% anthocyanin exhibited the highest J_{sc} and efficiency (η), but beyond this concentration both values start to decrease. Typically, the J_{sc} is directly related to concentration of dye. Hence, increased in adsorbed dye led to increase light collection and eventually to a larger J_{sc} (Yang et al., 2014). Increasing the dye solution concentrations, increased J_{sc} and efficiency of DSSCs as listed in Table 6.1. This is attributed to an increase in the amount of dye adsorbed onto the TiO_2 surface as reported by Ooyama & Harima (2012). On increasing the dye concentration (above 3 wt.%), the efficiency of DSSCs started to decrease. This can be attributed to the dye aggregation that made the molecules inactive. This inactive molecule of dyes reduced the electron injection into the conduction band of the photoanode. Aggregation of anthocyanin molecule resulted in inefficient electron injection thus decreasing DSSC performance (Arifin et al., 2017).

Further observation towards the extract concentration and magnitude of the collected photocurrent and their effects on series and shunt resistances. The use of highly concentrated anthocyanin extract introduces more series resistance (R_s) in the solar cell. This is mainly due to the path traversed by the photogenerated electrons (Jasim et al., 2012) in samples with dye concentration beyond 3 wt.%, which were (0.035 ± 0.004) Ω-cm^2 (4 wt.%) and (0.042 ± 0.003) Ω-cm^2, respectively as listed in Table 6.1. The increasing R_s means that electrons are lost, so the voltage decreased (Rho et al., 2015). This reduced the collected photocurrent which led to decrease in efficiency. At 3 wt.% anthocyanin concentration (D3), the *J-V* characteristics showed a better operation, a much lower series resistance (R_s) of (0.024 ± 0.003) Ω-cm^2 and a higher efficiency (1.076 ± 0.042)%. Low series resistance resulted in an improved *FF*. Highly diluted extracts less than 3 wt.%, reduced the magnitude of photocurrents and lowered the cell efficiencies (Jasim et al., 2012). The shunt resistance (R_{sh}) is due to the slow back electron

transfer rate from TiO_2 to electrolyte at the TiO_2/dye/electrolyte interface (Grätzel, 2001; Rho et al., 2015). In DSSC, low shunt resistance (R_{sh}) provides an alternative path for light generated current and hence lowered the *FF* and power output. The shunt resistance (R_{sh}) results from the recombination of electrons with holes in the dye and I_3^- ions in the redox couple. The decreasing R_{sh} means that there are recombination sites so the electrons are transferred to each DSSCs layer (Rho et al., 2015). This is the reason that at high concentrations of 4 (D4) and 5 wt.% (D5) the efficiency of (0.724 ± 0.036)% and (0.563 ± 0.073)%, respectively is low since R_{sh} values were also low (1.529 ± 0.022) Ω-cm^2 and (1.480 ± 0.026 Ω-cm^2), respectively. Hence, there will be more recombination of electrons. Decreasing the series resistance (R_s) and increasing the shunt resistance *(R_{sh})*, in addition to reducing the overvoltage for diffusion and electron transfer will cause the *FF* to rise, consequently resulting in better efficiency (Gong et al., 2017). High R_{sh} values can boost J_{sc} since R_{sh} restricts shunt currents on the cell structure. It has been stated that the R_{sh} values had to be high to improve the fill factor for better DSSC efficiency (Yang et al., 2012).

The charge transport resistance (R_2) as listed in Table 6.2 is affecting the overall DSSC performance of the cell and thus as expected, the lowest charge transfer resistance is (66.50 ± 0.12) Ω gave the highest efficiency of (1.076 ± 0.042)% and largest current density of (4.456 ± 0.101) mA cm^{-2} in DSSC of 3 wt.% dye (D3). It was suggested that decreasing the adsorbed concentration of dye could minimize the charge recombination in DSSC as well as improve the electron transport properties of TiO_2 film (Tang et al., 2013) as in this study 3 wt.% (D3) was the adequate percentage to improve the efficiency performance. The good DSSC results of (1.076 ± 0.042)% for DSSC sensitized with anthocyanin from *Ixora siamensis* may be related to the presence of delphinidin as one of the detected anthocyanin type found in fruit pericarp of *Ixora siamensis* from UPLC

analysis. As stated by Hamadanian et al. (2014), B-ring in delphinine anthocyanin structure that contain three –OH groups can form a strong bond with Ti(IV). This creates a sufficient number of the –OH binding sites to be available onto TiO_2 surface hence anthocyanin dyes are effectively bound to the TiO_2 surface.

Further improvement on the DSSCs based anthocyanin from fruit pericarp of *Ixora siamensis* were performed by producing composite TiO_2 photoanode in which the mesoporous layer is made up of TiO_2 NPs with addition of NRs at various percentages (10, 20, 30, 40 and 50 wt.%) and sensitized at 3 wt.% dye percentage. This dye percentage is considered as the optimized percentage since it exhibits the highest efficiency in the first DSSC system and were applied for other DSSC systems. There was enhancement observed in J_{sc} and η for DSSCs using 3 wt.% anthocyanin dye with composite mesoporous NPs-NRs layer as displayed in Figure 6.8 and Table 6.3. The relationship between efficiency and nanorod content can be observed in Figure 6.8. The inclusion of 10 wt.% NR (CP1) into the mesoporous layer, designated as DSSC CP1 exhibited the highest J_{sc} of (4.808 ± 0.105) mA cm^{-2} and efficiency (η) of (1.317 ± 0.035)% compared to DSSC of NPs electrode that showed J_{sc} of (4.456 ± 0.101) mA cm^{-2} with (1.076 ± 0.042)% efficiency. The inclusion of 10 wt.% NRs is sufficient to exhibited a good photovoltaic cell efficiency. The results are in agreement with other researchers Saji and Pyo (2010) and Park et al. (2013) that reported good photovoltaic cell efficiency with incorporation of 10 wt.% TiO_2 nanorods. Nevertheless, both researchers used synthetic dyes for their research.

The improvement in J_{sc} and η in DSSC systems containing TiO_2 nanoparticles-nanorods (NPs-NRs) can be correlated to electron mobility in TiO_2 nanorod and the specific contact area of TiO_2 nanoparticles with the dyes since DSSC performance mainly depend on these two indicators as reported by Park et al. (2013) and Huang et al. (2012).

The transport of electron through TiO_2 NRs is more efficient than through NPs alone due to their smaller grain interfaces. In contrast, due to large specific surface area, TiO_2 NPs can improve the contact with the dyes (Park et al., 2013; Huang et al., 2012). At 10 wt.% nanorod content (CP1), the DSSC performance was maximized. The increase in J_{sc} may also arise from the enhanced light scattering by the TiO_2 films containing nanorods (Huang et al., 2012; Chen et al., 2013). Although the high surface area of TiO_2 NPs is adequate for dye adsorption, however there are still possibilities for the recombination of photoinjected electrons with the oxidized dye and/or with the triiodide ions in the redox mediator. The NR 1-D TiO_2 electrodes could improve light harvesting, provide direct electron pathways and also have minimal light loss caused by back scattering. Hence, the design of the TiO_2 NP-NR composite film will balance the surface area and light scattering thus enhancing performance of the DSSC with TiO_2 NPs-NRs composite electrode is better than those with only NP or NR mesoporous electrode (Hafez et al., 2010).

The light scattering ability of composite photoelectrode was studied using the visible absorption spectroscopy. The porous structure inside nanorods may also help scatter incident light and effectively enhance its optical pathway. Figure 6.7 showed the visible absorption spectra of composite electrodes containing different contents of electrospun TiO_2 nanorods. As expected, the nanoparticles-nanorods composite electrodes showed increased light absorption in the visible region. The composite photoanode film containing TiO_2 nanorods showed a strong light reflectance from 400 to 800 nm. It can be ascribed partly to an elongated optical path length of the longer wavelength incident light caused by light scattering of the TiO_2 nanorods. In other words, light harvesting efficiency is improved by incorporating electrospun TiO_2 nanorods into TiO_2 particles films. The high scattering effect of porous nanorods will definitely increase the light

harvesting efficiency of photoanode film, thus lead to an enhanced J_{sc} for the DSSCs (Huang et al., 2012; Chen et al., 2013). The increase in J_{sc} is probably due to both the light scattering caused by the NRs and good dye uptake (Hong et al., 2014). The incident photon-to-current conversion efficiency IPCE is defined as the number of generated electrons divided by the number of incident photons and was shown in the Figure 6.9. The IPCE spectrum showed that the maximum efficiency of DSSC was increased and also indicated that efficient light harvesting by the TiO_2 nanorod (Song et al., 2005).

The inclusion of NRs in the composite photoanode has its advantages, since it can help to form viscous stable TiO_2 colloid and preserve film after coating and sintering. A pure TiO_2 nanoparticle film may have crack induced due to excessive contractions during sintering. In the composite TiO_2 colloid containing NRs, NR shrinkage is negligible during the coating and sintering. Hence, the low percentage addition of electrospun TiO_2 nanorods can prevent the film from contraction and continuous crack-free film formed, which have advantages in terms of diffusion and electrons transport (Huang et al., 2012). Figure 6.10 showed the EIS analysis of DSSCs containing TiO_2 nanoparticles-nanorods at different nanorod weight ratios. The calculated charge transfer resistance R_2 are listed in Table 6.4. Semicircle referring to R_2 indicates that the process of charge transfer at the TiO_2/dye/electrolyte interface that became a dominant factor for the DSSC photovoltaic performance (Zhu et al., 2014). The charge transport resistance (R_2) is affecting the overall DSSC performance of the cell and thus as expected, the lowest R_2 is given by highest efficiency DSSC. From the fitting results obtained using Nova software, the lowest value of charge transport resistance (R_2) is observed for TiO_2 NPs-NRs composite DSSC with inclusion of 10 wt.% NR (CP1) in which the values are (63.00 ± 0.13) Ω and also possesses highest efficiency of (1.317 ± 0.035)% from (1.076 ± 0.042)% (NPs electrode). Saji and Pyo (2010) have reported that the incorporation of 10 wt.% nanorods

into a nanoparticle matrix leads to reduced charge transport resistance (R_2). This is because the optimum material should have higher surface area, better light scattering properties and higher yield for electron transportation. Hence, we deduced that the enhanced transport of electron and light scattering are the main reasons for improved DSSC (Huang et al., 2012). All these results show that TiO_2 NRs are good photoanode candidates due to their enhanced dye loading, strong light scattering ability and excellent electron transport performance (Chen et al., 2013). This summarized that the contribution of 10 wt.% 1-D TiO_2 nanorods towards the improvement in the charge transport and resulted increase in cell efficiency. Hence, this TiO_2 nanorods percentages was further used for the next DSSC systems.

The effects of adding additives in order to improve the DSSC performance was also studied in the third DSSC system. There were two additives being used in these studies which were chenodeoxycholic (CDCA) acid and ferulic acid (FA). Figure 6.11 showed the absorption spectra anthocyanin-pigmented TiO_2 composite electrode with 10 wt.% TiO_2 NRs at different weight percentage (1, 2, 3, 4 and 5 wt.%) of CDCA additive. The addition of CDCA resulted in slight increase in maximum wavelength intensity. The addition of CDCA that improve the efficiency performance been observed in other published report. Ismail et al. (2018) stated that the addition of CDCA can slightly improve the efficiency of DSSC sensitized using anthocyanin from mangosteen pericarp from 0.36% to 0.56% efficiency. This is because CDCA acts as a co-absorbance by adding additional -COOH and -OH groups into the anthocyanin sensitizer that increased anchorage onto the TiO_2 surface. As referring to Figure 6.13 and Table 6.5, the *J-V* analysis showed that the addition of 1 wt% CDCA (C1) contribute to slight increase in the efficiency performance of (1.393 ± 0.039)% from (1.317 ± 0.035)% (without addition of CDCA). The J_{sc} value was (4.835 ± 0.095) mA cm^{-2}. On increasing the percentages

from 2 to 5 wt.% (C2 to C5), the J_{sc} and η values continuously decreased. This showed that the CDCA only slightly increase the DSSCs performance since previous results obtained without addition of CDCA was J_{sc} of (4.808 ± 0.105) mA cm^{-2} and efficiency (η) performance of (1.317 ± 0.035)%. This indicated that CDCA was unable to significantly improved the 10 wt.% NPs-NRs composite DSSCs based on anthocyanin from *Ixora siamensis* for this study.

Figure 6.12 shows the absorption spectra anthocyanin-pigmented TiO_2 composite electrode with 10 wt.% TiO_2 NRs at different weight percentage (1, 2, 3, 4 and 5 wt.%) of FA additive. The results showed that 3 wt.% of FA (F3) addition resulted in highest shift in maximum wavelength from 528 to 532 nm with highest intensity absorbance of 1.00. This result correlated with that published by Jiao et al. (2016) who also reported that FA addition affect the spectrophotometric curves and verified that FA promoted an increase in the maximum absorption wavelength known as bathochromic effect ($\Delta\lambda_{max}$) and absorbance intensity known as hyperchromic effect (ΔA_{max}). Both bathochromic and hyperchromic effect of visible spectroscopy depended on the concentration of the FA (Gris et al., 2007). The increase in peak absorption and maximum absorption shift to higher wavelength (bathochromic shift) are important properties that affect the DSSCs performance since this showed that the dye anchored to the surface of TiO_2 (Wongcharee et al., 2007).

Increasing the FA percentages, increased the intensity of maximum absorption in visible spectrum. This led to increase in light collection and eventually to a larger J_{sc} and increase in efficiency (Yang et al., 2014). This is attributed to an increase in the amount of dye adsorbed onto the TiO_2 surface as reported by Ooyama and Harima (2012). The results from the visible spectroscopy are comparable with the results from the *J-V* curves.

As referring to Figure 6.14 and Table 6.6, the addition of FA increased the intensity of maximum absorbance, J_{sc} and η values from 1 to 3 wt.% before decreasing beyond 3 wt.% FA. 3 wt.% FA (F3) exhibited to the highest J_{sc} and η values of (6.178 ± 0.128) mA cm^{-2} and (1.917 ± 0.045)%, respectively. This showed that FA significantly improved the 10 wt.% NPs-NRs composite DSSCs based on anthocyanin dyes since previous results obtained without addition of FA was J_{sc} of (4.808 ± 0.105) mA cm^{-2} and efficiency (η) performance of (1.317 ± 0.035)%. The high scattering effect of 3 wt.% FA (F3) as observed from visible spectroscopy is evidence of increase in the light collection efficiency of the photoanode leading to enhanced J_{sc} for the DSSCs (Huang et al*.,* 2012; Chen et al*.,* 2013). As the J_{sc} increase, the efficiency also increases, which shows the higher amount of electron can transfer from the sensitizer to TiO_2 surface (Ismail et al., 2018).

The lowest R_s (0.014 ± 0.004 Ω-cm^2) and high R_{sh} (2.505 Ω-cm^2 ± 0.050) obtained for 3 wt.% FA (F3) as displayed in Table 6.6 also contributed to the enhancement in efficiency. As expected, the lowest R_2 correlated with highest efficiency performance since the values of R_2 (39.78 ± 0.17) Ω for 3 wt.% FA was the lowest as listed in Table 6.8. The IPCE spectrum, Figure 6.16 also showed that the maximum efficiency of 36% for DSSC with 3 wt.% FA (F3) was the highest indicated efficient light harvesting. The results are comparable with 37% obtained by other researchers that also worked on the natural dyes (Chang et al., 2013). As mentioned before, decreasing the series resistance (R_s) and increasing the shunt resistance (R_{sh}), lead to reduce the overvoltage for diffusion and electron transfer will cause the *FF* to rise, consequently resulting in better efficiency (Gong et al*.,* 2017; Liu et al., 2018). Low shunt resistance (R_{sh}) implies that the current has alternative ways of crossing the cell other than the desired one which caused lower efficiency (Abdel-latif et al., 2015). The larger (R_{sh}) originate from reduced charge

recombination can be ascribed to the field-assisted charge collection which leads to lower possibilities for the electrons to back react at the TiO_2/electrolyte interfaces (Liu et al., 2018).

Godibo et al. (2015) stated that the natural dye mostly has hydroxyl (OH) ligands and O ligands and lacks the carboxyl (–COOH) ligands. Hence, the anthocyanin molecule without addition of FA have no –COOH functional groups to bind chemically onto the TiO_2 surfaces and facilitate electron injection from the LUMO of the dye to the conduction band of TiO_2 (Godibo et al., 2015). This possibility lead to low efficiency of NPs-NRs composite system without addition of additives while with added FA the DSSC performance increased. This indicated that FA was capable to act as anchoring group since it contained –COOH ligands that can combined with the –OH groups of the TiO_2 electrode to produce the ester moiety and boost the coupling effect of the electrons in the TiO_2 conduction band so as to provide a rapid electron-transport rate (Kim et al., 2014). The preferred –COOH anchoring groups, also because they react spontaneously with the surface hydroxylic groups of the oxide surfaces to form the corresponding esters, linkages that exhibit good stability (Longo & De Paoli, 2003). Efficient dyes for DSSCs must contain an anchoring group for adsorption onto a metal semiconducting oxide. Adsorption provides a means for electron injection, which is the process that initiated current flow in a DSSC. The carboxyl group –COOH is the most frequently used anchoring group, as in ruthenium-complex based dyes. It is well-known that the anchor group plays a crucial role not only in binding the dyes with the oxide surface, but also affecting electron injection rate and packing of adsorbed dyes (Zhang & Cole, 2015). Hence, more electrons were able to flow into the TiO_2 structure which led to improvement in photovoltaic performance. However, when increase the FA percentages beyond 3 wt.%, the J_{sc} and efficiency values decreased. The decreasing performance may

be related to the increased in series resistant (R_s) and decreased in shunt resistance (R_{sh}) since more electrons are lost and dropping of the voltage and results in reducing photocurrent. This also may be due to electron scattering and trap electrons led to conversion efficiency of DSSCs begin to fall (Rho et al., 2015).

Nevertheless, ferulic acid (FA) also act as the good UV absorber which can harvest more light and increase in J_{sc} values which led to an increase in efficiency performance. FA also known as light absorbers that can strongly absorb broad spectrum visible light. FA provided the good photostabilization as UV absorbers. Photostabilization effect appears to be due to a competitive energy absorption of UV photons by the absorber molecules (Lucero et al., 2012). FA also can act as co-pigments (Jiao et al., 2016) and can be added in the anthocyanin dye extract to prolong its lifetime and increase the energy conversion efficiency. Other researcher has reported the addition of co-pigment that can help in enhancing efficiency performance. Munawaroh et al. (2016) used ascorbic and malic acid to improve the performance of DSSC based mangosteen pericarp which showed that the efficiency increase to 0.292 and 0.303%, respectively compared to sample without addition of co-pigment that exhibited only 0.199%. Heera & Cindrella (2010) theoretically evaluated the potential of ferulic acid as a photosensitizer. They concluded that ferulic acid proved to be a potential pigment for efficient application in DSSC. In this study, addition of FA able to enhance the performance of the DSSCs in which addition of 3 wt.% FA (F3) significantly improved the DSSC performance.

CHAPTER 8: CONCLUSIONS AND SUGGESTIONS FOR FUTURE WORKS

The objectives of this study have been successfully accomplished. Firstly, it is the aim of this work to confirm that the natural dye extraction from fruit pericarps of *Ixora siamensis* contained anthocyanin. Hence, the extraction have proven to contain anthocyanin compounds which are cyanidin-3-rutinoside, delphinidin glucoside and peonidin-3-glucoside. The detection peak of fruit pericarp extraction on the visible spectroscopy at λ=522 nm also convinced the presence of anthocyanin. The potential of natural dyes from fruit pericarp of *Ixora siamensis* as a source of natural colourant have also been investigated, evaluated and highlighted in this study.

The second aim is to determine the optimized parameters for anthocyanin extraction from fruit pericarps of *Ixora siamensis* as the source of natural colourant. The extraction parameters have been optimized in terms of solvent composition, soaking time and extraction temperatures by means of the Response Surface Methodology (RSM) technique. The optimized extraction parameters obtained via RSM techniques are additions of 0.5% TFA content in methanol, 119 min soaking time of the TiO_2 assembly into the sensitizer solution and extraction temperature of 80 ºC. These parameters were further used to extract the natural dyes from fruit pericarp of *Ixora siamensis* to be used as the sensitizer for DSSC applications.

The next objective is to produce the TiO_2 nanostructures from combining sol-gel and electrospinning methods followed with post-treatment process. This study also demonstrated the production of TiO_2 nanofibers via sol-gel synthesis and optimizing the electrospinning parameter since it can be influenced by several factors which have been discussed in Chapter 2. We highlighted the effects of polymer concentrations and applied voltages for our study. Uniform beadless cylindrical TiO_2 nanofibers with average fiber

diameter of 177 nm were successfully obtained from 13.2 wt.% PVP polymer, with distance from tip-to collector of 14 cm, electrospun at 20 kV with electric field of 1.43 kV/cm in which the morphology of the obtained nanofibers was characterized through FESEM analysis and Image J software. The TiO_2 nanofibers were sintered at 500 ℃ with 2 ℃/min heating rate and ground to obtain the TiO_2 nanorods. TiO_2 nanorods with average diameter of 90 nm was produced which were examined using FESEM analysis and Image J software. EDX studies showed the presence of titanium and oxygen to confirm the nanorods obtained were pure TiO_2 with no other impurities. The dominant anatase TiO_2 phase, produced via sintering at 500 ℃ at a heating rate of 2 ℃/min as proven from XRD. Peaks were detected at 2θ angles of 25.5°, 37.2°, 37.9°, 38.8°, 48.2° and 54° representing the planes of (101), (103), (004), (200), (112) and (211) (JCPDS No. 21-1272) with strongest peak at 2θ=25.5°. Through different weight percentages of TiO_2 nanorods in the composite photoanode NPs-NRs, the surface morphology were examined via FESEM analysis in which these composite photoanodes were used for DSSC fabrications.

The final aim includes efforts in improving performance of the dye-sensitized solar cells (DSSCs) which has been fabricated using three different systems. For the first DSSC systems, the photoanode was made from commercial TiO_2 nanoparticles (NPs) sensitized at 3 wt.% of anthocyanin dye (D3) that exhibited J_{sc} of (4.456 ± 0.101) mA cm^{-2}, V_{oc} of (0.423 ± 0.006) V, FF of (0.571 ± 0.008), efficiency of (1.076 ± 0.042)%, R_s of (0.024 ± 0.003) Ω-cm^2, R_{sh} of (1.904 ± 0.040) Ω-cm^2 and R_2 of (66.50 ± 0.12) Ω. The DSSC performance further increased in the second DSSC systems with the combination of TiO_2 nanorods (NRs) (produced earlier in this study) and commercial TiO_2 nanoparticles (NPs) to form a composite photoanode NPs-NRs. The second DSSCs systems achieved improvement with inclusion of 10 wt.% NRs (CP1) to the optimized 3

wt.% anthocyanin dye with J_{sc} of (4.808 ± 0.105) mA cm^{-2}, V_{oc} of (0.458 ± 0.003) V, *FF* of (0.599 ± 0.005), efficiency of (1.317 ± 0.035)%, R_s of (0.019 ± 0.002) Ω-cm^2, R_{sh} of (2.179 ± 0.042) Ω-cm^2 and R_2 of (63.00 ± 0.13) Ω. For the third DSSC systems, CDCA and FA were used as additives and were added to the optimized 3 wt.% anthocyanin dye. These third systems used the composite photoanode with inclusion of 10 wt.% NRs. The performance was greatly enhanced by addition of 3 wt.% FA (F3). The J_{sc}, V_{oc}, *FF,* efficiency, R_s, R_{sh} and R_2 values were (6.178 ± 0.128) mA cm^{-2}, (0.473 ± 0.009) V, (0.656 ± 0.010), (1.917 ± 0.045)%, (0.014 ± 0.004) Ω-cm^2, (2.505 ± 0.050) Ω-cm^2 and R_2 values of (39.78 ± 0.17). CDCA was not suitable to be used in DSSC based anthocyanin from *Ixora siamensis* since it slightly increased the DSSC performance with J_{sc} of (4.835 ± 0.095) mA cm^{-2}, V_{oc} of (0.458 ± 0.006) V, *FF* of (0.629 ± 0.010), efficiency of (1.393 ± 0.039)%, R_s of (0.018 ± 0.005) Ω-cm^2, R_{sh} of (2.285 ± 0.035) Ω-cm^2 and R_2 values of (61.20 ± 0.15) Ω for 1 wt.% (C1). Based on the results obtained from the three systems, it can be summarized that the anthocyanin from fruit pericarp of *Ixora siamensis* have a big potential to be used as natural sensitizer in DSSCs application. The addition of 10 wt.% TiO_2 nanorod onto TiO_2 nanoparticle improved the DSSCs performance. Apart from that, the addition of 3 wt.% FA successfully increased the efficiency of DSSCs.

Based on the experience gained from this study, several suggestions for future work are recommended. Firstly, since ferulic acid (FA) additive showed great enhancement in energy conversion efficiency in our study, other possible additives as anchoring group could be considered to be added in order to improve the DSSC performance. Second, different preparation technique such as hydrothermal, electrochemical anodization and template-assisted method can be implemented to obtain the 1-D TiO_2 nanostructures. Sol-gel and electrospinning technique is our prime process to obtain the 1-D TiO_2 nanostructures. Lastly, other researchers can also look into potential of other different

one-dimensional (1-D) TiO_2 nanostructures such as nanofibers, nanotubes and nanowires as the possible choices of metal oxide semiconductor (MOS) materials since different morphologies will affect the DSSC performance. Herein, we used the 1-D TiO_2 nanorods as the MOS material.

REFERENCES

Abdel-latif, M. S., Abuiriban, M. B., Dahoudi, N. A., Al-Kahlout, A. M., Taya, S. A., El-Agez, T. M., & El-Ghamri, H. S. (2015). Dye-sensitized solar cells using fifteen natural dyes as sensitizers of nanocrystalline TiO_2. *Science, Technology and Development*, *34*(3), 135-139.

Achari, M. B., Elumalai, V., Vlachopoulos, N., Safdari, M., Gao, J., Gardnera, J. M., & Kloo, L. (2013). A quasi-liquid polymer-based cobalt redox mediator electrolyte for dye-sensitized solar cells. *Physical Chemistry Chemical Physics*, *15*(40), 17419-17425.

Adedokun, O., Titilope, K., & Awodugba, A. O. (2016). Review on natural dye-sensitized solar cells (DSSCs). *International Journal of Engineering Technologies*, *2*(2), 34-41.

Aduloju, K. A., Mohamed, B. S., & Simiyu, J. (2011). Effect of extracting solvents on the stability and performances of dye- sensitized solar cell prepared using extract from *Lawsonia inermis*. *Fundamental Journal of Modern Physics*, *1*(2), 261-268.

Ahn, Y. C., Park, S. K., Kim, G. T., Hwang, Y.-J., Lee, C. G., Shin, H. S., & Lee, J. K. (2006). Development of high efficiency nanofilters made of nanofibers. *Current Applied Physics*, *6*, 1030-1035.

Al-Bat'hi, S. A. M., Alaei, I., & Sopyan, I. (2013). Natural photosensitizers for dye sensitized solar cells. *International Journal of Renewable Energy Research*, *3*(1), 138-143.

Alhamed, M., Issa, A. S., & Doubal, A. W. (2012). Studying of natural dyes properties as photo-sensitizer for dye sensitized solar cells (DSSC). *Journal of the Electron Devices*, *6*, 1370-1383.

Andersen, O. M., & Jordheim, M. (2006). The anthocyanins. In O. M. Andersen & K. R. Markham (Eds.), *Flavonoids: chemistry, biochemistry and applications* (pp. 471-552). London, Taylor & Francis Group: CRC Publishers.

Anjusree, G. S., Nair, A. S., Nair, S. V., Vadukumpully, S., Subramanian, R. V., Sivakumar, N., Ramakrishna, S., Naira, S. V., & Nair, A. S. (2013). Fabricating fiber, rice and leaf-shaped TiO_2 by tuning the chemistry between TiO_2 and the polymer during electrospinning. *RSC Advances*, *3*(37), 16720-16727.

Armstrong, G. A., & Hearst, J. E. (1996). Carotenoids 2: Genetics and molecular biology of carotenoid pigment biosynthesis. *Federation of American Societies for Experimental Biology Journal*, *10*(2), 228-237.

Arifin, Z., Soeparman, S., Widhiyanuriyawan, D., & Suyitno, S. (2017). Performance enhancement of dye-sensitized solar cells using a natural sensitizer. *International Journal of Photoenergy*, *2017*, 1-5.

Arof, A. K., Amirudin, S., Yusof, S. Z., & Noor, I. M. (2014). A method based on impedance spectroscopy to determine transport properties of polymer electrolytes. *Physical Chemistry Chemical Physics*, *16*(5), 1856-1867.

Arof, A. K., Aziz, N., Mat Nor, N. A., Rahim, A. S., & Kufian, M. Z. (2017). Imaging of electrospun nanoparticle electrode materials. In A. Méndez-Vilas, (Eds.), *Microscopy and imaging science: practical approaches to applied research and education* (pp. 438-449). Spain: Formatex Research Center.

Aydar, A. Y., Bağdatlıoğlu, N., & Köseoğlu, O. (2017). Effect of ultrasound on olive oil extraction and optimization of ultrasound-assisted extraction of extra virgin olive oil by response surface methodology (RSM). *Grasas Aceites*, *68*(2), 1-11.

Aydar, A. Y. (2019). Statistical methods in optimization of food materials. *European International Journal of Science and Technology*, *8*(3), 33-40.

Aziz, M. F., Noor, I. M., Sahraoui, B., & Arof, A. K. (2014). Dye-sensitized solar cells with PVA–KI–EC–PC gel electrolytes. *Optical and Quantum Electronics*, *46*(1), 1-9.

Bai, S., Bu, C., Tai, Q., Liang, L., Liu, Y., You, S., Yu, Z., Guo, S., & Zhao, X. (2013). Effects of bis(imidazolium) molten salts with different substituents of imidazolium cations on the performance of efficient dye-sensitized solar cells. *ACS Applied Materials & Interfaces*, *5*(8), 3356-3361.

Bakhshayesh, A. M., & Mohammadi, M. R. (2013). Development of nanostructured porous TiO_2 thick film with uniform spherical particles by a new polymeric gel process for dye-sensitized solar cell applications. *Electrochimica Acta*, *89*, 90-97.

Bandara, T. M. W. J., Jayasundara, W. J. M. J. S. R., Dissanayake, M. A. K. L., Furlani, M., Albinsson, I., & Mellander, B.-E. (2013). Effect of cation size on the performance of dye sensitized nanocrystalline TiO_2 solar cells based on quasi-solid state PAN electrolytes containing quaternary ammonium iodides. *Electrochimica Acta*, *109*, 609-616.

Bandara, T. M. W. J., Aziz, M. F., Fernando, H. D. N. S., Careem, M. A., Arof, A. K., & Mellander, B.-E. (2015). Efficiency enhancement in dye-sensitized solar cells with a novel PAN-based gel polymer electrolyte with ternary iodides. *Journal of Solid State Electrochemistry*, *19*, 2353-2359.

Barnes, J. S., Nguyen, H. P., Shen, S., & Schug, K. A. (2009). General method for extraction of blueberry anthocyanins and identification using high performance liquid chromatography–electrospray ionization-ion trap-time of flight-mass spectrometry. *Journal of Chromatography A*, *1216*, 4728-4735.

Bas, D., & Boyaci, I. H. (2007). Modelling and optimization I. Usability of response surface methodology. *Journal of Food Engineering*, *78*, 836-845.

Bauer, C., Boschloo, G., Mukhtar, E., & Hagfeldt, A. (2002). Ultra-fast studies of electron injection in Ru dye sensitized SnO_2 nanocrystalline thin film. *International Journal of Photoenergy*, *4*(1), 17-20.

Bellan, L. M., & Craighead, H. G. (2011). Applications of controlled electrospinning systems. *Polymers for Advanced Technologies*, *22*(3), 304-309.

Bezerra, M. A., Santelli, R. E., Oliveira, E. P., Villar, L. S., & Escaleira, L. A. (2008). Response surface methodology (RSM) as a tool for optimization in analytical chemistry. *Talanta*, *76*(5), 965-977.

Bhardwaj, N., & Kundu, S. C. (2010). Electrospinning: A fascinating fiber fabrication technique. *Biotechnology Advances*, *28*(3), 325-347.

Birse, M. J. (2007). *The color of red wine*. (Doctoral dissertation). School of Agriculture, Food and Wine, University of Adelaide, Australia.

Bognitzki, M., Czado, W., Frese, T., Schaper, A., Hellwig, M., Steinhart, M., Greiner, A., & Wendorff, J. H. (2001). Nanostructured fibers via electrospinning. *Advanced Materials, 13*(1), 70-72.

Boschloo, G., & Hagfeldt, A. (2009). Characteristics of the iodide/triiodide redox mediator in dye-sensitized solar cells. *Accounts of Chemical Research*, *42*(11), 1819-1826.

Bridgers, E. N., Chinn, M. S., & Truong, V.-D. (2010). Extraction of anthocyanins from industrial purple-fleshed sweet potatoes and enzymatic hydrolysis of residues for fermentable sugars. *Industrial Crops and Products*, *32*, 613-620.

Cacace, J. E., & Mazza, G. (2003). Optimization of extraction of anthocyanins from black currants with aqueous ethanol. *Journal of Food Science*, *68*(1), 209-215.

Calandra, P., Calogero, G., Sinopoli, A., & Gucciardi, P. G. (2010). Metal nanoparticles and carbon-based nanostructures as advanced materials for cathode application in dye-sensitized solar cells. *International Journal of Photoenergy*, *2010*, 1-15.

Calogero, G., & Di Marco, G. (2008). Red Sicillian orange and purple eggplant fruits as natural sensitizers for dye-sensitized solar cells. *Solar Energy Material Solar Cell*, *92*, 1341-1346.

Calogero, G., Sinopoli, A., Citro, I., Di Marco, G., Petrov, V., Diniz, A. M., Parola, A.J., & Pina, F. (2013). Synthetic analogues of anthocyanins as sensitizers for dye-sensitized solar cells. *Photochemical & Photobiological Sciences*, *12*(5), 883-894.

Cameron P. J., & Peter L. M. (2003). Characterization of titanium dioxide blocking layers
in dye-sensitized nanocrystalline solar cells. *Journal of Physical Chemistry B*, *107*(51), 14394-14400.

Cao, S., Liu, Z., Hu, B., & Liu, H. (2010). Stabilization of electrospun poly(vinyl alcohol) nanofibrous mats in aqueous solutions. *Chinese Journal of Polymer Science*, *28*(5), 781-788.

Caratão, B., Carneiro, E., Sá, P., Almeida, B., & Carvalho, S. (2014). Properties of electrospun TiO_2 Nanofibers. *Journal of Nanotechnology*, *2014*, 1-5.

Carley, K. M., Kamneva, N. Y., & Reminga, J. (2004). Technical report of response surfaces methodology CASOS. USA: Carnegie Mellon University.

Castañeda-Ovando, A., Pacheco-Hernández, M. D. L., Páez-Hernández, M. E., Rodríguez, J. A., & Galán-Vidal, C. A. (2009). Chemical studies of anthocyanins: A review. *Food Chemistry*, *113*(4), 859-871.

Cavaliere, S., Subianto, S., Savych, I., Tillard, M., Jones, D. J., & Rozière, J. (2013). Dopant-driven nanostructured loose-tube SnO_2 architectures: alternative electrocatalyst supports for proton exchange membrane fuel cells. *Journal of Physical Chemistry C*, *117*, 18298-18307.

Chang, H., & Lo, Y.-J. (2010). Pomegranate leaves and mulberry fruit as natural sensitizers for dye sensitized solar cells. *Journal of Solar Energy*, *84*, 1833-1837.

Chang, H., Kao, M.-J., Chen, T.-L., Chen, C.-H., Cho, K.-C., & Lai, X.-R. (2013). Characterization of natural dye extracted from Wormwood and Purple Cabbage for dye-sensitized solar cells. *International Journal of Photoenergy*, *2013*, 1-8.

Charles, C. S., Sunao, S., & Janusz, N. (2005). *Materials for energy conversion devices*. New York: Woodhead Publishing Limited.

Chen, W., Sun, X., Cai, Q., Weng, D., & Li, H. (2007). Facile synthesis of thick ordered mesoporous TiO_2 film for dye-sensitized solar cell use. *Electrochemistry Communications*, *9*, 382-385.

Chen, H.-Y., Zhang, T.-L., Fan, J., Kuang, D.-B., & Su, C.-Y. (2013). Electrospun hierarchical TiO_2 nanorods with high porosity for efficient dye-sensitized solar cells. *ACS Applied Materials & Interfaces*, *5*(18), 9205-9211.

Chen, S., Yu, M., Han, W.-P., Yan, X., Liu Y.-C., Zhang, J.-C., Zhang, H.-D., Yu, G.-F., & Long, Y.-Z. (2014). Electrospun anatase TiO_2 nanorods for flexible optoelectronic devices. *RSC Advances*, *4*, 46152-46156.

Chien, C.-Y., & Hsu, B.-D. (2013). Optimization of the dye-sensitized solar cell with anthocyanin as photosensitizer. *Solar Energy*, *98*, 203-211.

Chien, C.-Y., & Hsu, B.-D. (2014). Performance enhancement of dye-sensitized solar cells based on anthocyanin by carbohydrates. *Solar Energy*, *108*, 403-411.

Chong, E. J., Phan, T. T., Lim, I. J., Zhang, Y. Z., Bay, B. H., Ramakrishna, S., & Lim, C. T. (2007). Evaluation of electrospun PCL/gelatin nanofibrous scaffold for wound healing and layered dermal reconstitution. *Acta Biomaterialia*, *3*(3), 321-330.

Chowdhury, M., & Stylios, G. (2010). Effect of experimental parameters on the morphology of electrospun nylon 6 fibres. *International Journal of Basic & Applied Sciences*, *10*(6), 70-78.

Chrissafis, K., Paraskevopoulos, K. M., Papageorgiou, G. Z., & Bikiaris, D. N. (2008). Thermal and dynamic mechanical behavior of bionanocomposites: fumed silica

nano particles dispersed in poly (vinyl pyrrolidone), chitosan, and poly (vinyl alcohol). *Journal of Applied Polymer Science*, *110*, 1739-1749.

Cissé, M., Bohuonb, P., Sambea, F., Kanea, C., Sakhoa, M., & Dornier, M. (2012). Aqueous extraction of anthocyanins from *Hibiscus sabdariffa*: experimental kinetics and modeling. *Journal of Food Engineering*, *109*(1), 16-21.

Cozzoli, P. D., Kornowski, A., & Weller, H. (2003). Low-temperature synthesis of soluble and processable organic-capped anatase TiO_2 nanorods. *Journal of American Chemical Society*, *125*, 14539-14548.

Cruz, R., Tanaka, D. A. P., & Mendes, A. (2012). Reduced graphene oxide films as transparent counter-electrodes for dye-sensitized solar cells. *Solar Energy*, *86*, 716-724.

Cuangchote, S., Sgawa, T., & Yoshikawa, S. (2008). Efficient dye-sensitized solar cells using electrospun TiO_2 nanofibers as a light harvesting layer. *Applied Physics Letters*, *93*, 1-3.

Cushing, B. L., Kolesnichenko, V. L., & O'Connor, C. J. (2004). Recent advances in the liquid-phase syntheses of inorganic nanoparticles. *Chemical Reviews*, *104*(9), 3893-3946.

Dalton, P. D., Vaquette, C., Farrugia, B. L., Dargaville, T. R., Brown, T. D., & Hutmacher, D. W. (2013). Electrospinning and additive manufacturing: converging technologies. *Biomaterials Science*, *1*(2), 171-185.

Davies, K. M. (2004). *Plant pigments and their manipulation*. USA: Blackwell Publishing Limited.

David, I., Ştefănuţ, M. N., Căta, A., Ienaşcu, I., Pop, R., Tănasie, C., & Balcu, I. (2009). Study of anthocyanins from *Vaccinium myrtillus* L. frozen fruits. *Journal of Agroalimentary Processes and Technologies*, *15*(3), 348-352.

De Block, P. (1998). The African species of *Ixora* (*Rubiaceae-Pavetteae*). *Opera Botanica Belgica*, *9*, 1-218.

De Freitas, J. N., Nogueira, A. F., & De Paoli, M.-A. (2009). New insights into dye sensitized solar cells with polymer electrolytes. *Journal of Materials Chemistry*, *19*(30), 5279-5294.

Deitzel, J. M., Kleinmeyer, J., Harris, D., & Beck Tan, N. C. (2001). The effect of processing variables on the morphology of electrospun nanofibers and textiles. *Polymer*, *42*, 261-272.

Delgado-Vargas, F., Jiménez, A. R., & Paredes-López, O. (2000). Natural pigments: carotenoids, anthocyanins, and betalains-characteristics, biosynthesis, processing, and stability. *Critical Reviews in Food Science and Nutrition*, *40*(3), 173-289.

Delgado-Vargas, F., & Paredes-López, O. (2003). Anthocyanins and betalains. In F. Delgado-Vargas and O. Paredes-Lopez (Eds.), *Natural colorants for food and nutraceutical uses* (pp. 167-219). USA: CRC Publishers.

Denaro, T., Baglio, V., Girolamo, M., Antonucci, V., Arico, A. S., Matteucci, F., & Ornelas, R. (2009). Investigation of low cost carbonaceous materials for application as counter electrode in dye-sensitized solar cells. *Journal of Applied Electrochemistry*, *39*, 2173-2179.

Dias, A. L. S., Rozet, E., Chataigné, G., Oliveira, A. C., Rabelo, C. A. S., Hubert, P. Rogez, H., & Quetin-Leclercq, J. (2012). A rapid validated UHPLC–PDA method for anthocyanins quantification from *Euterpe oleracea* fruits. *Journal of Chromatography B*, *907*, 108-116.

Dissanayake, M. A. K. L., Thotawatthage, C. A., Senadeera, G. K. R., Bandara, T. M. W. J., Jayasundara, W. J. M. J. S. R., & Mellander, B.-E. (2013). Efficiency enhancement in dye sensitized solar cells based on PAN gel electrolyte with Pr_4NI + MgI_2 binary iodide salt mixture. *Journal of Applied Electrochemistry*, *43*, 891-901.

Duan, W., Jin, S., Zhao, G., & Sun, P. (2015). Microwave-assisted extraction of anthocyanin from Chinese bayberry and its effects on anthocyanin stability. *Food Science and Technology*, *35*(3), 524-530.

Elayappan, V., Panneerselvam, P., Nemala, S., Nallathambi, K. S., & Angaiah, S. (2015). Influence of PVP template on the formation of porous TiO_2 nanofibers by electrospinning technique for dye-sensitized solar cell. *Applied Physics A*, *120*, 1211-1218.

Enache-Pommer, E., Boercker, J. E., Aydil, E. S. (2007). Electron transport and recombination in polycrystalline TiO_2 nanowire dye-sensitized solar cells. *Applied Physics Letters*, *91*, 1-3.

Esposito, S. (2019). "Traditional" sol-gel chemistry as a powerful tool for the preparation of supported metal and metal oxide catalysts. *Materials*, *12*(4), 1-25.

Fan, G., Han, Y., Gu, Z., & Chen, D. (2008). Optimizing conditions for anthocyanin extraction from purple sweet potato using response surface methodology (RSM). *LWT - Food Science and Technology*, *41*, 155-160.

Fang, X., Ma, T., Guan, G., Akiyama, M., & Abe, E. (2004). Performances characteristics of dye-sensitized solar cells based on counter electrodes with Pt films of different thickness. *Journal of Photochemistry and Photobiology A: Chemistry, 164*(1), 179-182.

Farooq, Z., Rehman, S., & Abid, M. (2013). Application of response surface methodology to optimize composite flour for the production and enhanced storability of leavened flat bread (Naan). *Journal of Food Processing and Preservation*, *37*, 939-945.

Fernando, J. M. R. C., & Senadeera, G. K. R. (2008). Natural anthocyanins as photo sensitizers for dye-sensitized solar devices. *Current Science*, *95*, 663-666.

Fosberg, F. R., & Sachet, M.-H. (1989). Lectotypification of *Ixora coccinea* L. (*Rubiaceae*). *Taxon*, *38*, 485-489.

Frenot, A., & Chronakis, I. S. (2003). Polymer nanofibers assembled by electrospinning. *Current Opinion in Colloid & Interface Science*, *8*, 64-75.

Fridrikh, S. V., Yu, J. H., Brenner, M. P., & Rutledge, G. C. (2003). Controlling the fiber diameter during electrospinning. *Physical Review Letters*, *90*(4), 1-4.

Fujihara, K., Kumar, A., Jose, R., Ramakrishna, S., & Uchida, S. (2007). Spray deposition of electrospun TiO_2 nanorods for dye-sensitized solar cell. *Nanotechnology*, *18*(36), 1-5.

Fukai, Y., Kondo, Y., Mori, S., & Suzuki, E. (2007). Highly efficient dye-sensitized SnO_2 solar cells having sufficient electron diffusion length. *Electrochemistry Communications*, *9*(7), 1439-1443.

Furukawa, S., Iino, H., Iwamoto, T., Kukita, K., & Yamauchi, S. (2009). Characteristics of dye-sensitized solar cells using natural dye. *Thin Solid Films*, *518*, 526-529.

Garcia, C. G., Polo, A. S., & Iha, N. Y. M. (2003). Photoelectrochemical solar cell using extract of *Qugenia jambolana* as a natural sensitizer. *Annals of the Brazilian Academy of Sciences*, *75*(2),163-165.

Ghorani, B., & Tucker, N. (2015). Fundamentals of electrospinning as a novel delivery vehicle for bioactive compounds in food nanotechnology. *Food Hydrocolloids*, *51*, 227-240.

Godibo, D. J., Anshebo, S. T., & Anshebo, T. Y. (2015). Dye sensitized solar cells using natural pigments from five plants and quasi-solid state electrolyte. *Journal of the Brazilian Chemical Society*, *26*(1), 92-101.

Gokilamani, N., Muthukumarasamy, N., Thambidurai, M., Ranjitha, A., & Velauthapillai, D. (2015). *Basella alba rubra* spinach pigment-sensitized TiO_2 thin film-based solar cells. *Applied Nanoscience*, *5*(3), 297-303.

Gomez-Ortiz, N. M., Vazquez-Maldonado, I. A., Perez-Espadas, A. R., Mena-Rejon, G. J., Azamar-Barrios, J. A., & Oskam, G. (2010). Dye-sensitized solar cells with natural dyes extracted from achiote seeds. *Solar Energy Materials and Solar Cells*, *94*, 40-44.

Gong, J., Liang, J., & Sumathy, K. (2012). Review on dye-sensitized solar cells (DSSCs): Fundamental concepts and novel materials. *Renewable and Sustainable Energy Reviews*, *16*, 5848-5860.

Gong, J., Sumathy, K., Qiao, Q., & Zhou, Z. (2017). Review on dye-sensitized solar cells (DSSCs): Advanced techniques and research trends. *Renewable and Sustainable Energy Reviews*, *68*, 234-246.

Gonnet, J. F. (1998). Colour effects of co-pigmentation of anthocyanins revisited – 1. A colorimetric definition using the CIELAB scale. *Food Chemistry*, *63*(3), 409-415.

Gouvêa, A. C. M. S., Araujo, M. C. P. D., Schulz, D. F., Pacheco, S., Godoy, R. L. D. O., & Cabral, L. M. C. (2012). Anthocyanins standards (cyanidin-3-O-glucoside and cyanidin-3-O-rutinoside) isolation from freeze-dried açaí (*Euterpe oleraceae* Mart.) by HPLC. *Food Science and Technology*, *32*(1), 43-46.

Grätzel, M. (2001). Photoelectrochemical cells. *Nature*, *414*, 338-344.

Grätzel, M. (2003). Review of dye-sensitized solar cells. *Journal of Photochemistry and Photobiology C: Photochemistry Reviews*, *4*, 145-153.

Grätzel, M. (2004). Conversion of sunlight to electric power by nanocrystalline dye sensitized solar cells. *Journal of Photochemistry and Photobiology A*, *164*, 3-14.

Gris, E. F., Ferreira, E. A., Falcão, L. D., & Bordignon-Luiz, M. T. (2007). Influence of ferulic acid on stability of anthocyanins from *Cabernet Sauvignon* grapes in a model system and a yogurt system. *International Journal of Food Science & Technology*, *42*(8), 992-998.

Hafez, H., Lan, Z., Li, Q., & Wu, J. (2010). High efficiency dye-sensitized solar cell based on novel TiO_2 nanorod/nanoparticle bilayer electrode. *Nanotechnology, Science and Applications*, *3*, 45-51.

Haghi, A. K., & Akbari, M. (2007). Trends in electrospinning of natural nanofibers. *Physica Status Solidi (A), 204*(6), 1830-1834.

Haider, S., Al-Zeghayer, Y., Ali, F. A. A., Haider, A., Mahmood, A., Al-Masry, W. A., Imran, M., & Aijaz, M. O. (2013). Highly aligned narrow diameter chitosan electrospun nanofibers. *Journal of Polymer Research*, *20*(105), 1-11.

Haider, A., Haider, S., & Kang, I.-K. (2018). A comprehensive review summarizing the effect of electrospinning parameters and potential applications of nanofibers in biomedical and biotechnology. *Arabian Journal of Chemistry*, *11*(8), 1165-1188.

Hao, S., Wu, J., Huang, Y., & Lin, J. (2006). Natural dyes as photosensitizers for dye-sensitized solar cell. *Solar Energy*, *80*(2), 209-214.

Hamadanian, M., Safaei-Ghomi, J., Hosseinpour, M., Masoomi, R., Jabbari, V. (2014). Uses of new natural dye photosensitizers in fabrication of high potential dye-sensitized solar cells (DSSCs). *Materials Science in Semiconductor Processing*, *27*, 733-739.

Han, D.-W., Heo, J.-H., Kwak, D.-J., Han, C.-H., & Sung, Y.-M. (2009). Texture, morphology and photovoltaic characteristics of nanoporous F:SnO_2 films. *Journal of Electrical Engineering and Technology*, *4*(1), 93-97.

Han, S. O., Son, W. K., Youk, J. H., Lee, T. S., & Park, W. H. (2005). Ultrafine porous fibers electrospun from cellulose triacetate. *Materials Letters*, *59*, 2998-3001.

Hara, K., & Arakawa, H. (2003). Dye-sensitized solar cells. In A. Luque & S. Hegedus (Eds.), *Handbook of photovoltaic science and engineering* (pp. 663-700). UK: John Wiley & Sons.

Hassan, H. C., Abidin, Z. H. Z., Chowdhury, F. I., & Arof, A. K. (2016). A high efficiency chlorophyll sensitized solar cell with quasi solid PVA based electrolyte. *International Journal of Photoenergy*, *2016*(2), 1-9.

Haque, S. A., Handa, S., Peter, K., Palomares, E., Thelakkat, M., & Durrant, J. R. (2005). Supermolecular control of charge transfer in dye-sensitized nanocrystalline TiO_2 films: towards a quantitative structure-function relationship. *Angewandte Chemie International Edition*, *44*, 5740-5744.

Heera, T. R., & Cindrella, L. (2010). Molecular orbital evaluation of charge flow dynamics in natural pigments based photosensitizers. *Journal of Molecular Modeling*, *16*, 523-533.

Heredia, F. J., Francia-Aricha, E. M., Rivas-Gonzalo, J. C., Vicario, I. M., & Santos-Buelga, C. (1998). Chromatic characterization of anthocyanins from red grapes. I. pH effect. *Food Chemistry*, *63*, 491-498.

Hernández-Martínez, V., Salinas-Moreno, Y., Ramírez-Díaz, J. L., Vázquez-Carrillo, G., Domínguez-López, A., & Ramírez-Romero, A. G. (2016). Color, phenolic composition and antioxidant activity of blue tortillas from Mexican maize races. *CyTA - Journal of Food*, *14*(3), 473-481.

Hoffmann, M. R., Martin, S. T., Choi, W., & Bahnemann, D. W. (1995). Environmental applications of semiconductor photocatalysis. *Chemical Reviews*, *95*(1), 69-96.

Hojnik, M., Škerget, M., & Knez, Ž. (2008). Extraction of lutein from Marigold flower petals -Experimental kinetics and modelling. *LWT- Food Science and Technology*, *41*(10), 2008-2016.

Hong, C. K., Jung, Y. H., Kim, H. J., & Park, K. H. (2014). Electrochemical properties of TiO_2 nanoparticle/nanorod composite photoanode for dye-sensitized solar cells. *Current Applied Physics*, *14*, 294-299.

Hoshino, T. (1991). An approximate estimate of self-association constants and the self-stacking conformation of malvin quinonoidal bases studied by 1 H NMR. *Phytochemistry*, *30*, 2049-2055.

Hosseinpour, I., Riccio, M., & Almeida, M. S. S. (2014). Numerical evaluation of a granular column reinforced by geosynthetics using encasement and laminated disks. *Geotextiles and Geomembranes*, *42,* 363-373.

Houbiers, C., Lima, J. C., Macanita, A. L., & Santos, H. (1998). Color stabilization of malvidin 3-glucoside: Self-aggregation of the flavylium cation and copigmentation with the Z-chalcone form. *Journal of Physical Chemistry B*, *102*, 3578-3585.

Huang, Z. M., Zhang, Y. Z., Kotaki, M., & Ramakrishna, S. (2003). A review on polymer nanofibers by electrospinning and their applications in nanocomposites. *Composites Science and Technology*, *63*, 2223-2253.

Huang, X., Shen, P., Feng, X., Tan, Z., Zhao, B., & Tan, S. (2012). Efficient TiO_2 nanoparticles/nanorods composite electrodes for dye-sensitized solar cells. *NANO: Brief Reports and Reviews*, *7*(2), 1-9.

Hug, H., Bader, M., Mair, P., & Glatzel, T. (2014). Biophotovoltaics: natural pigments in dye-sensitized solar cells. *Applied Energy*, *115*, 216-225.

Huizhi, Z., Wu, L., Gao, Y., Ma, T. (2011). Dye-sensitized solar cells using 20 natural dyes as sensitizers. *Journal of Photochemistry and Photobiology A: Chemistry, 219*, 188-194.

Inagaki, M., Yang, Y., & Kang, F. (2012). Carbon nanofibers prepared via electrospinning. *Advanced Materials*, *24*(19), 2547-2566.

Inai, R., Kotaki, M., & Ramakrishna, S. (2005). Structure and properties of electrospun PLLA single nanofibers. *Nanotechnology*, *16*, 208-213.

Ismail, M., Ludin, N. A., Hamid, N. H., Ibrahim, M. A., & Sopian, K. (2018). The effect of chenodeoxycholic acid (CDCA) in Mangosteen (*Garcinia mangostana*) pericarps sensitizer for dye sensitized solar cell (DSSC). *Journal of Physics Conference Series*, *1083*(1), 1-7.

Ito, S., Chen, C.-Y., Comte, P., Nazeeruddin, M. K., Liska, P., Péchy, P., & Grätzel, M. (2007). Fabrication of screen-printing pastes from TiO_2 powders for dye-sensitised solar cells. *Progress in Photovoltaics: Research and Applications*, *15*(7), 603-612.

Jackman, R. L., Yada, R. Y., Tung, M. A., & Speers, R. A. (1987). Anthocyanins as food colorants-A review. *Journal of Food Biochemistry*, *11*(3), 201-247.

Jasim, K. E., Al-Dallal, S., Hassan, A. M. (2012). Henna (*Lawsonia inermis* L.) Dye-sensitized nanocrystalline Titania solar cell. *Journal of Nanotechnology*, *2012*, 1-6.

Jiao, Y., Zhang, Y., He, Z., Zhai, W., Gong, H., & Yang, Z. (2016). Effect of ferulic acid on the formation of pyranoanthocyanins from purple corn (*Zea mays* L.) cob in a model system and their effects on color. *International Journal of Food Properties*, *19*, 847-858.

Jin, L., Hu, B., Li, Z., Li, J., Gao, Y., Wang, Z., & Hao, J. (2018). Synergistic effects of electrical stimulation and aligned nanofibrous microenvironment on growth behavior of mesenchymal stem cells. *ACS Applied Materials & Interfaces*, *10*, 18543-18550.

Jinchu, I., Sreekala, C. O., & Sreelatha, K. S. (2014). Dye sensitized solar cell using natural dyes as chromophores – Review. *Materials Science Forum*, *771*, 39-51.

Ju, Z. Y., & Howard, L. (2003). Effects of solvent and temperature on pressurized liquid extraction of anthocyanins and total phenolics from dried red grape skin. *Journal of Agricultural and Food Chemistry*, *51*, 5207-5213.

Jung, W. H., Kwak, N.-S., Hwang, T. S., & Yi, K. B. (2012). Preparation of highly porous TiO_2 nanofibers for dye-sensitized solar cells (DSSCs) by electro-spinning. *Applied Surface Science*, *261*, 343-352.

Jonathan, E., Onimisi, M. Y., & Eli, D. (2016). Natural pigments as sensitizers for dye sensitized solar cells. *Advances in Materials*, *5*(5), 31-34.

Jose, R., Kumar, A., Thavasi, V., & Ramakrishna, S. (2008). Conversion efficiency versus sensitizer for electrospun TiO_2 nanorod electrodes in dye-sensitized solar cells. *Nanotechnology*, *19*, 1-7.

Karruppuchamy, S., Jeong, J. M., Amalnerkar, D. P., & Minoura, H. (2006). Photoinduced hydrophilicity of titanium dioxide thin films prepared by cathodic electrodeposition. *Vacuum*, *80*, 494-498.

Karthikeyan, C. S., Thelakkat, M., & Willert-Porada, M. (2006). Different mesoporous Titania films for solid-state dye sensitised solar cells. *Thin Solid Films*, *511*, 187-194.

Kawashima, T., Ezure, T., Okada, K., Matsui, H., Goto, K., & Tanabe, N. (2004). FTO/ITO double-layered transparent conductive oxide for dye-sensitized solar cells. *Journal of Photochemistry and Photobiology A: Chemistry*, *164*, 199-202.

Khazaei, K. M., Jafari, S. M., Ghorbani, M., Kakhki, A. H., & Sarfarazi, M. (2016). Optimization of anthocyanin extraction from saffron petals with response surface methodology. *Food Analytical Methods*, *9*, 1993-2001.

Khelashvili, G., Behrens, S., Weidenthaler, C., Vetter, C., Hinsch, A., Kern, R., Skupien, K., Dinjus, E., & Bönnemann, H. (2006). Catalytic platinum layers for dye solar cells: A comparative study. *Thin Solid Films*, *511*, 342-348.

Khoo, H. E., Azlan, A., Tang, S. T., & Lim, S. M. (2017). Anthocyanidins and anthocyanins: colored pigments as food, pharmaceutical ingredients and the potential health benefits. *Food & Nutrition Research*, *61*(1), 1-21.

Ki, C. S., Baek, D. H., Gang, K. D., Lee, K. H., Um, I. C., & Park, Y. H. (2005). Characterization of gelatin nanofiber prepared from gelatin–formic acid solution. *Polymer*, *46*, 5094-5102.

Kim, S. S., Nah, Y. C., Noh, Y. Y., Jo, J., & Kim, D. Y. (2006). Electrodeposited Pt for cost-efficient and flexible dye-sensitized solar cells. *Electrochimica Acta*, *51*, 3814-3819.

Kim, T.-Y., Park, K.-H., Lee, J.-W., Han, S., & Cho, S.-Y. (2014). Adsorption equilibrium and kinetics of Gardenia Blue on photoelectrode for dye-sensitized solar cells. *International Journal of Photoenergy*, *2014*, 1-7.

Kim, J.-H., Lee, J.-H., Kim, J.-Y., & Kim, S. S. (2018). Synthesis of aligned TiO_2 nanofibers using electrospinning. *Applied Sciences*, *8*(309), 1-10.

Kishiomoto, S., Maoka, T., Sumitomo, K., & Ohmya, A. (2005). Analysis of carotenoid composition in petals of calendula (*Calendula of ficinalis* L). *Bioscience, Biotechnology and Biochemistry*, *69*, 2122-2128.

Koç, B., & Kaymak-Ertekin, F. (2009). Response surface methodology and food processing applications. *Gıda*, *7*, 1-8.

Kong, F.-T., Dai, S.-Y., & Wang, K.-J. (2007). Review of recent progress in dye-sensitized solar cells. *Advances in Optoelectronics*, *2007*, 1-13.

Kumar, A., Jose, R., Fujihara, K., Wang, J., & Ramakrishna, S. (2007). Structural and optical properties of electrospun TiO_2 nanofibers. *Chemistry of Materials*, *19*(26), 6536-6542.

Kumar, P. S., Sahay, R., Aravindan, V., Jayaraman, S., Ling, W. C., Thavasi, V., Mhaisalkar, S. G., Madhavi, S., & Ramakrishna, S. (2012). Free-standing electrospun carbon nanofibres-a high performance anode material for lithium-ion batteries. *Journal of Physics D: Applied Physics*, *45*(26), 1-5.

Kumara, G. R. A., Kaneko, S., Okuya, M., Onwona-Agyeman, B., Konno, A., & Tennakone, K. (2006). Shiso leaf pigments for dye-sensitized solid-state solar cell. *Solar Energy Materials and Solar Cells*, *90*, 1220-1226.

Kushwaha, R., Srivastava, P., & Bahadur, L. (2013). Natural pigments from plants used as sensitizers for TiO_2 based dye-sensitized solar cells. *Journal of Energy*, *2013*, 1-8.

Lai, W. H., Su, Y. H., Teoh, L. G., & Hon, M. H. (2007). Commercial and natural dyes as photosensitizers for a water-based dye-sensitized solar cell loaded with gold nanoparticles. *Journal of Photochemistry and Photobiology A: Chemistry*, *195*, 307-313.

Lan, Z., Wu, J., Wang, D., Hao, S., Lin, J., & Huang, Y. (2007). Quasi-solid-state dye sensitized solar cells based on a sol–gel organic–inorganic composite electrolyte containing an organic iodide salt. *Solar Energy*, *81*(1), 117-122.

Lan, Z., Wu, J., Lin, J., Huang, M., Li, P., & Li, Q. (2008). Influence of ionic additives NaI/I_2 on the properties of polymer gel electrolyte and performance of quasi-solid state dye-sensitized solar cells. *Electrochemica Acta*, *53*, 2296-2301.

Lau, C., & Mi, Y. (2002). A study of blending and complexation of poly(acrylic acid)/poly(vinyl pyrrolidone). *Polymer*, *43*(3), 823-829.

Laudenslager, M. J., & Sigmund, W. M. (2012). Electrospinning. In B. Bharat (Ed.), *Encyclopedia of nanotechnology* (pp. 769-775). New York, NY: Springer Publishers.

Lee, J., Durst, R. W., & Wrolstad, R. E. (2005). Determination of total monomeric anthocyanin pigment content of fruit juices, beverages, natural colorants, and wines by the pH differential method: collaborative study. *Journal of AOAC International*, *88*, 1269-1278.

Lee, D., Kim, B.-Y., Lee, S.-J., Lee, M.-H., Song, Y.-S., & Lee, J.-Y. (2006). Titania nanofibers prepared by electrospinning. *Journal of the Korean Physical Society*, *48*(6), 1686-1690.

Lee, B. H., Song, M. Y., Jang, S.-Y., Jo, S. M., Kwak, S.-Y., & Kim, D. Y. (2009). Charge transport characteristics of high efficiency dye-sensitized solar cells based on electrospun TiO_2 nanorod photoelectrodes. *Journal of Physical Chemistry C*, *113*, 21453-21457.

Lee, J.-S., Lee, Y.-I., Song, H., Jang, D.-H., & Choa, Y. H. (2011). Synthesis and characterization of TiO_2 nanowires with controlled porosity and microstructure using electrospinning method. *Current Applied Physics*, *11*(1), S210-S214.

Lee, Y.-I., Lee, J.-S., Park, E.-S., Jang, D.-H., Lee, J.-E., Kim, K., Myung, N. V., & Choa, Y.-H. (2014). Effect of calcination temperature on the photocatalytic properties of electrospun TiO_2 nanofibers. *Journal of Nanoscience and Nanotechnology*, *14*, 8005-8009.

Levy, D., & Zayat, M. (2015). The Sol-Gel Handbook: Synthesis, Characterization and Applications. *Wiley-VCH, Weinheim, 2*, 841-881.

Leydet, Y., Gavara, R., Petrov, V., Diniz, A. M., Parola, A. J., Lima, J. C., & Pina, F. (2012). The effect of self-aggregation on the determination of the kinetic and thermodynamic constants of the network of chemical reactions in 3-glucoside anthocyanins. *Phytochemistry*, *83*, 125-135.

Li, D., & Xia, Y. (2003). Fabrication of Titania nanofibers by electrospinning. *Nano Letters*, *3*(4), 555-560.

Li, D., & Xia, Y., (2004). Electrospinning of nanofibers: Reinventing the wheel? *Advanced Materials*, *16*(14), 1151-1170.

Li, Y., Hwang, D. S., Lee, N. H., & Kim. S. J. (2005). Synthesis and characterization of carbon-doped titania as an artificial solar light sensitive photocatalyst. *Chemical Physics Letters*, *404*, 25-29.

Li, D., McCann, J. T., Xia, Y., & Marquez, M. (2006). Electrospinning: A simple and versatile technique for producing ceramic nanofibers and nanotubes. *Journal of the American Ceramic Society*, *89*(6), 1861-1869.

Li, B., Wang, L., Kang, B., Wang, P., & Qiu, Y. (2006). Review of recent progress in solid-state dye-sensitized solar cells. *Solar Energy Materials and Solar Cells*, *90*(5), 549-573.

Li, Y., Ku, S.-H., Chen, S.-M., Ali, M. A., & AlHemaid, F. M. A. (2013). Photoelectrochemistry for red cabbage extract as natural dye to develop a dye-sensitized solar cells. *International Journal of Electrochemical Science*, *8*, 1237-1245.

Liu, G.-L., Guo, H.-H., & Sun, Y.-M. (2012). Optimization of the extraction of anthocyanins from the fruit skin of *Rhodomyrtus tomentosa* (Ait.) hassk and identification of anthocyanins in the extract using high-performance liquid

chromatography-electrospray ionization-mass spectrometry (HPLC-ESI-MS). *International Journal of Molecular Sciences*, *13*, 6292-6302.

Liu, X., Zhang, Q., Li, J., Valanoor, N., Tang, X., & Cao. G. (2018). Increase of power conversion efficiency in dye-sensitized solar cells through ferroelectric substrate induced charge transport enhancement. *Scientific Reports*, *8*, 1-8.

Liyana-Pathirana, C., & Shahidi, F. (2005). Optimization of extraction of phenolic compounds from wheat using response surface methodology. *Food Chemistry*, *93*(1), 47-56.

Longo, C., & de Paoli, M.-A. (2003). Dye-sensitized solar cells: a successful combination of materials. *Journal of the Brazilian Chemical Society*, *14*(6), 889-901.

Lotfi, L., Kalbasi-Ashtari, A., Hamedi, M., & Ghorbani. F. (2015). Effects of enzymatic extraction on anthocyanins yield of saffron tepals (*Crocus sativus*) along with its color properties and structural stability. *Journal of Food and Drug Analysis*, *23*(2), 210-218.

Loughrey, K. (2002). Overview of Color Analysis. *Current Protocols in Food Analytical Chemistry*, *3*(1), F5.1.1-F5.1.13.

Lu, D., Fang, P., Liu, X., Zhai, S., Li, C., Zhao, X., Ding, J., & Xiong, R. (2015). A facile one-pot synthesis of TiO_2-based nanosheets loaded with Mn_xO_y nanoparticles with enhanced visible light–driven photocatalytic performance for removal of Cr(VI) or RhB. *Applied Catalysis B: Environmental*, *179*, 558-573.

Luceño-Sánchez, J. A., Díez-Pascual, A. M., & Capilla, R. P. (2019). Materials for photovoltaics: state of art and recent developments. *International Journal of Molecular Sciences*, *20*, 1-42.

Lucero, A., Rebolledo, C., & Buono-Core, G. E. (2012). Effect of some natural UV-absorbers on the photostabilization of active ingredients in German Chamomille floral extracts. Part I. *Journal of the Chilean Chemical Society*, *57*(3), 1309-1312.

Ludin, N. A., Mahmoud, A. M. A., Mohamad, A. B., Kadhum, A. A. H., Sopian, K., & Karim, N. S. A. (2014). Review on the development of natural dye photosensitizer for dye-sensitized solar cells. *Renewable and Sustainable Energy Reviews*, *31*, 386-396.

Lupan, O., Guérin, V. M., Tiginyanu, I. M., Ursaki, V. V., Chow, L., Heinrich, H., & Pauportéa, T. (2010). Well-aligned arrays of vertically oriented ZnO nanowire electrodeposited on ITO-coated glass and their integration in dye sensitized solar cells. *Journal of Photochemistry and Photobiology A: Chemistry*, *211*(1), 65-73.

Maabong, K., Muiva, C. M., Monowe, P., Sathiaraj, T. S., Hopkins, M., Nguyen, L., Malungwa, K., & Thobega, M. (2015). Natural pigment as photosensitizers for dye-sensitized solar cells with TiO_2 thin films. *International Journal of Renewable Energy Research*, *5*(10), 54-60.

Mali, S. S., Betty, C. A., Bhosale, P. N., Patil, P. S., & Hong, C. K. (2014). From nanocorals to nanorods to nanoflowers nanoarchitecture for efficient dye-sensitized solar cells at relatively low film thickness: All hydrothermal process. *Scientific Reports*, *4*, 1-8.

Manna, L., Scher, E. C., Li, L. S., & Alivisatos, A. P. (2002). Epitaxial growth and photochemical annealing of graded CdS/ZnS shells on colloidal CdSe nanorods. *Journal of the American Chemical Society*, *124*, 7136-7145.

Maran, J. P., & Manikandan, S. (2012). Response surface modeling and optimization of process parameters for aqueous extraction of pigments from prickly pear (*Opuntia ficus-indica*) fruit. *Dyes Pigments*, *95*, 465-472.

Maran, J. P., Manikandan, S., Nivetha, C. V., & Dinesh, R. (2013). Ultrasound assisted extraction of bioactive compounds from *Nephelium lappaceum* L. fruit peel using central composite face centered response surface design. *Arabian Journal of Chemistry*, *94*, 1-13.

Mathew, S., Yella, A., Gao, P., Humphry-Baker, R., Curchod, B. F., Ashari-Astani, N., Tavernelli, I., Rothlisberger, U., Nazeeruddin, M. K., & Grätzel, M. (2014). Dye-sensitized solar cells with 13% efficiency achieved through the molecular engineering of porphyrin sensitizers. *Nature Chemistry*, *6*, 242-248.

Martinson, A. B. F., Elam, J. W., Hupp, J. T., & Pellin, M. J. (2007). ZnO nanotube based dye-sensitized solar cells. *Nano Letters*, *7*(8), 2183-2187.

Matabola, K. P., & Moutloali, R. M. (2013). The influence of electrospinning parameters on the morphology and diameter of poly(vinyledene fluoride) nanofibers-effect of sodium chloride. *Journal of Materials Science*, *48*(16), 5475-5482.

Maurya, I. C., Srivastava, P., & Bahadur, L. (2016). Dye-sensitized solar cell using extract from petals of male flowers *Luffa cylindrical* L. as a natural sensitizer. *Optical Materials*, *52*, 150-156.

McCann, J. T., Li, D., & Xia, Y. (2005). Electrospinning of nanofibers with core-sheath, hollow, or porous structures. *Journal of Materials Chemistry*, *15*(7), 735-738.

McCusker, L. B., & Baerlocher, C. (2013). Electron crystallography as a complement to x-ray powder diffraction techniques. *Crystalline Materials*, *228*, 1-10.

Megelski, S., Stephens, J. S., Chase, D. B., & Rabolt, J. F. (2002). Micro-and nanostructured surface morphology on electrospun polymer fibers. *Macromolecules*, *35*(22), 8456-8466.

Mehmood, U., Rahman, S.-U., Harrabi, K., Hussein, I. A., & Reddy, B. V. S. (2014). Recent advances in dye sensitized solar cells. *Advances in Materials Science and Engineering*, *2014*, 1-12.

Mit-uppatham, C., Nithitanakul, M., & Supaphol, P. (2004). Ultrafine electrospun polyamide-6 fibers: effect of solution conditions on morphology and average fiber diameter. *Macromolecular Chemistry and Physics*, *205*(17), 2327-2338.

Mohmeyer, N., Wang, P., Schmidt, H.-W., Zakeeruddin, S. M., & Grätzel, M. (2004). Quasi-solid-state dye sensitized solar cells with 1,3:2,4-di-O-benzylidene-d-sorbitol derivatives as low molecular weight organic gelators. *Journal of Materials Chemistry*, *14*(12), 1905-1909.

Mourabet, M., El Rhilassi, A., El Boujaady, H., Bennani-Ziatni, M., & Taitai, A. (2017). Use of response surface methodology for optimization of fluoride adsorption in an aqueous solution by Brushite. *Arabian Journal of Chemistry*, *10*(2), 1-11.

Munawaroh, H., Fadillah, G., Saputri, L. N. M. Z., Hanif, Q. A., Hidayat, R., Wahyuningsih, S. (2016). The co-pigmentation of anthocyanin isolated from mangosteen pericarp (*Garcinia Mangostana* L.) as natural dye for dye-sensitized solar cells (DSSC). *Materials Science and Engineering*, *107*, 1-6.

Myers, R. H., Montgomery, D. C., & Anderson-Cook, C. M. (2009). Two-level factorial designs: response surface methodology-process and product optimization using designed experiments (3th ed.). Canada: John Wiley & Sons.

Naczk, M., & Shahidi, F. (2004). Extraction and analysis of phenolics in food. *Journal of Chromatography A*, *1054*, 95-111.

Nair, A. S., Jose, R., Shengyuan, Y., & Ramakrishna, S. (2011). A simple recipe for an efficient TiO_2 nanofiber-based dye-sensitized solar cell. *Journal of Colloid and Interface Science*, *353*(1), 39-45.

Nakade, S., Kambe, S., Kitamura, T., Wada, Y., & Yanagida, S. (2001). Effects of lithium ion density on electron transport in nanoporous TiO_2 Electrodes. *Journal of Physical Chemistry B*, *105*, 9150-9152.

Nakata, K., & Fujishima, A. (2012). TiO_2 photocatalysis: design and applications. *Journal of Photochemistry and Photobiology C: Photochemistry Reviews*, *13*(3), 169-189.

Na-Phattalung, S., Smith, M. F., Kim, K., Du, M. H., Wei, S. H., Zhang, S. B., & Limpijumnong, S. (2006). First-principles study of native defects in anatase TiO_2. *Physical Review B*, *73*(12), 1-6.

Narayan, M. R. (2012). Review: Dye sensitized solar cells based on natural photosensitizers. *Renewable and Sustainable Energy Reviews*, *16*(1), 208-215.

Navas, M. J., Jiménez-Moreno, A. M., Bueno, J. M., Sáez-Plaza, P., & Asuero, A. G. (2012). Analysis and antioxidant capacity of anthocyanin pigments. Part IV: Extraction of anthocyanins. *Critical Reviews in Analytical Chemistry*, *42*(4), 313-342.

Nazeeruddin, M. K., Baranoff, E., & Grätzel, M. (2011). Dye-sensitized solar cells: A brief overview. *Solar Energy*, *85*, 1172-1178.

Nishantha, M. R., Yapa, Y. P. Y. P., & Perera, V. P. S. (2012). Sensitization of photoelectrochemical solar cells with a natural dye extracted from *Kopsia flavida* fruit. *Proceedings of the Technical Sessions*, *28*, 54-58.

Nuansing, W., Ninmuang, S., Jarernboon, W., Maensiri, S., & Seraphin, S. (2006). Structural characterization and morphology of electrospun TiO_2 nanofibers. *Materials Science and Engineering B*, *131*, 147-155.

Ooe, E., Ogawa, K., Horiuchi, T., Tada, H., Murase, H., Tsuruma, K., Shimazawa, M., & Hara, H. (2016). Analysis and characterization of anthocyanins and carotenoids in Japanese blue tomato. *Bioscience, Biotechnology, and Biochemistry*, *80*(2), 341-349.

Ooyama, Y., & Harima, Y. (2012). Photophysical and electrochemical properties, and molecular structures of organic dyes for dye-sensitized solar cells. *Chemphyschem*, *13*(18), 4032-4080.

O'regan, B., & Grätzel, M. (1991). A low-cost, high-efficiency solar cell based on dye-sensitized colloidal TiO_2 films. *Nature*, *353*(6346), 737-740.

Paliwal, H., Goyal, S., Singla, S., & Daksh, S. (2016). Pigments from natural sources: An overview. *International Journal of Research in Pharmacy and Pharmaceutical Sciences*, *1*(3), 1-12.

Palomares, E., Clifford, J. N., Haque, S. A., Lutz, T., & Durrant, J. R. (2003). Control of charge recombination dynamics in dye sensitized solar cells by the use of conformally deposited metal oxide blocking layers. *Journal of the American Chemical Society*, 125(2), 475-482.

Papageorgiou, N., Maier, W. F., & Grätzel, M. (1997). An iodine/triiodide reduction electrocatalyst for aqueous and organic media. *Journal of the Electrochemical Society*, *144*(3), 876-884.

Park, N.-G., van de Lagemaat, J., & Frank, A. J. (2000). Comparison of dye-sensitized rutile-and anatase-based TiO_2 solar cells. *Journal of Physical Chemistry B*, *104*(38), 8989-8994.

Park, Y. D., Anabuki, K., Kim, S., Park, K.-W., Lee, D. H., Um, S. H., Kim, J., & Cho, J. H. (2013). Fabrication of stable electrospun TiO_2 nanorods for high-performance dye-sensitized solar cells. *Macromolecular Research*, *21*(6), 636-640.

Patil, N., & Datar, A. (2015). Extraction, stability and separation of anthocyanins of *Ixora coccinea* Linn. *International Journal of Pharmacy and Pharmaceutical Sciences*, *7*(3), 198-202.

Patra, S. N., Easteal, A. J., & Bhattacharyya, D. (2008). Parametric study of manufacturing poly(lactic) acid nanofibrous mat by electrospinning. *Journal of Materials Science*, *44*(2), 647-654.

Patrocínio, A. O. T., Mizoguchi, S. K., Paterno, L. G., Garcia, C. G., & Iha, N. Y. M. (2009). Efficient and low cost devices for solar energy conversion: efficiency and stability of some natural-dye-sensitized solar cells. *Synthetic Metals*, *159*, 2342-2344.

Pervaiz, T., Songtao, J., Faghihi, F., Haider, M. S., & Fang, J. (2017). Naturally occurring anthocyanin, structure, functions and biosynthetic pathway in fruit plants. *Journal of Plant Biochemistry and Physiology*, *5*(2), 1-9.

Pillay, V., Dott, C., Choonara, Y. E., Tyagi, C., Tomar, L., Kumar, P., du Toit, L. C., & Ndesendo, V. M. K. (2013). A review of the effect of processing variables on the fabrication of electrospun nanofibers for drug delivery applications. *Journal of Nanomaterials*, *2013*, 1-22.

Pishgar-Komleh, S. H., Keyhani, A., Mostofi-Sarkari, M. R., & Jafari, A. (2012). Application of response surface methodology for optimization of Picker-Husker harvesting losses in corn seed. *Iranica Journal of Energy and Environment*, *3*(2), 134-142.

Polo, A. S., & Iha, N. Y. M. (2006). Blue sensitizers for solar cells: natural dyes from *Calafate* and *Jaboticaba*. *Solar Energy Materials & Solar Cells*, *90*, 1936-1944.

Pradeep, D., & Dubey, R. S. (2017). Experimental study of electrospun TiO_2 nanofibers. *International Research Journal of Engineering and Technology*, *4*(9), 1082-1084.

Prima, E. C., Yuliarto, B., & Suyatman. (2013). Performance of natural carotenoids from *Musa aromatica* and *Citrus medica* var lemon as photosensitizers for dye-sensitized solar cells with TiO_2 nanoparticle. *Advanced Materials Research*, *789*, 167-170.

Qiu, P., Cui, M., Kang, K., Park, B., Son, Y., Khim, E., Jang, M., & Khim, J. (2014). Application of Box-Behnken design with response surface methodology for modeling and optimizing ultrasonic oxidation of arsenite with H_2O_2. *Central European Journal of Chemistry*, *12*(2), 164-172.

Rajha, H. N., Darra, N. E., Hobaika, Z., Boussetta, N., Vorobiev, E., Maroun, R. G., & Louka, N. (2014). Extraction of total phenolic compounds, flavonoids, anthocyanins and tannins from grape byproducts by response surface methodology. Influence of solid-liquid ratio, particle size, time, temperature and solvent mixtures on the optimization process. *Food and Nutrition Sciences*, *5*, 397-409.

Ramakrishna, S., Jose, R., Archana, P. S., Nair, A. S., Balamurugan, R., Venugopal, J., & Teo, W. E. (2010). Science and engineering of electrospun nanofibers for advances in clean energy, water filtration, and regenerative medicine. *Journal of Materials Science*, *45*, 6283-6312.

Ramasamy, S., Mazlan, N. A., Ramli, N. A., Rasidi, W. N. A., & Manickam, S. (2016). Bioactivity and stability studies of anthocyanin-containing extracts from *Garcinia mangostana* L. and *Etlingera elatior* Jack. *Sains Malaysiana*, *45*(4), 559–565.

Reijnders, L. (2010). Design issues for improved environmental performance of dye sensitized and organic nanoparticulate solar cells. *Journal of Cleaner Production*, *18*, 307-312.

Reneker, D. H., & Yarin, A. L. (2008). Electrospinning jets and polymer nanofibers. *Polymer*, *49*(10), 2387-2425.

Revilla, E., Ryan, J.-M., & Martin-Ortega, G. (1998). Comparison of several procedures used for the extraction of anthocyanins from red grapes. *Journal of Agricultural and Food Chemistry*, *46*, 4592-4597.

Rezaee, R., Maleki, A., Jafari, A., Mazloomi, S., Zandsalimi, Y., & Mahvi, A. H. (2014). Application of response surface methodology for optimization of natural organic matter degradation by UV/H_2O_2 advanced oxidation process. *Journal of Environmental Health Science & Engineering*, *12*, 1-8.

Rezvani, F., Parvazian, E., & Hosseini, S. A. (2016). Dye-sensitized solar cells based on composite TiO_2 nanoparticle–nanorod single and bi-layer photoelectrodes. *Bulletin of Materials Science*, *39*(6), 1397-1402.

Rho, W.-Y., Jeon, H., Kim, H.-S., Chung, W.-J., Suh, J. S., & Jun, B.-H. (2015). Recent progress in dye-sensitized solar cells for improving efficiency: TiO_2 nanotube arrays in active layer. *Journal of Nanomaterials*, *2015*, 1-17.

Rühle, S., Shalom, M., & Zaban, A. (2010). Quantum-dot-sensitized solar cells. *ChemPhysChem*, *11*, 2290-2304.

Ruenroengklin, N., Zhong, J., Duan, X., Yang, B., Li, J., & Jiang, Y. (2008). Effects of various temperatures and pH values on the extraction yield of phenolics from litchi fruit pericarp tissue and the antioxidant activity of the extracted anthocyanins. *International Journal of Molecular Sciences*, *9*, 1333-1341.

Rutledge, G. C., & Fridrikh, S. V. (2007). Formation of fibers by electrospinning. *Advanced Drug Delivery Reviews*, *59*, 1384-1391.

Saito, Y., Kambe, S., Kitamura, T., Wada, Y., & Yanagida, S. (2004). Morphology control of mesoporous TiO_2 nanocrystalline films for performance of dye-sensitized solar cells. *Solar Energy Materials and Solar Cells*, *83*(1), 1-13.

Saji, V. S., & Pyo, M. (2010). Dye sensitized solar cell of TiO_2 nanoparticle/nanorod composites prepared via low-temperature synthesis in oleic acid. *Thin Solid Films*, *518*, 6542-6546.

Salar, R. K., Purewal, S. S., & Bhatti, M. S. (2016). Optimization of extraction conditions and enhancement of phenolic content and antioxidant activity of pearl millet fermented with *Aspergillus awamori* MTCC-548. *Resource-Efficient Technologies*, *2*, 148-157.

Sarker, S., Ahammad, A. J. S., Seo, H. W., & Kim, D. M. (2014). Electrochemical impedance spectra of dye-sensitized solar cells: fundamentals and spreadsheet calculation. *International Journal of Photoenergy*, *2014*, 1-17.

Sarkis, J. R., Jaeschke, D. P., Tessaro, I. C., & Marczak, L. D. F. (2013). Effects of ohmic and conventional heating on anthocyanin degradation during the processing of blueberry pulp. *LWT - Food Science and Technology*, *51*, 79-85.

Sawicka, K. M., & Gouma, P. (2006). Electrospun composite nanofibers for functional applications. *Journal of Nanoparticle Research*, *8*, 769-781.

Selvaraj, P., Roy, A., Ullah, H., Devi, P. S., Tahir, A. A., Mallick, T. K., & Senthilarasu, S. (2018). Soft-template synthesis of high surface area mesoporous titanium dioxide for dye-sensitized solar cells. *International Journal of Energy Research*, *2018*, 1-12.

Sill, T. J., & von Recum, H. A. (2008). Electrospinning: applications in drug delivery and tissue engineering. *Biomaterials*, *29*(13), 1989-2006.

Silva, S., Costa, E. M., Calhau, C., Morais, R. M., & Pintado, M. E. (2017). Anthocyanin extraction from plant tissues: A review. *Critical Reviews in Food Science and Nutrition*, *57*(14), 3072-3083.

Sima, C., Grigoriu, C., & Antohe, S. (2010). Comparison of the dye-sensitized solar cells performances based on transparent conductive ITO and FTO. *Thin Solid Films*, *519*(2), 595-597.

Singh, P. K., Kim, K.-W., Park, N.-G., & Rhee, H.-W. (2008). Mesoporous nanocrystalline TiO_2 electrode with ionic-liquid based solid polymer electrolyte for dye sensitized solar cell application. *Synthetic Metals*, *158*(14), 590-593.

Singh, L. K., Karlo, T., & Pandey, A. (2014). Performance of fruit extract of *Melastoma Malabathricum* L as sensitizer in DSSCs. *Spectrochimica Acta Part A: Molecular and Biomolecular Spectroscopy*, *118*, 938-943.

Sinha, K., Saha, P. D., & Datta, S. (2012). Extraction of natural dye from petals of flame of forest (*Butea monosperma*) flower: Process optimization using response surface methodology (RSM). *Dyes and Pigments*, *94*, 212-216.

Sohrabi, A., Shaibani, P. M., & Thundat, T. (2013). The effect of applied electric field on the diameter and size distribution of electrospun nylon 6 nanofibers. *Scanning*, *35*(3), 183-188.

Someswararao, M. V., Dubey, R. S., Subbarao, P. S. V., & Singh, S. (2018). Electrospinning process parameters dependent investigation of TiO_2 nanofibers. *Results in Physics*, *11*, 223-231.

Song, J. Y., Wang, Y. Y., & Wan, C. C. (1999). Review of gel-type polymer electrolytes for lithium-ion batteries. *Journal of Power Sources*, *77*(2), 183-197.

Song, M. Y., Ahn, Y. R., Jo, S. M., Kim, D. Y., & Ahn, J.-P. (2005). TiO_2 single-crystalline nanorod electrode for quasi-solid-state dye-sensitized solar cells. *Applied Physics Letters*, *87*(11), 1-3.

Song, M. Y., Kim, D. K., Ihn, K. J., Jo, S. M., & Kim, D. Y. (2005). New application of electrospun TiO_2 electrode to solid-state dye sensitized solar cells. *Synthetic Metals*, *153*, 77-80.

Spigno, G., Tramelli, L., & De Faveri, D. M. (2007). Effects of extraction time, temperature and solvent on concentration and antioxidant activity of grape marc phenolics. *Journal of Food Engineering*, *81*(1), 200-208.

Spillmann, D., & Burger, M. M. (1996). Carbohydrate–carbohydrate interactions in adhesion. *Journal of Cellular Biochemistry*, *61*, 562-568.

Suhaimi, S., Shahimin, M. M., Alahmed, Z. A., Chyský, J., & Reshak, A. H. (2015). Materials for enhanced dye-sensitized solar cell performance: Electrochemical application. *International Journal of Electrochemical Science, 10*(4), 2859-2871.

Sun, B., Long, Y. Z., Zhang, H. D., Li, M. M., Duvail, J. L., Jiang, X. Y., & Yin, H. L. (2014). Advances in three-dimensional nanofibrous macrostructures via electrospinning. *Progress in Polymer Science*, *39*, 862-890.

Shafi'i, S. N., Ahmad, N., Abidin, M. Z., Hani, N. M., & Ismail, N. (2013). Optimization of hydrocolloids and maltodextrin addition on roselle-based fruit leather using two-level full factorial design. *International Journal of Bioscience, Biochemistry and Bioinformatics*, *3*(4), 387-391.

Shaheen, S. E., Brabec, C. J., Sariciftci, N. S., Padinger, F., Fromherz, T., & Hummelen, J. C. (2001). 2.5% efficient organic plastic solar cells. *Applied Physics Letters, 78* (6), 841-843.

Shahid, M., Ul-Islam, S., & Mohammad, F. (2013). Recent advancements in natural dye applications: a review. *Journal of Cleaner Production*, *53*, 310-331.

Shalini, S., Balasundaraprabhu, R., Prasanna, S., Mallick, T. K., & Senthilarasu, S. (2015). Review on natural dye sensitized solar cells: Operation, materials and methods. *Renewable and Sustainable Energy Reviews*, *51*, 1306-1325.

Shalini, S., Balasundaraprabhu, R., Kumar, T. S., Prabavathy, N., Senthilarasu, S., & Prasanna, S. (2016). Status and outlook of sensitizers/dyes used in dye sensitized solar cells (DSSC): a review. *International Journal of Energy Research*, *40*, 1303-1320.

Sharif, A., Saim, N., Jasmani, H., & Ahmad, W. Y. W. (2010). Effects of solvent and temperature on the extraction of colorant from Onion (*Allium cepa*) skin using pressurized liquid extraction. *Asian Journal of Applied Sciences*, *3*(4), 262-268.

Shelke, R. S., Thombre, S. B., Patrikar, S. R. (2013). Status and perspectives of dyes used in dye sensitized solar cells. *International Journal of Renewable Energy Resources*, *3*, 54-61.

Shi, J., Yu, J., Pohorly, J., Young, J. C., Bryan, M., & Wu, Y. (2003). Optimization of the extraction of polyphenols from grape seed meal by aqueous ethanol solution. *Food, Agriculture & Environment*, *1*(2), 42-47.

Shibaev, L. A., Melenevskaya, E. Y., Ginzburg, B. M., Yakimanskii, A. V., Ratnikova, O. V., & Gribanov, A. V. (2008). Thermal and tribological properties of fullerene containing composite systems. Part 3. Features of the mechanism of thermal

degradation of poly-(N-vinyl-pyrrolidone) and its compositions with fullerene C-60. *Journal of Macromolecular Science, Part B-Physics*, *47*(2), 276-287.

Steytler, D. (1996). Supercritical fluid extraction. In A. S. Grandison & M. J. Lewis (Eds.), *Separation processes in the food and biotechnology industries* (pp. 41-42), Abington: Woodhead Publishing.

Sugathan, V., John, E., & Sudhakar, K. (2015). Recent improvements in dye sensitized solar cells: A review. *Renewable and Sustainable Energy Reviews*, *52*, 54-64.

Sukigara, S., Gandhi, M., Ayutsede, J., Micklus, M., & Ko, F. (2003). Regeneration of Bombyx mori silk by electrospinning - Part 1: Processing parameters and geometric properties. *Polymer*, *44*(19), 5721-5727.

Susanti, D., Nafi, M., Purwaningsih, H., Fajarin, R., & Kusuma, G. E. (2014). The preparation of dye sensitized solar cell (DSSC) from TiO_2 and Tamarillo extract. *Procedia Chemistry*, *9*, 3-10.

Swami, R. (2012). Solar cell. *International Journal of Scientific and Research Publications*, *2*(7), 1-5.

Tabaei, H. S. M., Kazemeini, M., & Fattahi, M. (2012). Preparation and characterization of visible light sensitive nano titanium dioxide photocatalyst. *Scientia Iranica, 19*(6), 1626-1631.

Tan, M. C., Khoo, H. E., & Tan, C. P. (2014). Optimization for extraction on total phenolic content and radical scavenging capacity of Henna (*Lawsonia inermis*) stems using response surface methodology. *International Food Research Journal*, *21*, 789-794.

Tang, X., Wang, Y., & Cao, G. (2013). Effect of the adsorbed concentration of dye on charge recombination in dye-sensitized solar cells. *Journal of Electroanalytical Chemistry*, *694*, 6-11.

Tarus, B., Fadel, N., Al-Oufy, A., & El-Messiry, M. (2016). Effect of polymer concentration on the morphology and mechanical characteristics of electrospun cellulose acetate and poly(vinyl chloride) nanofiber mats. *Alexandria Engineering Journal*, *55*(3), 2975-2984.

Taya, S. A., El-Agez, T. M., El-Ghamri, H. S., & Abdel-Latif, M. S. (2013). Dye-sensitized solar cells using fresh and dried natural dyes. *International Journal of Materials Science and Applications*, *2*(2), 37-42.

Taya, S. A., El-Agez, T. M., Elrefi, K. S., & Abdel-Latif, M. S. (2015). Dye-sensitized solar cells based on dyes extracted from dried plant leaves. *Turkish Journal of Physics*, *39*, 24-30.

Thavasi, V., Singh, G., & Ramakrishna, S. (2008). Electrospun nanofibers in energy and environmental applications. *Energy & Environmental Science*, *1*(2), 205-221.

Thirunavukkarasu, A., & Nithya, R. (2011). Response surface optimization of critical extraction parameters for anthocyanin from *Solanum melongena*. *Journal of Bioprocessing & Biotechniques*, *1*(1), 1-4.

Thomas, S., Deepak, T. G., Anjusree, G. S., Arun, T. A., Nair, S. V., & Nair, A. S. (2014). A review on counter electrode materials in dye-sensitized solar cells. *Journal of Materials Chemistry A*, *2*(13), 4474-4490.

Tsekouras, G., Mozer, A. J., & Wallace, G. G. (2008). Enhanced performance of dye sensitized solar cells utilizing platinum electrodeposit counter electrodes. *Journal of Electrochemical Society, 155*(7), K124-K128.

Tungprapa, S., Puangparn, T., Weerasombut, M., Jangchud, I., Fakum, P., Semongkhol, S., Meechaisue, C., & Supaphol, P. (2007). Electrospun cellulose acetate fibers: effect of solvent system on morphology and fiber diameter. *Cellulose*, *14*(6), 563-575.

Velmurugan, P., Kamalakannan, S., Balachandar, V., Lakshmanaperumalsamy, P., Chae, J.-C., & Oh, B.-T. (2009). Natural pigment extraction from five filamentous fungi for industrial applications and dyeing of leather. *Carbohydrate Polymers*, *79*(2), 262-268.

Wang, Z.-S., Kawauchi, H., Kashima, T., & Arakawa, H. (2004). Significant influence of TiO_2 photoelectrode morphology on the energy conversion efficiency of N719 dye-sensitized solar cell. *Coordination Chemistry Reviews*, *248*, 1381-1389.

Wang, T., & Kumar, S. (2006). Electrospinning of polyacrylonitrile nanofibers. *Journal of Applied Polymer Science*, *102*(2), 1023-1029.

Wang, Y. (2009). Recent research progress on polymer electrolytes for dye-sensitized solar cells. *Solar Energy Materials and Solar Cells*, *93*(8), 1167-1175.

Wang, L., Zhang, H., Wang, C., & Ma, T. (2012). Highly stable gel-state dye-sensitized solar cells based on high soluble polyvinyl acetate. *ACS Sustainable Chemistry & Engineering*, *1*(1), 205-208.

Wang, H., Guo, Z., Wang, S., & Liu, W. (2014). One-dimensional titania nanostructures: Synthesis and applications in dye-sensitized solar cells. *Thin Solid Films*, *558*, 1-19.

Wang, H., Wang, B., Yu, J., Hu, Y., Xia, C., Zhang, J., & Liu, R. (2015). Significant enhancement of power conversion efficiency for dye sensitized solar cell using 1D/3D network nanostructures as photoanodes. *Scientific Reports*, *5*, 1-9.

Wanninayake, W. M. N. M. B., Premaratne, K., & Rajapakse, R. M. G. (2016). High efficient dye-sensitized solar cells based on synthesized SnO_2 nanoparticles. *Journal of Nanomaterials*, *2016*, 1-8.

Watthanaarun, J., Pavarajarn, V., & Supaphol, P. (2005). Titanium (IV) oxide nanofibers by combined sol-gel and electrospinning techniques: preliminary report on effects of preparation conditions and secondary metal dopant. *Science and Technology of Advanced Materials*, *6*, 240-245.

Wen, Y., Chen, H., Zhou, X., Deng, Q., Zhao, Y., Zhao, C., & Gong, X. (2015). Optimization of the microwave-assisted extraction and antioxidant activities of anthocyanins from blackberry using a response surface methodology. *RSC Advances, 5*(25), 19686-19695.

Wongcharee, K., Meeyoo, V., & Chavadej, S. (2007). Dye-sensitized solar cell using natural dyes extracted from rosella and blue pea flowers. *Solar Energy Materials and Solar Cells*, *91*(7), 566-571.

Wrolstad, R. E., Durst, R. W., & Lee, J. M. (2005). Tracking color and pigment changes in anthocyanin products. *Trends in Food Science and Technology*, *16*(9), 423-428.

Wu, J., Lan, Z., Hao, S., Li, P., Lin, J., Huang, M., Fang, L., & Huang, Y. (2008). Progress on the electrolytes for-dye sensitized solar cell. *Pure and Applied Chemistry*, *80*, 2241-2258.

Würfel, U., Peters, M., & Hinsch, A. (2008). Detailed experimental and theoretical investigation of the electron transport in a dye solar cell by means of a three-electrode configuration. *Journal of Physical Chemistry C*, *112*(5), 1711-1720.

Yang, Z., Chen, Z., Yuan, S., Zhai, W., Piao, X., & Piao, X. (2009). Extraction and identification of anthocyanin from purple corn (*Zea mays* L.). *International Journal of Food Science and Technology*, *44*, 2485-2492.

Yang, R.-Y., Chen, H.-Y., & Lai, F.-D. (2012). Performance degradation of dye-sensitized solar cells induced by electrolytes. *Advances in Materials Science and Engineering*, *2012*, 1-4.

Yang, J. H., Bark, C. W., Kim, K. H., & Choi, H. W. (2014). Characteristics of the dye-sensitized solar cells using TiO_2 nanotubes treated with $TiCl_4$. *Materials*, *7*(5), 3522-3532.

Yarin, A. L. (2011). Coaxial electrospinning and emulsion electrospinning of core–shell fibers. *Polymers for Advanced Technologies*, *22*, 310-317.

Yen, M.-Y., Yen, C.-Y., Liao, S.-H., Hsiao, M.-C., Weng, C.-C., Lin, Y.-F., Ma, C.-C. M., Tsai, M.-C., Su, A., Ho, K.-K., & Liu, P.-L. (2009). A novel carbon-based nanocomposite plate as counter electrode for dye-sensitized solar cells. *Composite Science and Technology*, *69*, 2193-2197.

Yilmaz, F. M., Karaaslan, M., & Vardin, H. (2015). Optimization of extraction parameters on the isolation of phenolic compounds from sour cherry *(Prunus cerasus* L.*)* pomace. *Journal of Food Science and Technology*, *52*(5), 2851-2859.

Yoon, C. H., Vittal, R., Lee, J., Chae, W. S., & Kim, K. J. (2008). Enhanced performance of a dye-sensitized solar cell with an electrodeposited-platinum counter electrode. *Electrochimica Acta*, *53*(6), 2890-2896.

Yusuf, S. N. F., Aziz, M. F., Hassan, H. C., Bandara, T. M. W. J., Mellander, B.-E., Careem, M. A., & A. K. Arof. (2014). Phthaloylchitosan-based gel polymer electrolytes for efficient dye-sensitized solar cells. *Journal of Chemistry*, *2014*, 1-8.

Zallen, R., & Moret, M. P. (2006). The optical absorption edge of brookite TiO_2. *Solid State Communications, 137*, 154-157.

Zhang, Y. Z., Wang, X., Feng, Y., Li, J., Lim, C. T., & Ramakrishna, S. (2006). Coaxial electrospinning of (fluorescein isothiocyanate-conjugated bovine serum albumin)-encapsulated poly(e-caprolactone) nanofibers for sustained release. *Biomacromolecules*, *7*(4), 1049-1057.

Zhang, Y., Wu, L., Xie, E., Duan, H., Han, W., & Zhao, J. (2009). A simple method to prepare uniform-size nanoparticle TiO_2 electrodes for dye-sensitized solar cells. *Journal of Power Sources*, *189*(2), 1256-1263.

Zhang, L., & Cole, J. M. (2015). Anchoring groups for dye-sensitized solar cells. *ACS Applied Materials & Interfaces*, *7*(6), 3427-3455.

Zhou, H., Wu, L., Gao, Y., & Ma, T. (2011). Dye-sensitized solar cells using 20 natural dyes as sensitizers. *Journal of Photochemistry and Photobiology A: Chemistry*, *219*, 188-194.

Zhu, H., Zeng, H., Subramanian, V., Masarapu, C., Hung, K. H., & Wei, B. (2008). Anthocyanin-sensitized solar cells using carbon nanotube films as counter electrodes. *Nanotechnology*, *19*(46), 1-5.

Zhu, M., Chen, L., Gong, H., Zi, M., & Cao, B. (2014). A novel TiO_2 nanorod/nanoparticle composite architecture to improve the performance of dye-sensitized solar cells. *Ceramics International*, *40*(1), 2337-2342.

LIST OF PUBLICATIONS AND PAPERS PRESENTED

PUBLICATIONS

PAPERS

1) Arof, A. K., **Mat Nor, N. A.,** Ramli, N. R., Noor, I. M., Aziz, N., & Taha, R. M. (2018). Color analysis of Saffron (*Crocus sativus* L.) as potential natural colorant. *Pigment & Resin Technology, 47*(6), 485-489.

2) Arof, A. K., **Mat Nor, N. A.,** Ramli, N. R., Aziz, N., Noor, I. M., & Taha, R. M. (2017). Utilization of Saffron (*Crocus sativus* L.) as sensitizer in dye-sensitized solar cells (DSSCs). *Optical and Quantum Electronics, 49*, 1-8.

3) **Mat Nor, N. A.,** & Arof, A. K. (2016). On statistical analysis of factors affecting anthocyanin extraction from *Ixora siamensis. Optical Materials, 60*, 462-466.

4) **Mat Nor, N. A.,** & Arof, A. K. (2016). Optimization of extraction parameters for anthocyanin from *Ixora siamensis* by response surface methodology. *Optical and Quantum Electronics, 48*, 1-9.

5) **Mat Nor, N. A.,** Aziz, N., Mohd-Adnan, A. F., Taha, R. M., & Arof, A. K. (2016). Chromaticity and color saturation of ultraviolet irradiated poly(vinyl alcohol)-anthocyanin coatings. *Optical Materials, 56*, 18-21.

PAPERS PRESENTED

1) **Mat Nor, N. A.,** Noor, I. M., Aziz, N., & Arof, A. K. (2017). *The preparation of dye-sensitized solar cells (DSSCs) from TiO_2 and Ixora siamensis extract*. Paper presented at the National Workshop on Functional Materials (NWFM 2017), 17-18th January 2017, University of Malaya, Kuala Lumpur, Malaysia (National).

2) **Mat Nor, N. A.,** Noor, I. M., Aziz, N., & Arof, A. K. (2016). *Ixora siamensis as new natural dye source for dye-sensitized solar cells*. Paper presented at 2nd International Conference on Solar Energy Photovoltaic (ICSEP-16), 17-19th December 2016, Bhubaneswar, India (International).

3) **Mat Nor, N. A.,** Aziz, N., Mohd-Adnan, A. F., Buraidah, M. H., & Arof, A. K. (2016). *Identification of anthocyanin from Ixora siamensis and its potential use as photo-sensitizer in dye-sensitized solar cells*. Paper presented at the International Symposium on Materials and Assets Integrity 2016 (ISMAI 2016), 16-18th May, 2016, Putra World Trade Centre, Kuala Lumpur, Malaysia (International).

BOOK CHAPTER

1) Arof, A. K., Aziz, N., **Mat Nor, N. A.,** Rahim, A. S., & Kufian, M. Z. (2017). Imaging of electrospun nanoparticle electrode materials. In A. Méndez-Vilas, (Eds.), *Microscopy and imaging science: practical approaches to applied research and education* (pp. 438-449). Spain: Formatex Research Center. ISBN-13: 978-84-942134-9-6.